UNIVERSITÀ DEGLI STUDI
DI MODENA E REGGIO EMILIA

Dottorato di ricerca in

Information and Communication Technologies (ICT)

CICLO XXXVIII

High reliable and sustainable electrical machines for vehicle electrification

in cooperazione con l'University of Nottingham

Candidato: Gregorio Cutuli

Relatore italiano (Tutor): Prof. Davide Barater

Relatore inglese (Tutor): Prof. Tianjie Zou

Correlatore italiano (Co-Tutor): Prof. Stefano Nuzzo

Correlatore inglese (Co-Tutor): Prof. Chris Gerada

Coordinatore del Corso di Dottorato: Prof. Luigi Rovati

To those
I love.

Sommario

Le decisioni sociali, economiche e ambientali contemporanee sono sempre più orientate dai principi della sostenibilità. Dal punto di vista ambientale, una delle politiche più rilevanti per la riduzione delle emissioni consiste nell'elettrificazione del settore dei trasporti, responsabile attualmente di circa il 23 % della produzione globale di CO_2.

Tale transizione ha determinato una crescente attenzione verso la sostenibilità nella progettazione dei sistemi di trazione elettrica, con l'obiettivo di ridurre le emissioni lungo l'intero ciclo di vita del prodotto: dall'approvvigionamento delle materie prime e dalla produzione, fino alla fase di esercizio, al riciclo e al riutilizzo.

Limitando l'ambito di analisi allo sviluppo delle macchine elettriche destinate ad applicazioni di trazione, le attuali tendenze di ricerca promuovono strategie progettuali che impiegano materiali alternativi al fine di ridurre l'impatto ambientale e migliorare la riciclabilità, garantendo al contempo elevati livelli di affidabilità per assicurare una lunga durata operativa e la minimizzazione dei rifiuti.

L'implementazione di tali strategie, tuttavia, può introdurre diverse criticità: materiali a minore impatto ambientale o approcci progettuali innovativi comportano spesso compromessi in termini di prestazioni elettromagnetiche e termiche, nonché vincoli di natura produttiva, che richiedono l'adattamento delle linee di fabbricazione esistenti.

Questo lavoro di tesi affronta tali aspetti proponendo una progettazione sostenibile e ad alta affidabilità di macchine elettriche, mediante l'impiego di avvolgimenti hairpin in alluminio in sostituzione di quelli convenzionali in rame. In particolare, lo studio prende avvio con la progettazione e l'analisi elettromagnetica di macchine hairpin in alluminio, messe a confronto con le corrispondenti versioni in rame, al fine di definire linee guida di progettazione.

La fattibilità tecnica della soluzione in alluminio è successivamente verificata attraverso un'analisi termica comparativa, condotta in condizioni di raffreddamento identiche per le due configurazioni. Segue la presentazione dell'intero processo di fabbricazione di due statori hairpin in alluminio, evidenziando le differenze, le criticità e le migliori pratiche per l'adattamento dei parametri di processo rispetto alla produzione convenzionale in rame.

Infine, viene illustrato uno studio specifico sulla riduzione delle sollecitazioni di tensione negli avvolgimenti hairpin, con la definizione di linee guida per una progettazione orientata all'affidabilità, finalizzate a garantire l'integrità del sistema di isolamento e la durabilità dell'applicazione.

Lo studio intende contribuire al percorso di transizione sostenibile del settore dei trasporti verso l'elettrificazione, proponendo un processo di progettazione completo per macchine elettriche di trazione, con particolare attenzione alla tecnologia hairpin in alluminio come soluzione innovativa e a ridotto impatto ambientale.

Abstract

Many of today's social, economic and environmental decisions are driven by sustainability. From an environmental perspective, one key action to cut emissions is the electrification of transportation sector, as it is currently responsible of nearly 23 % of global CO_2 production.

This transition has prompted an increased emphasis on sustainability in the design of electric drives and powertrains, with the objective of reducing emissions throughout the entire product life cycle, from raw material sourcing and manufacturing to operation, recycling, and reuse.

Reducing the scope to the development of electric machines for traction applications, current research trends reflect this interest, leading to design strategies that adopt alternative materials to reduce environmental impact and improve recyclability, while improving reliability for guaranteeing long-term life and waste minimization.

Meanwhile, the implementation of these strategies can introduce several challenges: materials with lower environmental impact or alternative design approaches often lead to performance trade-offs in electromagnetic and thermal design, as well as manufacturing constraints, requiring re-adaptation of the existing manufacturing line.

This work addresses all these aspects by proposing a high reliable and sustainable design of electric machines, employing aluminum hairpin winding as a replacement for conventional copper ones. Specifically, the study begins with the electromagnetic design and analysis of aluminum hairpin machines, compared against their copper counterparts, in order to establish design guidelines.

The feasibility of the aluminum solution is then validated through a thermal analysis, comparing the performance of copper and aluminum versions under identical cooling conditions. Finally, the complete manufacturing process of two aluminum hairpin stators is presented, emphasizing the differences, challenges, and best practices for adapting process parameters relative to conventional copper hairpin production.

Additionally, a dedicated study on the voltage stress reduction in hairpin windings is reported, providing guidelines for reliability-oriented hairpin winding design that ensure the integrity of the insulation system and long-term operation.

This study aims to support the sustainable transition of the transportation sector toward electrification through a comprehensive design process for traction electric machines, with focus on aluminum hairpin technology.

Contents

Appendix

List of Figures

List of Tables

Introduction

Cutting emissions in road transportation means tackling the second highest source of greenhouse gasses (GHG), representing more than 12% of global production [1]. Although vehicle electrification poses a strong foundation for reaching this goal by eliminating direct tailpipe emissions, it alone is not enough to make the road transportation sector fully sustainable. A sustainable approach requires a life-cycle perspective that considers all stages, from raw material extraction and manufacturing to operation, recycling, and reuse.

To this end, awareness of sustainability in electric drive design is rapidly increasing, with efforts focusing on minimizing emissions throughout the entire product life-cycle.

Recent research reflects this trend [2], leading to electric drive design strategies for sustainability that:

1. implement solutions with reduced environmental impact from the early phases of the life-cycle, such as extraction and production of raw materials;
2. improve efficiency and power density, for minimizing energy losses during operation;
3. optimize recyclability by promoting disassembly easiness or using fully recyclable materials.

Meanwhile, the implementation of these strategies introduces several challenges in various areas of the design of electric machines, including electromagnetic and thermal performance, structural integrity, and reliability, as highlighted in Table 1.

In addition, the effective implementation of these strategies often introduces manufacturing challenges, as dealing with new materials and design approaches requires adjustments to process parameters and, in some cases, modifications to traditional and widespread manufacturing equipment.

Therefore, the inherent challenge of sustainable design lies in implementing solutions that minimize emissions throughout the entire product life-cycle without compromising performance.

As will emerge from this thesis, addressing the sustainability challenge for the development of electric machines for vehicle applications requires a paradigm shift in the definition of the

Sustainability Strategy	Solution		Challenges
Reduced environmental impact	Rare-earth free alternatives, such as ferrite [3] or Fe-N-based magnets [4]		Reduced torque density due to lower magnetic strength
	Magnets-free alternatives	Reluctance machines- synchronous [5] or switched [6]	Reduced power density due to lower power factor
		Wound-field Synchronous Machines (WFSM), with rotor coils [7]	Rotor cooling due to joule losses in excitation coils
Efficiency and Power density improvement	Wide-bandgap (WBG) devices [8]		Voltage stress induced on inter-turn insulation due to fast commutation
Recyclability through improved disassembly easiness	Modular Designs [9]		Reduced durability due to lower structural integrity
	Powder Composites instead of laminated cores [10]		Reduced torque density due to scarcer magnetic properties
Reduced environmental impact and full material recyclability	Aluminum instead of Copper in the windings [11]		Higher thermal load, as higher resistivity leads to higher joule losses

Table 1: Sustainable Strategy Solutions and related Challenges

design priorities: from performance-driven to application-driven, where the focus is no longer solely on the product itself, but on the user needs.

0.1 Project Description

With the aim of designing more sustainable and reliable electric machines for vehicle application, this Ph.D. project focuses on:

1. **the replacement of copper hairpin windings with aluminum ones and the manufacturing of two aluminum hairpin stators**, which feature a lower environmental impact and higher recyclability;
2. **the modeling and the reduction of the voltage stress on the inter-turn insulation of the hairpin windings**, induced by the fast commutation of the WBG devices, whose implementation enables higher electric drive efficiency and power density.

Aluminum is beneficial for reducing emissions during the material extraction, production, and end-of-life phases of the electric machine life-cycle. Similarly, strategies to reduce voltage stress in the windings enable the safe implementation of WBG-based power converters, which allow for efficient use of energy throughout the operation phase.

In this context, this Ph.D. research aims to reduce emissions across the entire life-cycle of the electric drive, addressing the fundamental sustainability challenge of achieving this goal without compromising performance.

Specifically, the electromagnetic and thermal challenges of the replacement of copper with aluminum are analyzed, comparing peak, nominal, and driving cycle performance, cost, weight, and environmental impact. Then, the manufacturing aspects are assessed thanks to the prototyping of two aluminum hairpin winding stators, which also proves the feasibility of the solution.

In addition, the combined effect of the hairpin winding diagram configuration and the rise time of the WBG devices on the voltage distribution is evaluated. This allows identification of the maximum inter-turn voltage stress and consequent selection of the winding configuration that minimizes it, ensuring proper insulation system design for partial discharge-free operation.

0.2 Objectives

The objectives (**OBJ**) of the thesis are the following.

OBJ1 *Motivate the potential of aluminum as a sustainable alternative*, making a detailed comparison with copper on a per-unit-volume basis, which focuses on the most relevant material properties for their use as winding conductors in electric machines. A sustainability index is used to quantitatively assess the environmental impact of design solutions.

OBJ2 *Identify suitable design approaches for the development of aluminum hairpin winding machines and establish general comparison strategies with copper.* Specifically, considerations are made on whether to design an aluminum hairpin winding machine from scratch or adapt it from an existing copper-based design. Furthermore, following a comprehensive literature review, generalized methodologies are proposed to allow a fair comparison of their electromagnetic and thermal performance.

OBJ3 *Provide guidelines for the electromagnetic and thermal designs of aluminum hairpin machines for traction of utility vehicle.* Based on results of the presented case studies, guidelines are provided for replacing copper hairpin with aluminum in traction machines of utility vehicles, thus achieving environmental targets without compromising performance. The findings are further validated through a case study comparing the experimental efficiency maps of copper and aluminum. In addition, thermal studies are performed for proving the electromagnetic design feasibility, assessing the peak and continuous performance, as well as the temperatures over a driving cycle, for both copper and aluminum.

OBJ4 *Validate the feasibility of implementing the aluminum hairpin winding solution.* This is done by showcasing the complete manufacturing process of aluminum hairpin stators within a production line originally designed for copper hairpin windings. The different material workability is discussed and best practices are proposed on how to adjust the process parameters when the aluminum hairpin stator is produced. The successful production of two aluminum hairpin stators, featuring increased complexity from a high slot count and the use of two different conductor sizes within the same slot, demonstrates the feasibility of implementing the aluminum solution.

OBJ5 *Define guidelines and best practices for the reliability-oriented design of hairpin winding electric machines.* This important yet often overlooked aspect is addressed through the analysis of the voltage distribution on the hairpin winding, with the aim of reducing the over-voltage stress on their inter-turn insulation caused by the fast commutation times of the WBG devices. Specifically, by evaluating the combined effect of the configuration of the winding diagram and the rise time value on the voltage distribution, this study provides guidelines for an effective winding design, which is partial discharge-free in each operating condition.

0.3 Thesis Outline

In Chapter 1, the motivation to select aluminum as a sustainable alternative is illustrated through a comparison with copper in terms of the material characteristics that are most relevant for their use as windings in an electric machine. The chapter concludes with some considerations on how to develop an aluminum hairpin machine to fairly evaluate it compared to copper.

Chapter 2 deals with the electromagnetic design of aluminum hairpin machines. Through a literature review and the results of the different case studies presented, the most suitable comparison strategy is determined between copper and aluminum for electric traction machines of utility cars. This is then validated through a comparison of the experimentally measured efficiency between copper and aluminum prototypes on the entire operating map.

A detailed thermal analysis is performed in Chapter 3 to confirm the trends resulting from the electromagnetic design. In detail, the peak and continuous thermal performance of copper and aluminum, as well as the maximum temperature reached over a driving cycle, are compared through dedicated computational fluid dynamics (CFD) and thermal simulations.

Chapter 4 covers the manufacturing aspects of the aluminum hairpin stator, assessing the effects of the different workability of the aluminum material on the different stages of production. To this purpose, this chapter describes the complete manufacturing process of an aluminum hairpin stator within a production line originally designed for copper hairpin windings. In this context, guidelines and best practices are provided on how to adjust the process parameters when using aluminum hairpin instead of copper.

Chapter 5 introduces the second part of the Ph.D. work, focusing on designing more reliable machines. It first reports a literature review on the various strategies to mitigate voltage stress in winding insulation caused by the fast switching transients of WBG devices. Then, a case study is presented, featuring a modular hairpin winding layout, which can be reconfigured by changing the series connection of its elementary paths. This reconfigurability enables a comparison of voltage distributions across different winding layout patterns, identifying the one that reduces the voltage stress. Following this, a high frequency voltage distribution model is presented, which is then validated through the experimental tests carried out on different winding layouts. In the final part of the chapter, the results are extended through a sensitivity analysis on the rise time conducted on the validated model, thus providing general guidelines on the voltage stress reduction as it allows to consider the combined effects of the rise time variation and the winding configuration.

Finally, Chapter 6 concludes this thesis, presenting general discussions and further work to be done.

1. Background: Copper vs Aluminum

In this chapter, the background for the comparison of copper and aluminum is presented. First, *the motivation* for replacing copper with aluminum hairpins is explained by examining key aspects of the design of electric machines. Then, *the development methodology* for an aluminum hairpin machine is described, forming the basis on which the overall study and subsequent chapters are built.

1.1 Motivation: Why Aluminum?

The motivation for adopting aluminum is illustrated through a comparison with copper in six main aspects, as shown in Fig. 1. A larger area in the radar graph indicates better overall performance.

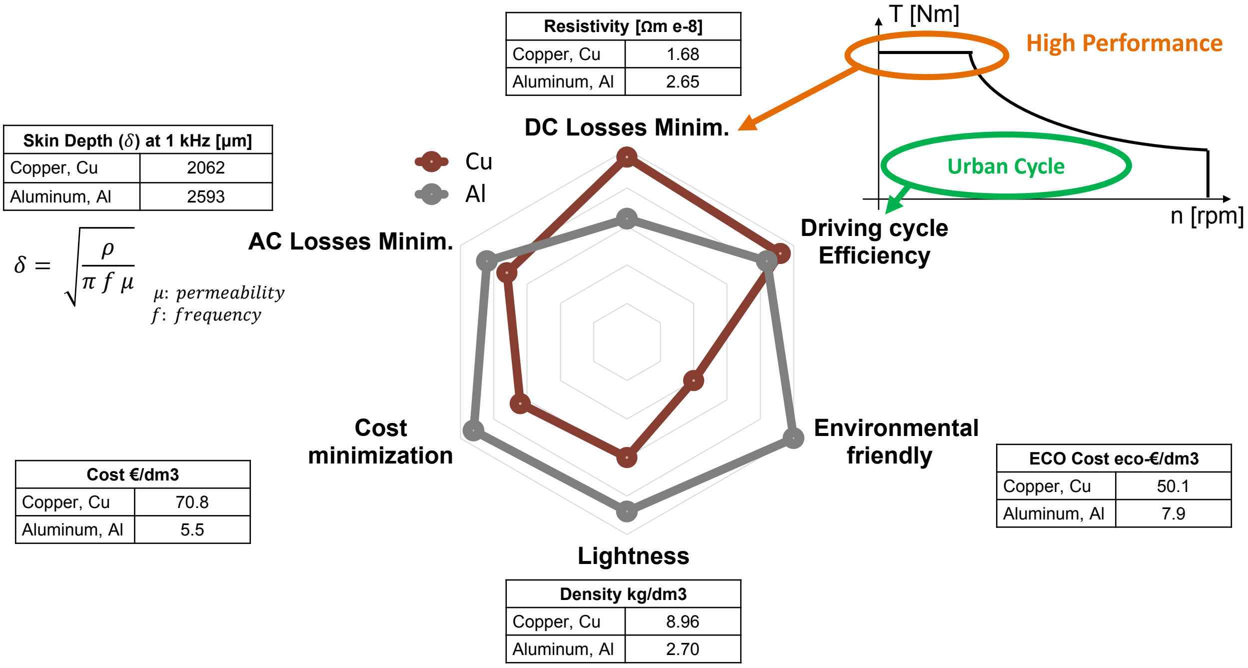

Resistivity [Ωm e-8]	
Copper, Cu	1.68
Aluminum, Al	2.65

Skin Depth (δ) at 1 kHz [μm]	
Copper, Cu	2062
Aluminum, Al	2593

$$\delta = \sqrt{\frac{\rho}{\pi\, f\, \mu}}$$

Cost €/dm3	
Copper, Cu	70.8
Aluminum, Al	5.5

ECO Cost eco-€/dm3	
Copper, Cu	50.1
Aluminum, Al	7.9

Density kg/dm3	
Copper, Cu	8.96
Aluminum, Al	2.70

Figure 1: Copper vs Aluminum

The comparison is made on a per-unit-volume basis, which is advantageous in electric machine design because key performance metrics, such as torque and losses, scale with the amount of active volume. In addition, in automotive applications, the machine's installation space is tightly constrained, which makes the volumetric power density (kW/L) a critical design requirement.

- *Weight and Cost*:

  The primary advantages of aluminum are its lightweight and cost efficiency. With a density roughly one-third that of copper, aluminum enables significantly lighter designs when the same volume is used. In addition, a liter of copper is considerably more expensive than a liter of aluminum [12], due to its greater scarcity and the complexity of extraction. Copper deposits are typically deeper and more difficult to access, and its extraction and refining processes are more energy-intensive.

- *Sustainability*:

  The index used to evaluate environmental impact is the eco-cost per unit volume [13], which expresses the results in terms of economic values. Specifically, it shows how much a liter of material costs the environment, including factors such as resource depletion, eco-toxicity, human health, and carbon footprint, all based on the utilization of virgin materials. Being the most abundant metal in the Earth's crust, aluminum has a much lower eco-cost for resource depletion compared to copper, thus contributing to its overall eco-cost reduction. In addition, recovering aluminum from electric machine windings during recycling is more efficient than recovering copper. The small amounts of aluminum residuals remaining in recycled steel are ineffective, whereas even minor copper contamination can negatively affect steel quality [14].

- *DC and AC Joule Losses*:

  The resistivity values refer to high-purity grades of copper and aluminum commonly used as electrical winding materials. Specifically, the aluminum corresponds to alloys from the 1xxx series. Because aluminum has a higher electrical resistivity than copper, it exhibits a higher DC resistance for conductors of the same geometry. Consequently, assuming identical current conditions and a uniform conductors current density distribution with no AC effects, aluminum conductors experience greater Joule losses (DC Joule Losses).

  However, a higher electrical resistivity is beneficial in minimizing the high-frequency skin and proximity effects, as it promotes a more uniform current distribution within the conductor cross section, thus reducing the additional Joule losses contribution given by these phenomena (AC Joule Losses) [15]. In this regard, Fig. 2 compares the copper and aluminum RMS current density distribution, calculated along the radial dimension for each conductor of the slot [16]. The analytical model compares the two materials for the same current conditions (80 Arms and 500 Hz) and slot geometry (6 conductors, each with a 3x2 mm2 cross section and 100 mm axial length). These results are validated through finite element analysis, as demonstrated by the close match in Fig. 2.

The model does not consider certain non-idealities present in the motor, such as iron saturation and the influence of the leakage flux crossing the airgap, such as the external field of the rotor permanent magnets. Saturation tends to reduce the AC effects, as it decreases the intensity of the slot leakage flux inside the slot. In contrast, the permanent magnet field amplifies these effects, particularly for the conductors located near the air gap.

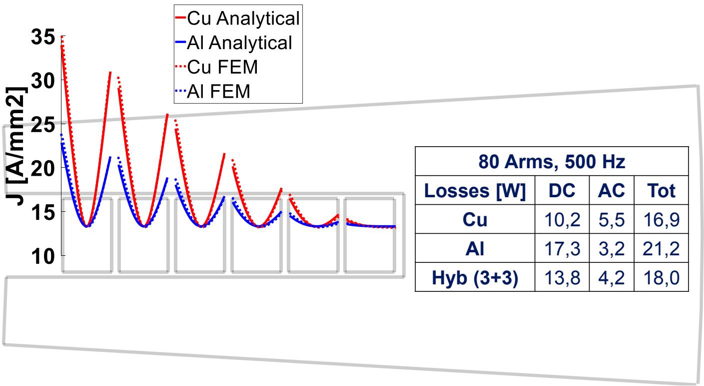

80 Arms, 500 Hz			
Losses [W]	**DC**	**AC**	**Tot**
Cu	10,2	5,5	16,9
Al	17,3	3,2	21,2
Hyb (3+3)	13,8	4,2	18,0

Figure 2: RMS current density distribution along the conductors radial direction.

The RMS current density plots of the aluminum conductors reach peak values lower than those of copper, demonstrating a more homogeneous distribution. This results in lower AC Joule losses for aluminum, as shown in the table of Fig. 2, while the DC losses are still higher than those for copper.

In addition, regardless of the material, the RMS current density distribution reaches higher peaks for the conductors closest to the airgap, where the slot leakage flux is more intense. This justifies the exploration of hybrid solutions, with aluminum for the first conductors close to the airgap where the AC effects are more prominent and copper for the remaining layers [17].

As frequency approaches higher values, AC Joule losses can be predominant, and their reduction can offset the increase in DC Joule losses caused by higher resistivity, minimizing overall winding losses. This is well shown in Fig. 3, where the results of the model of Fig. 2 are shown over the whole frequency range. Specifically, the inversion frequency beyond which the overall copper losses overcome those of aluminum is around 800 Hz.

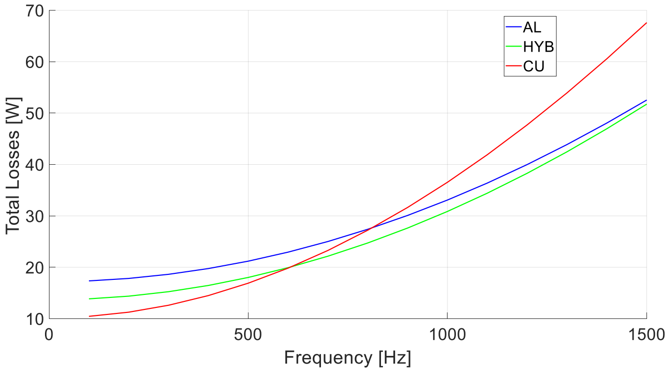

Figure 3: Copper vs Aluminum losses plot at varying operational frequencies.

It is interesting to notice that the hybrid solution can offer a balanced alternative throughout the whole frequency range, as will be deepen in Chapter 2 through a case study.

- *Automotive Application - Driving Cycle Efficiency*:

  Traction machines for utility vehicles operate at lower speeds and under light load conditions. In such operating conditions, the highest contribution to the overall electric machine losses over the driving cycle is in the iron cores, as iron losses increase with operational frequency. In fact, due to the relatively low frequencies (typically below 1 kHz), the AC phenomena discussed above are negligible to the total losses count. Similarly, light loads correspond to low current values, resulting in low DC Joule losses. This makes the impact of the higher resistivity, whether in terms of reduced AC losses or increased DC losses, less significant overall.

  Consequently, in urban and extraurban driving conditions, the choice of winding material becomes less critical from a driving efficiency point of view. In this context, aluminum emerges as a strategic option. As will be demonstrated, by preserving the same conductor geometry and accepting a slight decrease in driving cycle efficiency along with modest reductions in continuous and peak thermal performance, aluminum hairpin windings offer clear advantages in terms of sustainability, cost, and weight.

In response to the question that opened this paragraph *"Why aluminum?"*, the points discussed above address OBJ1 of this Ph.D. project, motivating the potential of aluminum hairpin windings for electric traction machines in utility vehicles, which offers a more sustainable, cost efficient and lightweight alternative to copper, without sacrificing driving-cycle efficiency.

The following chapters will provide detailed evidence and analysis to demonstrate these benefits in practice.

1.2 Development Methodology for the Aluminum Hairpin Machine

After motivating the choice of aluminum hairpin, a development methodology for its implementation should be defined.

Since copper is nowadays widely used in traction machines for automotive applications, any evaluation of aluminum as alternative winding material is made through comparisons with existing copper based designs.

There are two possible scenarios for developing an aluminum based design.

- **From scratch:** Design of an aluminum version from the ground up, optimizing both the stator and rotor geometries through a customized design process. Its evaluation is then performed by imposing the identity condition on one or more performance targets of the copper design, such as torque, losses under given operating conditions, or weight, and comparing the design results based on the other performance metrics.
- **Modification of existing copper reference design:** Optimization of an aluminum based solution by modifying an existing copper reference design. For stator intended aluminum windings, this involves a redesign of the stator and conductor geometry, while the same key design specifications as the copper baseline are kept, such as the stator winding diagram and the same rotor, as well as the same drive characteristics and operational limits (e.g., DC voltage and maximum phase current).

Although the first scenario is more straightforward from a technical perspective, the second reflects better the current industry practice, where motor manufacturers in the transportation sector typically build on their existing designs.

In addition, with this approach, an aluminum version can be developed by redesigning only the stator and conductor geometry of the copper reference design while keeping the rotor unchanged. Alternatively, aluminum rotor coils can be implemented in a WFSM by only redesigning to the rotor geometry, while leaving the stator unchanged. As will be discussed in Chapter 2, this development methodology allows for a direct comparison between the aluminum design and the copper reference under the same magnetic and electric loading, provided that no saturation occurs and the drive characteristics (DC bus voltage and maximum phase current) are unchanged.

Using this second methodology ensures a fair electromagnetic comparison and allows the results to be easily extended to any other case study, thus providing valuable guidelines that are even valid for the case in which the aluminum solution is designed from scratch according to the first scenario.

To this purpose, Chapter 2 is dedicated to the electromagnetic design of aluminum hairpin machines, which follows the second methodology, where the aluminum machine is optimized by redesigning the geometry of an existing copper machine. A first case study redesigns the stator of a copper reference machine to implement an aluminum hairpin winding, while a second redesigns the wound-field rotor to introduce aluminum rotor coils.

Further considerations regarding the choice of the development methodology are provided in Appendix A, where preliminary electromagnetic design case studies carried out following the first "from-scratch" scenario are reported.

2. Electromagnetic Design

This chapter focuses on the electromagnetic design of an electric machine with aluminum windings.

As discussed in the previous chapter, the chosen approach is based on modifying an existing copper reference design. The chapter begins by outlining the guidelines for applying this methodology, including three potential strategies for developing an aluminum version from the copper reference. Following these guidelines, two case studies are presented: the first implements an aluminum hairpin winding through a stator redesign, while the second introduces aluminum rotor coils via a redesign of the wound-field rotor.

Based on the results of these case studies and a review of the literature, which classifies existing examples based on the three comparison strategies introduces, the most suitable way to implement aluminum hairpin windings in traction machines for utility vehicles is identified.

To validate this choice, the selected strategy is applied in a practical scenario to the design of an electric machine for automotive traction. The experimentally measured efficiency maps of the copper and aluminum prototypes are compared, evaluating the performance of the driving cycle, and demonstrating the practical feasibility of implementing the aluminum solution in utility vehicles.

2.1 Strategies for Aluminum Conversion of Copper Machines

When an existing electric machine is converted from copper to aluminum windings, either the hairpin windings are replaced in a redesigned stator or, eventually, the rotor of a WFSM is redesigned for replacing the field coils. In both cases, the aluminum design is developed by modifying the existing copper reference, while maintaining the same rotor volume, i.e., preserving the active length l and the air-gap diameter D_g.

Furthermore, since the drive characteristics remain unchanged (DC voltage and maximum RMS phase current I_s), the same “internal” apparent power S_i (eq. (2.1)) is kept [18].

$$S_i = mE_m I_s \tag{2.1}$$

m is the number of phases and E_m is the RMS of the phase electromotive-force.

The electric loading $\hat{A}$ (eq. (2.2)) and magnetic loading $\hat{B}_\delta$ (eq. (2.3)) can be introduced:

$$\hat{A} = \frac{2\sqrt{2} I_s N_s m}{\pi D_g} \tag{2.2}$$

$$\hat{B}_\delta = \frac{\hat{\Psi}_m}{N_s k_{ws1} l \tau_p \alpha} \tag{2.3}$$

where N_s is the number of series turns, $\hat{\Psi}_m$ is the peak flux linked by the phase winding across the pole surface defined by l, the pole pitch τ_p, and the winding factor k_{ws1}, and α is a factor multiplying $\hat{B}_\delta$ for obtaining the average value of the flux density in the airgap ($\alpha = 2/\pi$ in the case of a sinusoidal distribution).

In this way, S_i can be rewritten (2.4)

$$S_i = C D_g^2 l f_m \tag{2.4}$$

where f_m is the mechanical synchronous frequency, while C is the machine constant, defined by $\hat{A}$ and $\hat{B}_\delta$.

$$C = \frac{\pi^2}{2} k_{\mathrm{ws1}} \hat{A} \hat{B}_\delta \tag{2.5}$$

With reference to eq. (2.4), the assumptions of identical apparent power S_i and rotor volume ensure that **aluminum and copper designs are evaluated under comparable machine constant C, which means comparable electric and magnetic loadings**, allowing for a fair electromagnetic comparison.

In order to develop the aluminum solution and evaluate it against copper, a precise comparison structure is followed, which first imposes the identity condition on certain performance targets (control conditions) and then compares the solutions on other performance metrics (compared variables). The structure of the comparison is defined in the following bullet points.

- **Terms of Comparison:** Copper and Aluminum Windings.
- **Development Strategy:** Maintaining same rotor volume and drive characteristics (maximum phase current and DC bus voltage).
- **Control Conditions:** Peak Losses (under the operating point defined by the maximum torque and the base speed), External Volume, Peak Torque T_{pk}.
- **Compared Variables:** Cost, Weight, Sustainability, Driving Cycle Efficiency.

Depending on the control condition imposed, the conversion of a copper electric machine to aluminum is done according to **three possible comparison strategies**. The following subsections outline these strategies both in the case of a redesign of the hairpin winding stator and the redesign of a wound-field rotor.

2.1.1 Hairpin Winding Stator Redesign

Following the comparison structure introduced above, converting a copper hairpin winding stator to aluminum leads to three possible strategies, depending on which control condition is imposed, as specified in Fig. 4.

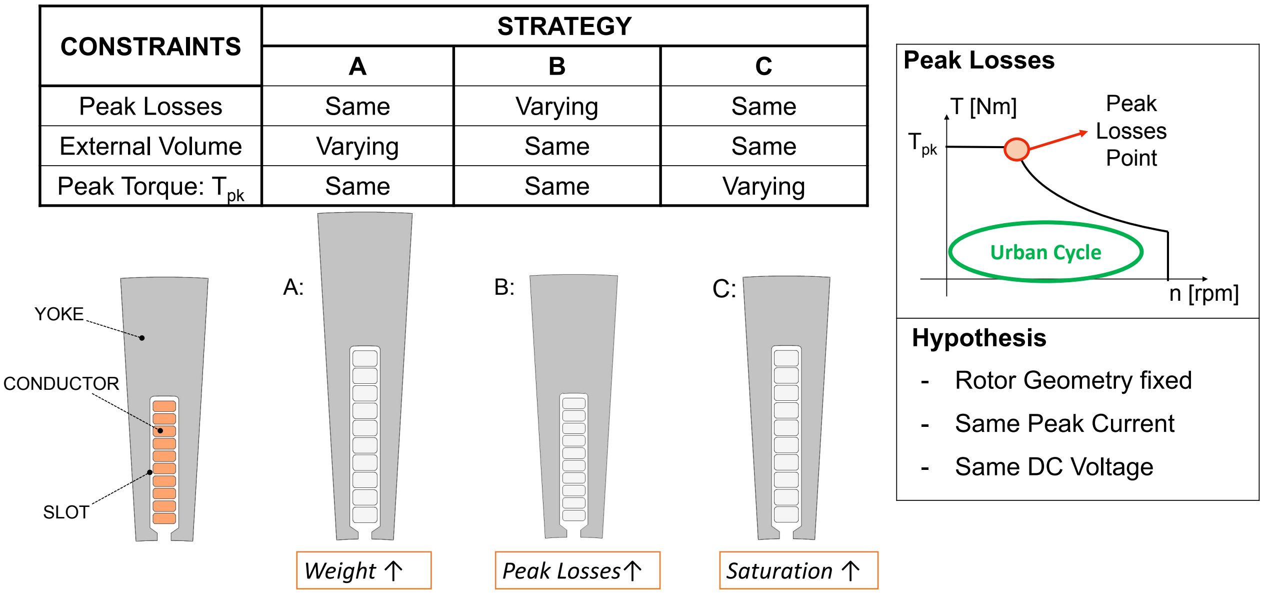

CONSTRAINTS	STRATEGY		
	A	B	C
Peak Losses	Same	Varying	Same
External Volume	Varying	Same	Same
Peak Torque: T_{pk}	Same	Same	Varying

Hypothesis

- Rotor Geometry fixed
- Same Peak Current
- Same DC Voltage

Figure 4: Hairpin Winding Stator Redesign - Comparison Strategies Copper vs Aluminum

Comparison A assumes equal peak losses for copper and aluminum, i.e., the same losses under the operating point defined by the maximum torque and the base speed, as illustrated in Fig. 4. This implies an identical peak thermal load, which typically serves as a reference for the design of the cooling system, as it is independent on the specific driving cycle. In this type of comparison, because of aluminum's higher resistivity, a lower current density is required, and the redesigned stator inevitably tends to a larger conductor cross section, thus larger slots. In addition, to maintain the same peak torque as the copper baseline, the external radius of the stator must be increased, as this both prevents excessive saturation of the yoke and accommodates larger slot dimensions. This causes the redesigned aluminum stator to lose its weight advantages. In fact, although aluminum conductors are lighter, the need for additional iron material results in a higher overall motor weight compared to the copper baseline. Also, a larger stator diameter requires a larger housing, which further increases the weight of the aluminum based solution. In terms of losses in urban and extraurban driving cycle conditions, i.e., within the operating area characterized by light load and medium-high speed (highlighted in green in Fig. 4), the aluminum solution performs slightly worse. This is due to the increased amount of iron that leads to higher iron losses.

In **comparison B**, the aluminum stator is redesigned through an optimization that aims at the same peak torque and external stator volume as the copper baseline. This results in the aluminum conductor dimensions (and overall stator dimensions) being similar to those of copper, thus ensuring the same maximum current density. Consequently, aluminum exhibits iron losses comparable to copper because of the same amount of iron used, but its higher resistivity causes additional winding losses at the peak power point, resulting in a higher peak thermal load. Meanwhile, the increase in aluminum DC losses is less influential at lower loads, namely under urban and extraurban driving cycle conditions. In fact, as will be shown, the driving cycle efficiency of the aluminum motor is only slightly lower and remains comparable to that of the copper motor. This is because the highest contribution to the overall machine losses under the driving cycle conditions is constituted by the iron losses.

Finally, **comparison C** imposes the same peak losses and external volume as the copper baseline. The identity condition on the peak losses leads to a larger conductor cross section for aluminum. In the meantime, the stator yoke must accommodate the larger slot dimensions while also remaining within the limits of the external volume. This will eventually lead to excessive iron saturation of the stator yoke, preventing the aluminum solution from achieving the same peak torque as the copper baseline. In fact, the underlying hypothesis of having comparable magnetic loading with the copper reference design is no longer valid due to the excessive saturation of the machine magnetic circuit. This is reflected by a lower rotor tangential stress σ_{tan} [18], which is defined as in eq. (2.6), where $cos\phi$ is the power factor.

$$\sigma_{tan} = \frac{\hat{A}\hat{B}_{\delta}cos\phi}{2} \tag{2.6}$$

2.1.2 Wound-field Rotor Redesign

The comparison structure introduced above can be also applied to the scenario in which the wound-field rotor is redesigned to replace the copper rotor coils with aluminum, while the stator geometry is fixed. In this case, the control conditions on keeping identical peak losses and external volume refer to the rotor field losses and the rotor volume, respectively. Furthermore, the methodology imposes comparable electric and magnetic loadings, which results in an equal number of rotor ampere-turns (eq. (2.7)) between copper and aluminum.

$$NI_f = const. \tag{2.7}$$

When eq. (2.7) holds, the rotor joule losses $P_{Joule,r}$ are proportional to the inverse of the slot field coil area $A_{slot,r}$, as highlighted in eq. (2.8).

$$P_{Joule,r} = R_{coil,r} I_f^2 \propto \frac{Nl'}{S_{cond,r}} I_f^2 \propto \frac{1}{NS_{cond,r}} \propto \frac{1}{A_{slot,r}} \tag{2.8}$$

$R_{coil,r}$ is the resistance of the rotor coil, whereas l' and $S_{cond,r}$ are the equivalent length and the cross section of a conductor of the rotor coil, respectively.

The comparison strategies are defined in Fig. 5.

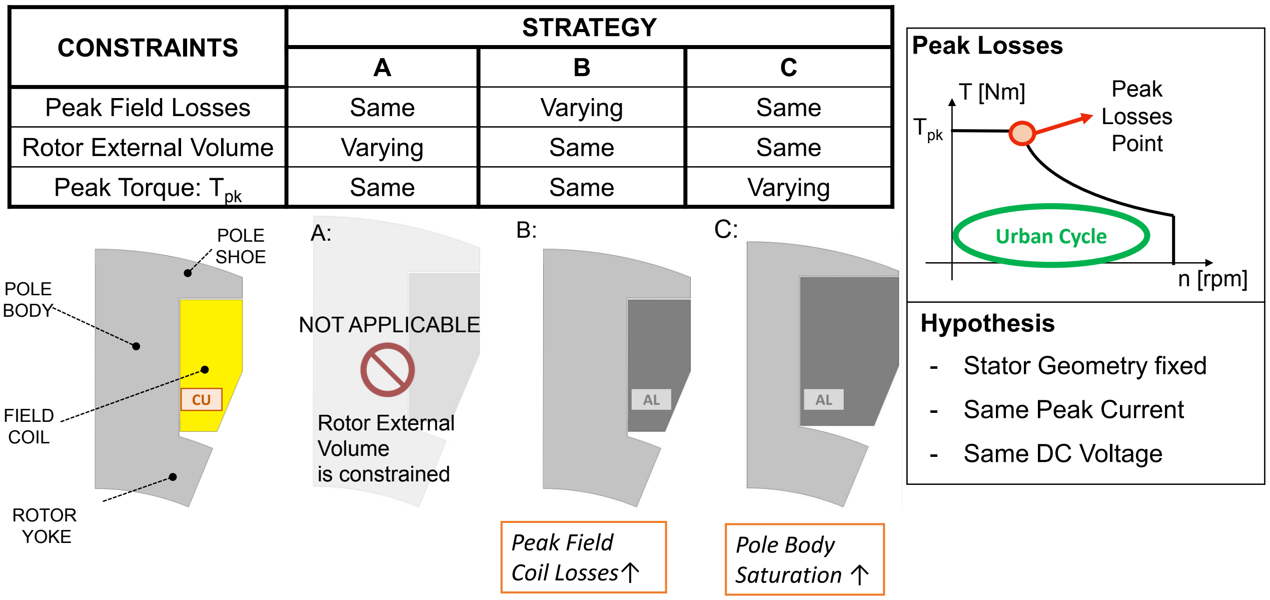

CONSTRAINTS	STRATEGY		
	A	B	C
Peak Field Losses	Same	Varying	Same
Rotor External Volume	Varying	Same	Same
Peak Torque: T_{pk}	Same	Same	Varying

Hypothesis

- Stator Geometry fixed
- Same Peak Current
- Same DC Voltage

Figure 5: Wound-field Rotor Redesign - Comparison Strategies Copper vs Aluminum

Comparison A cannot be applied due to the restriction on the maximum rotor volume. In fact, achieving identical peak field coil losses while maintaining the same peak torque would result in a larger overall rotor volume, both to accommodate a bigger field coil area (eq. (2.8)) and to avoid excessive saturation of the rotor pole. However, the wound-field rotor is redesigned for fixed stator geometry, which constrains the airgap radius.

Comparison B imposes the control condition on the maximum external rotor volume and peak torque. The optimization of the aluminum wound-field rotor would therefore converge towards a field coil area (and overall rotor dimensions) that is similar to that of copper. In this context, aluminum is expected to experience additional field coil winding losses at the peak point, and thus a higher peak thermal load. However, also in this case, it will be shown that this aspect is not as critical, as the machine is not expected to operate at the peak operation during the driving cycle but rather in low load / medium-high speed conditions, where the joule losses are less relevant with respect to the iron losses. This results in the efficiency of the aluminum motor being only slightly lower, yet comparable.

Comparison C enforces the same peak losses and external volume as the copper baseline. Matching the peak losses requires a larger field coil area when using aluminum. At the same time, the maximum rotor volume is limited by the inner diameter of the stator. As a result, the aluminum design tends toward configurations with less iron, such as a thinner rotor pole body and shoe, which can cause excessive magnetic saturation. Under these conditions, the magnetic loading of the machine is reduced, leading to a lower peak torque compared to the copper baseline.

2.1.3 Application of the Proposed Strategies in Two Case Studies

The strategies presented above are applied to two case studies that evaluate the feasibility of substituting copper windings with aluminum.

The first case study examines the replacement of copper hairpin windings with aluminum in the stator of an interior permanent-magnet (IPM) machine used for utility-vehicle traction.

The second case study focuses on redesigning the wound-field rotor of a traction machine intended for heavy-duty applications.

2.2 Multi-objective Optimizations of Copper and Aluminum Hairpin Windings: a Comparison

This work analyzes the possibility of adopting aluminum hairpin windings as an alternative to copper in electric traction machines for utility car applications, while ensuring the same peak torque. To this purpose, copper and aluminum hairpin winding solutions are compared on the basis of two strategies: **Comparison A**, which imposes the same winding Joule losses in peak operating conditions, and **Comparison B**, which maintains the same machine volume.

In both cases, copper and aluminum solutions are independently optimized through a Multi-Objective Genetic Algorithm (MOGA), with the aim of reaching the required peak torque performance, while reducing the weight and the losses in specific drive conditions, representative of the driving cycle. For both analyzed strategies, the optimal designs are compared in terms of weight/volume, costs, efficiency, and sustainability.

Finally, the same methodology is used to investigate the hybrid aluminum-copper design, consisting of the adoption of both conductor materials in the same slot. This resulted in a reasonable trade-off between cost, weight, efficiency, and sustainability.

The study is organized as follows. It begins by introducing the setup used for comparisons and optimizations. Then it presents the selection criteria applied to identify the most suitable candidates from the optimization results, followed by a detailed discussion of those results. Finally, the efficiency maps of the selected solutions are examined, forming the basis for the overall conclusions.

2.2.1 Reference Design

The reference motor is a three-phase 54 slots, 6 poles IPM motor designed for automotive application. The specifications and geometry of the reference design are shown in Fig. 17.

The stator geometry is redesigned through an MOGA optimization, with the aim of reducing the losses specific operating conditions and the weight of the machine, while keeping the same drive characteristics and maximum torque performance. To this purpose, an independent optimization process is performed for three different designs: copper (**CU**), aluminum (**AL**), and hybrid (**HYB**) hairpins.

The MOGA is an optimization process that iteratively generates progressively better popula-

In slot conductors number	10
Parallel paths number	3
Axial length, mm	100
Peak power, kW	150
Base speed, rpm	5000
Peak speed, rpm	18000
Peak Torque, Nm	270
Max Phase Current, Arms	300
DC Bus Voltage, V	650
Stator Inner Radius, mm	68

(a) Motor Specifications

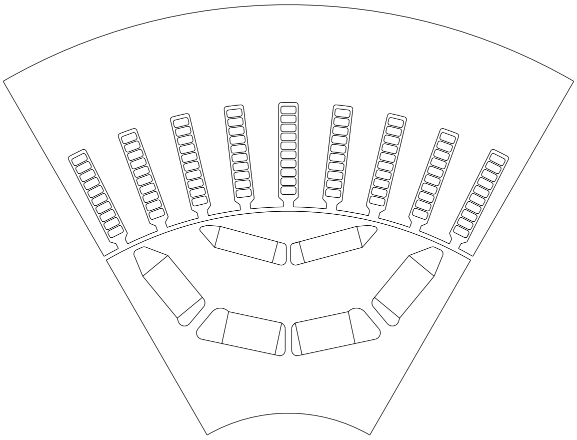

(b) Reference Design Geometry

Figure 6: Case Study 1 - Data Specifications and Reference Geometry

tions of individuals until an optimal design that satisfies the designer's requirements is reached. Each new population is generated based on the best-performing individuals of the previous generation. This is achieved through crossover and mutation operators, which respectively combine the genetic information of selected parents and ensure diversity within the sampled populations. In the JMAG optimization engine, the crossover operator implemented is the Simplex crossover, while a mutation operator is not supported, as diversity is already ensured by the crossover process.

The number of conductors is equal to 10, which gives the smallest possible radial dimension of the conductors to promote a more homogeneous current density distribution. This condition is in favor of copper, while decreasing the number of layers will shift the optimal solutions towards aluminum because of its better AC losses behavior. **HYB** deals with the first four conductors facing the rotor in aluminum and the remaining ones made of copper. In this way, aluminum is exploited in the conductors characterized by the most inhomogeneous current density distribution, to mitigate the associated AC effects. This is shown in Fig. 7(a), in which the RMS current density distribution on a reference slot geometry with 10 conductors is calculated through the analytical model reported in [15], [16] and in Chapter 1.

Using aluminum for the first four conductors facing the rotor and copper for the remaining six layers is practically feasible because the joint between the fourth and fifth layers of conductors (i.e. aluminum and copper) coincides with the welding side. The aluminum and copper conductors will be laser welded. As will be shown in Chapter 4, the welding resistance is negligible compared to the phase resistance and is therefore not considered in this analysis.

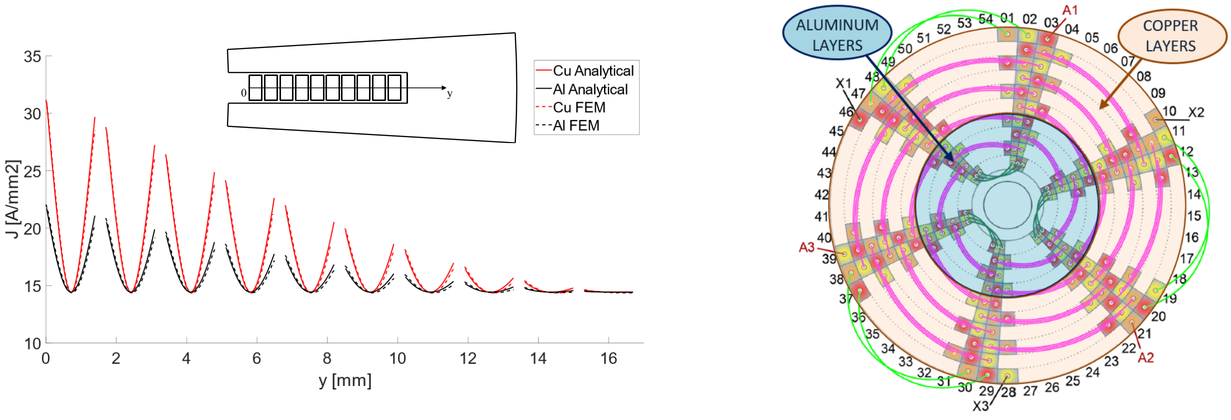

(a) **(b)**

Figure 7: (a) Analyitical and FE RMS current density distribution in aluminum and copper. Current supply: 80 A_{pk}, 500 Hz. Conductors dimensions: 1.4 x 2.8 mm^2. (b) Proposed Winding Diagram Layout. Bending connections are not represented.

This is highlighted in the winding layout shown in Fig. 7(b), where the purple lines represent the welding connections [19]. Circulating currents are not expected among the parallel paths because of the strong symmetry adopted in the winding layout. The feasible hybrid layouts for this specific winding diagram require an even number of aluminum conductors. Among the possible options, the hybrid configuration with four aluminum conductors was investigated, as it represents a reasonable trade-off between Joule DC losses and AC losses, as well as cost, weight, and sustainability metrics.

2.2.2 Optimizations Process

The stator geometry of each of the three design proposals (**CU**, **AL**, and **HYB**) is redesigned by varying both the conductor geometry and the stator yoke thickness, as illustrated in Fig. 8(a). Each generated individual during the optimization is simulated through an electromagnetic transient FEA, under two significant operating points, shown in Fig. 8(b):

- Point 1) peak torque at base speed.
- Point 2) delivered torque of 22 Nm at 11460 rpm, corresponding to highway operation at 130 km/h, where motor efficiency must be maximized.

The optimization setup follows the comparison strategies defined in Fig. 4 of Section 2.1.1. Specifically, two strategies are adopted:

- “Comparison A”, in which constraints and boundaries are selected so that the total losses

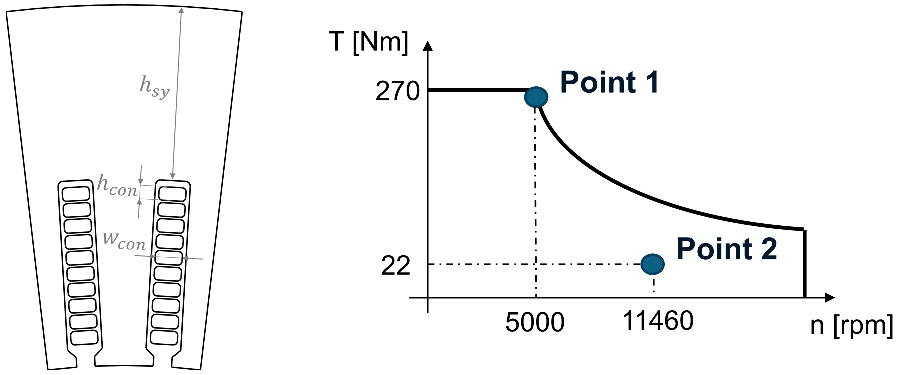

(a) (b)

Figure 8: Optimization Setup: (a) Design Variables: stator yoke h_{sy}, conductor width w_{con}, and height h_{con} (b) Operating Points

at Point 1 remain comparable among the copper, aluminum, and hybrid designs.

- "Comparison B", where a limit on the maximum stator external volume is imposed.

The optimization constraints depend directly on the chosen comparison strategy, meaning that each strategy leads to a distinct set of constraints. Consequently, two separate optimizations are performed for each of the three designs. The optimization constraints and objective functions for **CU**, **AL**, and **HYB** are reported for *Comparison A* and *Comparison B* in Table 2 and Table 3, respectively.

Table 2: *Comparison A* Optim. Setup

<table>
<tr><td colspan="5"><i>1) Design Variables Range</i></td></tr>
<tr><td colspan="2">h_{con}, mm</td><td colspan="3">0.8↔2.4</td></tr>
<tr><td colspan="2">w_{con}, mm</td><td colspan="3">2.0↔4.0</td></tr>
<tr><td colspan="2">h_{sy}, mm</td><td colspan="3">10↔25</td></tr>
<tr><td colspan="5"><i>2) Constraints from Comparison Strategy</i></td></tr>
<tr><td colspan="2" rowspan="2">Conductor Area, $mm^2 \geq$</td><td>CU:</td><td>AL:</td><td>HYB:</td></tr>
<tr><td>3.92</td><td>5.93</td><td>4.73</td></tr>
<tr><td colspan="5"><i>3) Optimization Constraints</i></td></tr>
<tr><td>Point</td><td>Parameter</td><td colspan="3">Constraint</td></tr>
<tr><td>1</td><td>DC Voltage, V</td><td colspan="3">≤ 650</td></tr>
<tr><td>1</td><td>Torque, Nm</td><td colspan="3">265↔270</td></tr>
<tr><td>2</td><td>Torque, Nm</td><td colspan="3">≥ 22</td></tr>
<tr><td colspan="5"><i>4) Objective Functions</i></td></tr>
<tr><td>Point</td><td>Parameter</td><td colspan="3">Type</td></tr>
<tr><td>1</td><td>Iron + Joule Losses, W</td><td colspan="3">Minimize</td></tr>
<tr><td>2</td><td>Iron + Joule Losses, W</td><td colspan="3">Minimize</td></tr>
<tr><td>1, 2</td><td>Rotor Weight, kg</td><td colspan="3">Minimize</td></tr>
</table>

Table 3: *Comparison B* Optim. Setup

<table>
<tr><td colspan="3"><i>1) Design Variables Range</i></td></tr>
<tr><td colspan="2">h_{con}, mm</td><td>0.8↔2.4</td></tr>
<tr><td colspan="2">w_{con}, mm</td><td>2.0↔4.0</td></tr>
<tr><td colspan="2">h_{sy}, mm</td><td>10↔25</td></tr>
<tr><td colspan="3"><i>2) Constraints from Comparison Strategy</i></td></tr>
<tr><td colspan="2">Conductor Area, $mm^2 \geq$</td><td>CU, AL, HYB: 3.92</td></tr>
<tr><td colspan="2">Stator Outer Radius, $mm \leq$</td><td>CU, AL, HYB: 105</td></tr>
<tr><td colspan="3"><i>3) Optimization Constraints</i></td></tr>
<tr><td>Point</td><td>Parameter</td><td>Constraint</td></tr>
<tr><td>1</td><td>DC Voltage, V</td><td>≤ 650</td></tr>
<tr><td>1</td><td>Torque, Nm</td><td>265↔270</td></tr>
<tr><td>2</td><td>Torque, Nm</td><td>≥ 22</td></tr>
<tr><td colspan="3"><i>4) Objective Functions</i></td></tr>
<tr><td>Point</td><td>Parameter</td><td>Type</td></tr>
<tr><td>1</td><td>Iron + Joule Losses, W</td><td>Minimize</td></tr>
<tr><td>2</td><td>Iron + Joule Losses, W</td><td>Minimize</td></tr>
<tr><td>1, 2</td><td>Rotor Weight, kg</td><td>Minimize</td></tr>
</table>

The MOGA is executed over 30 generations, each with 30 individuals, as the population and generations number should be at least ten times the number of parameters to optimize [20]. It should be noted that, although the overall losses at Point 2 are dominated by iron core losses, winding loss minimization was selected as an objective function at this operating point for thermal management and cooling purposes.

2.2.3 Candidates Selection

The selection of the best candidate for each design is made using 3D plots, scattering the solutions of each optimization. The graph axes are the optimization objectives to be minimized, namely the Losses in Point 1, Losses in Point 2, and stator weight (comprising the windings weight). In the following, the scatter plots relative to the "Comparison B" analysis are shown. The selection procedure for the results of “Comparison A” is the same, and in the following section the results of both comparisons are presented.

Each individual is represented by a point. In these plots some cases are missing, since the solutions which do not satisfy the above mentioned torque, voltage, and current density constraints have been filtered out. The results of the copper, aluminum and hybrid optimizations are shown in Figures 9(a), 9(b) and 9(c), respectively.

For a better visualization of the optimal solutions, some points have been marked in red, identifying the “Pareto front”. The Pareto front is populated by the “non-dominated solutions”, i.e., the cases for which no other solution performs simultaneously better in all objectives. In other words, for any of the red dots, it is impossible to find another solution which has simultaneously lower Losses in Point 1, in Point 2, and a lower weight.

All remaining individuals (shown in blue) are the “dominated” solutions. Each of these is indeed dominated by at least another individual, having simultaneously lower weight, Losses in Point 1, and Losses in Point 2. Consequently, such solutions have not been considered in the choice of the best candidates. Of all the Pareto front machines, the optimal ones are selected such that, for each design, minimum losses in Point 1 and Point 2 are achieved. These solutions are represented in the figures by green dots and are associated with text boxes that report the values of their corresponding objective parameters. For the hybrid design, in addition to the solution that minimizes the weight (**HYBa**), the one with minimum losses in Point 1 and Point 2 (**HYBb**) has been included.

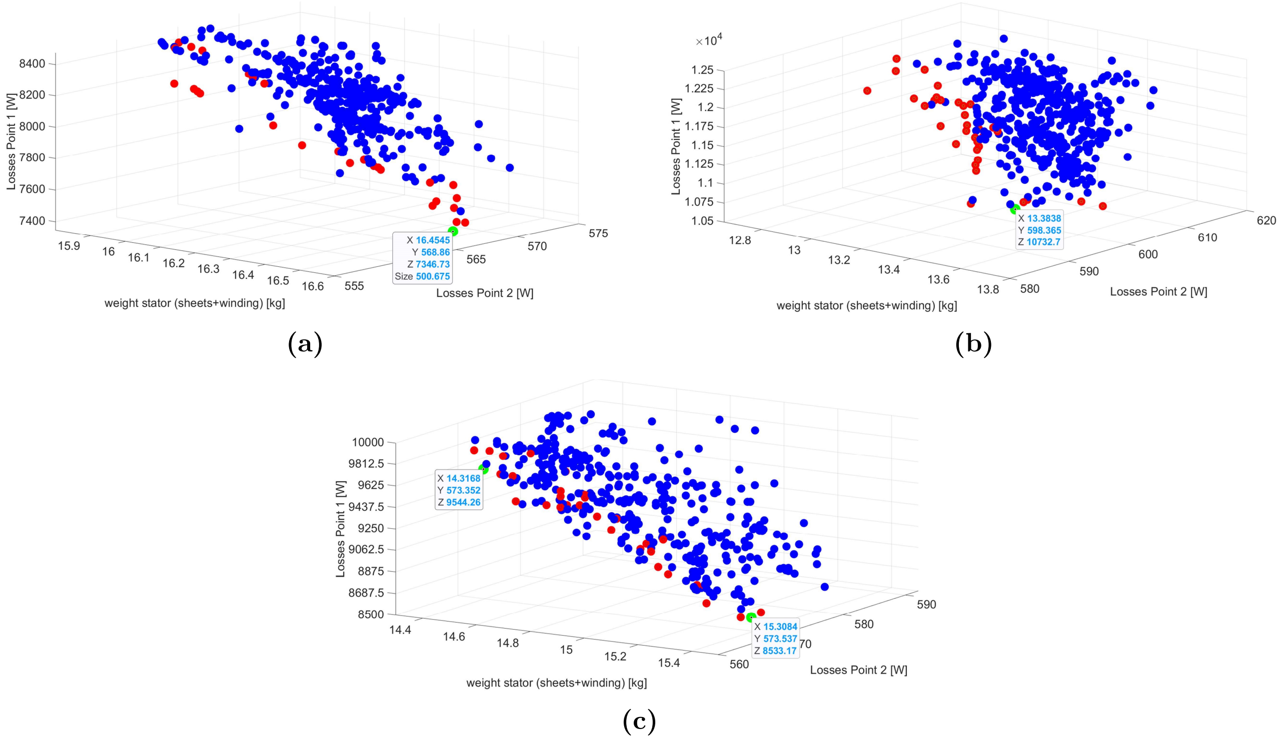

(a) **(b)**

(c)

Figure 9: Pareto fronts from "Comparison B" optimizations. a) Copper; b) Aluminum; c) Hybrid. X: Stator Weight; Y: Losses in Point 2; Z: Losses in Point 1

2.2.4 Results Comparison

Comparison A Results

The selected cases for comparison are presented in Fig. 10. The corresponding results are summarized in Table 4, where the solutions are evaluated in terms of stator geometry, including conductor cross section S_{cond}, outer radius SOR, and stator volume Vol_{stator}, as well as stator weight Wt_{stator}, winding cost C_w, and eco-cost eco-C_w. The table also reports the losses at points 1 (P1) and 2 (P2), along with the calculated efficiency η_{P2}. Joule losses account for both AC and DC losses in the active and end-winding regions.

	S_{cond} $[mm^2]$	SOR $[mm]$	Vol$_{stator}$ TOT$_{(wind.+iron)}$ $[dm^3]$	Wt$_{stator}$ TOT$_{(wind.+iron)}$ $[kg]$	C_w [€]	eco-C_w [eco-€]	$P_{tot,P1}$ $[W]$	$P_{tot,P2}$ $[W]$	$P_{iron,P2}$ $[W]$	$P_{Joule,P2}$ TOT$_{(DC+AC)}$ $[W]$	η_{P2} [%]
CU	4.67	105.5	$2.13_{(0.51+1.62)}$	$16.9_{(4.5+12.4)}$	36.11	25.55	7176	553	450	$103_{(94+9)}$	97.9
AL	7.23	113.6	$2.78_{(0.78+2.01)}$	$17.5_{(2.1+15.4)}$	4.29	6.16	7206	624	517	$107_{(87+20)}$	97.6
HYB	5.69	108.2	$2.36_{(0.62+1.74)}$	$17.2_{(3.9+13.3)}$	27.70	20.60	7154	594	488	$106_{(93+13)}$	97.8

Table 4: "Comparison A" Results

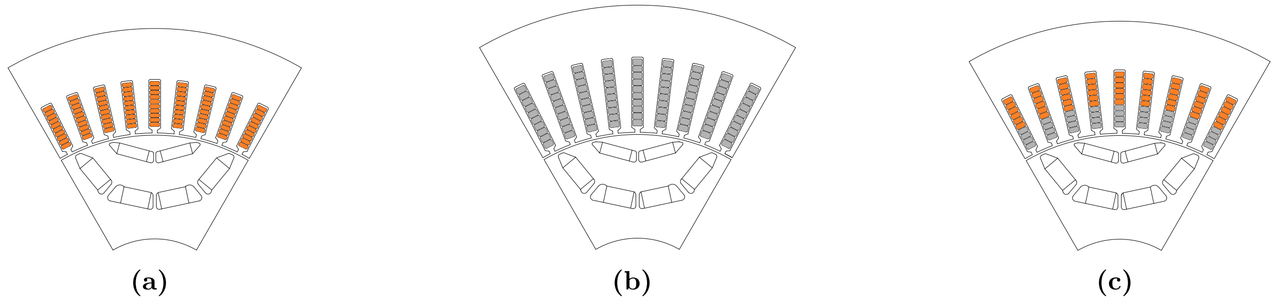

Figure 10: Layouts of selected individuals from "Comparison A". From left to right: **CU**, **AL**, and **HYB**.

It is clear that this comparison penalizes **AL**. Indeed, for having comparable losses in Point 1 with respect to the copper solution, the aluminum conductor cross section has to be increased. This means that the overall volume of the motor is higher, due to the twofold reason that more conductors' material is used, and, accordingly, more lamination material for reaching the required performance without excessive saturation, thus resulting in a larger stator outer diameter. Nonetheless, the weight of **AL** is still comparable with **CU**. Additionally, **AL** has a lower efficiency in Point 2, mainly because of the higher amount of stator iron, leading to higher iron losses which are predominant in this point. It should be noticed that total losses in Point 1 are similar, as expected from the optimization constraints. However, for automotive applications, this last aspect is not so relevant. Indeed, it would be more convenient to minimize the losses for operation at medium-low load and medium-high speed, i.e., where the machine is supposed to work during a Worldwide Harmonized Light Vehicles Test Procedure (WLTP) cycle. This is the reason why "Comparison B" is needed for a fairer analysis. Finally, **HYB** stands out as a good trade-off for this comparison, because, for the same peak torque, it stays in between the **CU** and **AL** solutions, both in terms of efficiency in Point 2, losses in Point 1, cost, weight, and sustainability.

Comparison B Results

the selected cases for comparison B are shown in Figure 11, while the results are reported in Table 5.

Although in Point 1 **AL** generates more losses than **CU** due to its higher phase resistance, the losses in Point 2 are comparable to the other solutions, because all the configurations have nearly the same amount of stator iron losses. Furthermore, **AL** is more lightweight (with a reduction of ≈ 3 kg), less expensive and more sustainable. Regarding the hybrid solution, two

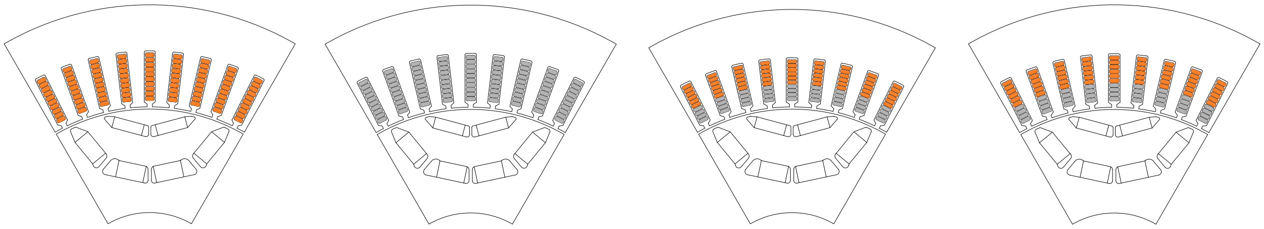

(a) (b) (c) (d)

Figure 11: Layouts of selected individuals from “Comparison B”. From left to right: **CU**, **AL**, **HYBa**, and **HYBb**.

	S_{cond} $[mm^2]$	SOR $[mm]$	Vol$_{stator}$ TOT$_{(wind.+iron)}$ $[dm^3]$	Wt$_{stator}$ TOT$_{(wind.+iron)}$ $[kg]$	C_w [€]	eco-C_w [eco-€]	$P_{tot,P1}$ $[W]$	$P_{tot,P2}$ $[W]$	$P_{iron,P2}$ $[W]$	$P_{Joule,P2}$ TOT$_{(DC+AC)}$ $[W]$	η_{P2} [%]
CU	4.56	104.7	$2.07_{(0.49+1.58)}$	$16.5_{(4.4+12.1)}$	34.69	24.55	7347	569	462	$107_{(96+11)}$	97.9
AL	4.54	104.7	$2.07_{(0.49+1.58)}$	$13.4_{(1.3+12.1)}$	2.70	3.87	10734	598	454	$144_{(138+6)}$	97.8
HYBa	4.09	103.0	$1.94_{(0.44+1.50)}$	$14.3_{(2.8+11.5)}$	19.66	14.62	9544	573	439	$134_{(129+5)}$	97.9
HYBb	4.62	104.8	$2.08_{(0.5+1.58)}$	$15.3_{(3.2+12.1)}$	22.34	16.61	8533	574	453	$121_{(114+7)}$	97.9

Table 5: "Comparison B" Results

optimal cases have been identified, namely **HYBa** (having the minimum weight) and **HYBb** (having minimum Point 1 losses). Both solutions are promising, meaning that the aluminum solution can in general be a good alternative to the traditional **CU** design.

Considerations on Results

The results of the two comparisons are summarized in Fig. 12 using radar charts.

Adopting the approach of comparison A, which considers losses equivalence at peak operating conditions (Point 1), leads to a larger overall stator volume, as more conductor and lamination material are required, resulting in a heavier stator.

For this reason, the study indicates that converting a copper hairpin stator to an aluminum design while maintaining the same maximum volume (comparison B) is the most advantageous approach when the goal is to preserve identical drive characteristics and peak torque. In this scenario, although losses at Point 1 are higher, the aluminum solution offers benefits in terms of cost (≈ 30 €), weight (≈ 3 kg), and sustainability (≈ 21 eco-€), while achieving comparable efficiency at Point 2. This is mainly because Point 2 corresponds to low-load, medium-to-high speed operation, characterized by relatively low currents and medium-to-high electrical frequencies. Under these conditions, which represent the typical duty cycle of passenger vehicles, the

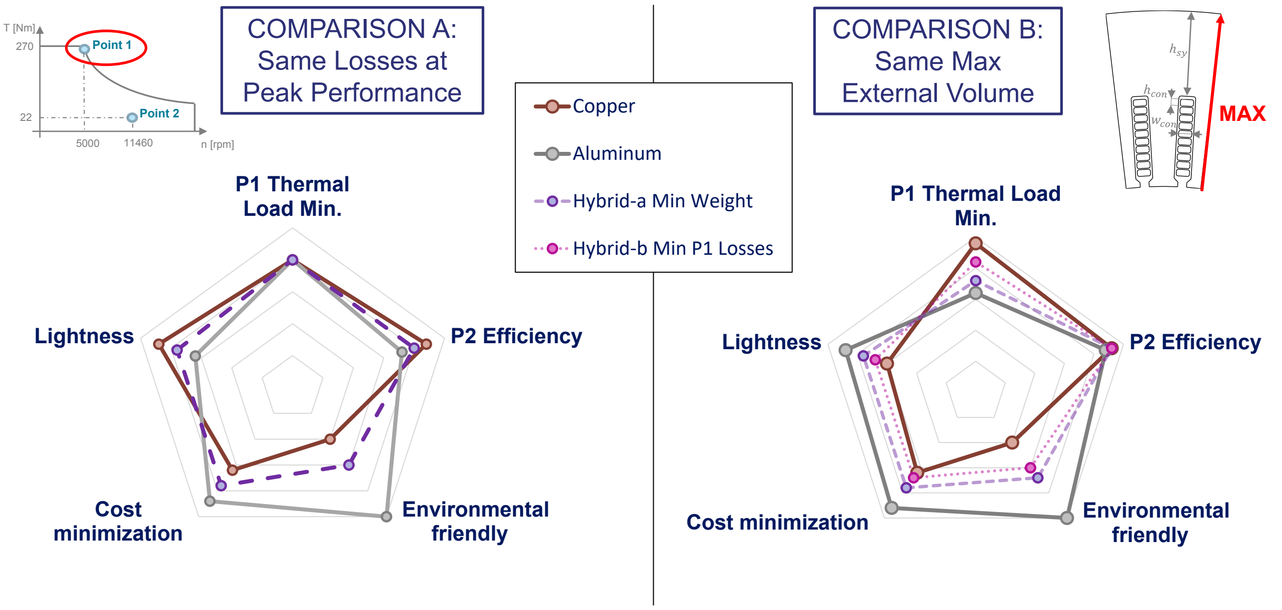

Figure 12: Results Summary of Comparison A and Comparison B

dominant contributors to total losses are iron losses, so the higher DC resistance of aluminum has a limited effect on overall efficiency throughout the driving cycle.

In the following sections, these observations are further validated by analyzing the driving cycle efficiency of **CU** and **AL** from comparison B.

Efficiency Maps

Focusing on the solutions of Comparison B, accurate losses maps are calculated in JMAG using the Maximum Torque Per Losses (MTPL) control strategy. The electric steel of the stator is NO20, whereas for the rotor 35HXT780T is used. N42UH is adopted as magnet material. For each conductor, the end winding losses are calculated as a continuation of the Joule losses of the active length part, considering only the DC losses contribution. This is a reasonable assumption due to the relatively low fundamental frequency during the cycle (below 600 Hz) [21], as well as to the low values of the flux density in the end regions.

Considering the worst-case scenario, a constant temperature of 180 °C and 100 °C was used for defining the conductors resistivity and the permanent magnets properties, respectively.

Fig. 13 shows the efficiency maps of the four solutions.

Performing a comparison in terms of peak efficiency, the highest is registered for the copper winding layout. Nevertheless, the aluminum map shows comparable efficiency results, which proves that an optimized design can lead to a lightweight, cost-friendly, and sustainable solution.

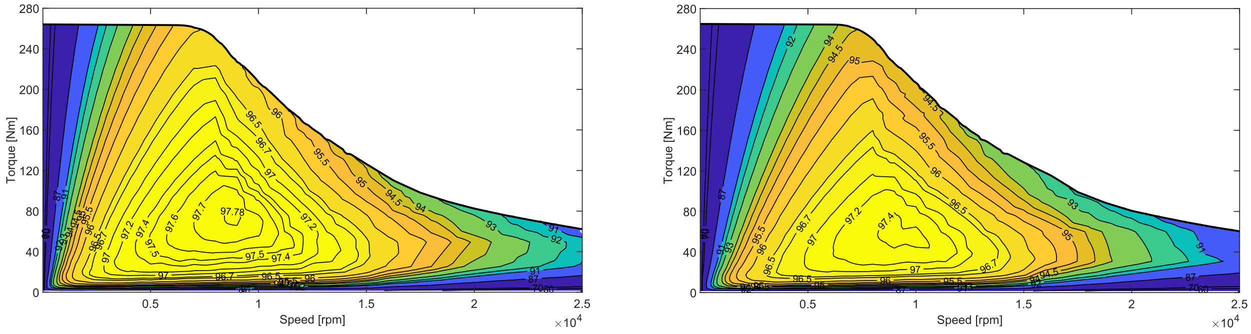

(a) Copper **(b)** Aluminum

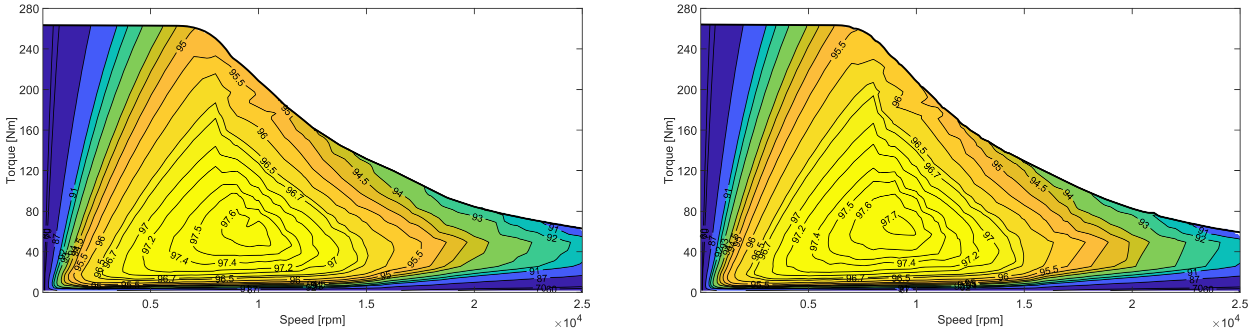

(c) Hybrid A (minimum weight) **(d)** Hybrid B (minimum peak losses)

Figure 13: Efficiency maps of Comparison B Results

Finally, the hybrid design confirms to be an interesting compromise, which is worthy of further analysis concerning other design aspects, such as welding and mechanical interface behaviors, given the different melting temperatures and coefficient of thermal expansion between the two materials.

2.2.5 Driving Cycle Analysis

The results of the efficiency maps indicate that aluminum has a slightly lower, yet comparable efficiency in the low load medium-to-high speed range, which is representative of the driving cycle conditions. To assess the practical impact of these differences, a detailed loss analysis is performed on a representative driving cycle, demonstrating that the higher DC resistance of aluminum has only a minor effect on overall driving cycle efficiency.

This analysis is made on the Worldwide harmonized Lightduty vehicles Test Cycles Class 3 (WLTC), which was initially designed for comparing CO2 and pollutant emissions globally among commercial light vehicles and passenger cars. The cycle is segmented into four subparts that simulate different driving scenarios, including urban, suburban, rural, and highway conditions. It spans a duration of 1800 seconds, and the vehicle's speed and acceleration profiles are depicted in Fig. 14.

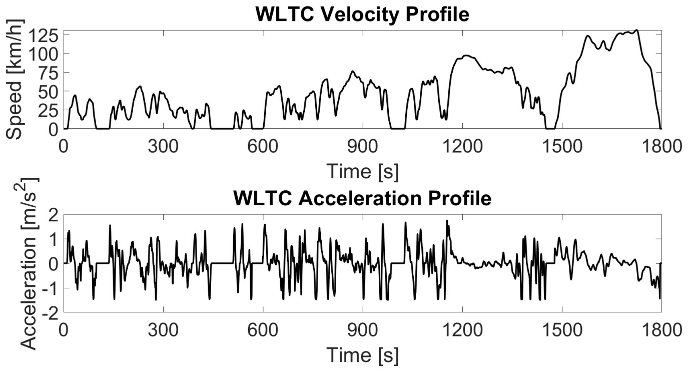

Figure 14: Velocity and acceleration profiles in the WLTP cycle [22]

The cycle is analyzed by modeling it as a sequence of 1800 steady-state operating conditions. For each operating condition, the instantaneous velocity and acceleration are used for calculating the resistive forces of the vehicle, adopting the vehicle's longitudinal dynamic equilibrium, from which the corresponding torque and speed required by the motor are determined. To this purpose, the data of the Tesla Model 3 are employed, assuming a gear ratio of 10.5. This allows to map the operating points of the WLTP cycle onto the torque versus speed characteristic curve. Regeneration is not considered in this study, meaning that deceleration is simulated as driver braking.

The operating points of the cycle are superimposed on the efficiency maps of copper and aluminum in Fig. 15.

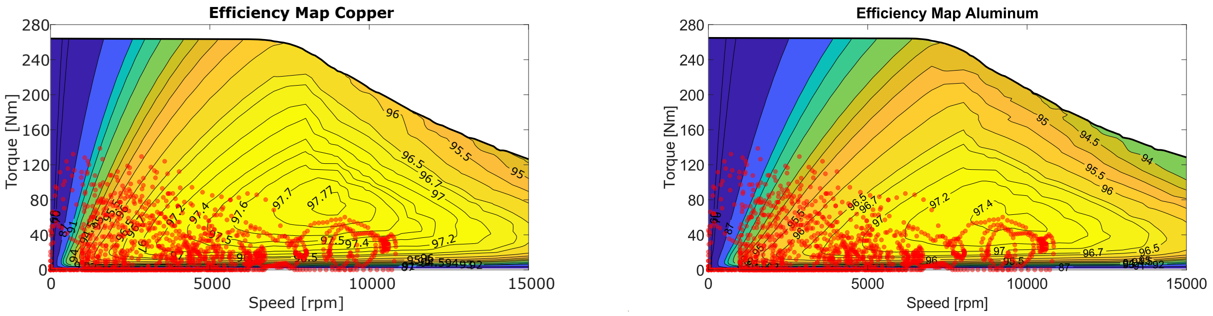

(a) **(b)**

Figure 15: WLTP Driving Cycle Points on (a) Copper and (b) Aluminum Efficency Maps

The detailed maps of losses are extracted in all the motor sub-components, Including stator yoke, stator teeth, rotor yoke, rotor magnet pole, rotor magnets, and each individual conductor.

As a result, the losses versus time for the entire cycle duration are extracted for each sub-component. An example of losses in the stator teeth for the copper solution during the cycle is reported in Fig. 16.

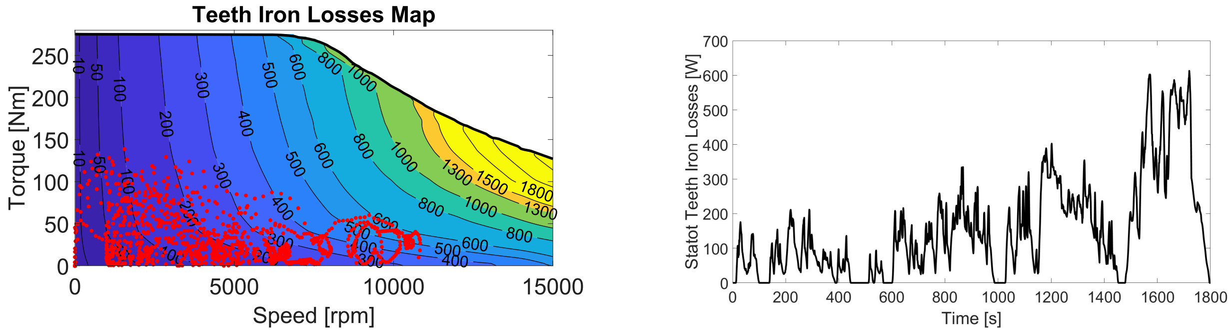

(a) Driving Cycle Points over the Stator Teeth Iron Losses Map [W] - Copper Solution

(b) Stator Teeth Iron Losses versus time for the entire driving cycle duration - Copper Solution

Figure 16: Example of Stator Iron Teeth Losses over the Driving Cycle - Copper Solution

Driving Cycle Efficiency Comparison

In Table 6, copper and aluminum are compared in terms of energy loss during the WLTC, breaking down the contributions of various loss components.

Table 6: Losses over a WLTC and Efficiency - Copper vs. Aluminum

	Copper	**Aluminum**
Energy used for traction, Wh	4529.8	4529.8
Iron Losses, Wh	279.9	275.8
DC + AC Joule Losses, Wh	132.8 + 2.7	200.0 + 2.5
Magnet Losses, Wh	0.4	0.4
Total Losses, Wh	415.8	478.7
Cycle efficiency, %	91.59	90.44

As anticipated, the iron losses contribute the most among all the different loss components, accounting for nearly 64% of the total motor losses for copper and approximately 58% for aluminum. This is due to the relatively high electrical frequency due to the speed profile of the last portion of the driving cycle. Adopting a higher gear ratio to reduce the iron losses would result in a heavier transmission. To strike a balance, a trade-off is necessary to achieve a reasonable gear ratio value.

Due to its higher resistivity, the aluminum solution exhibits increased DC losses. On the other hand, this higher resistivity also promotes a more uniform current density distribution at high frequency operation, thereby reducing skin and proximity effects. Consequently, the aluminum solution demonstrates lower AC losses compared to copper. Nevertheless, at the given fundamental frequencies and current amplitudes, the reduction in AC losses with aluminum cannot be appreciated in this context, as it does not significantly impact the overall motor losses.

In terms of efficiency, copper exhibits a slightly higher value. However, when considering the cycle's performance in terms of absolute loss generation, they can be deemed reasonably comparable. Over the cycle, the aluminum solution generates 0.063 kWh more than copper. In terms of cost analysis, assuming two driving cycles per day, five working days per week, and 52 weeks per year, the life-cycle cost associated with an additional 0.063 kWh of losses per driving cycle amounts to approximately 166 € over 10 years (with an electricity cost of 0.5 €/kWh). Finally, considering that a driving cycle covers 23.25 km and that the energy used for traction by the analyzed machine is 4529.8 Wh, the additional 0.063 kWh of losses results in a reduction of approximately 0.320 km in the WLTP range.

2.2.6 Final Considerations on the Case Study

This case study showed how to convert a copper hairpin stator into aluminum, when the same rotor and drive characteristics are kept. Two comparison strategies were investigated for developing an aluminum solution with the same peak torque as the copper one, namely comparison A and comparison B. Comparison A keeps the same peak losses (at peak torque and base speed), whereas comparison B the same maximum external volume. For both strategies, the aluminum and copper designs were independently optimized using a MOGA at two operating points (peak condition and efficiency condition) and subsequently compared. In addition, a hybrid solution was examined in each comparison, featuring copper conductors at the bottom of the slot (near the stator yoke) and aluminum conductors on the airgap side.

Although designing an aluminum hairpin using comparison A achieved losses comparable to copper under peak operating conditions, this approach is not convenient for utility car applications, since such operation is not representative of real driving. Moreover, the aluminum design obtained through comparison A required additional iron in the stator to accommodate the increased conductor cross section. This led to a heavier overall solution that is also slightly less efficient at low load and medium–high frequencies (conditions that better represent typical driving cycles) due to the increase in iron losses.

Therefore, the most convenient way of converting a copper hairpin stator into aluminum is following comparison B, that is, keeping the same maximum external volume. In this scenario, although losses at peak conditions are higher, the aluminum solution offers benefits in terms of cost, weight, and sustainability, with a comparable efficiency in typical driving operation.

This is because typical driving involves low load, medium-to-high-speed operation, where currents are relatively low and electrical frequencies are moderate to high. In these regions, iron losses are the highest contribution in total loss count, which mean that the higher DC resistance of aluminum has only a minor impact on overall efficiency throughout the driving cycle.

To validate these findings, a driving cycle efficiency analysis was performed for both the copper and aluminum designs resulting from comparison B.

Specifically, the aluminum cycle efficiency is 90.44% and the one of copper is 91.59%. In absolute terms, this signifies that aluminum produces only 64 Wh more than copper across the entire duty cycle. Besides, the aluminum solution offers a reduction in cost, weight, and environmental impact of 35.8 USD, 3.1 kg, and 20.67 eco-C, respectively, confirming that aluminum can be a valuable alternative to copper for utility cars application.

In Chapter 3, thermal analyses will be performed with the aim of verifying whether the increase in losses associated with aluminum under peak conditions does not significantly impact the motor thermal performance in a typical driving cycle of a passenger car when the same cooling system as copper is employed.

2.3 Aluminum and Copper Comparison in Wound-Field Synchronous Motors for Traction Applications

This section presents a case study to evaluate the possibility of replacing the copper winding of a wound-field rotor with aluminum ones.

For this reason, a WFSM is proposed as a replacement to an IPM for heavy duty truck application. The study assesses copper and aluminum solutions as potential winding materials for both the stator and rotor sides, with the aim of minimizing the environmental impact of the motor. Specifically, the rotor optimization process is carried out for both solutions independently, while the stator geometry remains unchanged, thus following the comparison strategy of Fig. 5.

First, the solutions are compared based on the same torque output (**Comparison B**), and then for similar rotor Joule losses (**Comparison C**).

Ultimately, a comparison between the original IPM motor and the optimized Copper and Aluminum WFSM designs is conducted in terms of weight, cost, peak torque performance, efficiency, and gravimetric power density, providing a comprehensive assessment of the potential of the proposed solutions.

The initial part of the study introduces the reference machine, providing details on its dimensions, characteristics, and chosen operating points. Then the optimization process is performed, which is carried out using a MOGA. This approach involves a thorough sensitivity analysis to identify key optimization variables [23]. The resulting optimization outcomes for both copper and aluminum machines will then be compared based at first on identical output torque, and then on identical rotor Joule losses. The final part of the study draws the conclusions by comparing the solutions.

2.3.1 Reference Design

The eco-cost values presented in Table 7 depict the Life-Cycle Assessment (LCA) findings for the most commonly used motor components [13].

An alternative to the reference IPM design is proposed to eliminate the materials with the highest eco-cost. In particular, the stator geometry of the reference IPM design remains unchanged, while the rotor will be redesigned to implement the WFSM solution, allowing for the elimina-

Table 7: Eco-cost values for different materials

Eco-cost, €$/dm^3$	
Neodymium magnets	622.7
Copper, Cu	50.1
Aluminum, Al	7.9
Polyester, unsaturated resin	2.13

tion of magnets. This aims to reduce the overall environmental impact without compromising efficiency and peak torque performance requirements.

Detailed motor specifications can be found in Fig. 17(a), featuring a six-phase, 96-slot, 8-pole configuration. The reference IPM topology designed for heavy-duty truck applications is illustrated in Fig. 17(b). An non-optimal version of the proposed WFSM is shown in Fig. 17(c), where the six parameters fully defining the rotor geometry are highlighted [24]. Such parameters are identified as t_{min} for the minimum airgap, t_{max} for the maximum airgap, WP for the pole body width, WT for the pole shoe width and HTP for the side height of the pole shoe plus the rotor yoke.

Parallel paths number	2
Axial Length, mm	140
Stator Inner Radius, mm	96
Peak Power, kW	315
Base Speed, rpm	5000
Peak Torque, Nm	615
Max Phase Current, Arms	250
Min DC Bus Voltage, V	700

(a) Motor Specifications

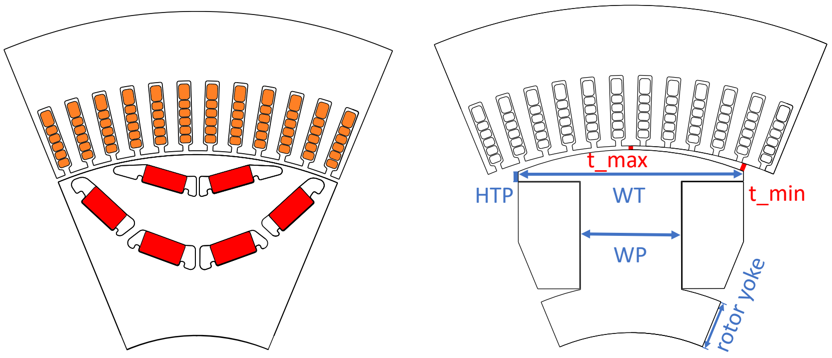

(b) IPM Rotor geometry

(c) WFSM Rotor geometry

Figure 17: Data Specifications and Reference Geometry

Two alternative WFSM designs are proposed: one uses copper windings on both the stator and rotor (namely **CU**), while the other employs aluminum windings on both the stator and rotor (namely **AL**), which further reduces motor's environmental impact, as can be seen in Table 7. Hence, two independent MOGA optimizations are performed to design the rotor of the two proposed solutions.

Hairpin windings, featuring a six-layer configuration, are employed on the stator to enhance torque and power density. Specifically, the final layer, placed at the slot bottom, has a larger size compared to the other conductors. This is done to increase the DC phase resistance while minimizing AC losses, which are more significant for the conductors facing the air gap. Conversely, the rotor is equipped with round conductors measuring 1 mm in diameter, achieving a fill factor of 0.7.

2.3.2 Optimizations Process

The output of the optimization is a WF rotor that replaces the IPM rotor of the original design. While the rotor geometry is optimized, the stator geometry and the hairpin winding are kept identical to the IPM machine. This is done for both **CU** and **AL** solutions.

The chosen optimization algorithm is the MOGA. The population size is 40, and the number of generations is 40, thus ensuring the optimization convergence.

Operating points of the optimization

The optimization is performed in two operating points, represented in Fig. 18:

- *Peak Condition (PC)*: at peak torque and base speed, reflecting the peak power requirements.
- *Efficiency Condition (EC)*: at 96 Nm and 9000 rpm, which is where efficiency needs to be optimized, as it is one of the most frequent and energy-intensive points encountered during the considered heavy-duty truck's driving cycle.

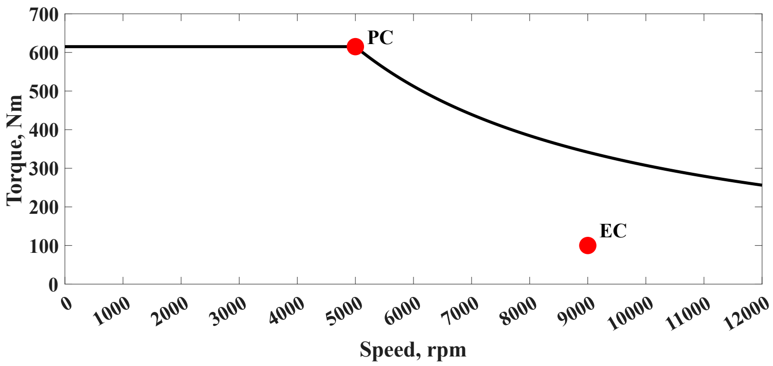

Figure 18: Torque Speed Curve

Specifically, the optimization is set with the requirement of identical peak power and torque (in *PC*) as the reference IPM motor, while maximizing the efficiency in *EC* and minimizing material weight and cost. Finally, the optimal designs for **CU** and **AL** will be compared in terms of efficiency, cost, weight, and sustainability.

Every newly generated individual in the optimization is evaluated for both the operating points *PC* and *EC*, by means of separate two electromagnetic transient analyses. The simulation setup at these operating points requires the definition of three input parameters: stator current amplitude (I_s), stator current phase angle (γ), and rotor field current (I_f).

To this end, the values of I_s, γ, and the rotor magnetomotive force $N_f I_f$ in *PC* are found following the Maximum Torque Per Ampère (MTPA) criterion, whereas in *EC* the Maximum Torque Per Losses (MTPL) is adopted. This is done for both **CU** and **AL** considering the reference geometry of Fig. 17(c).

Table 8 summarizes the input parameters for *PC* and *EC*.

Table 8: Current Amplitude and Phase Angle settings

Simulation setup			
Operating Point	**Parameter**	**CU**	**AL**
PC	I_s, *[Arms]*	250	250
PC	γ, *[deg]*	12	11
PC	N_f I_f, *[At]*	3240	3240
EC	I_s, *[Arms]*	61.2	65.0
EC	γ, *[deg]*	24.2	24.3
EC	N_f I_f, *[At]*	882	860

The approach of using the same $N_f I_{f,PC}$ and $N_f I_{f,EC}$ for every newly generated individual during the optimization ensures a fixed electric loading on both the stator and rotor sides. This means that, despite the geometry variation, the optimal $(I_s, \gamma)_{PC}$ and $(I_s, \gamma)_{EC}$ previously calculated can be reasonably kept constant, still obtaining the required torque.

In addition, the geometry of each individual is characterized by its own rotor coil region (A_{coil}). Given that the size of the rotor conductors and the rotor coil fill factor are fixed, any variation in the A_{coil} will consequently lead to a variation in the number of conductor turns (N_f). Based on the value of N_f and the rotor magnetomotive force in *PC* and *EC* ($N_f I_{f,PC}$ and $N_f I_{f,EC}$), the corresponding value of I_f is consequently derived.

Trend of convergence of the optimization algorithm

As stated above, the size variation of the coil region A_{coil} reflects in a variation of the N_f for each geometry. This means that, to maintain the same magnetomotive force ($N_f I_f$, see (2.9)), the value of the field current (I_f) and thus that of the current density (J_f) on the rotor side has to vary accordingly, as per (2.10).

$$T \propto N_f I_f = const \rightarrow I_f \propto \frac{1}{N_f} \tag{2.9}$$

$$(A_{coil} \propto N_f \quad and \quad I_f \propto J_f) \rightarrow \frac{1}{J_f} \propto A_{coil} \tag{2.10}$$

From (2.9) and (2.10), the trend of the field coil losses can be described as in (2.11).

$$P_j \propto N_f I_f^2 \rightarrow P_j \propto \frac{1}{A_{coil}} \tag{2.11}$$

In simpler terms, if a newly generated individual had a wider field coil region, it would result in a higher number of coil turns. For the same magnetomotive force, this would result in a lower current density, and thus rotor Joule losses. At the same time, a wider coil region eventually would lead to higher saturation in the rotor body, as its amount would be lower due to limited rotor space. Consequently, the required level of torque could not be reached due to the higher equivalent reluctance of the magnetic circuit. Aligned with the optimization objectives and constraints outlined in the subsequent sections, this strategy enables the algorithm to converge to those solutions which minimize the rotor Joule losses with incipient iron saturation, while still satisfying the specified torque requirements. The concept predicting how the algorithm will converge is schematized in Fig.19.

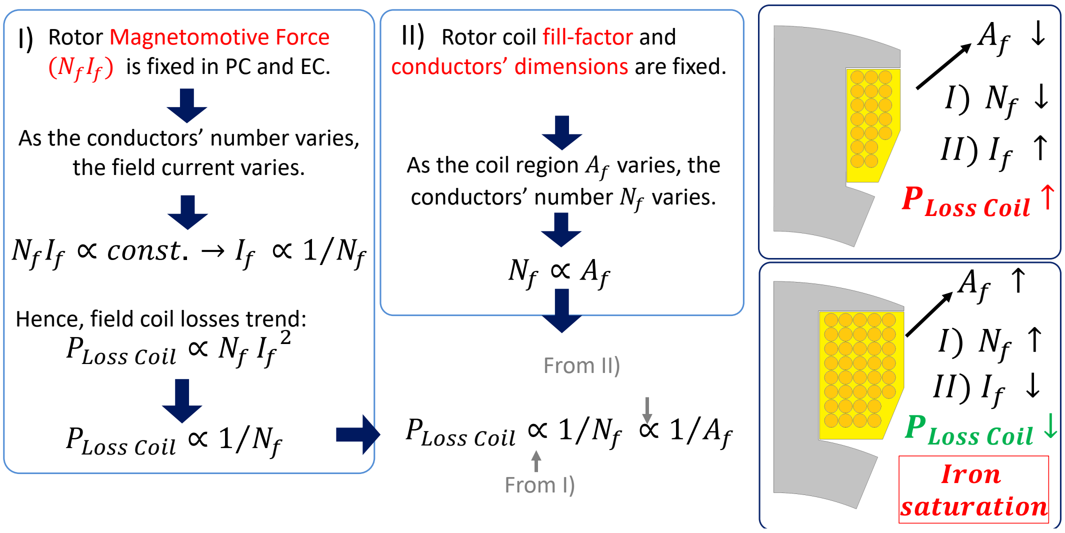

Figure 19: Strategy for optimization algorithm convergence.

Design variable definition: Sensitivity analysis

The optimal geometry needs to simultaneously minimize the losses in the *EC* and reduce the overall motor weight, while ensuring that in *PC* the desired torque can be met without overcoming the DC voltage limit.

Based on these objectives, the most influential rotor geometrical parameters are selected. These selected variables will then function as the designated design variables for the optimization process.

To achieve this, a sensitivity analysis is conducted between each objective function and the six independent parameters highlighted in Fig 17(c). The purpose of this sensitivity analysis is to compute the Pearson coefficient, which quantifies the level of correlation between the geometrical parameters and the objective functions. Parameters with a stronger correlation will be prioritized.

The range of variability for each parameter used in the sensitivity is reported in Table 9.

Table 9: Sensitivity Parameters Range and Average Value

Parameters Range			
Parameter	**Min.**	**Max.**	**Avg.**
t_{min}, *mm*	0.8	1.2	1
t_{max}, *mm*	1	3	2
HTP, *mm*	1	4	2.5
WP, *mm*	8	18	13
WT, *mm*	25	33	29
rotor yoke, *mm*	10	15	12.5

Such ranges are identified considering both geometrical and saturation limitations. Table 9 also highlights the average value for each variable, defining the reference geometry of Fig. 17(c), for which the input parameters (rotor magnetomotive force and (I_s,γ)) in *PC* and *EC* have been calculated, as previously mentioned.

The sensitivity analysis is carried out considering a sample of 100 randomly generated geometries, with each of the six observed geometrical variables varying within their range limits. The correlation tables for both materials are displayed for both the *PC* and *EC* in Fig. 20. Due to the eventual saturation effects, the highest correlation with the torque is obtained for the pole body width. The weight is mainly linked to the pole head width. The pole body width has strong correlations with overall losses, this because the wider it is, the smaller the field

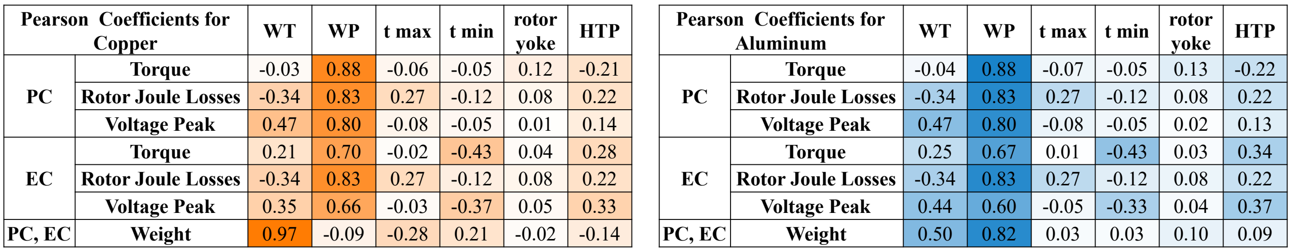

Pearson Coefficients for Copper		WT	WP	t max	t min	rotor yoke	HTP
PC	Torque	-0.03	0.88	-0.06	-0.05	0.12	-0.21
	Rotor Joule Losses	-0.34	0.83	0.27	-0.12	0.08	0.22
	Voltage Peak	0.47	0.80	-0.08	-0.05	0.01	0.14
EC	Torque	0.21	0.70	-0.02	-0.43	0.04	0.28
	Rotor Joule Losses	-0.34	0.83	0.27	-0.12	0.08	0.22
	Voltage Peak	0.35	0.66	-0.03	-0.37	0.05	0.33
PC, EC	Weight	0.97	-0.09	-0.28	0.21	-0.02	-0.14

(a)

Pearson Coefficients for Aluminum		WT	WP	t max	t min	rotor yoke	HTP
PC	Torque	-0.04	0.88	-0.07	-0.05	0.13	-0.22
	Rotor Joule Losses	-0.34	0.83	0.27	-0.12	0.08	0.22
	Voltage Peak	0.47	0.80	-0.08	-0.05	0.02	0.13
EC	Torque	0.25	0.67	0.01	-0.43	0.03	0.34
	Rotor Joule Losses	-0.34	0.83	0.27	-0.12	0.08	0.22
	Voltage Peak	0.44	0.60	-0.05	-0.33	0.04	0.37
PC, EC	Weight	0.50	0.82	0.03	0.03	0.10	0.09

(b)

Figure 20: Pearson Coefficient: for **CU** (a) and for **AL** (b)

coil area, as expected from (2.11). The reason why the correlation between WP and the rotor weight is high for **AL** and almost zero for **CU** is due to the different mass density values of copper and aluminum, equal to 8.96 and 2.7 kg/dm^3, respectively. The outcome of the sensitivity analysis highlights that the most influential parameters to be designated as optimization design variables are WP, WT, t_{max} and HTP.

Optimization setup

The optimization is set by defining the relevant constraints, objective functions and design variables. In particular, for the aluminum design the constraints will be chosen based on the way it is compared to copper.

As mentioned earlier, identical external rotor radii and design variable ranges are applied to both **CU** and **AL**. This implies that the comparison between the two types of machines is set by establishing a common limit on the value of the maximum field coil volume, Fig. 5. With such assumptions, there are two ways of performing the comparison:

- *Comparison B*: same peak torque for **CU** and **AL** machines. This implies that, due to the identical field coil volume spatial limitation, **AL** is expected to generate more losses in PC, because of its higher resistivity. In this comparison, identical constraints are applied on the torque value in PC for both **AL** and **CU**, as shown in Table 10.
- *Comparison C*: same field coil losses generated in PC, see Table 11. In particular, the optimization constraints in the **AL** optimization are specifically implemented to ensure that the field coil losses do not exceed those of the reference **CU** design, which is identified as the optimal solution from the **CU** optimization results of *Comparison B*.

  In *Comparison C*, to compensate the resistivity disparity, the **AL** optimization tends to generate individuals with larger field coil volumes than the reference **CU** design, proportional to the resistivity ratio. Such convergence towards the maximum field coil volume limit results in a lower amount of iron in the rotor. Consequently, the **AL** is expected to be unable to achieve the same peak torque as the **CU**, as it becomes more likely to saturate.

Table 10 and 11 show the optimization settings of *Comparison B* and *C* respectively, including constraints, objective functions and design variables, for both **CU** and **AL** optimizations. The total losses in *EC* include the stator and rotor iron losses, and the stator windings and rotor coil Joule losses. Suitable modelling adjustments are included to account for end-winding losses and the influence of iron sheet manufacturing on iron losses. Specifically, on the stator end windings only DC losses are supposed, as AC losses are expected to be negligible in the end windings within a wide frequency range. Furthermore, in *PC*, the resistivity is defined using rotor and stator winding temperatures of 180°C and 150°C, respectively. In *EC*, the corresponding temperatures are 150°C for the rotor and 120°C for the stator windings.

Table 10: *Comparison B* Strategy

1) Design Variables Range		
WP, *mm*		8↔18
WT, *mm*		25↔33
HTP, *mm*		1↔4
t_{max}, *mm*		1↔3
2) Optimization Constraints		
Point	**Parameter**	**Constraint**
PC, *EC*	DC Voltage, *V*	≤ 700
PC	Torque, *Nm*	610 ↔ 620
EC	Torque, *Nm*	≥ 90
3) Objective Functions		
Point	**Parameter**	**Type**
PC	Rotor Joule Losses, *W*	Minimize
EC	Total Losses, *W*	Minimize
PC, *EC*	Rotor Weight, *kg*	Minimize

Table 11: *Comparison C* Strategy

1) Design Variables Range		
WP, *mm*		8↔18
WT, *mm*		25↔33
HTP, *mm*		1↔4
t_{max}, *mm*		1↔3
2) Optimization Constraints		
Point	**Parameter**	**Constraint**
PC, *EC*	DC Voltage, *V*	≤ 700
PC	Rotor Joule Losses, *W*	≤ 3400
3) Objective Functions		
Point	**Parameter**	**Type**
PC	Torque, *Nm*	Maximize
EC	Total Losses, *W*	Minimize
PC, *EC*	Rotor Weight, *kg*	Minimize

2.3.3 Candidates Selection

For each optimization, the optimal candidate is chosen based on 3D scatter plots including all the generated individuals which satisfied the optimization constraints. Hence, three 3D scatter plots are reported: **CU** *Comparison B*, **AL** *Comparison B* and **AL** *Comparison C*. In the following 3D plots, the non-dominated solutions belonging to the Pareto front are distinguished with a different colour from the dominated cases, that are shown in black.

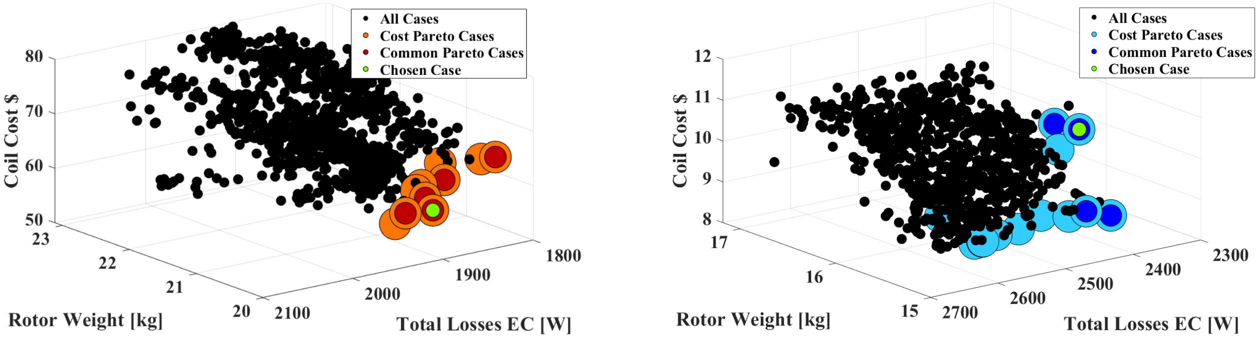

(a) **(b)**

Figure 21: Pareto front for Cost: **CU** (a) and **AL_B** (b)

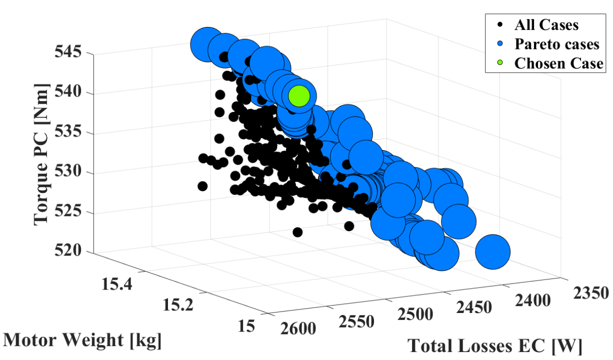

Figure 22: Pareto front for **AL_C** with same **CU** rotor Joule losses in *PC*

- *Comparison B*: the optimization objectives are the weight and the total losses in *EC*. However, in the selection process of the best case, additional objective functions related to rotor coil cost and *PC* rotor Joule losses minimization are taken into account. Specifically, two types of 3D Pareto fronts are derived: one incorporating weight, total losses in *EC*, and rotor coil cost as objective functions (Cost Pareto front), and the other involving weight, total losses in *EC*, and rotor Joule losses in *PC* (*PC* Rotor Joule Losses Pareto front, that is not shown). To further refine the selection, the decision is made among the solutions that appear in both Pareto fronts. In Fig. 21(a) and (b), the solutions from the Cost Pareto front are depicted in orange for **CU**, and in light blue for **AL**. Among these, the solutions that would also appear in the rotor Joule losses *PC* Pareto front are specifically highlighted in a darker orange or blue, for **CU** and **AL** plots respectively. The selected cases are marked in green, identified as **AL_B** for aluminum, and as **CU** for copper. As mentioned above, the value of the rotor Joule losses in *PC* of the **CU** design is used as a constraint for the **AL** optimization of *Comparison C*, see Table 11.

- *Comparison C*: in this comparison, maximizing the peak torque is an explicit optimization objective, as shown in Table 11. Conversely, the rotor Joule losses in *PC* are now set as a constraint and only the solutions with similar rotor Joule losses in *PC* for **CU** are represented in this plot. The light blue dots in Fig. 22 denote the Pareto front including as objectives the weight, the total losses in *EC* and the peak torque. The selected case is marked in green and identified as **AL_C**.

2.3.4 Results Comparison

In this section, a comprehensive analysis is conducted among the four machines: the initial IPM, **CU**, **AL_B**, and **AL_C**, which are shown in Fig. 23.

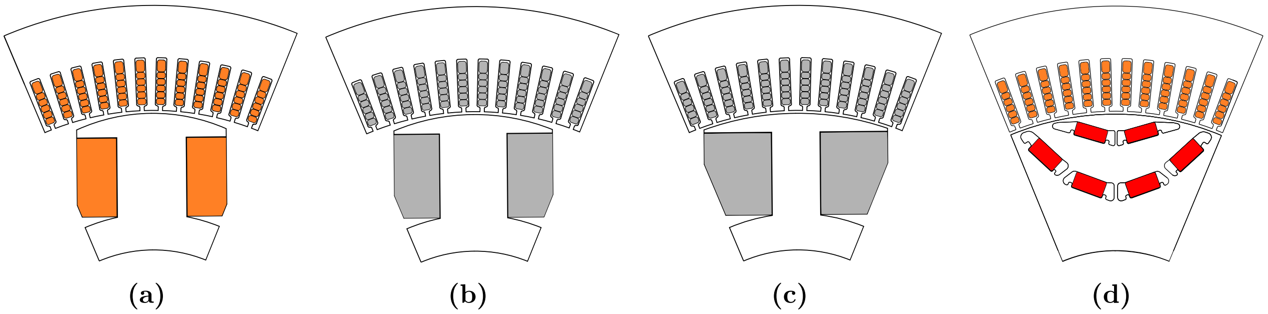

Figure 23: Selected Solutions: **CU** (a), **AL_B** (b), **AL_C** (c) and **IPM** (d)

The results are shown in Table 12, where the gravimetric power density refers to the motor active parts only, shaft excluded, while the rotor coil eco-cost includes also the resin the current density in PC refers to the rotor one. Figure 24 presents a radar chart that visually compares the results.

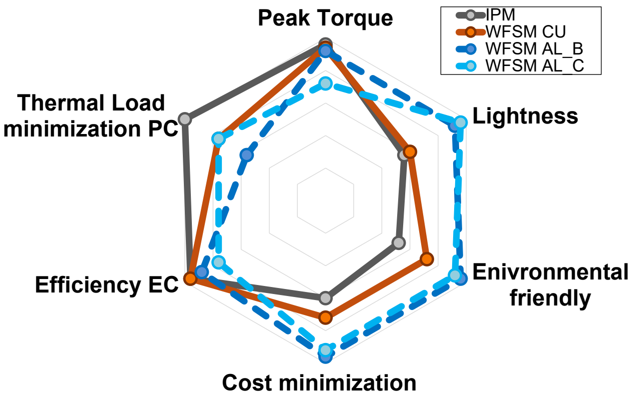

Figure 24: Comparison Radar Chart

Table 12: Optimal Solutions Comparison

Optimal Solutions Performance Evaluation				
Parameter	**CU**	**AL_B**	**AL_C**	**IPM**
Torque *PC*, *Nm*	611	612	540	615
Torque *EC*, *Nm*	93	91	82	96
Current Density *PC*, A/mm^2	12.7	10.7	7.8	/
Rotor Joule Losses *PC*, *W*	3425	4685	3488	/
Rotor Iron Losses *PC*, *W*	34	40	79.72	187.5
Total Losses *EC*, *W*	1895	2406	2480	2017
Efficiency *EC*, %	97.9	97.3	96.8	97.8
Rotor Core Weight, *kg*	12.9	12.4	11.1	17.8
Rotor Coil or PMs Weight, *kg*	7.3	3.1	4.2	2.9
Stator Winding Weight, *kg*	8.9	2.7	2.7	8.9
Total Motor Weight, *kg*	50.5	39.6	39.4	51.0
N° field conductors	325	385	525	/
Rotor Coil or PMs Cost, $	62.9	6.9	9.5	106.0
Stator Winding Cost, $	76.3	6.0	6.0	76.3
Rotor coil or PMs eco-cost, €	31.8	7.6	10.51	240.8
Stator Winding eco-cost, €	49.8	7.9	7.9	49.8
Power Density, *kW/kg*	6.34	8.11	7.18	6.31

In the following, the results are discussed in detail. First, a side-by-side comparison of the IPM and copper WFSM solutions is presented, followed by a comparison between the **CU** and **AL** WFSM solutions. Finally, the most suitable strategy for the aluminum design is selected, and the corresponding design is compared with the original IPM reference machine.

IPM vs CU WFSM

As clearly highlighted by the eco-cost results, switching from the IPM configuration to the WFSM one allows for a significant reduction pf the environmental impact of the motor, thanks to the removal of the magnets. In addition, the absence of magnets in the WFSM also offers advantages in terms of weight and cost, with these benefits being even more pronounced when aluminum is used instead of copper. However, this comes at the expenses of having higher rotor losses in both *PC* and *EC*, attributable to the presence of the DC winding. This reflects in slightly lower efficiency in *EC*. The results are summarized in Fig. 25.

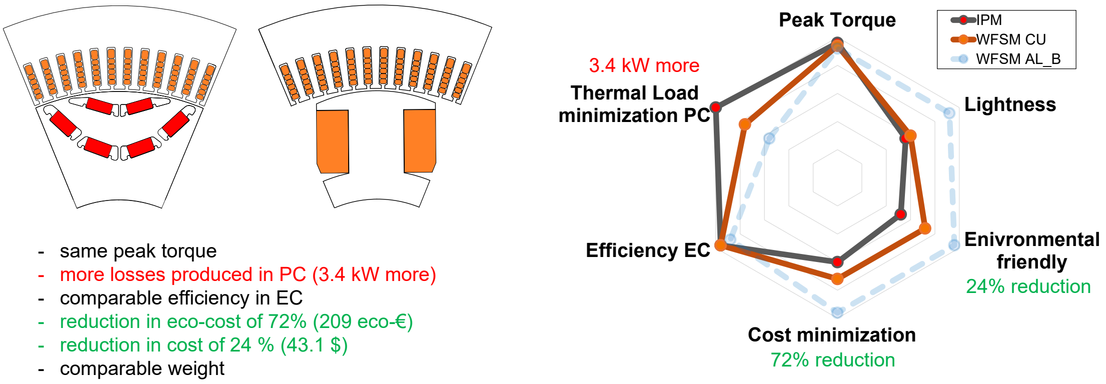

- same peak torque
- more losses produced in PC (3.4 kW more)
- comparable efficiency in EC
- reduction in eco-cost of 72% (209 eco-€)
- reduction in cost of 24 % (43.1 $)
- comparable weight

Figure 25: IPM vs Copper WFSM Comparison

CU vs AL WFSMs

The comparison between **AL_B** and **CU** reveals that the former has higher losses in *PC*, due to the higher stator phase and rotor coil resistances. However, in *EC*, the efficiency is comparable because at this point, the stator iron losses represent the major contribution to the total losses generation. If one considers **AL_C**, and thus similar losses as **CU 1** in *PC*, then the peak torque requirement can no longer be satisfied due to excessive rotor iron saturation. This is a consequence of having a smaller WP to accommodate more conductor turns, necessary to remain within the rotor Joule losses limit. When comparing the WFSM solutions in terms of cost, weight, and sustainability, the aluminum designs outperform the copper one. This is evident in the remarkable values of the gravimetric power density for the aluminum designs, which meets the 2025 "Advanced Propulsion Centre" target requirement of 7 kW/kg [25]. Fig. 26 shows the comparison between **CU** and **AL_B**.

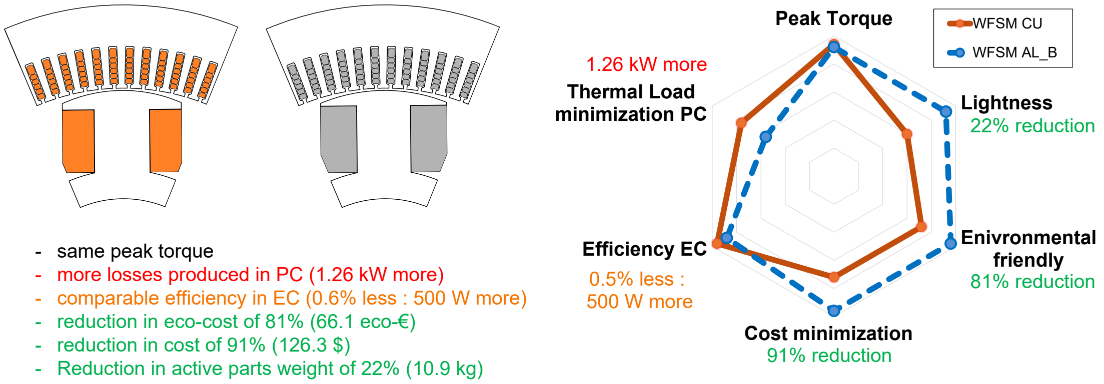

- same peak torque
- more losses produced in PC (1.26 kW more)
- comparable efficiency in EC (0.6% less : 500 W more)
- reduction in eco-cost of 81% (66.1 eco-€)
- reduction in cost of 91% (126.3 $)
- Reduction in active parts weight of 22% (10.9 kg)

Figure 26: Copper WFSM vs Aluminum_B WFSM Comparison

IPM vs AL_B

When it comes to compare copper with aluminum in a WFSM, the designer can either opt to maintain the peak torque or prioritize the rotor joule losses in *EC*. In this work, the choice is to select **AL_B** due to the highest priority given to the peak torque requirement in the application at hand. As mentioned, this results in higher rotor joule losses. However, for this type of application, this aspect is not as critical, as the machine is not expected to operate in *PC* during the driving cycle but rather in the *EC* region. **AL_B** exhibits comparable efficiency in *EC* to **CU 1**, with the additional advantages of being lighter, cheaper, and more sustainable. Fig. 27 highlights the comparison between the selected aluminum design (**AL_B**) and the original IPM reference machine.

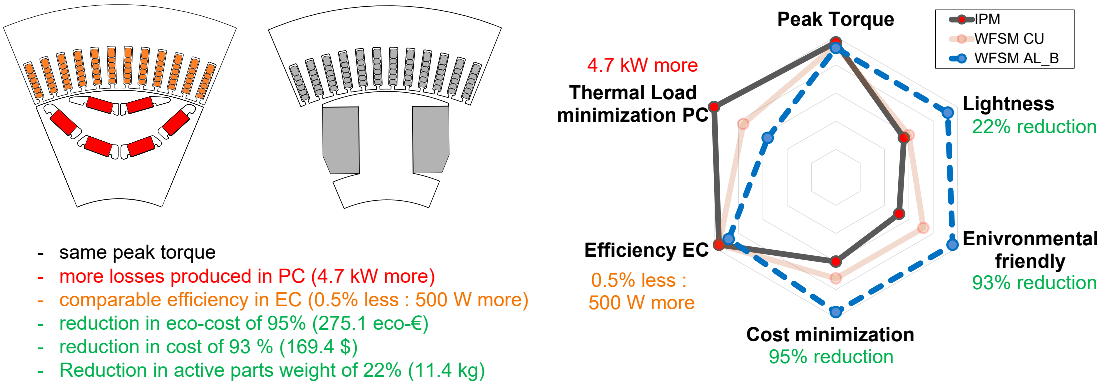

Figure 27: IPM vs Aluminum_B WFSM Comparison

2.3.5 Final Considerations on the Case Study

The study proposed a WFSM alternative to a reference IPM for heavy truck-duty applications, aiming to minimize the motor environmental impact. Copper and aluminum were compared as potential winding materials for both stator and rotor windings of the WFSM. Two main comparisons were performed between copper and aluminum for the redesign of the WFSM rotor: one aimed at maintaining the same output torque value (Comparison B), and the other focused on keeping the same losses (Comparison C). The comparative elements were found performing independent MOGA optimizations for the two solutions, which optimized the most influential rotor parameters selected through a detailed sensitivity analysis.

With respect to the original IPM reference, the study revealed that despite a slightly lower efficiency, the copper WFSM enables a reduction in eco-cost of nearly 72% (209 eco-€), with a decrease of 24% (43.1 $) in terms of cost. When comparing the aluminum WFSM to the copper WFSM, a further reduction in eco-cost of nearly 77% (80.2 eco-€) and in cost of 88% (123 $) can be achieved, while still maintaining comparable efficiency. In terms of weight, the aluminum WFSM solution is nearly 22 % (11 kg) lighter than the IPM and copper WFSM counterparts, thus allowing to achieving up to 8.11 kW/kg gravimetric power density, provided that the higher rotor joule losses in peak conditions can be accepted.

The selected strategy for the conversion of the wound-field rotor design into aluminum is Comparison B, which preserves the peak torque and field coil area similar to the copper design. Although higher resistivity leads to increased higher joule losses than copper at peak conditions, the efficiency in the low load area (typical of driving cycle conditions) remains comparable due to the higher influence of the iron losses.

2.4 Case Studies from Literature

This section reviews case studies from the literature on aluminum hairpin winding designs for automotive traction applications, classifying them according to the comparison strategies defined above.

This classification shows that all case studies reported in the literature can be assigned to the comparison strategies introduced in the previous sections, confirming the generality of the guidelines provided to convert a copper hairpin winding machine to aluminum.

All identified examples from the literature are summarized in Table 13, which also includes the two cases of Sections 2.2 and 2.3.

Specifically, in [26], the authors propose two aluminum hairpin winding solutions by optimizing the stator and rotor parameters under the same design constraints as the copper baseline, namely, identical DC voltage, maximum phase current, active parts volume, peak torque, and base speed. The first design follows the comparison strategy B, achieving a magnetic loading similar to that of the copper reference. However, this results in higher peak point losses. The second design adopts the comparison strategy C, imposing equivalence in peak point losses with the reference copper machine. To achieve the same peak torque, this configuration requires a higher magnetic loading, which is realized by increasing the amount of permanent magnet material in the rotor.

The studies [17], [27], and [29] are those reported in the previous sections.

In [28], a reference copper hairpin induction machine is compared with both an aluminum variant and a hybrid copper–aluminum version using comparison strategy B, as all designs share the same conductor geometry. The chosen hybrid configuration demonstrates reduced winding cost and weight relative to the copper baseline, resulting in improved gravimetric torque and power densities.

In [30], strategy B is adopted to perform electromagnetic and thermal system-level analyses in Matlab Simulink comparing the driving cycle performance of a benchmark WFM under four winding configurations: all-copper, all-aluminum, and hybrid arrangements with copper and aluminum alternated between stator and rotor. Aluminum-based designs increase Joule losses and slightly reduce efficiency, with larger penalties in urban driving and moderate effects in mixed and high-speed cycles. Thermally, they cause torque derating at low speeds, especially

REF.	COMPARISON STRATEGY	STUDY DESCRIPTION APPLICATION	RESULTS
[26]	B – C	Two aluminum hairpin designs (each with a distinct comparison) with optimized stator and rotor. Automotive traction application, 210 kW peak power.	In strategy B, identical current density and magnetic loading is imposed, resulting in around 30% higher losses for aluminum at peak torque over the whole constant torque region. In strategy C, identical losses and external volume are imposed, but aluminum could reach same peak torque performance due to higher magnetic loading (21% more magnets).
[17], [27]	A - B	Stator optimization for pure aluminum and hybrid (Cu–Al) hairpin configurations, each evaluated in two design versions based on distinct comparison strategies against copper. Automotive traction application, 150 kW peak power.	Strategy B is preferable for aluminum implementation, as it offers cost (-36 USD), sustainability (-20.6 eco-€), and weight (-3.1 kg) benefits with only a limited loss increase in the driving-cycle operating range (+60 Wh). The hybrid configuration provides a flexible trade-off, allowing designers to balance copper and aluminum amount to achieve the desired performance for a given application.
[28]	B	An aluminum and a hybrid (Cu–Al) hairpin solution for induction machine, compared against copper. Automotive traction application, 140 kW peak power.	The hybrid configuration reduces winding cost (-46.6%) and weight (-36.1%) compared to the copper baseline, leading to higher power density (around +3.7%).
[29]	B - C	Rotor optimization of two WFSMs configurations for heavy-duty applications (250 kW continuous power): one using copper in both stator hairpins and rotor windings, and the other using only aluminum. Each configuration is optimized according to two distinct comparison strategies.	Although aluminum results in higher rotor Joule peak losses (+46%), it provides notable advantages in cost (-88%), eco-cost (-77%), and weight (-4.2 kg in the rotor, -57%), thereby lowering centrifugal forces on the rotor. Strategy C, which imposed identical maximum rotor volume and peak losses, resulted in reduced peak torque due to higher rotor pole saturation.
[30]	B	Electromagnetic and thermal system-level analyses comparing the driving cycle performance of a 130 kW prototype WFM under four winding configurations: all-copper (CuCu), all-aluminum (AlAl), and hybrid arrangements with copper and aluminum alternated between stator and rotor (CuAl - with aluminum on the rotor - and AlCu).	CuAl slightly reduces efficiency with respect to CuCu, with larger penalties in urban driving (up to +20% total losses) and moderate effects in mixed and high-speed cycles (less than +5%). Configuration with aluminum in the stator windings (AlCu and AlAl) exhibit higher total losses (from +10% up to +30% in extreme scenarios). In both stator and rotor, the average driving cycle temperature increases by 5% when aluminum is used.
[31]	B	Conductors' geometry optimization of an aluminum and a copper hairpin stator. Automotive traction application, 150 kW peak power.	Aluminum winding losses are 40% higher in peak torque operation and 11.9% higher at peak power / maximum speed. However, the aluminum design achieves 13.4% higher gravimetric power density.
[32]	B	Aluminum hairpin to replace copper of a reference machine (170 kW peak power) first optimized for traction in utility cars application. Same conductor geometry with no design modification is adopted, illustrating practical implications for automotive companies of directly replacing copper with aluminum.	Aluminum shows comparable WLTP driving cycle efficiency (+65 Wh cycle energy loss) with advantages in cost (-55 $), weight (-5 kg), and sustainability (-33 eco-€). The findings are validated through experimental testing on two identical prototypes that differ only in conductor material.

Table 13: Literature-available Aluminum and Hybrid (Cu+Al) Hairpin Winding Case Studies, classified based on Comparison Strategy to Copper

when used in the stator. In hybrid configurations, rotor aluminum mitigates this effect but increases excitation requirements, while reducing mechanical stress due to lower rotor mass.

Finally, in [31], the copper and aluminum winding technologies are compared under the constraint of the same active part volume and identical maximum torque, corresponding to comparison strategy B. The results show that, at the peak power point, the aluminum design exhibits higher overall losses. However, it also achieves a higher gravimetric power density compared to the copper counterpart.

The results of the case studies shown in this table confirm that comparison strategy B is the most effective approach for replacing copper with aluminum, when identical drive characteristics to the copper baseline (i.e., the same DC voltage and maximum phase current) and a fixed rotor volume are imposed. This strategy preserves both maximum external volume and peak torque, making it particularly suitable for automotive applications, where cost, weight, and sustainability are critical factors.

In fact, if higher losses under peak conditions were acceptable, aluminum would offer advantages in terms of cost, weight and sustainability, while maintaining comparable efficiency over a WLTP driving cycle.

This is shown through the detailed breakdown of total losses over the driving cycle as performed in Section 2.2, which highlights that iron losses contribute the most significantly, thereby explaining the minimal impact of aluminum windings on overall efficiency. The increase in total energy losses with aluminum is limited to only a few tenths of a watt hour, compared to the approximately 4.5 kWh required for vehicle traction.

Adopting strategy B supports the approach of "drop-in replacement" of copper hairpin windings with aluminum, without any modification of the existing stator and conductor geometry. From a practical standpoint, this approach is well suited to the automotive sector, as it enables straightforward implementation without the need to redesign components or retool hairpin assembly line equipment.

The practical implications of the “drop-in replacement” are shown by the study in [32]. This study is also presented in detail in Section 2.5 and validates the adoption of comparison strategy B for the development of an aluminum hairpin winding machine intended for utility car applications.

Specifically, experimental tests are conducted on two otherwise identical traction machine prototypes equipped with copper and aluminum hairpin windings, and their measured efficiency maps are directly compared.

The investigated traction machine is first designed and optimized with copper hairpin winding, serving as a reference geometry to develop the aluminum design. The aluminum variant is subsequently obtained by simply replacing the conductor material while the stator layout and conductor geometry are kept unchanged, thereby validating the feasibility of adopting comparison strategy B.

2.5 Replacing Copper With Aluminum in Hairpin Windings Motors Intended for Utility Cars

The outcome of the previous sections suggests that the most advantageous way to develop an aluminum hairpin winding stator from a reference copper machine is keeping similar conductors' geometry (**Comparison B**), which supports the idea of simply replacing copper with aluminum conductors of the same dimensions.

To this purpose, this study analyses the adoption of aluminum to directly replace the hairpin windings of an automotive 400 V IPM machine, originally optimized with copper windings. First, a detailed optimization process for a copper-based motor is carried out, adopting a MOGA. Consequently, the efficiency map of the resulting design is compared with that of its aluminum-based version, which is obtained through a "drop-in replacement" of the winding material. To validate simulation and optimization trends, a copper-based prototype and its identical aluminum version are built and tested, and their efficiency maps are comprehensively compared and discussed. The alignment between the experimental trends and the simulated ones validates the proposed model.

The drop-in replacement approach is particularly well suited to the automotive sector, which currently relies on established copper-based designs. In the context of developing aluminum hairpin windings to improve sustainability, adopting aluminum conductors with the same geometry as existing copper ones represents the simplest and most practical solution for today's automotive manufacturers, as this strategy eliminates the need to redesign the stator or modify the dimension of the conductors, thus minimizing modifications to existing designs and production processes.

Consequently, this paper aims to show the outcomes that automotive companies can expect when replacing copper windings with aluminum while preserving the original design and manufacturing line. By avoiding a stator redesign and retooling of hairpin assembly equipment, this approach enables a straightforward transition toward more sustainable solutions.

This study is outlined as follows. The first part is focused on the design of the reference copper machine. Following a slot-pole combination analysis, the stator and rotor dimensions are optimized using a MOGA, aimed to maximize the efficiency while reducing the magnets utilization and active parts weight. To this end, two independent optimization approaches were employed and compared: a conventional single-level strategy, in which all design variables are optimized simultaneously, and a multilevel approach, where design parameters are categorized in two groups according to their influence and optimized across two distinct hierarchical levels, thereby reducing the number of variables handled at each stage. The best design resulting from the optimization process is then compared to the aluminum version obtained by directly replacing the conductor material. The comparison is made on their losses and efficiency maps, as well as on their weight, cost, sustainability , and driving cycle efficiency.

Finally, the simulated efficiency maps are validated against experimental results obtained from tests on both the copper-based prototype and its corresponding aluminum version.

2.5.1 Slot-Pole Combination Analysis

The motor typology selected for this study is a three-phase IPM machine, with copper hairpin winding on the stator and a double V-shape layers rotor. Table 14 shows the motor requirements, including maximum power, DC bus voltage and volumetric constraints.

Table 14: Motor Requirements

Motor Characteristics	
Peak Power, kW	170
Base Speed, rpm	4000
Peak Torque, Nm	400
Max Phase Current (RMS), A	900
DC Bus Voltage, V	400
Axial Length, mm	160
Max Stator Outer Radius, mm	125

On the basis of these specifications, the best slot-pole combination has been selected according to the following reasoning. All possible slot-pole combinations have been found by varying the pole pairs number pp, the number of conductors within the slot n_L, the number of slots per pole per phase q, according to the values defined in Table 15.

Table 15: Motor parameters for the slot-pole combination analysis

pole pairs, pp	3 - 4 - 5 - 6
slots per pole per phase, q	1 - 2 - 3 - 4
conductors per slot, n_L	4 - 6 - 8

The number of stator slots Z_s for each combination is calculated according to (2.12), which refers to a three phase machine.

$$Z_s = 6\,q\,pp \tag{2.12}$$

Then, the winding factor k_w is computed as the product between the distribution factor k_d and the pitch factor k_p, reported in (2.13) and (2.14) respectively.

$$k_d = \frac{2\sin\left(\frac{\pi}{6}\right)}{\left(\frac{Z_s}{3pp}\right)\sin\left(\frac{\pi pp}{Z_s}\right)} \tag{2.13}$$

$$k_p = \sin\left(\frac{y\pi}{y_q 2}\right) \tag{2.14}$$

In (2.14), $\pi\ y_q\ /\ y$ is the short pitch angle, with y and y_q being the numbers of slots which define the coil pitch and the pole pitch, respectively [33].

With some assumptions on the airgap flux density amplitude B_{gap} which exerts on the pole area S_{pole}, (2.15) allows to estimate the number of series turns N_s, based on the selected DC link constraints, which limits the maximum line peak voltage (V) at the desired base speed ω_{base}.

$$V = \omega_{\text{base}} B_{\text{gap}} S_{\text{pole}} N_s k_w \approx 400\,V \tag{2.15}$$

This inherently implies that the number of series turns of the feasible slot pole combinations is fixed and equal for all of them. As a consequence, since the data specifications of Table 14 are kept constant, the same peak torque and base speed can be expected for every combination, thus comparing them on the same characteristic curve.

Finally, the number of parallel paths per phase N_{pp} is calculated through eq. (2.16)

$$N_{pp} N_s = pp\, q\, n_L \tag{2.16}$$

The manufacturing feasibility of each combination is evaluated based on Z_s and sensible values of N_{pp} (i.e., integer values). In particular, slot pole combinations with Z_s either higher than 96 or lower than 48 were discarded, as for a fixed stator outer radius, this resulted in excessively thin or wide stator teeth, respectively. At the same time, layouts with N_{pp} higher than 3 were discarded, for avoiding complex winding diagrams. The final step is to check that the winding diagram exhibits strong symmetry [34]. Fig. 28 is a flowchart of the analysis.

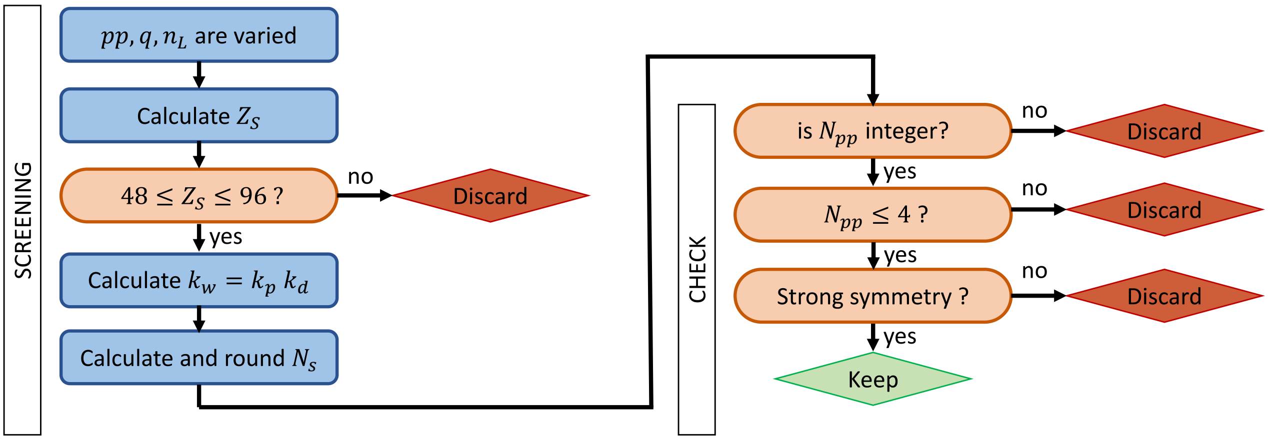

Figure 28: Slot-pole combinations selection: flowchart

The same procedure can be applied to an aluminum design, taking into account that solutions with fewer layers (4 to 6) and larger cross sections would be preferred over designs with more conductors. This would improve the handling of the conductors during certain stages of the hairpin assembly process, such as straightening and bending. While a larger cross section may negatively impact AC losses, this effect is mitigated by aluminum's higher resistivity, which helps to promote a more uniform current density distribution. As a result, this trend would allow for slightly larger fill factors, as fewer conductors with larger cross sections can be used.

In this study, the resulting combinations for the copper design are the following:

- 6 poles, 72 slots, 4 layers, 3 parallel paths (3PP72S4L);
- 8 poles, 48 slots, 4 layers, 2 parallel paths (4PP48S4L);

- 8 poles, 72 slots, 4 layers, 3 parallel paths (4PP72S4L);
- 8 poles, 96 slots, 4 layers, 4 parallel paths (4PP96S4L);
- 12 poles, 72 slots, 4 layers, 3 parallel paths (6PP72S4L).

For each of the feasible combinations, a fast optimization has been performed on the twelve geometric parameters shown in Fig. 29, i.e., yoke thickness $Yoke$, conductor height h and width w, stator inner diameter $SD2$, PMs thicknesses $MT1$ and $MT2$, PMs widths $MW1$ and $MW2$, V-angles $MA1$ and $MA2$, and relative positions $DMAG1$ and $DMAG2$.

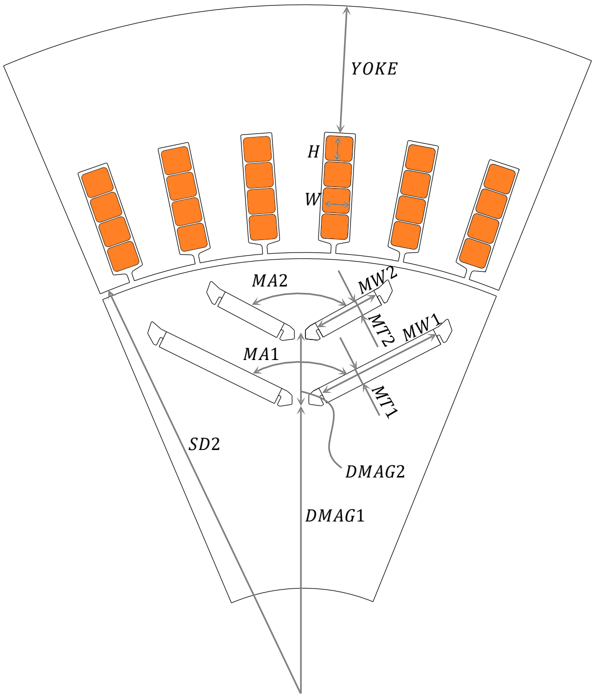

Figure 29: Slot-pole combinations analysis: design variables

The optimization objectives are maximizing the WLTP driving cycle efficiency and minimizing the magnet utilization, with the constraints of providing the peak torque without exceeding the peak current density, the DC link voltage and the maximum outer stator radius. Table 16 summarizes the optimization settings. The optimization relies on a MOGA, which is run for 15 generations, each of which made of 60 individuals. For each individual, the efficiency map is extracted using a reduced-order model to reduce the computation times. The model extends the results obtained from few calculation points to the entire characteristic curve by scaling the losses according to varying speed and current amplitude values. The driving cycle points are extracted from the vehicle longitudinal dynamic equations, using the vehicle parameters and a gear ratio equal to 10. Fig. 30 shows the results of the optimization and compares the Pareto

Table 16: Preliminary Optimization: Setup

Design Variables	
Yoke, h, w, SD2, DMAG1, DMAG2	
MT1, MT2, MW1, MW2, MA1, MA2	
Optimization Constraints	
Peak Torque (Nm)	390–410
DC Voltage (V)	≤ 400
Max RMS Current Density (A/mm^2)	≤ 23
Max Stator Outer Radius (mm)	≤ 125
Objective Functions	
Drive Cycle Efficiency (%)	Maximize
Magnets Utilization (kg)	Minimize

fronts resulting from the optimizations of each slot-pole combination. The best combination for the set of specifications presented in Table 14 is the 8 poles, 48 slots, 4 layers, 2 parallel paths (4PP48S4L). The motor highlighted with a green dot in Fig. 30 is shown in Fig. 29. Although the efficiency maps rely upon a reduced-order model, this is deemed to be a reasonable choice for the sake of the comparative analysis aimed at selecting the best slot-pole combination.

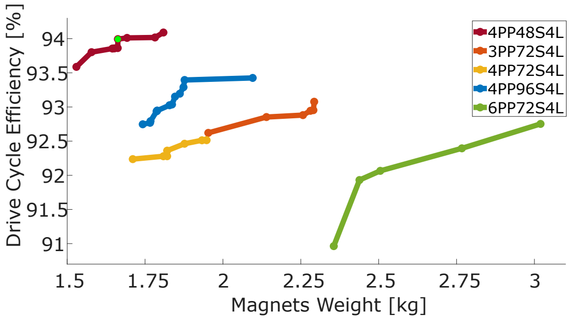

Figure 30: Slot-pole combinations analysis: Pareto fronts

In the following section, two different optimization approaches will be conducted, starting from the best individuals of the selected slot-pole combination, whose active parts and magnets weight are 55.4 *kg* and 1.7 kg, respectively.

2.5.2 Optimization Process

Starting from the results of the previous section, a more detailed optimization is performed. This study is more accurate since it does not rely on a reduced order model anymore, but comprehensively includes the DC and AC losses in the conductors, as well as the losses in the PMs and in the stator and rotor cores' materials. Therefore, two single points are considered in the analysis. One is at base speed and peak torque (peak condition: PC), thus ensuring this condition can be met without overcoming the DC link voltage and maximum current density constraints. The other point (efficiency condition: EC) is at low load and medium-high speed. This point represents the condition where improved efficiency is required, as it is deemed highly representative of the WLTP cycle, based on considerations of energy intensity and frequency of repetition of the WLTP operating points [35]. The two points are shown in the Torque vs Speed characteristic curve reported in Fig. 31.

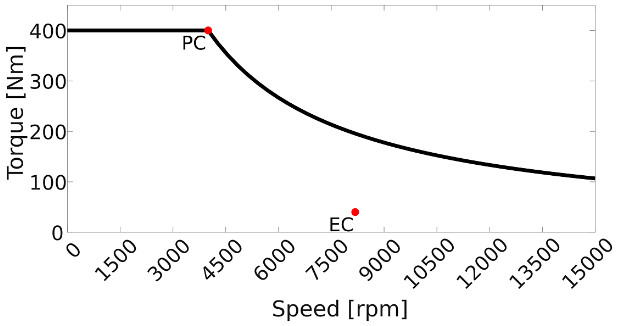

Figure 31: Two points for Optimization: PC and EC

Each newly generated individual is evaluated in these two points, performing two electromagnetic transient simulations. The setup of the simulations is defined by means of the current amplitude (I_s), current angle (γ) and speed. Specifically, the (I_s, γ) couple is found by following the Maximum Torque per Ampère (MTPA) strategy. Table 17 shows the parameters for the two points, where the angle γ=0 is chosen considering to feed the machine with q-axis current only.

Table 17: Current Amplitude Peak and Phase Angle settings

Parameter	PC	EC
(I_s,γ), (A,deg)	(900, 49)	(102, 24)
(Torque, Speed), (Nm,rpm)	(400, 4000)	(27, 8180)

The objective of the optimization is to find the optimal values for the twelve geometric parameters shown in Table 16, with the aim of maximizing the efficiency of the machine in the operating region of interest, while reducing the magnets utilization and the overall weight of the motor active parts. The optimization relies on a MOGA. The suggested number of generations and individuals per generation depend on the number of design variables. With N geometric parameters, 10xN is suggested for both generations number and population size [36]. As a consequence, optimizing a large number of parameters results in a high computational effort. Another challenge which may arise is the risk of convergence inaccuracy due to the enlargement of the search space, leading the algorithm to stuck to local minima instead of finding the global optimal solution. However, dealing with a large number of design variables is unavoidable when the stator and rotor geometries must be simultaneously optimized. In this section, the best optimization procedure is found by comparing the standard approach of optimizing all the variables at once, against a multilevel approach [37], [38]. The latter consists of executing several rounds, each involving a reduced number of design variables. Specifically, the strategy aims to optimize in the first round only those geometric parameters which are most influential for the optimization objectives. Finally, the optimal candidate is selected from the best Pareto front of the two approaches. In the following section, the chosen solution will be compared with its aluminum version, made by directly replacing the copper hairpin material with aluminum.

"All in one" Optimization

This procedure deals with optimizing all the twelve parameters in one round. Table 18 summarizes the optimization setup.

Table 18: Optimization settings for *"All in one"*

<table>
<tr><td colspan="3"><i>1) Design Variables Range</i></td></tr>
<tr><td><i>Yoke, mm 10↔25</i></td><td><i>DMAG1, mm 50↔65</i></td><td><i>DMAG2, mm 8↔20</i></td></tr>
<tr><td><i>H, mm 1↔4</i></td><td><i>MT1, mm 2↔4.5</i></td><td><i>MT2, mm 2↔4.5</i></td></tr>
<tr><td><i>W, mm 2.5↔5</i></td><td><i>MW1, mm 17↔23</i></td><td><i>MW2, mm 8↔12</i></td></tr>
<tr><td><i>SD2, mm 162.5↔187.5</i></td><td><i>MA1, deg</i> 110↔130</td><td><i>MA2, deg 115↔125</i></td></tr>
<tr><td colspan="3"><i>2) Optimization Constraints</i></td></tr>
<tr><td colspan="2">Parameter</td><td>Type</td></tr>
<tr><td colspan="2">Torque PC, Nm</td><td>390↔410</td></tr>
<tr><td colspan="2">PC Line Voltage, V</td><td>≤ 400</td></tr>
<tr><td colspan="2">Max RMS Current Density, A/mm^2</td><td>≤ 23</td></tr>
<tr><td colspan="2">Stator Outer Radius, mm</td><td>≤ 125</td></tr>
<tr><td colspan="3"><i>3) Objective Functions</i></td></tr>
<tr><td colspan="2">Parameter</td><td>Type</td></tr>
<tr><td colspan="2">Losses EC, W</td><td>minimize</td></tr>
<tr><td colspan="2">Magnets Weight, kg</td><td>minimize</td></tr>
<tr><td colspan="2">Active Parts Weight, kg</td><td>minimize</td></tr>
</table>

The first population is generated based on the Pareto front of the slot-pole combination analysis, following the orthogonal array method. The number of generations is 120, as well as the number of generated individuals per population. In total, 14400 cases are generated. The results are shown on the 3D chart of Fig. 32, whose axes are the objectives outputs: losses in Point EC, active parts weight and magnets weight.

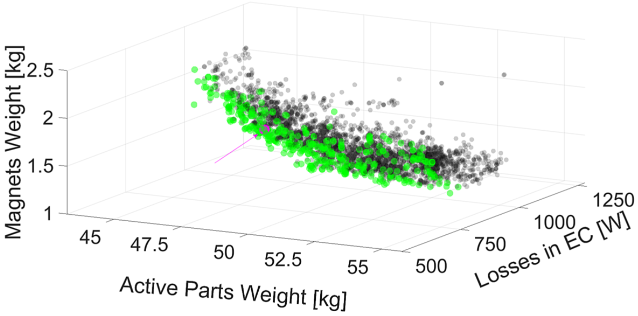

Figure 32: Pareto front resulting from the "all in one" optimization

Each dot represents an individual, whose outputs values are defined by its position in the graph. Only the individuals satisfying the torque, DC voltage and current density optimization constraints are shown. The green dots represent qualitatively the Pareto front, for which no other individual exists, which simultaneously performs lower active parts weight, magnets weight and losses in Point EC. The selected case is marked in magenta, and its characteristics are shown in Table 19.

Table 19: "All in one": Selected Case

Magnets Weight, *kg*	1.65
Active Parts Weight, *kg*	47.2
Losses in EC, *W*	893

"Multilevel" Optimization

In this section, a two-level optimization is performed to reduce the number of design variables to be used in each round. The design variables are divided so as to prioritize the most influential parameters with respect to the optimization objectives. To properly categorize the parameters in the two optimization levels, an initial sensitivity analysis is performed. To this purpose, the 12 parameters are randomly varied to generate 300 different geometries, each simulated in Point PC and Point EC. The obtained results are used to evaluate the influence of the input parameters (geometric variables) with respect to the outputs involved in the optimization, such as losses in EC, torque and line voltage in PC, magnet utilization and overall weight. Specifically, a Pearson coefficient analysis is initially performed to find the correlation between each single input parameter and each output parameter [23]. Then, an F-test is conducted to evaluate the relevance of the interaction of each couple of input variables with respect to each output variable [38]. Since these statistical figures imply a linear relationship between the input and the output parameters, the sensitivity analysis is performed in a linear regime. This is ensured by setting a constant permeability for the stator iron, thus avoiding the non-linear saturation effect.

1) Pearson Coefficient Analysis

The Pearson coefficient measures the linear correlation between the design variables and the main optimization outputs. The results are shown in Fig. 33. While this analysis effectively catches the influence of each single input parameter to each single output, it fails to evaluate the cross-influence of two different parameters. The following analysis is performed to overcome this challenge.

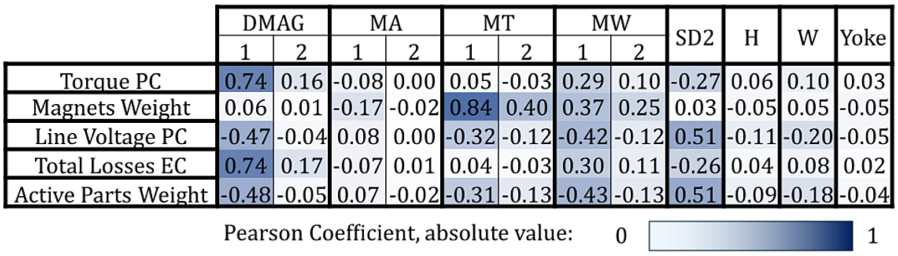

	DMAG		MA		MT		MW		SD2	H	W	Yoke
	1	2	1	2	1	2	1	2				
Torque PC	0.74	0.16	-0.08	0.00	0.05	-0.03	0.29	0.10	-0.27	0.06	0.10	0.03
Magnets Weight	0.06	0.01	-0.17	-0.02	0.84	0.40	0.37	0.25	0.03	-0.05	0.05	-0.05
Line Voltage PC	-0.47	-0.04	0.08	0.00	-0.32	-0.12	-0.42	-0.12	0.51	-0.11	-0.20	-0.05
Total Losses EC	0.74	0.17	-0.07	0.01	0.04	-0.03	0.30	0.11	-0.26	0.04	0.08	0.02
Active Parts Weight	-0.48	-0.05	0.07	-0.02	-0.31	-0.13	-0.43	-0.13	0.51	-0.09	-0.18	-0.04

Figure 33: Pearson Coefficient Calculation

2) F-test: Cross Interaction Influence

This analysis is performed to evaluate the impact of the parameters' interaction on each of the output variables. Regardless of the Pearson Coefficient value of each single variable, if the interaction between two variables is significant, they should be grouped in the same optimization level. Considering the two generic input variables $X1$ and $X2$ and the output variable Y, the regression model shown in (2.17) can be used to describe the relationship between each input variable pair and each output variable. β_i are coefficients.

$$Y \approx \beta_0 + \beta_1 X_1 + \beta_2 X_2 + \beta_3 X_1 X_2 \tag{2.17}$$

To assess the interaction's influence, two linear regression models are compared: the full model including the interaction term ($\beta_3 \neq 0$), and the reduced one, without the interaction term ($\beta_3 = 0$). If the interaction term $\beta_3 X_1 X_2$ significantly improves the reduced model, then the combined effect of $X1$ and $X2$ is influential with respect to Y. First, the interaction dataset is defined, multiplying each value of the dataset of $X1$ with the corresponding value of the dataset $X2$. Then, the comparison between the two models is performed by calculating F as in (2.18), as a function of the residual sum of squares of the reduced model RSS_R and full model RSS_F.

$$F = \frac{\frac{RSS_R - RSS_F}{df_R - df_F}}{\frac{RSS_F}{df_F}} \tag{2.18}$$

$$F \geq F_{\alpha,(df_R,df_F)} \tag{2.19}$$

The couple (df_R, df_F) are the degrees of freedom of the reduced and full model, respectively. If F is higher than the F-distribution critical value defined by the significance level α, see (2.19), then the interaction term improves the model. The couples which pass the test with significance level α equal to 0.005 are shown in Table 20.

Table 20: Significant Parameters Interactions

	Influential Interactions
Losses EC	$(DMAG1$x$MW2)(DMAG1$x$SD2)(MW2$x$Yoke)$ $(DMAG1$x$MW2)$ $(SD2$x$W)$
Line Voltage PC	$(DMAG1$x$SD2)$
Magnets Weight	$(MT1$x$MW1)$

3) Optimization

The way of sorting the design variables in the two different rounds, as suggested by the statistical analysis above, is strategically interesting. Table 21 shows the variables selected for each optimization level.

Table 21: Design Variables in each Optimization Level

First Level	$Yoke$, W, H, $SD2$, $DMAG1$, $MW2$
Second Level	$MT1$, $MT2$, $MA1$, $MA2$, $MW1$, $DMAG2$

The first level mainly defines the overall weight of the solution, with the magnet utilization remaining nearly constant. The second level mainly defines the weight of the magnets, with the overall active parts weight, as determined in the previous level, remaining fixed.

This parameter subdivisions allowed the separation of optimization objectives in the two levels. In the first level, the objectives are the minimization losses in EC and active parts weight, whereas in the second level they are the minimization of the losses in EC and the magnets weight.

Table 22 summarizes the multilevel optimization settings. In each of the two levels, 60 generations are made, each populated by 60 individuals. In total, 7200 cases are generated.

Table 22: Optimization settings for *"Multilevel"*

FIRST LEVEL		
1) Design Variables Range		
Yoke, mm 10↔25	*W, mm 2.5↔5*	*H, mm 1↔4*
SD2, mm 162.5↔187.5	*DMAG1, mm 55↔70*	*MW2, mm 9↔11.5*
1b) Fixed Design Variables		
MT1, MT2, MA1, MA2, MW1, DMAG2		
2) Optimization Constraints		
Parameter		**Type**
Torque PC, Nm		390↔410
PC Line Voltage, V		≤ 400
Max RMS Current Density, A/mm^2		≤ 23
Stator Outer Radius, mm		≤ 125
3) Objective Functions		
Parameter		**Type**
Losses EC, W		minimize
Active Parts Weight, kg		minimize
SECOND LEVEL		
1) Design Variables Range		
MT1, mm 2↔4.5	*MA1, mm 110↔130*	*MW1, mm 17↔22*
MT2, mm 2↔4.5	*MA2, mm 115↔130*	*DMAG2, mm 5↔15*
1b) Fixed Design Variables		
Yoke, H, W, SD2, DMAG1, MW2		
2) Optimization Constraints		
Parameter		**Constraint**
Torque PC, Nm		390↔410
PC Line Voltage, V		≤ 400
3) Objective Functions		
Parameter		**Type**
Losses EC, W		minimize
Magnets Weight, kg		minimize

In the first optimization level, the initial individual, namely the first level seed, is the green-highlighted case in Fig. 30, also shown in Fig. 29. The value of its six variables ($MT1$, $MT2$, $MA1$, $MA2$, $MW1$, $DMAG2$) are fixed, because they will be optimized in the second level.

The seed of the second level is selected from the Pareto front of the first level. In particular, it is selected to have the same motor weight as the optimal case chosen from the previous "all in one" optimization, shown in Table 19. This ensures a fair comparison between the two optimization processes, thus allowing to assess eventual improvements brought by the multilevel approach, as highlighted in the following subsection. Two Pareto fronts result from the multilevel optimization, one for each level. Both are plotted in Fig. 34.

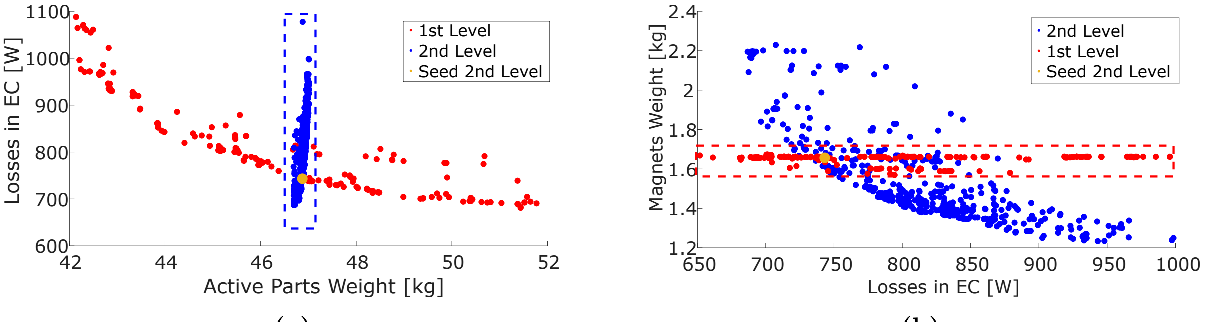

(a) **(b)**

Figure 34: Multilevel Optimization Results. (a) First Level Pareto Front. (b) Second Level Pareto Front.

The red Pareto front corresponds to the first level. Since the geometry of the PMs barriers is mainly fixed (apart from $MW2$) the resulting Pareto front in the 3D chart will nearly lay on a horizontal plane identified by the magnets weight of the first level seed. The second level seed, marked in orange, is chosen from this sets of non-dominated solutions. The blue Pareto front is the result of the second level. The active parts weight is practically fixed as it is defined by the weight of the second level seed. As a consequence, the Pareto front of the second level will nearly lay on a vertical plane.

Optimizations Comparison and Best Case Selection

The comparison between the two optimization strategies is made through the 3D charts shown in Fig. 35a). As the combination of the two Pareto fronts of the multilevel procedure are closer to the bottom left corner of the chart, then this optimization method converges towards individuals outperforming the "all in one" optimal cases. This is further highlighted by the 2D Pareto front plotted in Fig. 35b) for the cases laying in correspondence of the vertical plane defined by an active parts weight of nearly 47 kg. As observed in this figure, the optimal

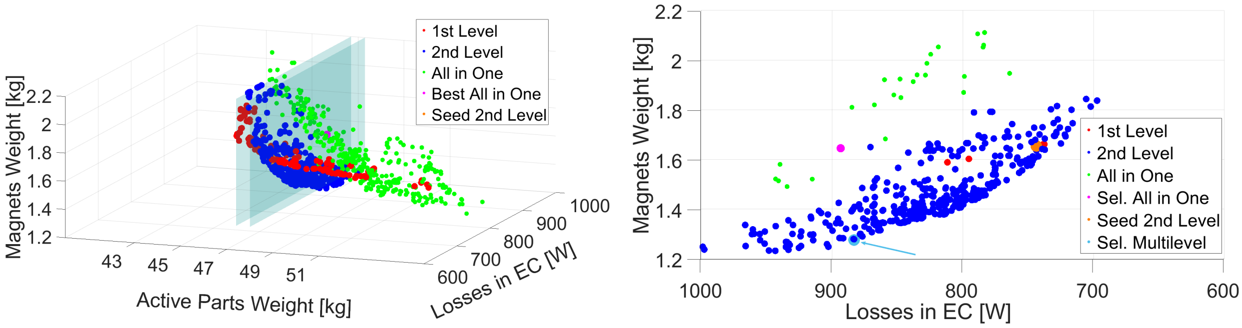

(a) (b)

Figure 35: (a) 3D Pareto Front comparison. (b) 2D Pareto Front comparison, for same weight

cases of the “all in one” optimization are suboptimal with respect to those of the multilevel approach. The chosen optimal solution is marked in light blue, and its outputs are compared to the optimal case of the “all in one” method, in Table 23, where the total weight is calculated by adding the end- winding weight, which is considered equal to the weight of the active conductors as first approximation.

Table 23: Selected Cases

Characteristics	All in One	Multilevel
Magnets Weight, kg	1.65	1.28
Active Parts + End Winding Weight, kg	47.2 + 3.8	47.0 + 3.5
Losses in EC, W	893	883

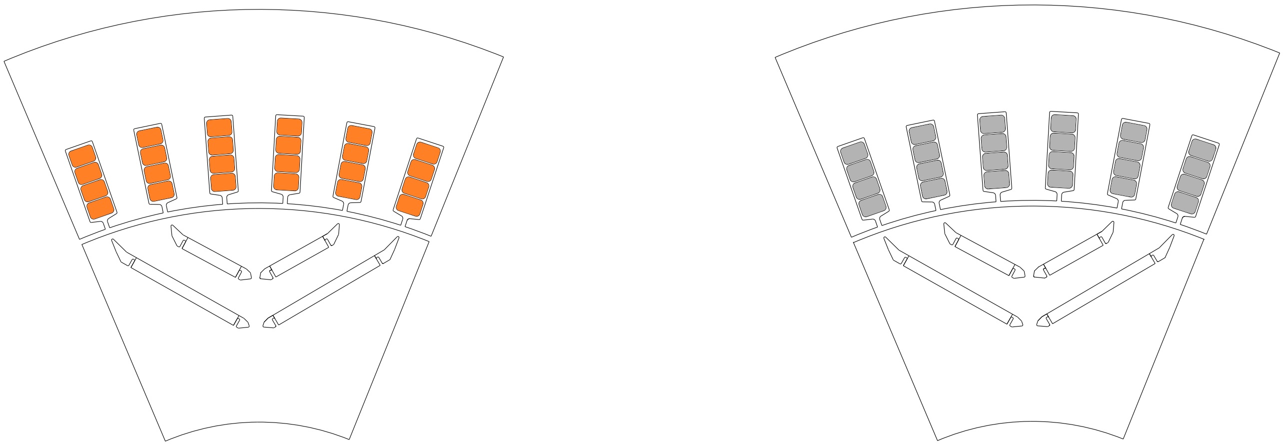

(a) (b)

Figure 36: Selected Geometry. (a) Copper, (b) Aluminum

In this study, the multilevel approach brings several advantages, such as convergence to better solutions, higher controllability and lower computational effort, with only 7200 individuals being generated, compared to the 14400 cases of the “all in one” process. On the other hand, a sensitivity study is needed, to perform statistical analyses on the input vs output relationships. The main contribution of the proposed multi-level approach is the way the objective functions and the design parameters have been chosen in each level. In particular, the adopted strategy ensures that the parameters affecting the optimization objective of one level are independent of those affecting the optimization objective of another level. In fact, in this study, the parameters influencing the motor’s overall weight are in the first level and these are practically independent on those impacting the weight of the IPMs, involved in the second level. This resulted in the Pareto Fronts lying on two distinct planes (the horizontal and vertical ones) of the 3D plot defined by the objective functions. The advantage is that the designer can arbitrarily tailor the direction of convergence of the optimization algorithm to the specific design requirements. As shown in the study, the Pareto front of the second level can be shifted depending on the selection of the second level seed (represented by the orange dot in Fig. 34). This allows to arbitrarily shift the the loss vs PM-utilization compromise, according to the definition of the overall motor weight. The geometry of the selected case (i.e. the one marked in light blue in Fig. 35b) is shown in Fig. 36, where the aluminum solution is obtained by simply changing the conductor material. The efficiency maps of both aluminum and copper versions are shown in the following section. Based on their comparison, some considerations are drawn on the WLTP driving cycle operation.

2.5.3 Copper to Aluminum results comparison

Efficiency Maps

The efficiency maps for the copper and aluminum versions are shown in Fig. 37.

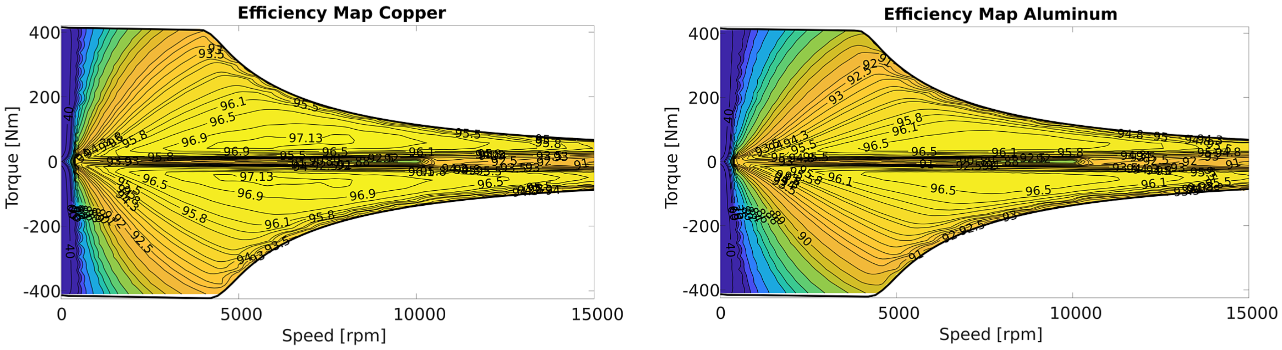

(a)

(b)

Figure 37: (a) Copper Efficiency Map. (b) Aluminum Efficiency Map.

The losses used for the efficiency calculations correspond to operating conditions which refer to the Maximum Torque Per Losses strategy. These losses include PMs losses, iron losses and winding losses. For the latter, the end-winding losses component is included as a DC joule loss contribution. Figure 38 illustrates the Joule losses across the torque-speed map for both copper and aluminum, with the winding temperature set at 155 °C. The contour lines represent the Joule loss values, while the color map indicates their relative contribution to the total losses. Areas in the purple scale signify a higher contribution from iron losses, including the marginal contribution of the magnets losses, whereas areas in the blue scale indicate a greater contribution from Joule losses.

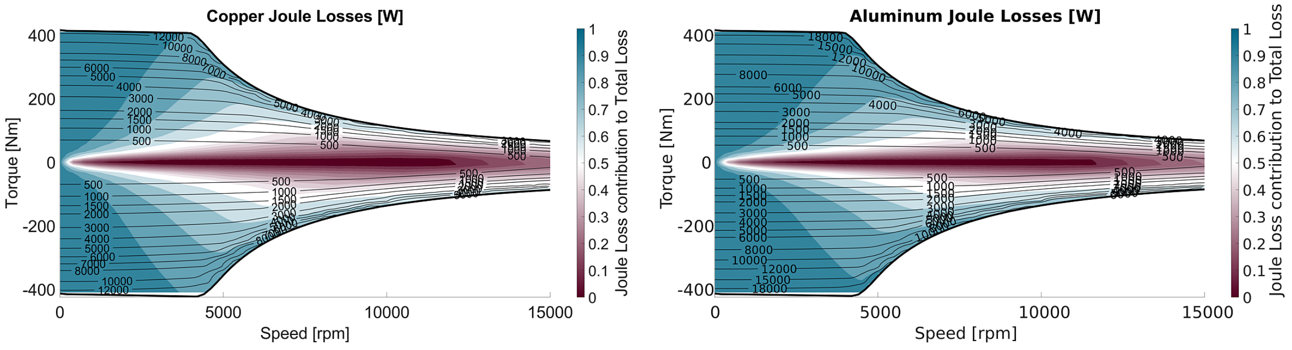

(a)

(b)

Figure 38: Joule loss and relative contribution to total loss for (a) Copper and (b) Aluminum.

As the electric machine is intended for traction application in utility cars, the efficiency is also evaluated under a WLTC, Fig. 14.

The overall cycle duration is 1800 seconds. Modelling each second as a steady state point, the driving cycle request is translated into motor torque and speed by means of the vehicle's longitudinal dynamic equilibrium, considering the instantaneous vehicle acceleration, and the rolling and aerodynamic resistive forces. The Volvo XC40 electric is used as a reference for the vehicle parameters. The resulting driving cycle points are shown on the torque vs. speed maps of Fig. 39, superimposed on the contour map illustrating the difference in total losses (Fig. 39a)) and overall efficiency (Fig. 39b)) for copper and aluminum. At high torque, where high values of current are needed, the losses difference is more pronounced. As the speed increases and the load decreases, the difference decreases, as the iron loss contribution becomes relatively higher in the overall loss breakdown, as shown in Fig. 38.

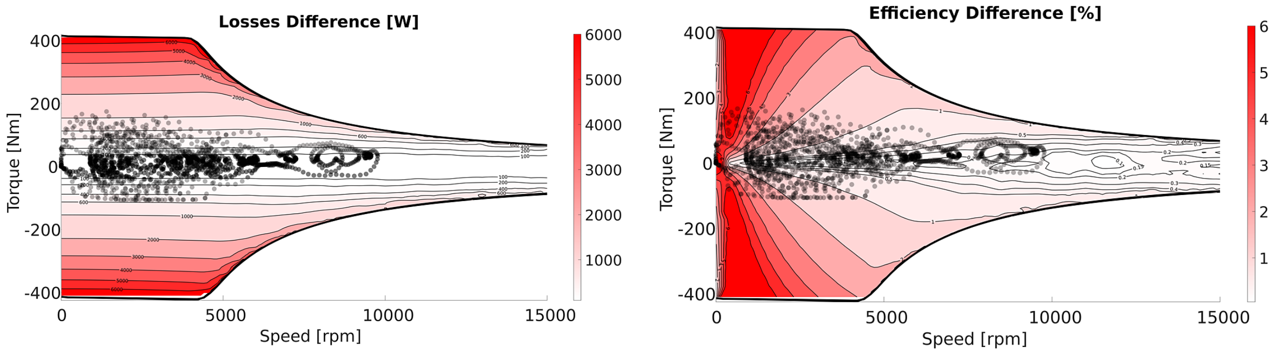

(a) **(b)**

Figure 39: Maps Difference. (a) Losses (b) Efficiency.

Comparison on a driving cycle

The driving cycle points in Fig. 39 are concentrated in an area of the Torque vs Speed chart characterized by a relatively small difference in the overall losses. This shows that the aluminum version results in a slightly lower driving cycle efficiency compared to the copper one, but yet comparable. The reason is that, in most of the points of the driving cycle, the iron losses contribution is relatively high, as seen in Fig. 38, meaning that the winding material has low influence on the overall efficiency for this kind of application.

The overall driving cycle efficiency is calculated from the integration of the losses and the absolute mechanical power over the whole cycle. The results are shown in Table 24.

Table 24: WLTC Efficiency and Losses Breakdown: Copper vs. aluminum

	Copper	**Aluminum**
Mechanical Energy, Wh	6539.8	6522.8
Iron Energy Loss, Wh	130.3	131.9
DC + AC Joule Energy Loss, Wh	127.8 + 9.4	193.8 + 6.4
Magnet Energy Loss, Wh	0.1	0.1
Total Energy Loss, Wh	267.6	332.2
Cycle efficiency, %	96.07	95.15

Cost, Weight, and Sustainability Comparison

Table 25 compares the two versions in terms of cost, sustainability, and weight. If a marginal decrease in the efficiency of the driving cycle is accepted, the table indicates that replacing copper with aluminum in the considered application brings about a cheaper, more lightweight, and more sustainable solution.

Table 25: Copper vs Aluminum - Optimal Design

	Copper	**Aluminum**
Windings Cost, $	69.80	16.02
Windings eco-cost, eco-€	39.14	6.17
Total Weight (Windings), kg	50.5 (7)	45.6 (2.1)

2.5.4 Experimental results

Two prototypes sharing the same geometry but different winding material (copper and aluminum) are tested. A picture relative to the prototyped machine with aluminum windings is shown in Fig. 40a), where an in-zoom on the bus bars can be observed. The measurement setup is in Fig. 40b).

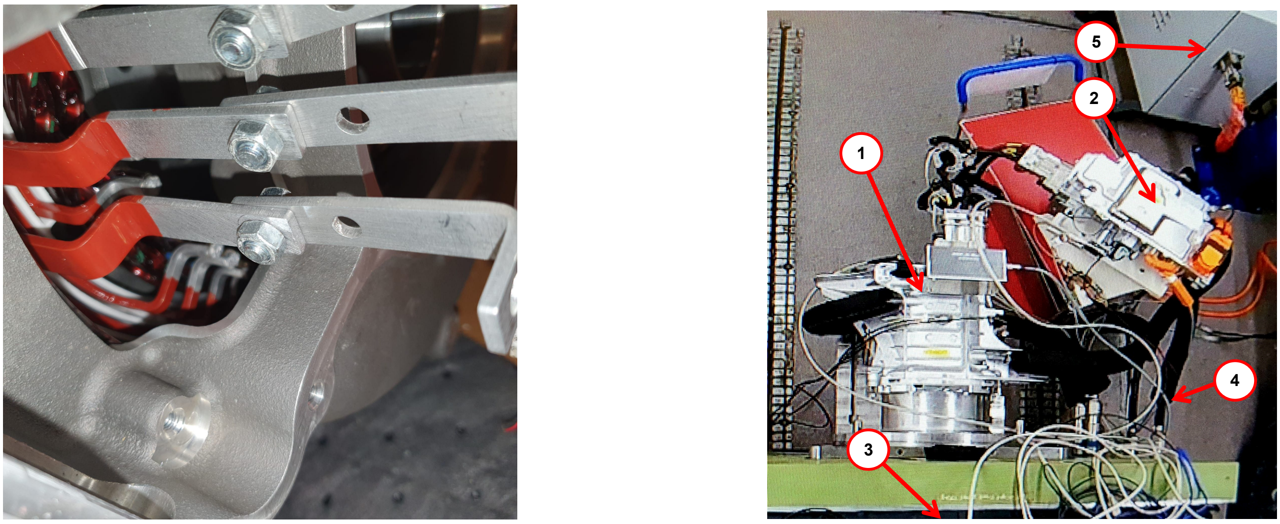

(a) **(b)**

Figure 40: (a) Prototype with aluminum hairpin winding: bus bars. (b) Measurement setup: 1) Motor, 2) Inverter, 3) Prime mover, 4) Cooling pipes, 5) Power supply.

While the detailed internal geometry of the machine remains confidential, the design analyzed in the previous section is well representative of the prototypes. Consequently, a comparison in terms of torque versus speed characteristics and efficiency maps is performed to validate the simulation results, as well as to draw the same conclusions outlined in the previous section.

The measurements are performed once the thermal steady state is reached. The processed quantities are the electrical power at the bi-directional power-supply terminals P_{bat}, the speed and the torque at the shaft, for the mechanical power calculation P_{mech}. Using this information, the motor + inverter efficiency in the test points represented by dots in the efficiency maps of Fig. 41 are calculated according to (2.20):

$$\eta_{\text{inv+mot}} = \begin{cases} \dfrac{P_{\text{mech}}}{P_{\text{bat}}} & \text{if } P_{\text{mech}} > 0 \\ \dfrac{P_{\text{bat}}}{P_{\text{mech}}} & \text{if } P_{\text{mech}} < 0 \end{cases} \tag{2.20}$$

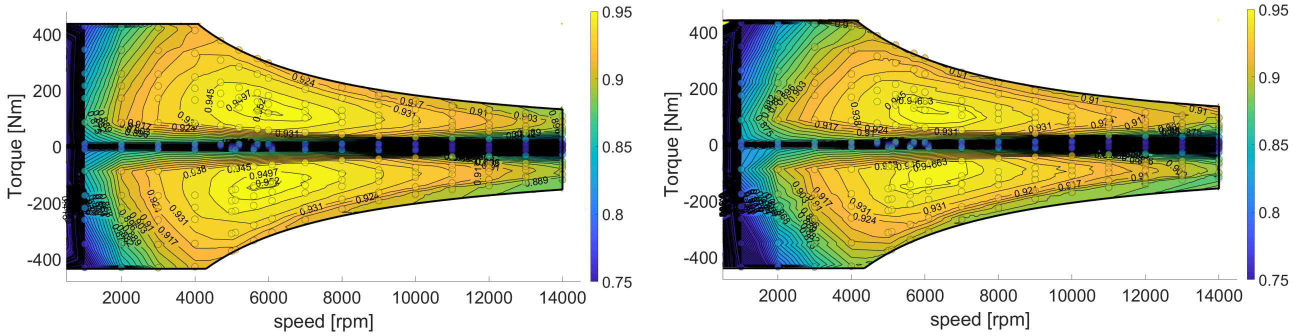

(a) **(b)**

Figure 41: Experimental Efficiency Maps. (a) Cu (b) Al

The efficiency maps are extracted performing a linear interpolation among the efficiencies calculated in the test points. Fig. 42 shows the difference between the efficiency and the losses maps.

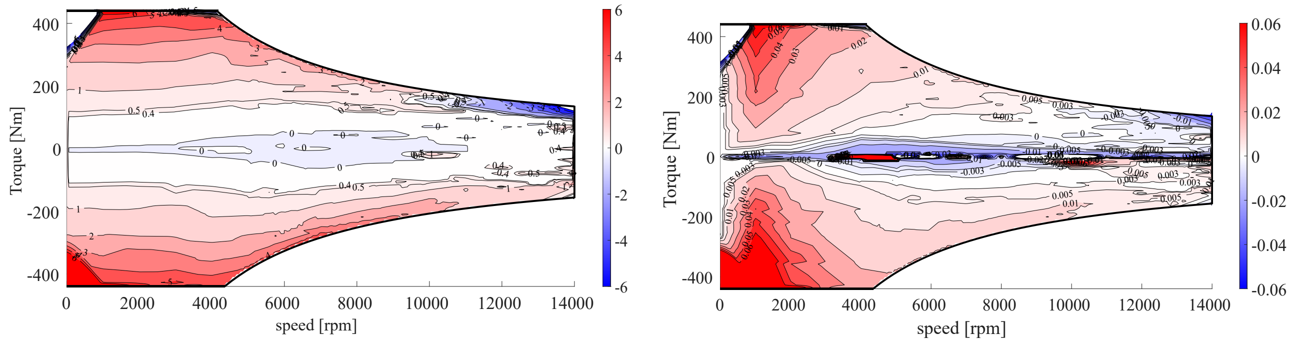

(a) **(b)**

Figure 42: (a) Losses and (b) Efficiency Difference Map.

The same trends observed in the simulations are registered, as well as similar numerical values. The differences in numerical values between simulations and measurements are attributed to the inclusion of the inverter losses in the measured experimental data and to the expected discrepancies between the simulation and the testing conditions, such as temperatures, material properties, mechanical losses and 3D effects. In Fig. 42, negative values (blue) of the difference are noticed at maximum power and high electrical frequency, as the contribution of the conductors' AC losses becomes significant in the overall losses' breakdown. As aluminum has higher resistivity than copper, it promotes a more homogeneous current density distribution across the conductor cross section at high frequency, thus reducing skin and proximity losses. However, this effect is not seen in the simulated results probably due to the small differences in the geometry design between the experimental and simulated solutions. At very low power, the negative difference is due to measurement and numerical errors, as the losses are minimal when motor torque is nearly zero.

2.5.5 Final Considerations on the Case Study

This study investigated the practical feasibility of a "drop-in" replacement of copper hairpin winding with aluminum in IPM machine intended for automotive application. To this end, a copper hairpin machine was first designed using a multilevel optimization approach, and the resulting design was then compared with its aluminum counterpart, which differs only in the conductor material. The losses breakdown and the difference efficiency map indicate that in the operating range of utility cars, efficiency remains comparable, as the contribution of iron losses becomes relatively more significant. In this scenario, the choice of winding material has less influence. As a result, the increase in DC losses due to aluminum's higher resistivity has minimal impact on the overall WLTP driving cycle efficiency. Specifically, for the application examined in this study, aluminum generated an additional 65 Wh of losses over the entire driving cycle, with respect to copper.This results in a WLTP range decrease of just 0.23 km out of a total 23.25 km, along with an estimated lifetime energy cost of about €169 over 10 years, assuming an energy price of €0.5 per kWh. On the other hand, aluminum offers the following advantages regarding the winding material: it is 54 $ cheaper, weights 5 kg less and is more sustainable than copper, reducing the environmental impact of 33 eco-€, with a reduction of 77 %, 10 %, and 77 %, respectively. The simulation results were validated against experimental tests performed on a copper-based prototype and its identical aluminum version. The measured losses and efficiency values and the relevant maps showed trends which accurately correlate with the simulation ones. The study demonstrates that replacing copper with aluminum hairpin winding of the same dimensions is well suited for utility car application. In fact, it provides benefits in terms of cost, weight, and sustainability, while maintaining a slightly lower yet comparable driving-cycle efficiency, despite the increase in DC resistance.

2.6 Conclusions

This chapter addressed the electromagnetic design of a machine with aluminum windings. As outlined in Chapter 1, the considered scenario involves the development of an aluminum-based machine by modifying an existing copper reference design. This process involves the redesign of either the hairpin-winding stator or the WFSM rotor.

Within this framework, three possible conversion strategies are identified in Section 2.1, depending on the performance targets that are kept identical between the copper and aluminum designs. These strategies are illustrated in Fig. 4 for the stator redesign and in Fig. 5 for the wound-field rotor redesign.

Specifically, Strategy A preserves both the peak torque and the peak losses under peak conditions (peak torque and base-speed), which leads to a larger overall machine size when aluminum is used. Strategy B maintains the same peak torque and maximum external volume, at the expense of increased losses under peak operating conditions. Finally, Strategy C enforces identical external volume and peak-condition losses, which may result in excessive iron saturation that hinders the magnetic loading and ultimately reduces the achievable peak torque.

Based on these considerations, this chapter aims to provide guidelines for identifying the most suitable conversion strategy for automotive applications.

To this end, a first case study focusing on stator redesign is presented in Section 2.2, in which aluminum and hybrid (copper–aluminum) alternatives are optimized according to Strategy A and Strategy B. Figure 12 shows that developing an aluminum hairpin stator following Strategy B represents the most suitable approach, as it delivers advantages in terms of cost, weight, and sustainability, while maintaining comparable efficiency under low-load, medium-to-high-speed operating conditions. Further analysis based on the WLTP driving cycle supports these findings, demonstrating that, despite the higher DC resistance of aluminum, the overall driving-cycle efficiency remains comparable. This is because, under these operating conditions, iron losses constitute the dominant contribution to total losses, as reported in Table 6.

Section 2.3 presents the case study in which a WFSM rotor with aluminum field coils is developed from the copper reference design following Strategy B and Strategy C. For this heavy-duty application, Strategy B is identified as the most suitable approach, as it preserves the peak torque requirement (see Table 12 and Fig. 24). The slight increase in losses under low-load, medium-to-high-speed conditions, where the vehicle is expected to operate, is considered acceptable.

The findings of these two sections are further supported by the literature review in Section 2.4, where other case studies are categorized according to the strategies defined in Section 2.1.

Strategy B is identified as the most advantageous approach, demonstrating that for utility vehicle applications an aluminum machine can be realized by simply replacing the copper windings while preserving the same dimensions. This solution is particularly well suited to current automotive industry needs, as it eliminates the need for stator or conductor redesign and avoids any retooling of the hairpin assembly line equipment. This "drop-in replacement" approach is validated through experimental results in Section 2.5, where the efficiency map of a copper hairpin prototype is compared with that of an identical aluminum hairpin prototype. The comparison of Fig. 42 confirms the simulation trends discussed in the previous sections. In particular, despite the higher DC resistance due to aluminum's greater resistivity, no significant efficiency degradation is observed across typical urban and extra-urban driving cycles.

2.7 Contributions to research

In this chapter, the electromagnetic design of an aluminum hairpin winding machine is presented, contributing to the research in the following ways:

- Three general strategies are established for the development of the aluminum machine starting from a copper reference design. This addresses the second objective of this Ph.D. project **OBJ2**.
- Electromagnetic design guidelines are provided for the optimal conversion of copper-based machines to aluminum in utility vehicle applications, based on analyses under typical driving-cycle conditions. The focus is on a drop-in winding replacement that preserves the existing design and manufacturing process. This addresses part of the third objective of the Ph.D. project **OBJ3**.

The three comparison strategies are discussed and analyzed in the following publications.

- G. Cutuli, S. Nuzzo, T. Zou, G. Franceschini, C. Gerada and D. Barater, "Multi-objective Optimizations of Copper and Aluminum Hairpin Windings: a Comparison," 2023 IEEE Energy Conversion Congress and Exposition (ECCE), Nashville, TN, USA, 2023, pp. 3796-3801, doi: 10.1109/ECCE53617.2023.10362293.

- G. Petrelli, G. Cutuli, D. Barater S. Nuzzo, T. Zou, and C. Gerada, "On Comparing Aluminum and Copper in Wound Field Synchronous Motors for Traction Applications," 2024 International Conference on Electrical Machines (ICEM), Torino, Italy, 2024, pp. 1-7, doi: 10.1109/ICEM60801.2024.10700570.
- M. Raimondo, G. Cutuli, S. Nuzzo and D. Barater, "Assessing Thermal and Efficiency Aspects of Aluminum Hairpin Motors in Passenger Cars," 2024 International Conference on Electrical Machines (ICEM), Torino, Italy, 2024, pp. 1-7

  doi: 10.1109/ICEM60801.2024.10700377.

Furthermore, the drop-in replacement approach for effectively converting a copper hairpin machine into an aluminum one is detailed in this journal, validating the trends observed in the aforementioned publications through experimental tests.

- G. Cutuli, S. Nuzzo, D. Barater, T. Zou, S. Nategh and T. Bertoncello, "Replacing Copper With Aluminum in Hairpin Windings Motors Intended for Utility Cars," in IEEE Journal of Emerging and Selected Topics in Industrial Electronics, vol. 6, no. 3, pp. 864-876, July 2025, doi: 10.1109/JESTIE.2025.3546030.

3. Thermal Analysis

As discussed in Chapter 2, the most effective approach for converting a copper machine to an aluminum one for utility vehicles is a winding “drop-in replacement”, in which the conductor material is changed while preserving the same geometry and overall machine design. However, this approach leads to increased DC Joule losses under peak operating conditions, due to the higher DC resistance of aluminum, resulting in a greater thermal load on the machine.

In addition, aluminum has different thermal properties than copper, as shown in Table 26.

Thermal Property	**Copper**	**Aluminum**
Thermal Conductivity $[W/mK]$	401	237
Thermal Capacity $[J/cm^3K]$	3.45	2.42

Table 26: Thermal Properties of Copper and Aluminum at ambient temperature (25°C)

The thermal conductivity of the conductor itself has little effect on the equivalent thermal conductivity of the slot, which is largely determined by the slot resin, a material with low thermal conductivity [39]. Consequently, for the same slot fill factor, aluminum and copper exhibit identical slot equivalent thermal conductivity.

However, aluminum’s lower volumetric heat capacity causes its temperature to change more rapidly for a given amount of heat input or removal, leading to faster heating and cooling compared to copper.

Given these considerations, a thermal assessment is crucial to determine whether, and to what extent, the increased losses under peak conditions and the different thermal properties of aluminum impact the motor’s thermal behavior during both steady-state and transient operation, when the machine retains the same design, conductor geometry, and cooling system as the copper reference.

The objective of this chapter is to validate, through a comprehensive thermal evaluation, the findings of Chapter 2, which propose a “drop-in replacement” of the winding as a strategy for developing the aluminum machine from the reference copper design.

To this end, a comparative thermal analysis is conducted under driving cycle conditions, as well as for continuous and peak power performance. In both cases, a standard cooling jacket is used, which is the same as for copper and aluminum designs.

3.1 Driving Cycle Thermal Performance

This analysis compares the thermal performance of copper and aluminum machines under the WLTP driving cycle, assuming identical conductor geometry. Specifically, the machines considered correspond to the case study presented in Section 2.2, in which the same maximum stator volume is maintained (Comparison B), consistent with the drop-in replacement approach. The motor specifications and the geometries of the two machines are summarized in Fig. 43.

Axial length, mm	100
Peak power, kW	150
Base speed, rpm	5000
Peak speed, rpm	18000
Peak Torque, Nm	270
Max Phase Current, Arms	300
DC Bus Voltage, V	650

(a) Motor Specifications

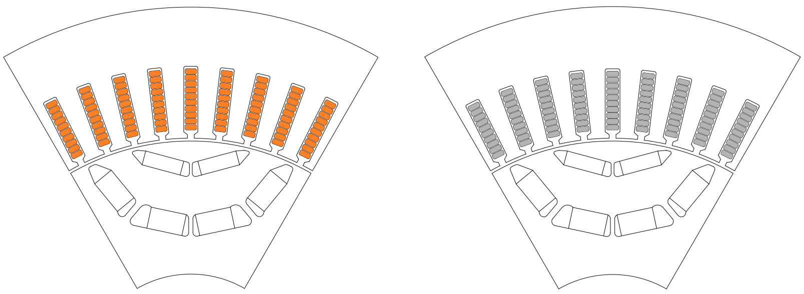

(b) Copper Design **(c)** Aluminum Design

Figure 43: Data Specifications and Reference Geometries

Despite higher DC losses under peak operating conditions, Section 2.2 showed that the WLTP driving cycle efficiency of the aluminum machine is comparable to that of the copper machine, with only 63 Wh of additional losses throughout the entire duty cycle. This is mainly because iron losses represent the dominant contribution to total losses under these operating conditions.

Nevertheless, losses associated with aluminum conductors are higher than those in copper conductors. Consequently, assessing the thermal differences between the two designs is essential to prevent any potential overheating during the WLTP cycle.

To this purpose, the loss variations over the driving cycle, previously used for the efficiency evaluation, are extracted for each motor subcomponent and applied as thermal heat sources in the thermal model.

This approach reduces the computational burden compared to fully coupled electromagnetic–thermal transient analyses. The positive dependence of resistivity on temperature (leading to increased losses and, consequently, higher temperatures through a positive feedback mechanism) is accounted for by evaluating the winding losses in the electromagnetic model at the maximum allowable winding temperature (i.e., the insulation thermal limit). In this way, the losses calculated in the electromagnetic model and applied in the thermal model represent a conservative assumption, since for all temperatures below the insulation limit the modeled heat source exceeds the actual one. Calculated temperatures below the thermal limit confirm effective control of thermal runaway.

The thermal assessment is carried out using a one-way coupled Conjugate Heat Transfer (CHT) approach, in which the fluid-dynamic and thermal analyses are decoupled.

This approach enables a straightforward determination of the heat transfer coefficients through CFD simulations, which are then employed in the thermal finite-element analysis to compute the temperature evolution over the driving cycle. The resulting temperature profiles for the copper and aluminum designs are subsequently compared and conclusions are drawn.

3.1.1 Thermal modeling

Water Jacket Design

Before proceeding with the analysis, a water jacket is designed and implemented in both motors. A helical topology is chosen and its main geometrical and operative characteristics are reported in Fig 44. It is worth highlighting that, since the objective of this study is the thermal comparison of the two designs, the helical geometry is not optimized, i.e. a preliminary design is carried out and employed for the subsequent analyses.

Water Jacket Design Parameters	
Number of turns	6
Channel width, *mm*	20
Channel height, *mm*	10
Coolant	EWG 50/50
Flow rate, *l/min*	10

(a) Water Jacket Design Parameters

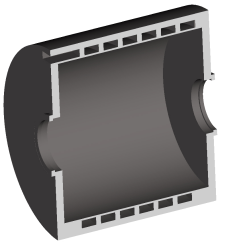

(b) Water Jacket Geometry

Figure 44: Water Jacket Specifications and Geometry

Approach

First, preliminary evaluations were conducted in Motor-CAD [40] to provide a rough estimate of the heat transfer coefficients and an initial forecast of the pressure drop.

Subsequently, the thermal model is set up using a one-way coupled CHT approach, which decouples the fluid-dynamic and thermal analyses [41]. In this methodology, the fluid-dynamic solution serves as a boundary condition for the thermal simulation. Compared to a two-way coupled CHT, this approach is faster and well-suited to the study's objective of evaluating the transient thermal behavior over a WLTP cycle lasting 1800 seconds. This choice is further justified by the steady-state nature of the fluid flow, which eliminates the need for a two-way coupled CHT that would solve the transient thermal and fluid-dynamic behavior simultaneously.

Separating the fluid-dynamic and thermal analyses enabled the use of two distinct modeling approaches. For the fluid-dynamic solution, the Moving Particle Simulation (MPS) method, implemented in Particleworks 8.0, is employed. The MPS technique solves the Navier-Stokes equations in Lagrangian form by discretizing the flow into small particles [42], [43]. This approach offers several advantages, including the ability to efficiently simulate transient fluid behavior and to easily visualize flow patterns.

The thermal simulation, on the other hand, is performed using the finite-element (FE) method in Ansys Fluent 22.1 to ensure higher accuracy. A three-dimensional model of the motor under investigation is shown in Fig. 45.

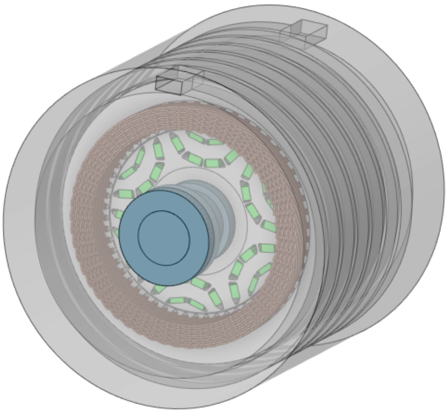

Figure 45: 3D motor model including stator, rotor, end winding, magnets and water jacket

The setup of the fluid-dynamic and thermal models is described in detail in the following.

Fluid dynamic model

The primary objective of the fluid dynamic simulation is the extraction of the spatial Heat Transfer Coefficient (**HTC**) mapping on the water jacket walls when the coolant flow is at steady state. The major steps are as follows.

The Ethylene-Water/Glycol 50/50, **EWG 50/50**, discretized in 1mm diameter particles, is injected in the water jacket with a flow rate of 10 l/min.

All the fluid properties such as density, thermal conductivity, specific heat and dynamic viscosity are set as temperature-dependent by means of user-defined functions on the base of data extracted from Motor-Cad.

Even if the flow is not expected to show relevant turbulence, the Detached Eddy Simulation (**DES**) is used to model it [44]. The initial fluid temperature and the steady state housing temperature are assumed equal to 60° C and 70° C respectively, according to preliminary calculations run in Motor-Cad. The HTC calculation is specified for laminar, transitional and turbulent flow as a function of the Nusselt number (**Nu**) correlation adopted.

While in laminar flow condition the formulation for flow in rectangular channel is used [45], in turbulent condition the Gnielinsky's one is adopted [46]. The HTC in transitional flow is assumed to linearly change between the extremes calculated for laminar and turbulent flows. More details can be found in Appendix B. The obtained HTC map is shown in the Fig. 46.

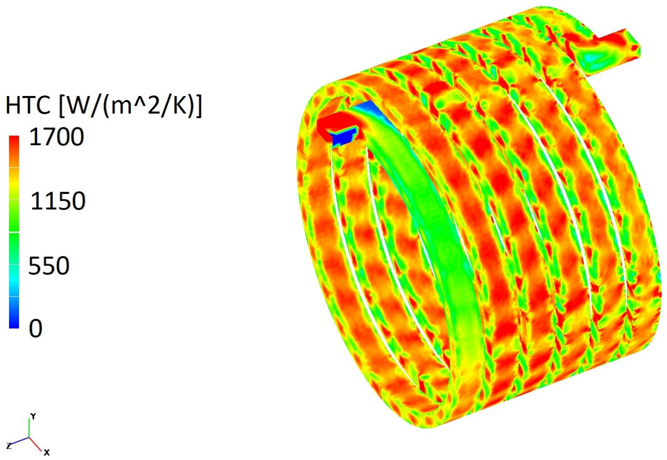

Figure 46: HTC on water jacket walls

Apart from inlet and outlet effects, the HTC value presents an almost uniform behavior in the jacket. The average value is around 1400 [W/(m^{2}K)], while the maximum value is above 2000 [W/(m^{2}K)]. The maximum and minimum values are strongly affected by the inlet and outlet effects.

Thermal models

Due to the absence of any symmetry in the water jacket geometry, the entire motor is simulated. Hence, a major modeling effort is devoted to keep the model as light as possible while preserving the reliability of the results. To this purpose, a polyhedral mesh containing 7.3 millions c.a. of cells with a minimum orthogonality of 0.13. The material properties for each modeled motor sub-component are reported in Appendix B.

An assumption in modeling is the substitution of air with its convective heat transfer coefficients (HTCs). This models the thermal conduction between solids and air, thus reducing the computational load of the simulation while maintaining reasonable accuracy. Accordingly, the HTC values over the WLTP cycle, used as boundary conditions, are extracted from Motor-CAD and applied to the surfaces exposed to air [47], [48].

In this context, the end-windings, which are the hottest components in air, have HTC values that account for rotor ventilation. Specifically, the HTC varies across the different winding layers in the end-winding region. The first winding layer, adjacent to the rotor, exhibits the highest HTC due to the increased velocity of the surrounding air. Conversely, the frontal surfaces facing the housing end plate, the outermost winding layer (the 10th layer), and the "bulky region" of the end-winding show lower HTC values because of reduced ventilation. Appendix B explains how heat transfer coefficients on the end windings are modeled. The heat transfer through the airgap is modeled through a heat transfer coefficient applied on the rotor cylindrical surface and on the inner cylindrical surfaces of the teeth, calculated through Taylor's correlations, as detailed in Appendix B.

Finally, a convective coefficient of $15[\mathrm{W}/(\mathrm{m}^2\mathrm{K})]$ is assigned to the stator yoke, while no convection is assumed on the tooth sides, where heat transfer is modeled through conduction. A single value varying over time is used to represent convection on the rotor, magnets, and housing.

Another important feature of the model is the lack of a geometrical entity for both the enamel coating on the hairpins and the slot liner. Their effect is considered using thermal resistances at the corresponding interfaces that are modeled by means of thermal conductivity and layer thickness [49] (more details in Appendix B, explaining how the in-slot thermal conductivity and the thermal resistances at the interfaces have been modeled). As an initial condition, all solid components are set to a temperature of 60 °C, matching the coolant and air temperature, while the external ambient temperature is assumed to be 40 °C.

3.1.2 Results comparison

This section presents the results of the thermal simulations performed over the WLTP driving cycle. Figure 47 illustrates the evolution of the maximum temperature of each motor subcomponent throughout the cycle.

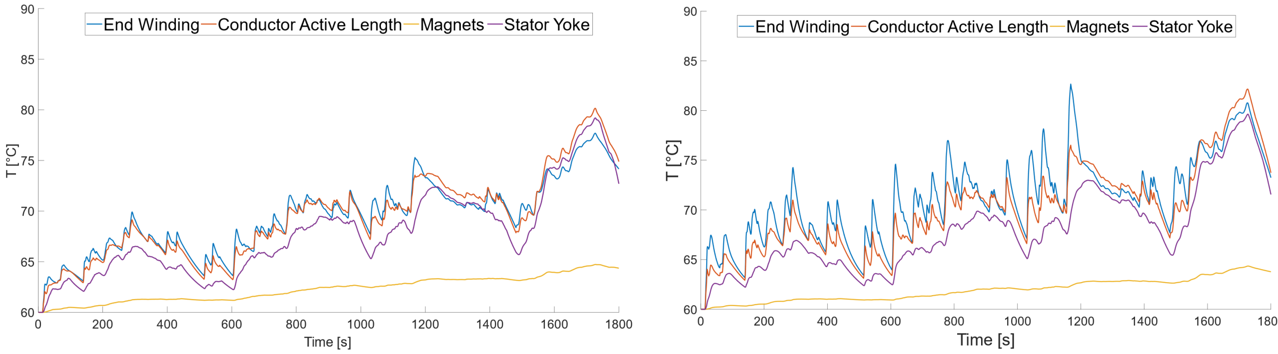

(a) **(b)**

Figure 47: Temperature evolution over the whole WLTP cycle (a) Cu (b) Al

Temperature evolution over the WTLP: Copper Design

The maximum temperature evolution over the driving cycle for each component of the copper machine is reported in Fig.47 a). The peak motor temperature, equal to 80,°C, is reached in the first conductor in the active length at 1726 s. At the same time, the maximum temperatures in the active and end conductors is approximately the same. In fact, although the first layer experiences higher AC losses due to its proximity to the slot opening, it remains cooler than the second layer as a result of the rotor-induced ventilation effect.

Temperature evolution over the WTLP: Aluminum Design

The maximum temperature evolution over the driving cycle for each component of the aluminum machine is reported in Fig. 47b). The highest temperature is 83° C, which is approximately 6° C higher than the maximum temperature of the copper case at the same instant, and it is registered in the end-winding, in the second conductor layer. Additionally, the maximum temperature is reached at a different time instant than copper, i.e. at 1167 s.

Temperature evolution over the WTLP: Copper vs Aluminum

Fig. 48 shows the maximum winding temperature of copper and aluminum end-windings over the driving cycle.

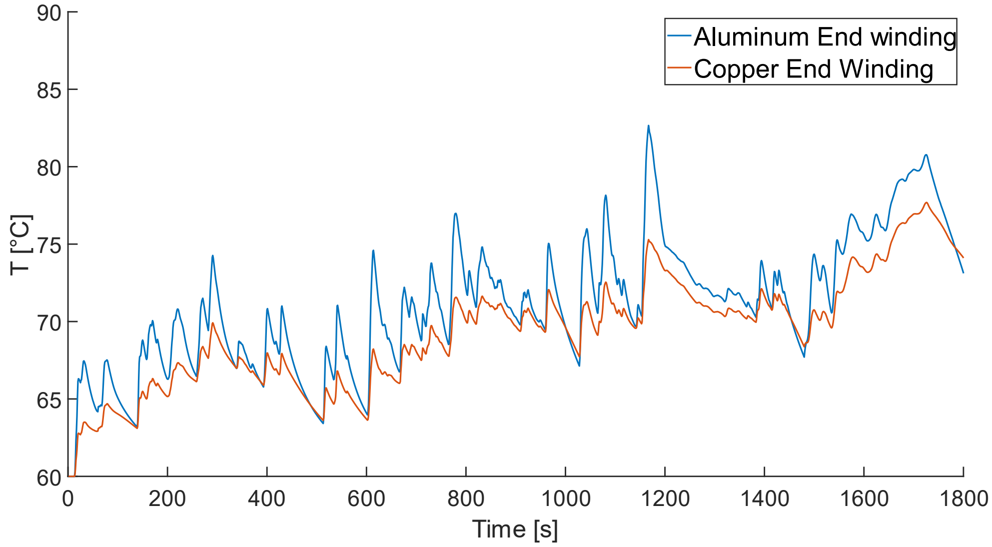

Figure 48: Temperature of the end-winding hotspot of copper and aluminum over time

The main difference in the end winding temperature trends between copper and aluminum lies in the transient operation, i.e., during fast acceleration and deceleration. Specifically, the temperature rise and fall for aluminum is faster than that of copper.

This is due to the combination of the following aspects:

- The losses are higher for the aluminum case, as the injected current is the same with respect to the copper case, as well as the conductor section and length, but the resistivity is different. In the aluminum windings, for approximately the same conductors volume, there is more generated heat to be dissipated.
- The thermal capacity of aluminum is lower. As the end winding volume of copper and aluminum can be considered the same, it is worth comparing the volumetric heat capacity, which for aluminum is 895 [J / kg K] x 2.699 [kg / dm3] = 2415.61 [J / dm3 K] and for copper is 381 [J / kg K] x 8.978 [kg / dm3] = 3420.62 [J / dm3 K].

In particular, the temperature fluctuations are more pronounced in the end-winding conductors because they are more thermally isolated, being surrounded by air. This effect is especially evident for the inner conductors, as the air velocity on their surfaces is essentially zero, making heat dissipation more challenging.

Therefore, the fast temperature fluctuations observed in the aluminum end windings are mainly due to their lower thermal capacity and higher losses in a motor region where heat dissipation is already critical.

The highest temperature for aluminum is observed in the end windings, and it is 83 °C, while copper reaches a maximum of 77 °C. However, both solutions are well below the thermal limit imposed by insulation classes F or H commonly adopted in automotive traction machines.

Temperature Contour Plot: Copper vs Aluminum

The temperature differences highlighted in Fig. 47a) and Fig. 47b) are also reflected in the corresponding contour plots of Fig. 49, which are shown at the time instant 1167 s, when the peak temperature in the aluminum design is reached.

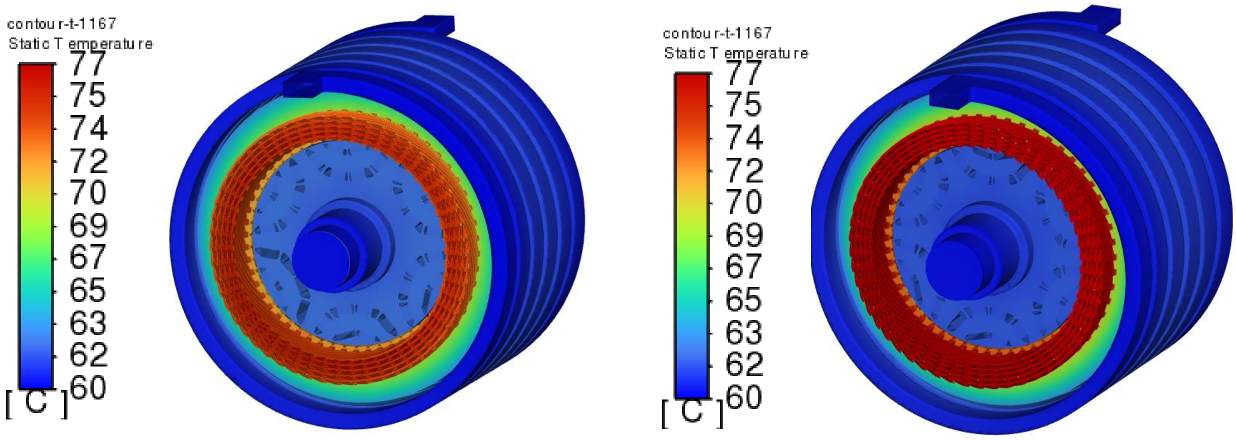

(a)

(b)

Figure 49: Temperature contour at the moment of maximum temperature during the driving cycle: (a) Copper (Cu), (b) Aluminum (Al)

3.1.3 Final Considerations on the Case Study

A transient thermal simulation was performed over the WLTP driving cycle to compare the thermal behavior of copper and aluminum hairpin winding designs, assuming the same stator and conductor geometry as well as an identical cooling system based on a water jacket.

To this purpose, loss maps of the various sub-components were extracted and used as heat sources in the thermal analysis, while the heat transfer coefficients (HTCs) for the water jacket were obtained from a separate fluid-dynamic simulation, following a one-way coupled CHT approach.

The thermal comparison over the driving cycle indicated that the motor with aluminum hairpins exhibits slightly higher temperatures, with an average increase of approximately 2 °C throughout the WLTP cycle. The maximum temperature difference occurs in the end windings, reaching about 6 °C at the time of peak temperature. Furthermore, due to aluminum's lower thermal capacity, faster temperature rises and drops were observed during vehicle acceleration and deceleration.

Nevertheless, in the aluminum motor, the peak conductor temperatures never exceeded 100 °C, well below the limits of insulation classes F and H (155 °C and 180 °C, respectively) commonly used in traction applications.

The results confirm that, when a copper motor is converted to an aluminum hairpin winding with a drop-in replacement approach and the same cooling system is used, the potential increase in losses under peak conditions does not significantly affect the motor's thermal performance during a typical passenger car driving cycle.

3.2 Peak and Continuous Thermal Performance

The previous section showed that, for the aluminum design maintaining the same stator geometry as the copper version, the increase in DC resistance in the typical operating region can still be managed by the same cooling system, with the maximum temperature remaining well below the insulation class limit.

The next step is to carry out the motor thermal characterization, focusing on both peak transient and continuous thermal performance for the aluminum versus copper design.

This study is performed on the resulting motor designs of Section 2.5, where the aluminum version was obtained with a winding "drop in replacement" of the copper machine. The motor specifications and layout are reported in Fig. 50.

Axial length, mm	160
Peak power, kW	170
Base speed, rpm	4000
Peak Torque, Nm	400
Max Phase Current, Arms	900
DC Bus Voltage, V	400

(a) Motor Specifications

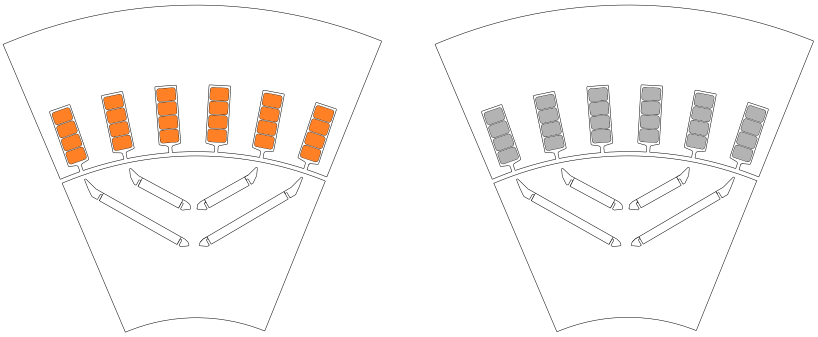

(b) Copper Design

(c) Aluminum Design

Figure 50: Data Specifications and Reference Geometries

The adopted cooling system is the same for the copper and aluminum designs, featuring a water jacket cooling, with helical topology, whose characteristics and main geometrical parameters are the same as the one used in Section 3.1, shown in Fig. 44. Ambient temperature is maintained at 40 °C and the water jacket inlet temperature is set to 60 °C. The analysis is conducted in MotorCAD.

3.2.1 Temperature Rise at Peak Condition

The losses used as input for the peak performance evaluation are calculated through a simulation conducted at 4500 rpm and peak torque (400 Nm), using the same current conditions outlined in Table 17. A transient thermal simulation is carried out, with the stopping criterion defined by the maximum temperature limits of the magnets (120 °C) or the winding (155 °C). Under these conditions, the winding reaches its temperature limit first. The results are shown in

Fig. 51, comparing the time required for the hotspot in the winding to reach 155 °C for both copper and aluminum. Since aluminum exhibits lower thermal capacitance and higher DC losses in PC, it reaches first the thermal limit. Specifically, aluminum reaches its thermal limit in roughly 15 seconds, whereas copper takes more than twice as long, around 36 seconds.

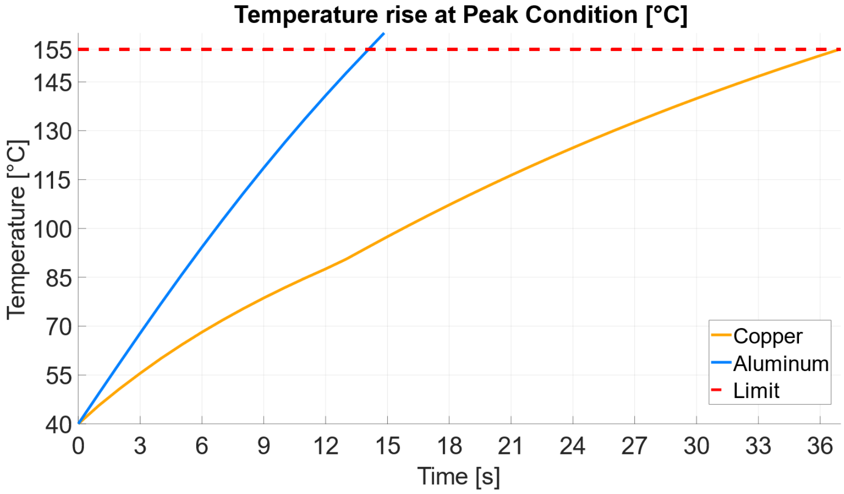

Figure 51: Temperature Rise at Peak Conditions

3.2.2 Continuous Performance

The result of this evaluation is the maximum torque that can be delivered continuously without exceeding the temperature limits of the winding (155°C) or magnets (120°C). Specifically, for each speed, an iterative process adjusts the current settings based on the steady-state temperatures of the magnets or the winding. When either one of the steady-state temperatures reaches its limit, the corresponding torque value is recorded for that speed, representing the continuous torque. Figure 52 shows the continuous torque for both copper and aluminum. The difference is more significant at lower speeds (approximately 20 % less torque) and diminishes at higher speeds, where the continuous torque values of copper and aluminum converge. This occurs because iron losses become more dominant, as previously observed in Fig. 38. Finally, an operating point for a 10% slope at 40 km/h and another representing highway conditions at 130 km/h, are analyzed. These points are deemed as the most critical conditions under which the machine can operate continuously. Both points fall within the thermal limits for both copper and aluminum.

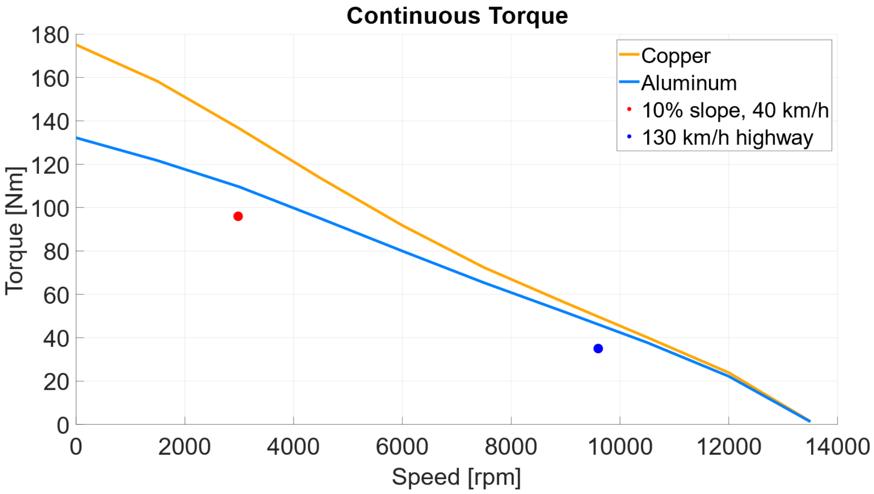

Figure 52: Continuous Torque for Copper and Aluminum

3.2.3 Final Considerations on the Case Study

A coupled thermal–electromagnetic analysis was conducted in MotorCAD on both the copper and aluminum machines, which share the same geometry and cooling system. Specifically, a transient thermal simulation was performed at peak torque and base speed to assess the peak thermal performance, while a series of steady-state simulations at the machine's thermal limit were carried out to estimate the maximum continuous torque. The overall results demonstrate a slight decrease in thermal performance for aluminum, mainly attributed to its higher DC losses. However, it still satisfies the design requirements. Indeed, the aluminum machine is capable of sustaining peak torque at base speed for more than 14 seconds. Moreover, it can continuously operate under the most demanding conditions, such as a 10% gradient at 40 km/h and highway driving at 130 km/h.

3.3 Conclusions

Two complementary thermal studies were conducted on the copper and aluminum hairpin winding machines, both sharing identical stator geometry and a water jacket cooling system.

The first study involved a transient simulation over the WLTP driving cycle to evaluate the motor's thermal behavior under typical operating conditions, with component loss maps serving as heat sources and heat transfer coefficients derived from a separate fluid-dynamic analysis, following a one-way coupled conjugate heat transfer approach.

The second study focused on motor thermal characterization under critical operating conditions, comprising a transient simulation at peak torque and base speed to assess the peak thermal response, as well as steady-state simulations at the machine's thermal limit to determine the maximum continuous torque.

Quantitative results indicate that the aluminum motor exhibits moderately higher temperatures compared to the copper counterpart, with an average increase of approximately 2 °C over the WLTP cycle and a maximum temperature difference of around 6 °C in the end windings. Faster temperature transients were also observed due to the lower thermal capacity of aluminum. Nevertheless, peak conductor temperatures remain below 100 °C, well within the allowable limits for insulation classes F (155 °C) and H (180 °C). The aluminum machine is capable of sustaining peak torque at base speed for over 14 seconds (against 36 seconds for copper) and can operate continuously under demanding conditions, including a 10 % gradient at 40 km/h and highway driving at 130 km/h.

These findings confirm the feasibility of implementing a copper-to-aluminum hairpin conversion under a drop-in replacement approach and with the same cooling system, as the resulting thermal performance satisfies the operational requirements of traction applications.

3.4 Contributions to research

In this chapter, a thermal analysis is presented, offering the following research contributions and thereby fully addressing the third objective of this Ph.D. work (**OBJ3**), which concerns the development of guidelines for the electromagnetic and thermal design of an aluminum hairpin machine for traction utility vehicles.

1. Comprehensive thermal comparison of copper and aluminum machines: a detailed analysis is performed under identical machine geometry and cooling system, considering both driving-cycle maximum temperatures and peak and continuous thermal performance.
2. Feasibility assessment for drop-in replacements: it establishes that a copper-to-aluminum hairpin "drop-in replacement" conversion, maintaining the same geometry and cooling system, can achieve satisfactory thermal performance, supporting design decisions in traction applications.

The driving cycle thermal comparison is performed in this conference publication:

- M. Raimondo, G. Cutuli, S. Nuzzo and D. Barater, "Assessing Thermal and Efficiency Aspects of Aluminum Hairpin Motors in Passenger Cars," 2024 International Conference on Electrical Machines (ICEM), Torino, Italy, 2024, pp. 1-7,

  doi: 10.1109/ICEM60801.2024.10700377.

The peak and continuous thermal performance of copper versus aluminum is discussed in this journal paper:

- G. Cutuli, S. Nuzzo, D. Barater, T. Zou, S. Nategh and T. Bertoncello, "Replacing Copper With Aluminum in Hairpin Windings Motors Intended for Utility Cars," in IEEE Journal of Emerging and Selected Topics in Industrial Electronics, vol. 6, no. 3, pp. 864-876, July 2025, doi: 10.1109/JESTIE.2025.3546030.

4. Manufacturing Aspects

The aim of this chapter is to take a step further by demonstrating the practical feasibility of developing an aluminum hairpin machine. This is achieved by addressing the manufacturing aspects and evaluating the practical implications on both the design and production process.

To this purpose, the initial part of the chapter highlights the main differences in material workability between copper and aluminum, reporting examples from the literature that exploit these differences to implement alternative manufacturing solutions for aluminum-wound machines.

With regard to hairpin manufacturing, the different workability of aluminum can ease manufacturing constraints in some steps of the production, thus consequently increasing flexibility in the electromagnetic design choices. This highlights the importance of addressing the workability aspects from the early stage of the design through a Design for Manufacturing approach. In this context, a detailed case study is presented that focuses specifically on the hairpin manufacturing process. The study compares the material behavior of copper and aluminum during hairpin bending, examining how this may influence electromagnetic design choices.

Finally, the chapter concludes with a complete manufacturing process for an aluminum hairpin stator within a production line originally designed for copper hairpin windings. As the aluminum version maintains the same geometric dimensions as its copper counterpart, no retooling of the production line is required, facilitating straightforward implementation in the automotive market sector. However, process parameters must be adjusted to account for the different material properties of aluminum. The influence of these material differences on workability is discussed, and the corresponding process guidelines are provided.

4.1 Winding Workability Differences between Copper and Aluminum

This section provides a comparison between copper and aluminum in terms of the winding workability, which refers to the practicality of manufacturing a material into functional winding components. The main differences, together with some examples from the literature [50], are listed below:

- *Castability:* Because of the lower melting point and higher fluidity, aluminum notably exhibits higher castability than copper. Many examples can be found in the literature on aluminum die-casted rotor cages, which, beyond cost advantages, offer higher flexibility of the rotor bar shapes for design optimizations because of aluminum's higher castability [51]. Furthermore, in [52], an aluminum-cast coil design is used for a fractional slot-concentrated winding machine with direct cooling.
- *Weldability:* The lower thermal and electrical conductivity of aluminum enables improved heat retention during welding. As a result, good quality welds can be achieved at lower power levels, reducing the risk of incomplete fusion or insufficient penetration. However, aluminum readily forms refractory oxide layers during welding which, if not properly controlled, can adversely affect both the structural integrity and electrical performance of the joint.
- *Printability:* Additive manufacturing techniques, particularly laser powder bed fusion (LPBF), are more established and reliable for aluminum alloys than for copper alloys, owing to aluminum's more favorable material properties, such as a higher energy absorption rate and lower thermal conductivity. As a result, additively manufactured aluminum windings have attracted significant attention in recent years, enabling increased geometric design flexibility. In [53], aluminum winding coils are fabricated via LPBF to enhance the slot fill factor of a permanent magnet synchronous machine. To mitigate AC losses, an asymmetrical hairpin winding configuration within the slot is proposed in [54], while an optimized Z-shaped conductor cross section is introduced in [55]. In other designs, improved thermal performance is achieved through the use of hollow aluminum conductors, as demonstrated by heat pipe integration in [56].
- *Anodizability:* Aluminum provides the possibility of growing a natural oxide layer (alu-

mina, Al_2O_3) on its surface via an electrolytically controlled process. The oxide can be used as an insulation layer, eventually replacing conventional insulating organic materials. This solution has been widely adopted in aluminum foil windings of inductors, transformers, and electromagnets. Furthermore, in [57], they were used in a yokeless and segmented armature axial flux permanent magnet synchronous machine (YASA AFPMSM), achieving a higher slot fill factor and equivalent slot thermal conductivity.

- *Formability:* Lower rigidity module and yield stress, as well as greater deformation at break, result in higher ductility and lower spring-back of the material. This makes aluminum more formable than copper, that is, more suitable for bending or compressing with low effort and without breaking. These properties have been exploited for producing aluminum precompressed stator coils, which enable high slot fill factor and thermal conductivity. In [58] and [59] the coils are compressed into a void through a mold, whereas in [60] a custom-made mandrel is adopted.

These examples highlight how the different workability of aluminum compared to copper alters the interaction between product design and the manufacturing process, thus promoting the adoption of alternative winding solutions or, alternatively, requiring adjustments to specific process parameters when the same manufacturing process is used.

With regard to hairpin winding solutions, limited research is available. Meanwhile, it will be shown that using aluminum instead of copper can provide advantages in certain production steps, as aluminum's higher formability relaxes some manufacturing constraints and allows greater flexibility in electromagnetic design choices.

This highlights the need to consider these aspects from the early stages of design through a Design for Manufcaturing approach, which not only enhances electromagnetic performance but also reduces material waste, supporting a more sustainable production process.

In this context, the following section presents a case study comparing the material behavior of copper and aluminum during the hairpin bending process. In particular, aluminum demonstrates greater stability and controllability during bending, allowing for increased flexibility in selecting conductors with lower cross-sectional aspect ratios.

4.2 Comparison between Aluminum and Copper Hairpins on the Torsional-Flexural Instability Phenomenon in the Bending Process

The previous section highlights the importance of considering the aluminum workability aspects since the early design stages through a Design for Manufacturing approach, which allows for enhancement the electromagnetic performance and reduction the material waste, thus promoting a sustainable design.

Following this approach, this study investigates how the different material formability of copper and aluminum changes the hairpin cross section geometrical constraints introduced by the bending process, during which the straightened pin is shaped into the characteristic U-form defining the hairpin structure. Specifically, the onset of torsional-flexural instability is examined, which occurs when undesirable pin twisting combines with the intended pure bending during the process, thus compromising the geometric control of the final hairpin shape.

In [61], simulations of the bending process were specifically conducted for copper hairpins, identifying the range of conductor cross section aspect ratios that prevent torsional–flexural instability. In [62] the modeling approach is validated through experimental testing.

The case study presented in this section builds on that work by providing a comparative analysis of the torsional–flexural behavior of copper and aluminum. The results will determine whether the more sustainable aluminum option offers greater stability during bending and, as a result, increased flexibility in defining hairpin cross-sectional dimensions during the design phase, while accounting for manufacturing-related constraints.

To this end, the section begins by presenting the bending process and the fundamentals of torsional–flexural instability. Then it describes the finite element model setup and the simulation methodology. Finally, the results compare the stability matrices of copper and aluminum to identify which material exhibits the highest stability.

4.2.1 Bending Process

The assembly process of hairpin stators typically involves the following steps: wire de-coiling, straightening, cutting, insulation stripping, bending, insertion in the stator, twisting, laser welding and impregnation [63]. This section focuses on the hairpin bending process, which is a crucial stage since the success of the subsequent insertion phase relies on the quality of the hairpin shape formed during this step.

Wires can be bent into the characteristic hairpin shape using two methods: one involving a die setup and the other utilizing a free-bending process with CNC machines.

In the die-based method, the process is divided into two phases. The first phase involves creating a 2D U-shape, achieved either through a single step three-point bending [64] or through swivel bending [65], which incrementally bends the conductor step by step around a mandrel. The second phase uses a separate die to shape the 2D U pin into its final 3D hairpin form [66].

In the second method, the wire is continuously fed through a nozzle, while the CNC machine bends it into the desired 3D shape using one or two multi-axis tools [67]. The latter approach offers the advantage of producing hairpin windings of any size or shape without the extended lead times and additional costs associated with die manufacturing. For this reason, the setup used in this case study to simulate the bending process is designed to resemble CNC free-form bending.

Figure 53 illustrates the finite element (FE) model used to simulate this type of bending. The conductor is firmly secured by a nozzle that acts as a guide, providing precise directional control as the conductor is continuously fed through it. A multi-axis bending tool, in direct contact with the conductor, applies force at a specific distance from the nozzle to achieve the desired angle, guided by the controlled initial and final positions of the bending tool. The complete hairpin geometry is formed through a series of these multiple bends in different directions and at various target angles.

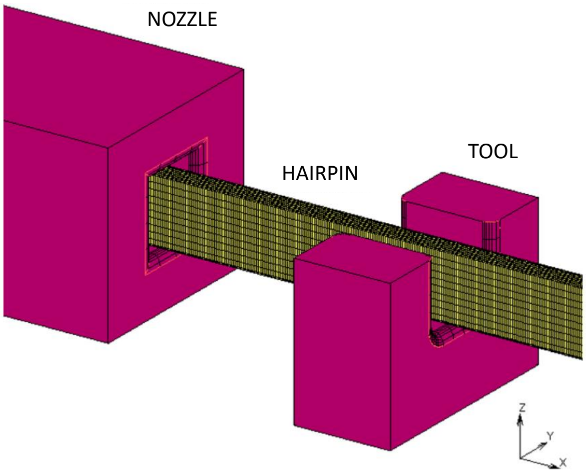

Figure 53: FE Model of the hairpin bending process

The transient simulation in this study focuses on a single bend, where the bending tool, always in contact with the conductor, moves from its initial position to its final position, giving the desired angle to the conductor. The analyzed bending is the one creating the angle between the first hairpin leg and the roof of the 2D U-shape of the hairpin. Consequently, the bending axis is parallel to the conductor's side along the radial dimension of the machine (H, conductor height), which is generally kept smaller than the dimension along the circumferential direction (B, conductor base), to mitigate the AC conductor losses.

Torsional-Flexural Instability

As mentioned above, this type of bending could be susceptible to torsional-flexural instability. Figure 54 illustrates the instability phenomenon on a cantilever beam, which represents the pin to be bent, deflected downwards by the force P.

Under pure bending conditions, the beam bends without any rotation or horizontal displacement (along y direction) of the cross section. This is highlighted in the front view, where the free section of the beam (shown in black) translates vertically along the loading plane, reaching the position of the dashed rectangular free section, denoted as stable condition.

In reality, the shear load axis does not pass through the geometric centroid of the beam's cross section due to geometric non-idealities or material imperfections. This can lead to instability, as a continuously increasing torsional load may develop, causing the beam to suddenly deflect laterally and twist out of the loading plane. Torsion and bending of the section occur along the entire length of the beam, with the magnitude of deflection increasing as the load application point is approached. This condition is represented by the green rectangular section in the front view of the deformed case and is referred to as unstable condition.

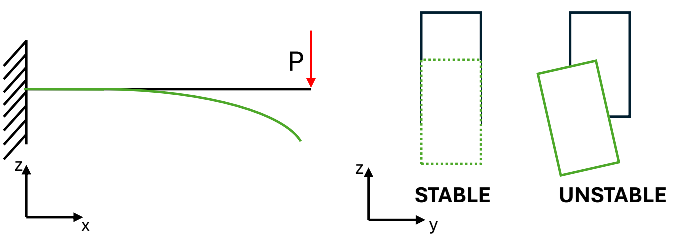

(a) (b)

Figure 54: Torsional-flexural instability of a cantilever beam. Black elements: undeformed beam; green elements: deformed beam. (a) Lateral and (b) Front view

Torsional-flexural instability is a well-known phenomenon in civil engineering [68]. The onset of instability in a generic beam is due to unavoidable non-idealities in the geometry, material specifications or load application (i.e. load eccentricity). Under certain critical operating conditions (defined by operating variables (OV), such as the load application distance and the beam cross-section aspect ratio) these non-idealities trigger the torsional-flexural instability, [69]. The schematic in Fig. 55 a) summarizes the conditions leading to the onset of this phenomenon.

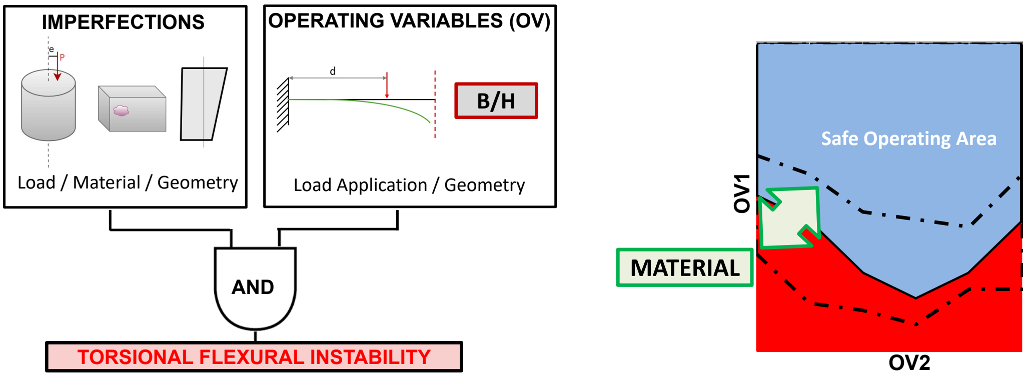

(a) (b)

Figure 55: (a) Torisonal-flexural Instability Onset Conditions. (b) Safe Operating Area of the Stability Matrix.

Avoiding torsional–flexural instability requires the definition of a stability matrix, in which the ranges of OVs that ensure stable operation are identified. These ranges draw the safe operating area, as shown in Fig. 55 b). Notably, the adoption of a different beam's material can shift the boundaries of the safe operating area, potentially leading to improved stability.

In the civil engineering context, the compromise typically involves balancing the weight and structural properties, such as bending modulus relative to the bending axis and torsional modulus.

However, in the field of electric machine windings, an additional factor is introduced into the trade-off: DC and AC Joule losses. For the same current amplitude and frequency, these losses are, respectively, reduced by increasing the cross-sectional area and flattening the conductor, thus increasing its aspect ratio B/H. On the other side, increasing B/H would make the conductor more susceptible to instability [69].

In the hairpin manufacturing process, there are additional factors that slightly influence the onset of instability. Specifically, these include manufacturing characteristics such as equipment geometries, process parameters, and insulation properties, including material characteristics, the coefficient of friction with the tools, and adhesion to the bulk conductor material (copper or aluminum). To simplify the simulation and reduce computation time without sacrificing too much accuracy, the adopted model uses a simple rectangular geometry with no fillet radii, no insulation, and no friction between the pin and the tools, as shown in Fig. 53.

Preventing the onset of torsional-flexural instability is essential, as it leads to unpredictable, and thus undesired deformation. Excessive distortion of the conductor can pose significant challenges in highly automated manufacturing processes, potentially jeopardizing the success of the subsequent insertion phase. This may result in outer coating failure, or even make the pin insertion into the stator slot basically impossible.

The aim of the simulations in the following section is to perform a sensitivity analysis to determine the safe range of manufacturing and conductor geometrical parameters that can prevent the occurrence of the instability phenomenon.

4.2.2 Finite Element Model

The simulated scenario deals with a tool that bends a straight conductor to achieve a desired bending angle. This is achieved through a vertical movement of the tool (on the direction z) from the moment it touches the conductor. The process control parameters define the initial distance of the tool from the nozzle along the x direction, and the effective vertical excursion made by the tool to bend the conductor along the z direction (*d* and *V* respectively, in Fig. 56). A single bend is sufficient to identify the conditions that lead to instability. The analyzed bend imposes a desired angle of 45°, which implies $d = V$.

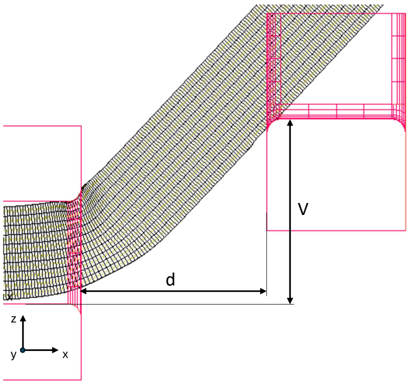

Figure 56: *d* and *V* distances, lateral view.

As anticipated, a rectangular cross section hairpin is analyzed, which offers the most favorable conditions for structural stability. Insulation coatings are not considered and friction is not considered. In this way, the only factors influencing the instability are the material properties and the geometrical parameters B/H, d and V.

The objective is to use the same model for copper and aluminum, in order to finally define the critical B/H and d and V, beyond which torsional-flexural instability occurs. In [61], important insights into these parameters are provided, and the methodology has been validated through experimental tests in [62]. Nonetheless, results are limited to copper hairpins. For the sake of comparative analysis, the same methodology outlined in [61] has been applied in this study.

Model Setup

The commercial software MSC Marc-Mentat has been employed for pre-processing, simulation, and post-processing. For modeling the contacts, the hairpin has been set as a deformable body, while the nozzle and tool infinitely rigid. The contact interactions have been considered non-linear due to the progressive contact between nozzle-hairpin and hairpin-tool, induced by the rounded edges of the nozzle and tool, see Fig. 53.

A fixed boundary condition has been applied to the free section of the hairpin on the nozzle side, preventing translations and rotations in space. The hairpin has been unrestrained laterally.

Regarding the mesh, the model employs 64240 hexahedral elements for the hairpin. The nozzle and tool have been defined as geometric contact bodies, i.e., independent of mesh discretization, due to the aforementioned assumption of infinite rigidity for the two components. In particular, the mesh size along the conductor axial dimension is finer in the contact regions with the nozzle and tool, to better capture deformations in the contact zone, and coarser in the non-relevant areas, such as the cantilevered extremity. Figure 57 shows the discretized cross section of the conductor, highlighting its perfect symmetry.

To potentially promote instability, a geometric non-ideality is introduced into the copper and aluminum model by misaligning the same node of each section, which has been shifted by 0.0001 mm along the B-direction (indicated by the red circle in Fig. 57). This introduces a numerical instability that eventually triggers the instability phenomenon when critical values of B/H, d and V, are reached. This mesh modification does not alter the cross section geometry.

The material properties are determined by conducting a series of tensile stress experimental tests. These are made on real hairpins, thus intrinsically considering residual stresses from the extrusion process. After obtaining the engineering-type stress–strain plots, reported in Fig. 58,

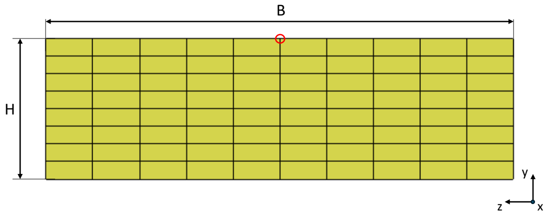

Figure 57: Discretized hairpin cross section. The red circle identifies the shifted nodes

the material properties are derived as in Table 27. Then, the derived material properties are input into Marc Mentat software.

The material kinematic hardening rule is adopted to better represent the hardening of the materials during plastic deformation. Additionally, the experimental tests were repeated at several strain rates to catch eventual differences in the plastic deformation behavior. Nonetheless, no significant differences were observed. This justifies the adoption in the simulations of a quasi-static model without accounting for material properties changes attributable to the different test strain rates.

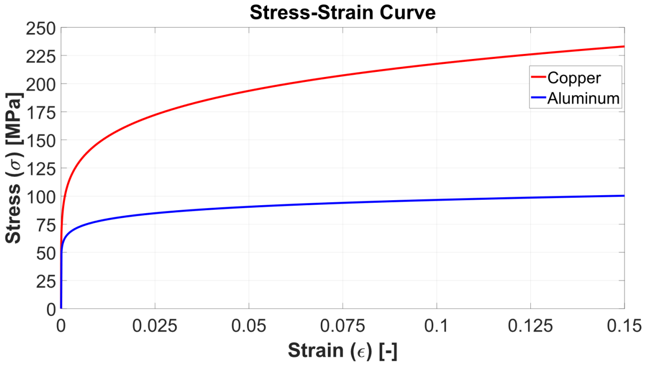

Figure 58: Experimental true strain-true stress curves of copper and aluminum

Table 27: Mechanical properties of Copper and Aluminum

Property	Copper	Aluminum
Young Modulus	90600 MPa	51000 MPa
Poisson Ratio	0.3	0.3
Yield Stress	102 MPa	64 MPa

In the next section, the aim is to compare the two materials, showing the results in terms of stability threshold defined by the parameter B/H, d and V. For varying B/H, B is kept constant at $3.33mm$, and H is varied from $2.35mm$ to $0.8mm$. The dimensions of the tool and the nozzle are accordingly scaled with the value of H.

In this study, the value of d is chosen as a multiple of B, varying from $3.33mm$ to $13.32mm$. A value of d less than B might promote too high shear loads, leading to progressive damage to the hairpin.

4.2.3 Results

The results obtained from the FE simulations are presented in Fig. 59 a) and Fig. 59 b), which show the tables for aluminum and copper, respectively. In these tables, blue cells indicate the safe operating area, while red cells highlight the occurrence of torsional-flexural instability. A threshold, marked by a bold black line, separates, for each d, the "B/H" values that promote instability from those that remain stable.

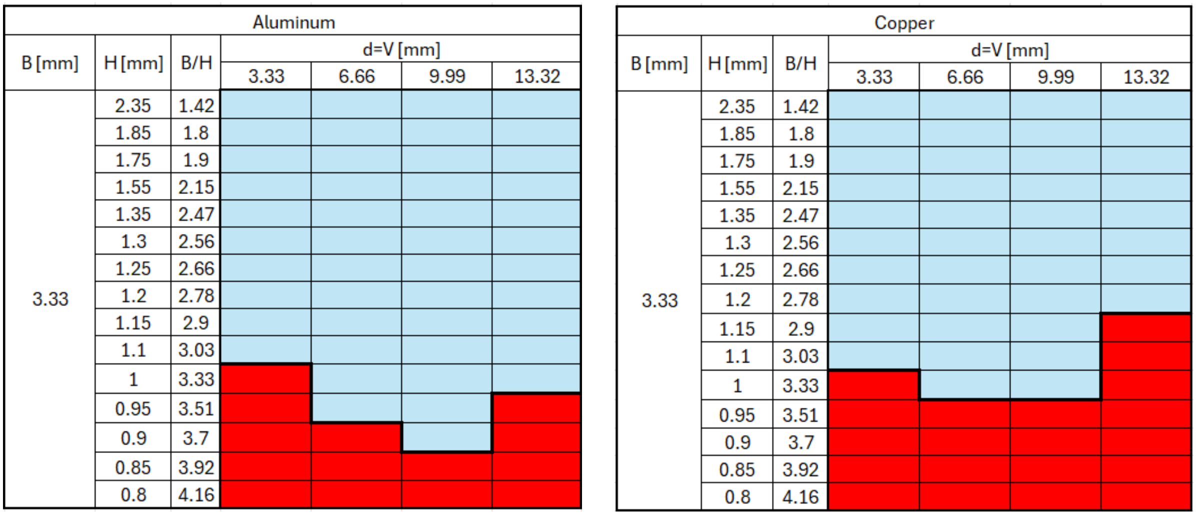

Aluminum

B [mm]	H [mm]	B/H	d=V [mm]			
			3.33	6.66	9.99	13.32
3.33	2.35	1.42	🟦	🟦	🟦	🟦
	1.85	1.8	🟦	🟦	🟦	🟦
	1.75	1.9	🟦	🟦	🟦	🟦
	1.55	2.15	🟦	🟦	🟦	🟦
	1.35	2.47	🟦	🟦	🟦	🟦
	1.3	2.56	🟦	🟦	🟦	🟦
	1.25	2.66	🟦	🟦	🟦	🟦
	1.2	2.78	🟦	🟦	🟦	🟦
	1.15	2.9	🟦	🟦	🟦	🟦
	1.1	3.03	🟦	🟦	🟦	🟦
	1	3.33	🟥	🟦	🟦	🟦
	0.95	3.51	🟥	🟦	🟦	🟥
	0.9	3.7	🟥	🟥	🟦	🟥
	0.85	3.92	🟥	🟥	🟥	🟥
	0.8	4.16	🟥	🟥	🟥	🟥

(a)

Copper

B [mm]	H [mm]	B/H	d=V [mm]			
			3.33	6.66	9.99	13.32
3.33	2.35	1.42	🟦	🟦	🟦	🟦
	1.85	1.8	🟦	🟦	🟦	🟦
	1.75	1.9	🟦	🟦	🟦	🟦
	1.55	2.15	🟦	🟦	🟦	🟦
	1.35	2.47	🟦	🟦	🟦	🟦
	1.3	2.56	🟦	🟦	🟦	🟦
	1.25	2.66	🟦	🟦	🟦	🟦
	1.2	2.78	🟦	🟦	🟦	🟦
	1.15	2.9	🟦	🟦	🟦	🟥
	1.1	3.03	🟦	🟦	🟦	🟥
	1	3.33	🟥	🟦	🟦	🟥
	0.95	3.51	🟥	🟥	🟥	🟥
	0.9	3.7	🟥	🟥	🟥	🟥
	0.85	3.92	🟥	🟥	🟥	🟥
	0.8	4.16	🟥	🟥	🟥	🟥

(b)

Figure 59: FE results for (a) aluminum hairpins and (b) copper hairpins

In the following, the results for copper and aluminum are compared, followed by an analysis correlating the trend of instability onset with variations in B/H and d. Finally, some considerations will be made about the hypothesis adopted.

Instability: Comparison of Copper and Aluminum

Comparing the stability matrices shown in Fig. 59, a lowering of the critical threshold is observed for aluminum hairpins, indicating that copper is more susceptible to instability than aluminum. This difference is attributable to the higher ductility of aluminum. Figure 60 a) presents the simulation results for the aluminum hairpin with B/H=3.7 and d=9.99 mm, showing an upper view of the scenario at the final instant. Figure 60 b) illustrates the results for copper, for the same parameters values. As observed, unlike copper, the aluminum solution does not exhibit any signs of instability, because the outlines of the deformed configuration perfectly overlap the undeformed ones, with no lateral deflection or twisting out of the load plane.

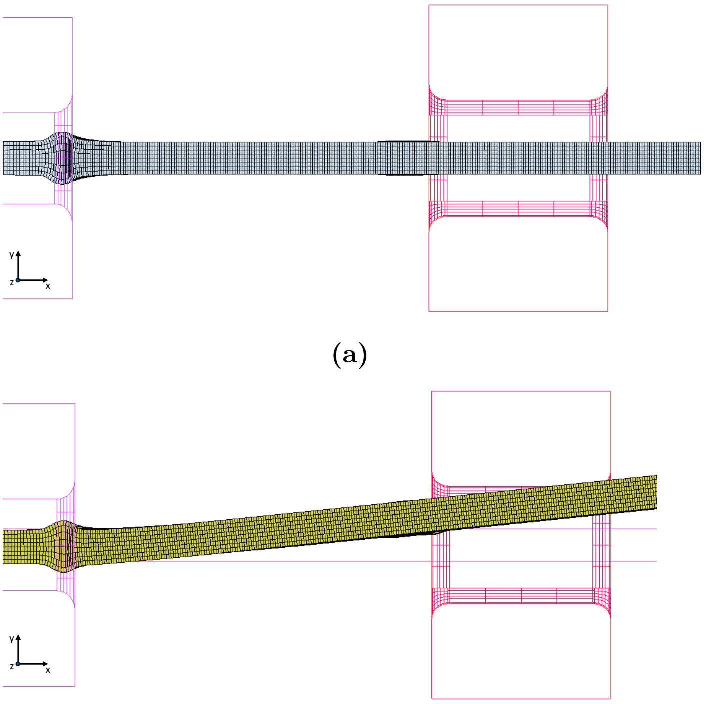

(a)

(b)

Figure 60: B/H ratio of 3.7 and d of 9.99 mm; top view of aluminum (a) and copper (b) FE results

Instability Trends: Correlation with B/H and d variations

Independently of the material considered, it is not straightforward to identify a unique trend for the onset of instability. This difficulty arises because, in this case, the material undergoes plastic deformation, whereas all formulations available in the literature that describe this phenomenon are based on the assumption of an elastic regime. This further highlights the need to investigate the phenomenon through accurate finite element (FE) analyses. In general, as expected, a higher instability is observed for increasing values of B/H.

For both copper and aluminum, at given B/H in correspondence of the threshold, the pin becomes more susceptible to instabilities as d increases. This is because, as the distance of the load application point grows, the conductor is granted more axial freedom for torsional deformation. This effect was also observed in [61], where it is even more pronounced due to the presence of fillet radii. The fillet radii make the geometry more susceptible to instability by reducing the torsional strength modulus, as they decrease the amount of material available to resist deformation. The tendency for instability at B/H values near the threshold is also observed when d approaches small values. As d decreases, the relative influence of shear stress compared to flexural stress increases. This is because shear stress remains constant regardless of the load point location, whereas flexural stress decreases with a reduction in d, due to the shorter moment arm.

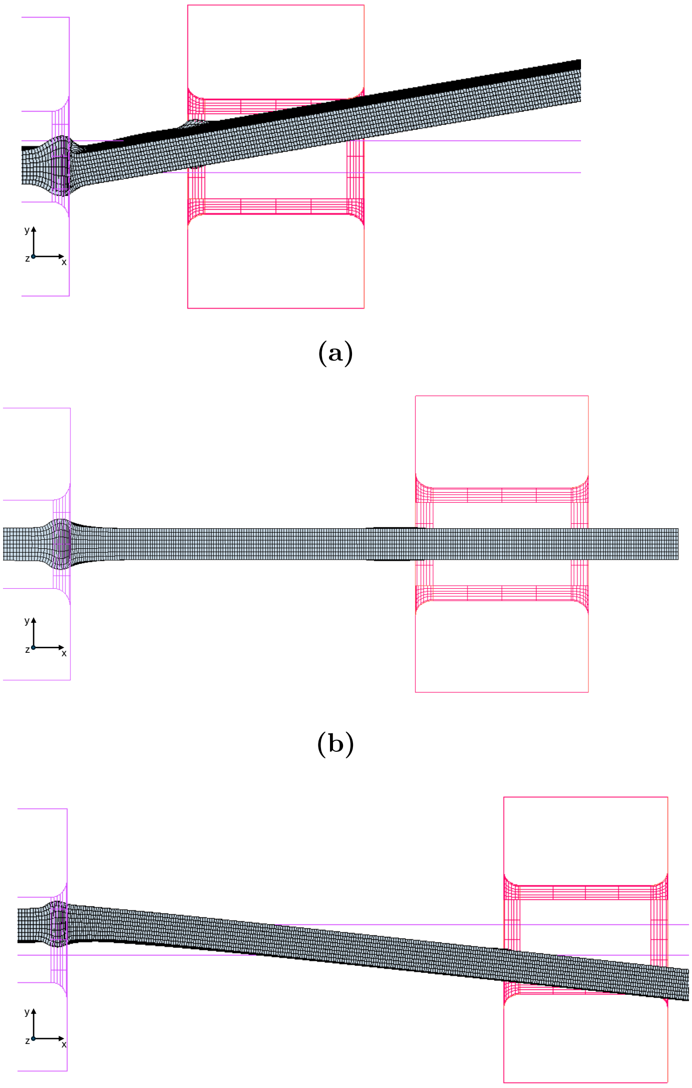

(a)

(b)

(c)

Figure 61: Top view FE results for aluminum with B/H ratio of 3.7 and d of 3.33 mm (a), 9.99 mm (b), 13.32 mm (c)

The maximum relative contribution of the shear stress is reached at $d = 3.33\ mm$, which is the minimum value for bending the conductor without cutting the material, as d equals B. The trend of instability seems to increase with d approaching smaller values, mirroring the rise in the relative contribution of shear stress over bending stress. In light of this observation, it could be hypothesized that shear stress plays a role in influencing instability.

Based on the above considerations, a given B/H may or may not result in instability, depending on the value of d, underscoring the importance of optimizing the bending process parameters for specific B/H values. This trend is clearly demonstrated in the aluminum table, where B/H equals 3.7. In this scenario, the instability occurs with $d = 3.33\ mm$, but as d increases, no instability is observed. Finally, the instability reoccurs when d is further increased to 13.32 mm. This is shown in Fig. 61, observing for aluminum pin with B/H=3.7 an unstable (a), stable (b) and unstable (c) scenarios, corresponding to d equal to 3.33 mm, 9.99 mm and 13.32 mm, respectively.

Discussion on Findings

In this study, a rectangular cross section is used, involving the application of more material, which significantly increases the structure's stability. This helped identify a threshold of critical parameter combinations below which hairpins with filleted sections will inevitably exhibit instability. This insight offers valuable guidelines for the design of hairpin windings, providing clear indications of parameter combinations to avoid. The insulating material is not considered in this analysis, as its effect on the instability phenomenon is expected to be marginal.

Finally, the model does not account for friction, which could enhance the adhesion of the hairpin to the tool, thereby reducing structural deflection and providing additional stability.

These choices were made to minimize the geometric and physical variables influencing instability, thereby ensuring the research maintains general validity and can serve effectively as a guideline for identifying thresholds in real-world cases.

4.2.4 Final Considerations on the Case Study

This study investigated the phenomenon of torsional-flexural instability during the CNC free-form bending process, which is common in the manufacturing of stator hairpin windings. The behaviors of copper and aluminum were compared to identify, for each material, the critical cross-sectional aspect ratios of the hairpin conductors and the bending process parameters that prevent the onset of instability. Avoiding instability is crucial to maintaining control over the final hairpin geometry, thereby ensuring successful stator insertion and preserving insulation integrity.

The outcome of this study is a reference stability matrix that serves as a valuable guide for hairpin winding stator designers from the earliest stages of design. Specifically, it defines the maximum cross-sectional aspect ratio that can be used to prevent instability. This ensures that design choices align with the requirements of manufacturing processes, improving assembly efficiency, reducing material waste, and ultimately promoting a more sustainable design approach.

When comparing copper and aluminum, the latter offers greater stability as a result of its higher ductility. This provides several advantages in electromagnetic design, as aluminum hairpins give designers greater flexibility in adopting higher cross-sectional aspect ratios, which are beneficial for further reducing AC losses. This indicates that aluminum hairpins may be more suitable for high-frequency designs, where AC losses are more significant, as the high frequency phenomena can be mitigated not only due to aluminum's higher resistivity but also because of the ability to achieve higher aspect ratios.

4.3 Aluminum Hairpin Stator Manufacturing

The electromagnetic and thermal analyses indicate that, for automotive applications, the development of an aluminum hairpin winding solution is best pursued through a drop-in approach that preserves the stator geometry of the copper reference design. This strategy is easy to implement and avoids the need to retool the existing production line. Nevertheless, as seen in the previous section, aluminum's different workability requires adjustments to the manufacturing process parameters.

To this end, this section presents the complete manufacturing process of an aluminum hairpin stator implemented on a production line originally designed for copper hairpin windings. The objective is to demonstrate the practical feasibility of the drop-in approach and to analyze the impact of aluminum's different workability at each manufacturing step, thereby defining the corresponding process guidelines.

4.3.1 Case Study

The case study is an existing stator that was originally designed with copper hairpins but is now produced with aluminum hairpins. It is a six phase 250 kW continuous power machine for heavy duty traction applications, i.e., the same stator analyzed in Section 2.3. The main characteristics are resumed in Table 31. The stator is shown in Fig. 62. The leftmost subfigure shows the stator bending side on top, while the middle one shows the twisting side. On the rightmost subfigure, a top view on the bending side is shown, with a detail highlighting with a section view the geometry of the slot and the conductors.

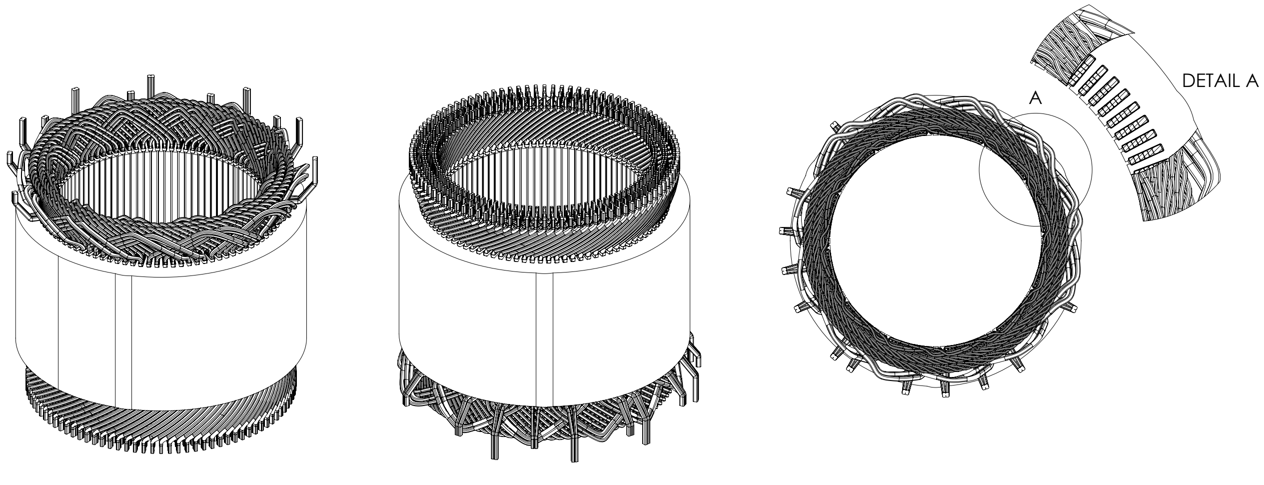

Figure 62: Stator Geometry

((a)) Stator Characteristics

Material	NO 20
Slots Number, Z_s	96
Poles Number, p	8
Layers per Slot, n_c	6
Active Length $[mm]$, l_a	140
Inner Diameter $[mm]$, SID	192
Outer Diameter $[mm]$, SOD	264

((b)) Conductors Characteristics

Active material	Aluminum
Insulation	Enamel
Width $[mm]$, w	3
Height 1 $[mm]$, h_1	2.2
Height 2 $[mm]$, h_2	4.2

Table 28: Main Characteristics

The sixth conductors' layer, placed at the bottom of the slot, is larger than the other layers. This is done to reduce AC losses, which are higher for conductors facing the air gap. The characteristics of the conductors are shown in Table 28(b). The stator design presents significant manufacturing complexity, due to the high number of slots and the presence of two different conductor sizes within the slot. This proves the feasibility of producing an aluminum hairpin stator.

4.3.2 Manufacturing Process

In the following, the complete aluminum hairpin stator assembly process is described, as carried out on the manufacturing line of the Power Electronics Machines and Control (PEMC) Research Institute. The process from a form-wound wire bobbin to the final hairpin stator involves a series of sequential steps, including wire decoiling and straightening, insulation stripping, hairpin shaping, stator insertion, widening, twisting, and finally welding. An in-depth examination of each manufacturing step is presented, highlighting the differences compared to the copper version. Finally, outlines and practices for effectively handling aluminum as a hairpin winding material are provided.

Wire Straightening and Cutting

Wire decoiling is the first step in the manufacturing process. The wire bobbin is mounted on the straightening machine, which unwinds the wire and feeds it continuously through rollers that straighten it.

The rollers act as guides on the vertical and horizontal sides of the wire, with the aim of removing any bobbin-residual deformation and straightening it. The straight portion of the conductor is then cut to the desired length through two automatic blades placed on opposite wire sides. Fig. 63 shows the straightening machines.

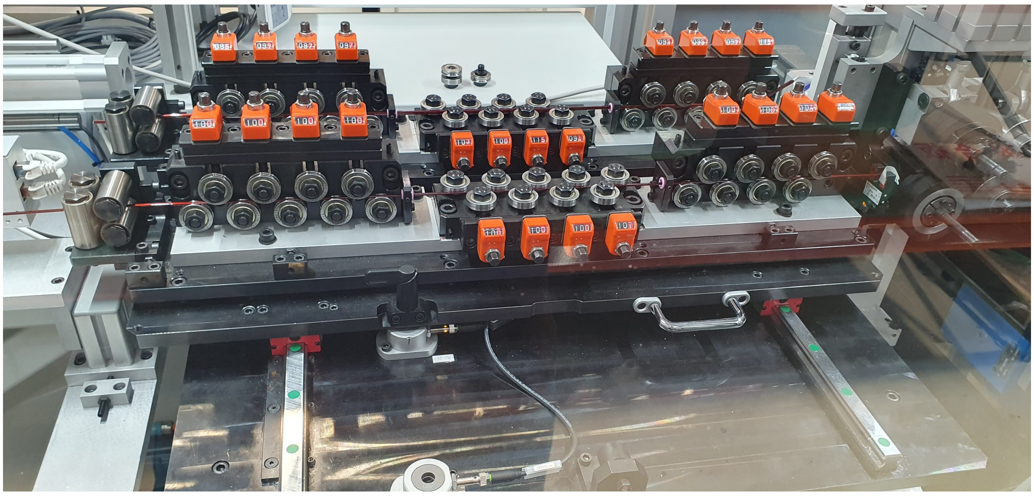

Figure 63: Straightening Machine

The first rollers encountered by the wire are mainly responsible for canceling residual deformation, while the last rollers primarily contribute to straightening the conductor. By adjusting the position of the roller axes relative to the wire, the conductor shape can be controlled and straightened.

The combined effect of aluminum softness and lightness makes it very sensitive to these adjustments. A small variation in the roller settings results in a high deformation of the material, especially for the small conductor dimension. Consequently, the setup of the straightening machine for the aluminum wire required higher precision and accuracy. The bigger wire mitigated these difficulties because of its larger dimensions. This suggests that for better controllability of the process, orienting the electromagnetic design towards the adoption of enough thick aluminum wires helps their workability.

The softness of aluminum also requires a modification of the blade settings, consisting of increasing the cutting speed to avoid the blades jamming and blocking.

Insulation Stripping

The straightened I-pins must be stripped at their terminals to remove a portion of the enamel coating, as their ends are laser welded in the final step of the process.

Ensuring surface cleanliness through proper insulation stripping is essential to achieve a high-quality weld. To this end, laser stripping has been implemented, which is a non-contact method that effectively eliminates any dielectric contaminants.

The laser beam parameters have been set to adapt the process to the aluminum conductor. Specifically, the laser power was reduced compared to the copper setting to prevent overheating and burning of the insulation, since aluminum heats up more quickly because of its lower thermal capacity at equal volume.

In parallel, the hatching distance, which identifies the distance between consecutive scan lines, was adjusted coherently to the decrease in power. The percentage was slightly decreased to increase the overlap between passes, thereby improving material removal efficiency.

The final result for aluminum conductors is shown in Fig. 64.

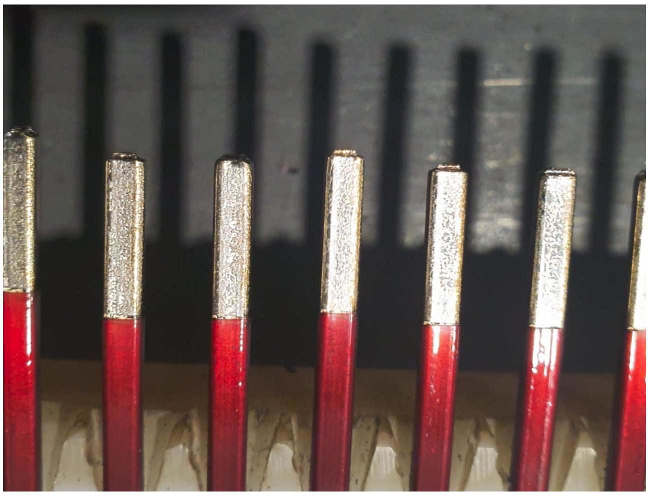

Figure 64: Stripped conductors ends

Hairpin Forming

The I-pin is formed into the final U-shaped hairpin through a free-bending process with CNC machines. Unlike more traditional bending processes that involve a die setup, the adopted approach allows hairpin windings to be produced without extended lead times and additional costs associated with die manufacturing. In this process, highlighted in Fig. 65, the I-pin is fed in a controlled way through a nozzle, and two CNC robotic multi-axis arms sequentially bend it into the desired 3D shape. Controlling the starting and ending position of each of the robotic arms (in orange in Fig. 65) in each step, it is possible to define the shape of the bend. It is crucial to perform the bending accurately and achieve the correct pin shape, as deviations from the ideal geometry can create difficulties during the subsequent insertion step. The misalignment may cause the pin to scratch the insulation against the walls of the slot when inserted into the stator.

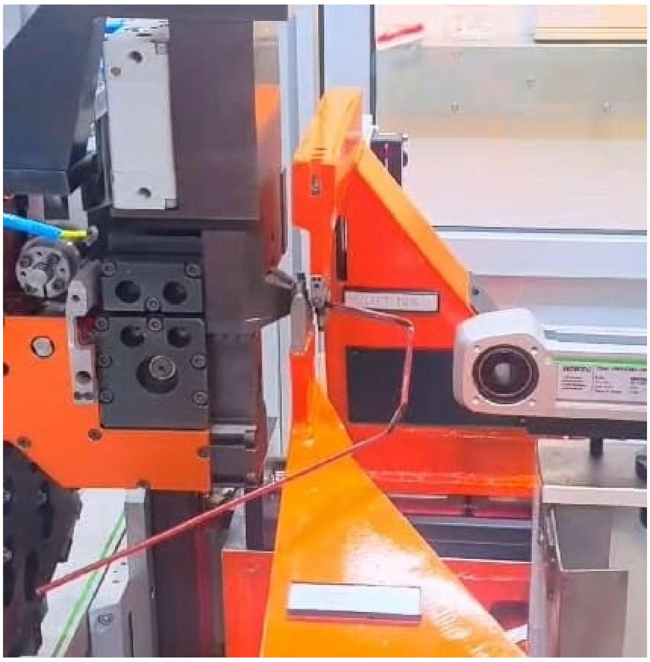

Figure 65: Hairpin Forming

Performing simulations to predict the set of arm movements required at each step is challenging due to the presence of two materials and their interface, as well as small machine misalignments or gaps that are difficult to predict. For this reason, the sequence of movements defining a single pin shape is determined through a trial-and-error procedure, which may require several hours and significant expertise.

The aluminum hairpins were shaped by re-adapting the copper receipts. This allowed to spare some time. The modifications often dealt with increasing the axes excursion in any axes movement, because the aluminum spring back is lower than copper's. With a small spring-back, the conductor tends to stay in position once the contact between the moving arms bending the pin and the pin itself is released. This makes the bend shape to be more predicable, easing the process of finding the right final receipt. In addition, aluminum is more formable, which results in higher stability against the torsional-flexural phenomenon, as discussed in Section 4.2.

Meanwhile, similarly to what was observed during the wire straightening process, aluminum showed high sensitivity to the action of the robotic arms. Due to the aluminum's lightness, especially in the case of small wires, the bending motion of the robotic arms induced oscillations at the free end of the conductor, making the process more difficult to control. This issue was mitigated by slightly reducing the process speed.

The larger wire did not exhibit this behavior, confirming the earlier assumption that avoiding thin aluminum hairpin windings improves process controllability.

Hairpin Insertion

Once all pins have been bent, they are arranged within the stator following the specific winding diagram. Hairpin insertion is a critical process as there are different pin shapes and a small clearance space. Additionally, it is fundamental to arrange the pins without errors, as the subsequent twisting and contacting of a stator with mistaken insertion leads to complete unfunctionality of the machine and cannot be recovered.

For this reason, the insertion is typically done manually, even in many series production processes. The arrangement is done layer by layer, starting from the outermost, to the innermost. The process of insertion is shown in Fig. 66.

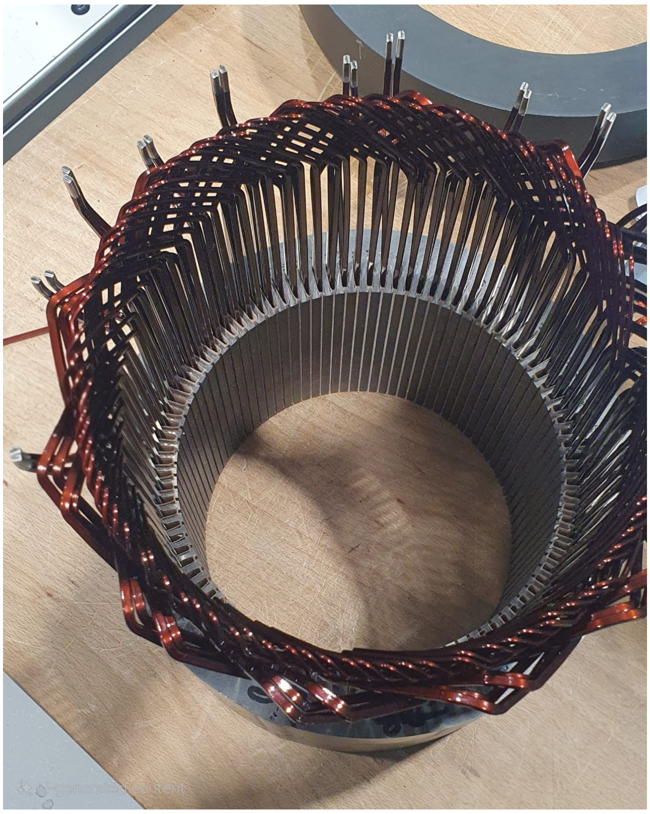

Figure 66: Insertion Process

The layout of this machine deals with six phases, with two parallel branches per phase. For avoiding circulating currents within the different parallel branches of one phase, a strong symmetry winding diagram is provided, which allows each branch to have the same impedance, under each machine operating condition. Strong symmetry is achieved through proper wire transposition. To this end, the conductors of each parallel branch are progressively arranged from the sixth to the first slot layer, or from the first to the sixth when the winding direction is reversed. As a result, one hairpin shape has its legs in layers 4 and 5, another in layers 2 and 3, and additional hairpin shapes, used to reverse the winding direction and commonly referred to as jumpers, have their legs exclusively in either the sixth or the first layer.

This winding arrangement minimizes the number of distinct hairpin shapes, improving the efficiency of the overall stator assembly process.

The higher the quality of the bending phase, the easier it is to insert the hairpins. Aluminum hairpins are advantageous because of their malleability, which allows the shape of the pin to be easily adjusted during insertion into the slot. This flexibility provides some tolerance in the bending process, meaning that the bending receipt does not need to be fully precise. However, it is necessary to maintain a small air gap (on the order of tens of microns) between the conductor and the slot walls to avoid resistance during insertion. Forcing the aluminum conductor into the slot could deform it due to its high malleability, compromising the pin shape. In this context, the use of a thicker conductor increases the stiffness and makes it less susceptible to deformation.

Hairpin Widening

Once the pins have been inserted, the bending side of the stator is complete. On the opposite side (the twisting side), the protruding straight ends of the conductors remain and must be prepared for the twisting process. To achieve this, hairpin widening is performed, which radially expands the overhanging straight ends to create the necessary space for the upcoming process.

The widening process begins with the outermost pins, where couples of conductors of different layers are progressively deformed to reach higher radii.

Since there are six layers of conductors, the pins will be formed to three distinct radial crowns, each consisting of a pair of layers.

First, the fifth and sixth layers are widened, forming the outermost crown with the largest circumference. The first and second layers remain in their original position, forming the innermost crown. Finally, the third and fourth layers are widened to an intermediate circumference, positioned between the inner and outer crowns. In Fig. 67, a portion of the outermost crown, including the fifth and sixth pin layers, has been widened. This is shown in contrast to the straight pins, which have yet to undergo widening.

Figure 67: Widening Process

The widened crown of the conductors is formed by simultaneously widening each pair of conductors from the two layers that make up the crown. To maintain the straightness of the conductor ends, the widening is performed in two steps. First, an automatic gripping tool pulls the conductors outward to a radius slightly larger than the target. Then, without releasing them, the tool moves them back to the desired final radius. This over-widening compensates for the spring-back effect of the conductor material, which would otherwise cause the pins to separate further after release.

The same widening settings used for copper conductors were applied to aluminum. Due to the lower spring-back effect of aluminum, better results were achieved, as the facing conductors remained closer together after the pliers were released. In the specific design layout of this case study, where the fifth and sixth conductor layers have different dimensions, the reduced spring-back of aluminum proved particularly advantageous. It effectively compensated for the differing spring-back behavior of pins with varying sizes, preventing excessive separation between them.

Hairpin Twisting

Once the widening operation is completed, sufficient space is available to twist the pins. Twisting consists of circumferentially bending the straight conductor ends by an angle defined by the hairpin coil span, so that each conductor of a layer is aligned with its corresponding conductor of another layer for welding.

The winding diagram is designed to maintain a constant coil span for consecutive series-connected conductors on the twisting side, meaning that the number of slots separating them remains the same regardless of their layer positions within the slot. This allows for a simpler and more efficient twisting operation, with each conductor layer bent circumferentially at a fixed angle corresponding to the coil span.

However, this approach requires greater flexibility on the bending side, as the coil span of the conductors being bent can vary, necessitating different hairpin shapes. This requirement is addressed using CNC-based bending equipment, which provides the necessary precision and adaptability.

In this case study, the twisting process involves simultaneously twisting all conductors of a single layer using the twisting ring of a modular manual twisting machine. Each layer is twisted individually by rotating the mounted ring by a controlled angle.

This differs from fully automatic twisting, where all layers are twisted simultaneously by concentric twisting rings controlled by actuators. Fully automatic twisting significantly reduces process time compared to the sequential manual approach.

However, the fully automatic method is less flexible and reliable. Since the twisting rings are inserted simultaneously, it is more difficult to correct for possible pin misalignments in the grooves, which can compromise the success of the process.

The final twisted stator is shown in Fig. 68, where the circumferential bending of each conductor layer is visible, and each pin is positioned side by side with the corresponding pin to which it will be welded in the subsequent process.

For compensating the hairpin material spring-back, the twisting rings over-twist the conductors by a small additional angle with respect to the coil span angle, before the stator is taken out from the twisting machine. For copper, the over-twist angle is generally on the order of half the mechanical angle of one stator slot. As aluminum has a lower spring-back, the adopted over-twist angle is half that used for copper.

After the twisting process, a partial delamination of the insulation is observed at the stripped end of the conductor. The bend of the conductor at the insulation edge generated shear stresses at the interface between the insulation and the bare aluminum. While this does not compromise the functionality of the stator connections, it highlights a weaker adhesion at the insulation–aluminum interface when enamel is used, attributable to the different surface characteristics of aluminum compared to copper, which influence adhesion performance during the insulation application process.

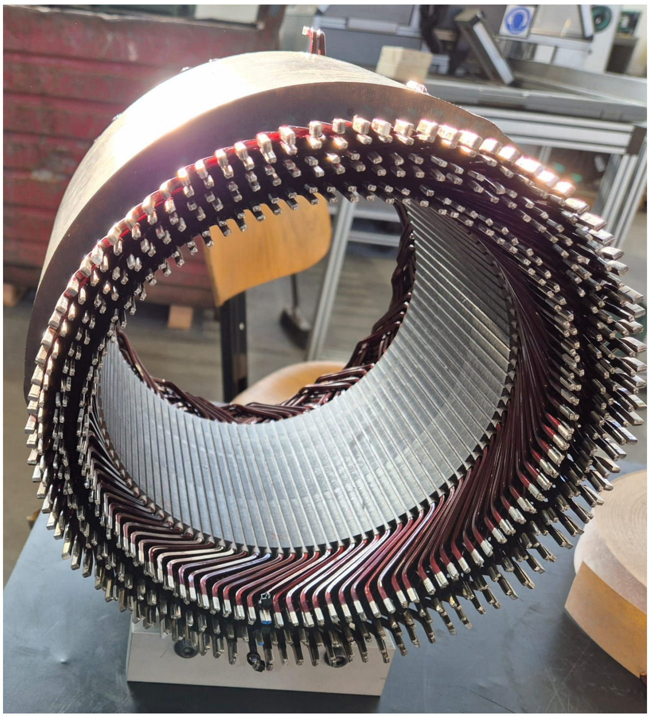

Figure 68: Twisted Stator

Hairpin Welding

The final station on the hairpin assembly line is the welding machine. After the twisting process, the skinned terminals of each pin are positioned next to their corresponding ends, aligned side by side for welding. Welding is performed with a laser. However, because of the high density of pins in a confined area, the laser can only access the joints from above. As a result, the laser acts on the two rectangular top surfaces during the welding process.

The objective of the laser welding process is to achieve deep penetration. This ensures a larger cross-sectional area for current flow, thereby reducing electrical resistance at the welded joints. In addition, it improves the structural strength of the weld.

The welding process requires specifying several conditions, including the definition of process phases, the laser path, and the energy density applied to the welded surface, which depends on the laser's power and velocity.

The welding conditions for aluminum differ significantly from those used for copper as a result of its different thermal properties. In fact, compared to copper, aluminum is characterized by lower thermal conductivity, lower melting point, and lower volumetric thermal capacity, as highlighted in Table 29.

Table 29: Thermal Properties: Al vs Cu

Thermal Property	Aluminum	Copper
Thermal Conductivity, W/mK	237	398
Melting Point, $°C$	660	1100
Volumetric Heat Capacity, $J/(cm^3K)$	2.422	3.450

The details for the setup of each welding conditions for the aluminum weld are in the following, highlighting the differences with copper:

- *Process phases definition:* The process phases may include pre-heating, heating, and post-heating. Specifically, pre-heating is applied to help reduce pore formation and promote better mixing of the molten material before the core heating phase, during which the actual welding takes place. Following this, post-heating ensures proper melting of the surrounding metal and, more importantly, slows the cooling rate of the weld. This controlled cooling helps prevent excessive brittleness and preserves the structural integrity of the joint.

  Based on the thermal behaviour differences, copper requires an additional post-heating phase due to its lower ductility and significantly higher thermal conductivity compared to aluminum. This post-heating helps to smooth out the cooling rate gradient, reducing the risk of embrittlement. In contrast, when welding aluminum, a post-heating step is typically unnecessary. Its lower thermal conductivity allows it to cool more slowly, maintaining sufficient ductility and preventing the formation of brittle welds.

- *Laser Path:* The laser path, which defines the trajectory of the laser over the joint, is crucial in achieving a proper mix of the molten material and ensuring adequate weld penetration. The path definition in this study is material-independent. Hence, both copper and aluminum use the same spiral-shaped trajectory.

- *Energy density on the weld:* Since aluminum has a lower volumetric thermal capacity and a lower melting point than copper, lower energy is needed in. As a consequence, a reduced laser power at a higher velocity is used to prevent over-welding for aluminum.

Another key difference between the two materials is their oxidation behavior. Aluminum readily reacts with oxygen and is more prone to oxidation than copper, often leading to a higher presence of pores within the weld. These pores can negatively affect the weld's electrical conductivity.

The quality of the laser weld can initially be visually inspected, checking whether a good penetration is achieved. Subsequently, several tests are carried out to verify the goodness of the weld. These include electrical tests, such as DC resistance measurements using a micro-ohmmeter; structural tests, which evaluate tensile shear strength or micro-hardness; metallographic analysis, to detect internal porosity that could increase electrical resistance; and microstructural analysis, to examine the composition and characteristics of the microstructures within the weld.

In Fig. 69 the welding process is illustrated, carried out without the use of shielding gas. The figure also shows the metallographic analysis of the aluminum large-to-small weld, corresponding to the joint between the fifth- and sixth-layer conductors. The observed pore content is considered acceptable, as it is sufficiently low not to adversely affect the weld DC resistance.

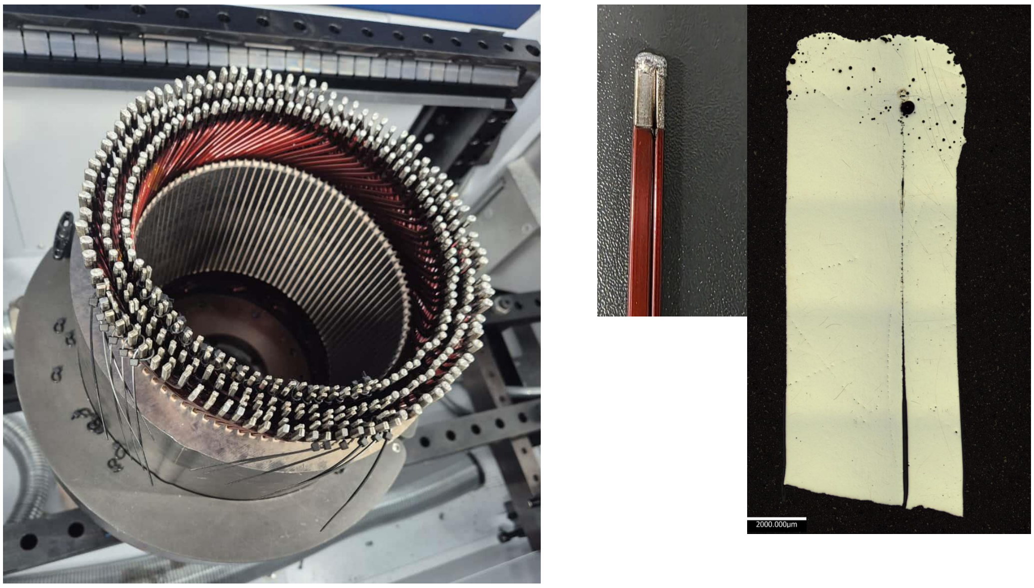

Figure 69: Welding process and Metallographic Analysis of the large-to-small weld sample

The DC resistance of each weld was measured directly using a micro-ohm meter. Specifically, the resistance of an array of nine series-connected sample pins was measured (R_{tot}), and the contribution from the pin lengths ($R_{cond,tot}$) was subtracted to isolate the resistance of the welded joints ($R_{weld,tot}$). This value was then divided by eight to obtain the resistance of a single weld ($R_{weld,i}$), see Fig. 70. This method helps reduce measurement uncertainty, and it is adopted for the DC resistance measurement of the optimized copper-to-copper, aluminum-to-aluminum, and copper-to-aluminum welds. Based on the estimated DC weld resistance values reported in Table 30, the weld quality can be considered satisfactory. The hybrid array is composed by 5 copper conductors and 4 aluminum ones. The resulting copper-to-aluminum weld exhibits higher resistance due to the formation of intermetallic compounds at the interface.

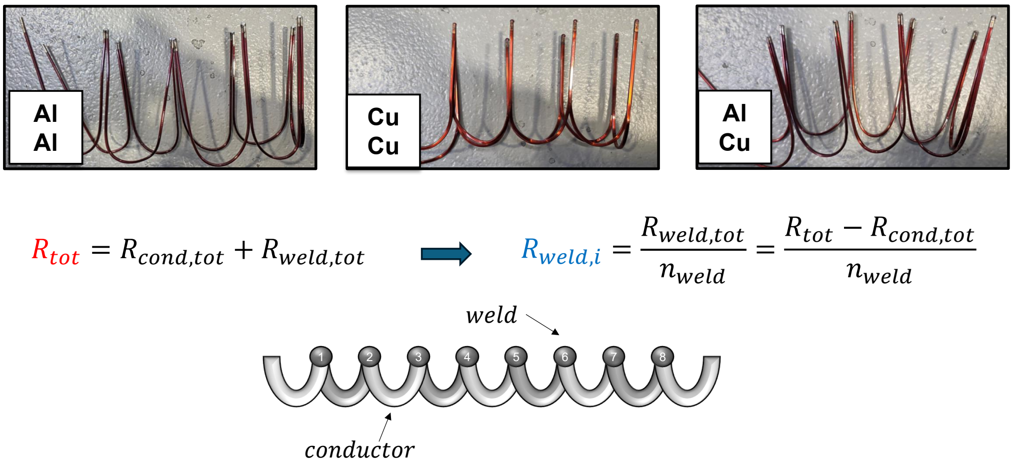

$$R_{tot} = R_{cond,tot} + R_{weld,tot} \quad \Rightarrow \quad R_{weld,i} = \frac{R_{weld,tot}}{n_{weld}} = \frac{R_{tot} - R_{cond,tot}}{n_{weld}}$$

Figure 70: Weld DC Resistance Measurement Methodology

Table 30: DC resistance of the small-to-small weld.

Measurement	Cu–Cu	Al–Al	Cu–Al
Array Resistance R_{tot} $[m\Omega]$	6.77	11.46	9.02
Weld Resistance $R_{weld,i}$ $[\mu\Omega]$	39	41	60

4.3.3 Final Results and Considerations

A complete aluminum hairpin stator manufacturing process is developed, highlighting guidelines on how to adjust key process parameters. Thinner aluminum hairpins demand tighter process control and higher precision, as their greater flexibility increases the likelihood of pin misalignment. However, the larger conductors showed higher controllability, effectively mitigating this issue. At the same time, aluminum's greater flexibility and easier handling provided improved adaptability and operational freedom in several manufacturing steps. Lastly, high quality welds were achieved even without the use of shielding gas. In addition to the cost savings of eliminating a shielding gas system, this approach is particularly advantageous in flexible manufacturing lines that process both copper and aluminum, as it removes the need to manage two separate shielding gases. Two aluminum hairpin stators are shown in Figures 71 a) and b), while in Fig. 71 c) both the aluminum and copper versions are shown. The successful production of two aluminum hairpin stators, featuring increased complexity from a high slot count and the use of two different conductor sizes within the same slot, demonstrates the feasibility of implementing aluminum hairpin technology.

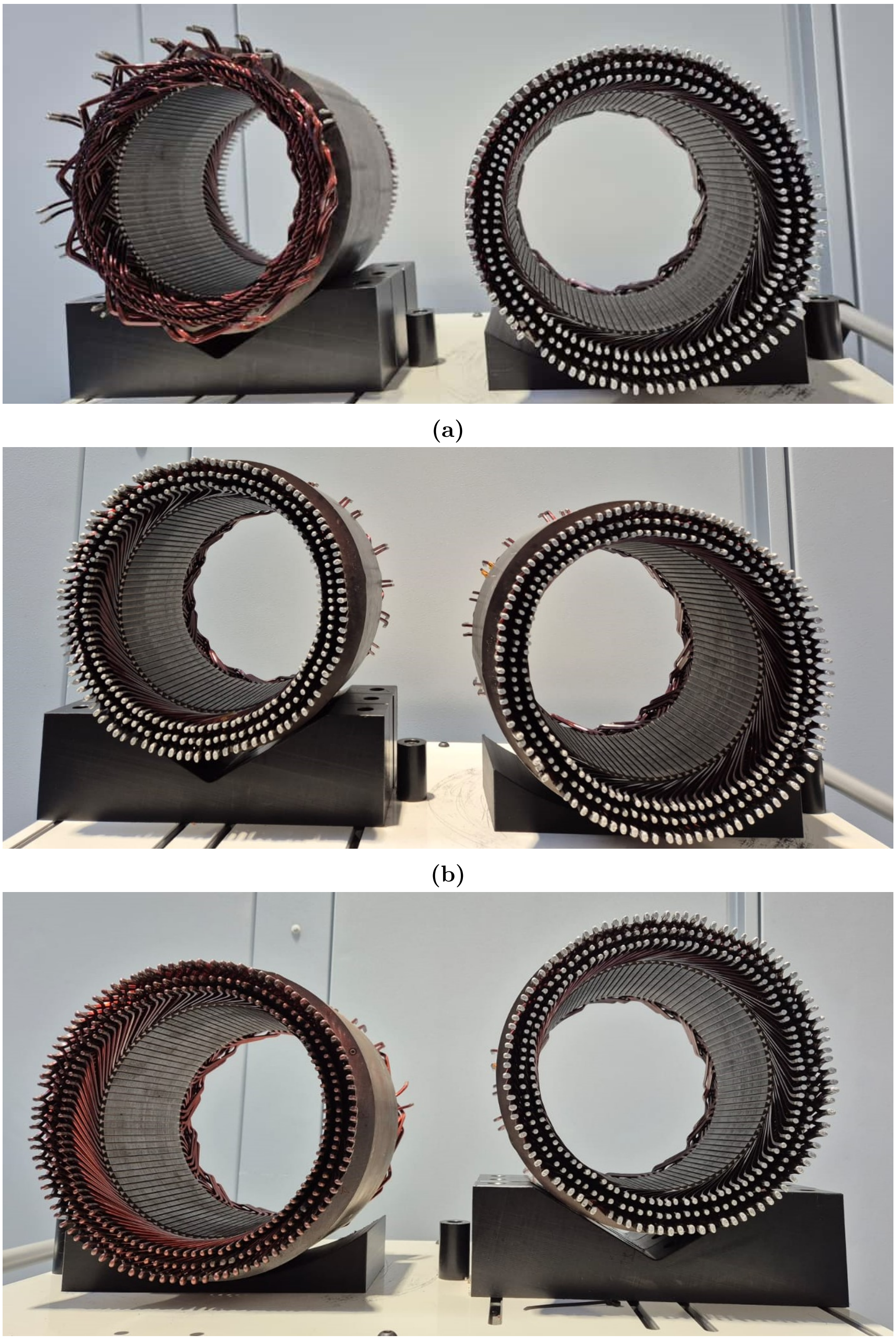

(a)

(b)

(c)

Figure 71: Two aluminum hairpin stators a) Welding sides b) Bending and Welding sides b) Aluminum and copper hairpin stator versions

4.4 Conclusions

This chapter analyzed the implications of a drop-in replacement of copper with aluminum in hairpin winding stator manufacturing, with particular attention to the different material workability, hairpin bending behavior, and production process adaptation. To this purpose, a literature review introduced alternative manufacturing solutions enabled by aluminum, followed by a detailed case study on hairpin bending and a complete manufacturing process for an aluminum hairpin stator implemented on a copper-based production line.

The results show that aluminum's different workability significantly affects the interaction between design and manufacturing, requiring adjustments to specific process parameters when the same manufacturing process as copper is used. In addition, its higher ductility enhances stability against torsional–flexural phenomenon during hairpin bending, enabling the use of higher conductor aspect ratios with potential reductions in AC losses. Finally, the practical feasibility of the winding "drop-in replacement" approach is validated through the successful development of two aluminum hairpin stators produced on an existing copper hairpin manufacturing line, for which no retooling was necessary. Best practices are identified to fine-tune the process parameters to suit aluminum conductors.

4.5 Contributions to research

In this chapter, the following research contributions are presented, successfully addressing **OBJ4** of this thesis:

- The impact of aluminum's different workability on the hairpin manufacturing process and its implications for electromagnetic design choices are investigated.
- The feasibility of a drop-in replacement is validated through the development of two aluminum hairpin stators on a production line originally designed for copper hairpin windings.
- Hairpin winding process parameters are adapted to account for the different workability of copper and aluminum, providing practical guidelines and best practices.

The case study evaluating how the different formability of copper and aluminum affects the geometric constraints of hairpin cross sections imposed by the bending process is presented in the following conference paper:

- P. Falletta, G. Cutuli, S. G. Barbieri, V. Mangeruga, T. Zou and S. Nuzzo, "Comparison between Aluminum and Copper Hairpins on the Torsional-Flexural Instability Phenomenon in the Bending Process," 2025 IEEE Workshop on Electrical Machines Design, Control and Diagnosis (WEMDCD), Valletta, Malta, 2025, pp. 1-6,

  doi: 10.1109/WEMDCD61816.2025.11014164.

The complete aluminum hairpin stator assembly process and the associated guidelines are presented in a journal article that has recently been submitted to IEEE Industrial Electronics Magazine (IEM) Transaction.

Finally, the two aluminum hairpin stators will undergo busbar mounting and impregnation, after which they will be tested to investigate additional aspects of aluminum hairpin winding implementation that are not yet supported by experimental results.

5. Reliability Aspects for Sustainability

In previous chapters, the replacement of copper hairpin windings with aluminum was explored. This material-focused sustainability strategy reduces the environmental impact during the early stages of the electric drive life-cycle, such as raw material extraction and production, as well as at its end-of-life, enhancing recyclability.

Extending this perspective, the present chapter shifts focus to reliability as a pathway to sustainability.

A reliability-oriented design approach enables the safe integration of technologies that improve the efficiency of electric drives, thus playing a crucial role in reducing emissions during operation. Combined with the material-focused strategy addressed in previous chapters, this approach is complementary to the design of an electric drive that is sustainable throughout the entire life-cycle, from material selection and production to operation and end-of-life.

Specifically, the safe implementation of WBG devices will be addressed from the perspective of the reliability of the electric machine. While these devices offer high switching frequencies that can significantly improve power density and efficiency, the resulting rapid voltage transitions (high dV/dt) can trigger early partial discharge (PD) inception, challenging the reliability of the stator winding insulation system.

In this context, the aim of this chapter is presenting a case study which establishes design guidelines for hairpin winding layouts that minimize inter-turn voltage stress. This is made by evaluating the voltage distribution of various winding diagram configurations and their response to different rise times. The different winding configurations are implemented using a modular hairpin stator prototype, featuring a multiphase, multibranch design that can be flexibly reconfigured by reconnecting its accessible phase terminals and neutral points. Consequently, a high frequency electrical lumped parameter model is employed to simulate the time-domain voltage distribution across all configurations, enabling the selection of that reducing the maximum inter-turn voltage stress. This model relies on a detailed semi-analytical parameter identification procedure, allowing for fast and accurate simulation of node voltages throughout the machine sections, without exceeding in complexity. The simulation results have been validated through an experimental campaign conducted across all the different winding configurations. Finally, a sensitivity analysis is performed to evaluate how the maximum voltage stress varies with the rise time of the input waveform and its effects on the different winding configurations.

5.1 Voltage Stress Reduction in Hairpin Windings: Guidelines and Critical Aspects

This study provides guidelines to minimize the inter-turn insulation voltage stress in hairpin winding, induced by the fast-switching operation of the WBG devices. In the following, the background and state of the art related to insulation reliability under fast switching conditions are first reviewed. The representative stator case study is then introduced, followed by the development of a high frequency model aimed at modeling the voltage distribution in hairpin winding conductors, as a function of the high frequency pulse input voltage given by the inverter. The experimental setup adopted to validate the proposed model is subsequently described, and the corresponding results along with the model validation are presented. Finally, a sensitivity analysis on voltage rise time is carried out to assess its influence on insulation stress and provide general guidelines for the effective reduction of the inter-turn voltage insulation stress.

5.1.1 Background and State of the Art

The pursuit for improved efficiencies and power densities of electric drives has driven the diffusion of inverters based on WBG fast switching semiconductors [70], [71]. These can operate at higher frequencies and reduced losses compared to more traditional semiconductor devices. These specific characteristics make them particularly suitable also for traction applications, where operating speeds and fundamental frequencies are gradually increasing. Meanwhile, their faster commutation times (tens of nanoseconds) can lead to voltage wave reflections along the cables connecting the inverter to the motor terminals (even when short cables are used), resulting in voltage overshoots at the motor terminals. This, in turn, can cause internal turn-to-turn over-voltage, placing additional stress on the insulation system of the machine windings. The increased voltage stress can trigger early PD inception [72], [73], leading to a premature insulation failure.

Most studies have focused on mitigating the observed voltage overshoots at motor terminals, as these points are easily accessible, allowing straightforward quantification of improvements through direct measurement. Different approaches have been proposed through the years: from dissipative procedures, such as passive filters [74] or reduced voltage slew rate [75] through increased gate resistance, to "lossless" active filtering [76], [77].

Other works have instead focused on how the terminal voltage waveform affects the internal turn-to-turn insulation voltage stress. In fact, adjacent conductors within a motor slot can experience important voltage gradients, depending on the winding connections and on how fast voltage rise and fall times are [73], [78].

Hence, several studies have been conducted to quantify the voltage stress within the machine windings, also referred to as uneven voltage distribution problem. However, most research has focused on machines equipping random windings [78], [79], [80], [81], [82], as they are the most adopted in the industry field. Their main challenge is that the exact location of all the conductors cannot be known a-priori. Therefore, it may happen that adjacent conductors are far located in the series connections, leading to potentially high transient voltage gradients during device commutations [78].

The introduction of hairpin windings in the global market, especially for traction applications, led to the need for further research on this topic. Contrarily to random windings, the ability to know the exact location of each conductor poses a stronger basis for reliability-oriented designs, which should therefore consider an accurate choice of the winding internal connections, as will be discussed in this study.

The normally adopted models for the internal winding voltage stress estimation is the high frequency equivalent circuit approach, as per the random winding machines.

The number of remarkable publications on this topic is relatively limited, although some first important results are present. In [83], [84], a simple high frequency equivalent circuit, solved in the time domain, is adopted for the estimation of the voltage gradients between the different layers of one hairpin windings phase. All parameters were extracted through finite element analysis (FEA). The presented studies aim at providing a first experimental validation of the proposed model and also some guidelines for the realization of reduced stress configurations. The main recommendation is that, when possible, the distance in the series connection of adjacent conductor layers should be minimized. A proposed connection scheme has also been provided for a 4 layer configuration.

A slightly different slot model is proposed in [85], with the aim of also considering the iron loss damping effect. The high frequency parameters have been estimated through direct impedance measurement.

In [86], [87], the studies have focused more on the modeling approach, rather than providing specific guidelines. The equivalent circuits have been solved in the frequency domain through a modified nodal analysis, allowing for a frequency-dependent characterization of the parameters. In particular, the results in [86] provide an improved match, at the cost of a more complex procedure and longer parameter extraction. In fact, the equivalent parameters have been extracted through FEA, but a set of simulations needs to be performed for each selected step within the considered frequency spectrum. Direct and inverse Fourier transforms must also be performed for the decomposition of the original time-domain input waveform and the reconstruction of the node voltages from the frequency solutions, respectively.

An alternative modeling approach can be found instead in [88], where a grey-box model, based on impedance measurements, has been adopted to avoid the use of FE simulations and to estimate the time domain voltage distribution within different sections of a hairpin windings permanent magnets synchronous machine.

5.1.2 Case Study

The study focuses on a 250 kW (continuous power) machine for heavy duty traction application, with IPMs and hairpin windings, which has been analyzed in Section 2.3 and Section 4.3. The stator characteristics are reported in Table 31, while more details about the electromagnetic analysis of such configuration can be found in [89].

Table 31: Stator Characteristics

Material	NO 20
Slots Number, Z_s	96
Poles Number, p	8
Conductors per Slot, n_c	6
Active Length $[mm]$, l_a	140

The hairpin windings layout features a modular short pitch arrangement with high flexibility of re-connection. As already mentioned, it has been intentionally designed to feature a multi-phase, multi-branch configuration which can be flexibly re-configured by re-connecting only the phase terminals and neutral points. Information on how to design the modular winding diagram are provided in the following subsections. The reconfigurability allows one to change the number of series turns per phase (N_s), thus adapting in a modular way the electromagnetic characteristics of the design according to the specific application. This avoids to redesign the entire winding diagram through modifications to its internal connections and transposition strategy. It is worth observing that the findings of this study relative to the voltage stress reduction can be extended to any other slot-pole combination, as the same winding connection guidelines apply.

In the following, two different configurations are presented, as shown in Fig. 72:

1. *Parallel*: dual-three phase, with two parallel paths per phase, namely $A1_1$ and $A1_2$ for phase **A1**, and $A2_1$ and $A2_2$ for phase **A2**.
2. *Series*: three phases, with four series paths per phase, namely $A1_1$, $A1_2$, $A2_1$ and $A2_2$.

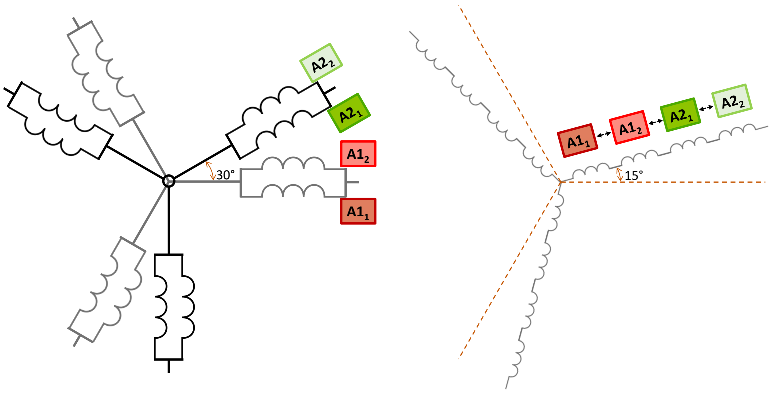

(a) **(b)**

Figure 72: Parallel (a) and Series (b) Configurations.

The electromagnetic properties of the two configurations are resumed in Table 32.

Table 32: Parallel vs Series Configurations

(a) Parallel	(b) Series
$N_s = 24$	$N_s = 96$
Lower MMF for same current	Higher MMF for same current
Lower back-emf at same speed	Higher back-emf at same speed
Suitable for high speed - low torque applications	Suitable for low speed - high torque applications

By recombining the four series paths in different ways, the series configuration gives rise to multiple case studies which, while sharing the same electromagnetic characteristics, are compared in this study through voltage distribution analysis, to identify the option that minimizes voltage stress on the inter-turn insulation.

Parallel configuration

The original hairpin windings configuration is the parallel configuration, dealing with a dual three-phase machine, displaced by 30 electrical degrees (Fig. 72(a)).

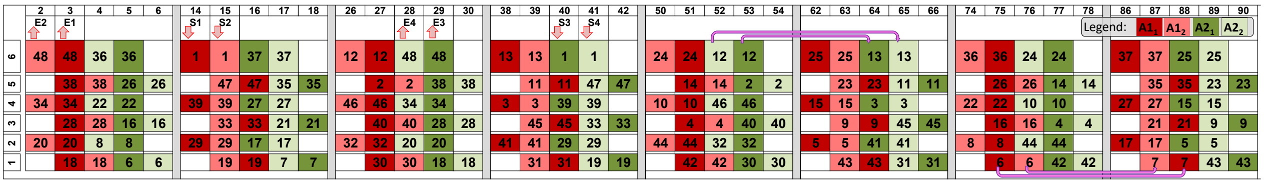

	2	3	4	5	6	14	15	16	17	18	26	27	28	29	30	38	39	40	41	42
	E2	E1				S1	S2						E4	E3				S3	S4	
6	48	48	36	36		1	1	37	37		12	12	48	48		13	13	1	1	
5		38	38	26	26		47	47	35	35		2	2	38	38		11	11	47	47
4	34	34	22	22		39	39	27	27		46	46	34	34		3	3	39	39	
3		28	28	16	16		33	33	21	21		40	40	28	28		45	45	33	33
2	20	20	8	8		29	29	17	17		32	32	20	20		41	41	29	29	
1		18	18	6	6		19	19	7	7		30	30	18	18		31	31	19	19

	50	51	52	53	54	62	63	64	65	66	74	75	76	77	78	86	87	88	89	90
6	24	24	12	12		25	25	13	13		36	36	24	24		37	37	25	25	
5		14	14	2	2		23	23	11	11		26	26	14	14		35	35	23	23
4	10	10	46	46		15	15	3	3		22	22	10	10		27	27	15	15	
3		4	4	40	40		9	9	45	45		16	16	4	4		21	21	9	9
2	44	44	32	32		5	5	41	41		8	8	44	44		17	17	5	5	
1		42	42	30	30		43	43	31	31		6	6	42	42		7	7	43	43

Figure 73: Parallel Configuration - Phases A1 and A2 Winding Diagram.

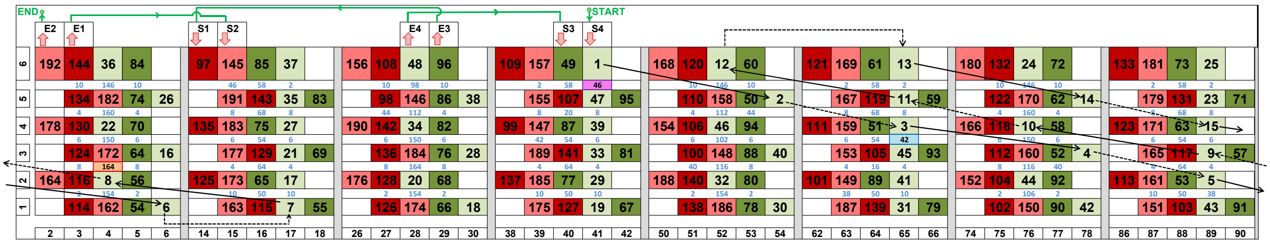

	2	3	4	5	6	14	15	16	17	18	26	27	28	29	30	38	39	40	41	42
	E2	E1				S1	S2						E4	E3				S3	S4	
6	192	144	36	84		97	145	85	37		156	108	48	96		109	157	49	1	
		10	146	10			46	58	2			10	98	10			2	58	46	
5		134	182	74	26		191	143	35	83		98	146	86	38		155	107	47	95
		4	160	4			8	68	8			44	112	4			8	20	8	
4	178	130	22	70		135	183	75	27		190	142	34	82		99	147	87	39	
		6	150	6			6	54	6			6	150	6			42	54	6	
3		124	172	64	16		177	129	21	69		136	184	76	28		189	141	33	81
		8	164	8			4	64	4			8	164	8			4	64	4	
2	164	116	8	56		125	173	65	17		176	128	20	68		137	185	77	29	
		2	154	2			10	50	10			2	154	2			10	50	10	
1		114	162	54	6		163	115	7	55		126	174	66	18		175	127	19	67

	50	51	52	53	54	62	63	64	65	66	74	75	76	77	78	86	87	88	89	90
6	168	120	12	60		121	169	61	13		180	132	24	72		133	181	73	25	
		10	146	10			2	58	2			10	146	10			2	58	2	
5		110	158	50	2		167	119	11	59		122	170	62	14		179	131	23	71
		4	112	44			8	68	8			4	160	4			8	68	8	
4	154	106	46	94		111	159	51	3		166	118	10	58		123	171	63	15	
		6	102	6			6	54	42			6	150	6			6	54	6	
3		100	148	88	40		153	105	45	93		112	160	52	4		165	117	9	57
		40	116	8			4	16	4			8	116	40			4	64	4	
2	188	140	32	80		101	149	89	41		152	104	44	92		113	161	53	5	
		2	154	2			38	50	10			2	106	2			10	50	38	
1		138	186	78	30		187	139	31	79		102	150	90	42		151	103	43	91

Figure 74: Series Configuration: 4312 - Phase A Winding Diagram. "Difference Numbers" in blue. Critical Locations 1F, 2F, and MAX highlighted in purple, light blue and orange, respectively.

The winding diagram is shown in Fig. 73. The horizontal axis corresponds to the stator's circumferential direction, while the vertical axis represents the radial one, which extends from the first layer at the bottom, facing the air gap, to the sixth layer at the top. The number in each cell is the progressive series number. The conductors highlighted in dark and light red correspond to the two parallel elementary paths of phase **A1** ($A1_1$ and $A1_2$, respectively), whereas those in dark and light green to the parallel paths of **A2**, i.e., to $A2_1$ and $A2_2$, respectively. For clarity sake, elementary paths in hairpin windings are composed by the minimum series of conductors strategically placed to avoid the circulating currents which could be produced by the different impedances featured by the conductors along the slot. This is achieved through the strong symmetry rule, (as already mentioned in Section 2.3 and 4.3), which ensures the same impedance in each operating condition for all the elementary paths. Specifically, the winding diagram features strong symmetry when the conductors of each elementary path are transposed to occupy all positions in all slots of the pole-phase belt an equal number of times [90].

As it can be observed, in the proposed diagram the basic winding pattern deals with transposing the conductors by changing both the layer and the phase belt slot position. Particularly, the conductors' position is progressively changed from the sixth to the first layer when the conductors are wound in a clockwise direction, while the path is reversed when the winding direction is counterclockwise. The winding direction is reversed through special connections, namely the jumpers, highlighted in purple. The red connections are the elementary path terminals, where the letter S identifies the series start, while the letter E the series end. In the original configurations, the terminals of the phase **A1** and **A2** are connected in the following way: $S1 = S2$, $E1 = E2$, $S3 = S4$ and $E3 = E4$, as highlighted by the green connections in Fig. 73, thus obtaining a dual three-phase configuration, with disconnected neutrals. The elementary paths are highlighted in the stator angular sector representing one pole pair of Fig. 75, where the short pitch configuration can be observed, along with the conductor geometry. As already mentioned in Section 2.3 and 4.3, the sixth layer features a larger cross section [89].

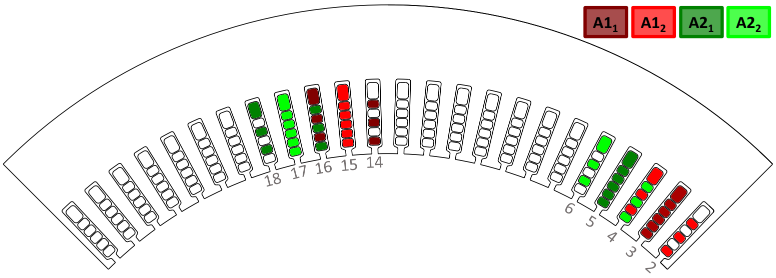

Figure 75: Stator Angular Sector representing one Pole Pair

The number of slots comprised in one phase belt Z_{belt} is 3, due to the short pitch, but the equivalent number of slots per pole per phase q is equal to 2.

Series configuration

In this study, the windings are reconfigured such to obtain a three-phase stator, Fig. 72(b), thus doubling q from 2 to 4, while Z_{belt} becomes 5. In the series configuration, the 4 elementary paths represented in Fig. 75 are connected in series. For the sake of clarity, an identification number (ID) is first assigned to each elementary path, as specified in Table 33. Arranging the four elementary paths identification numbers in a sequence of four digits without repeating any member, $4! = 24$ different permutations are obtained. The order of each elementary path in this sequence identifies its position in the phase series, with the leftmost digit associated to the first elementary series path, and the rightmost to the last path. For example, combination 4312 identifies the phase series configuration obtained by the series $A2_2$, $A2_1$, $A1_1$ and $A1_2$ placed in this exact order, as shown in its corresponding winding diagram of Fig. 74.

Table 33: Elementary Paths Identification Numbers

$A1_1$	$A1_2$	$A2_1$	$A2_2$
1	2	3	4

The terminals connections are represented by the green lines, made as follows: START = $S4$, $E4 = S3$, $E3 = S1$, $E1 = S2$, $E2$ = END.

Since all four elementary paths are connected in series, the progressive numbering ranges from 1 to 192. "Difference numbers", highlighted in blue, are introduced between adjacent layers within the same slot to indicate the number of series conductors between them.

When assessing the linear voltage distribution across the series-connected conductors, the insulation between the two adjacent conductors with the highest difference number will experience the greatest steady-state voltage drop. However, the voltage distribution is inherently non-linear under normal conditions due to the transient nature of the pulse-width modulated (PWM) voltage input, as well as the inductive and capacitive footprint of the electrical circuit. Consequently, during normal operation, the maximum voltage may occur at different locations.

Specifically, another critical point is at the "front", namely the first conductors in the series. This is because the high frequency voltage harmonic content is at its maximum and has not been attenuated yet by the winding's turn inductance and parasitic capacitance, combined with eventual reflection phenomena between the inverter and motor terminals. At those conductors, the over-peak voltage can theoretically reach up to twice the DC link voltage or even higher in double-pulse conditions.

In light of these considerations, the criticality of the voltage distribution for each configuration is compared by evaluating the difference number at three different locations, namely:

1. First Front (1F): voltage difference between the first conductor in the series and its facing excited conductor.
2. Second Front (2F): voltage difference between the second conductor in the series and its facing excited conductor. If this can be measured with both the upper and bottom adjacent conductor, the voltage with the highest difference number is preferred.
3. Maximum (MAX): maximum difference number in the series. If this is measured in two different locations, the first is preferred in series order. It basically represents the winding position between two facing conductors that are the farthest in the series connection.

In the following sections, it will be shown that the most critical voltage difference can occur in either of these locations, depending on the series combination. These critical points have been highlighted for a specific configuration in Fig. 74 as an example. In particular, 1F is between the sixth and fifth layer of slot 41, 2F is between the fourth and third layer of slot 65, whereas

MAX is between the third and second layer of slot 4. Checking the difference number of these locations for each combination, the most representative ones are selected. In particular, for each subgroup of combinations with any of the four elementary path at the beginning of the series, both the best and the worse combinations are selected. The best combination minimizes the number of series conductors corresponding to MAX, while the worst maximizes it. Table 34 summarizes the selected combinations, which will be analyzed in the following.

Table 34: Selected Series Combinations

Initial Path ID	**1**	**2**	**3**	**4**
Best	1432	2413	3142	4213
Worse	1243	2134	3421	4312

The voltage distribution for each combination of Table 34 will be assessed both experimentally and by simulations through the model described in the next section, to find the one minimizing the maximum voltage stress.

5.1.3 Voltage Distribution Model

This section introduces the high frequency model, which allows to calculate the voltage distribution within the conductors as a function of the high frequency pulse input voltage given by the inverter.

The model includes the inverter cables and the stator winding series conductors, represented as a lumped parameter network of resistances R, inductances L, and capacitances C to characterize the high frequency response.

The first subsection introduces the slot and the stator winding models, along with the adopted connection method for reconfiguring the series elementary. Next, the calculation methodology for all the slot parameters is shown. After the parameters have been estimated, the high frequency model can be simulated entirely in Matlab-Simulink environment, thus enabling fast simulations, in the order of a few seconds on a commercial personal computer.

Slot and Winding Model

Figure 76 shows the model of the k^{th} slot, where $k = 1, .., Z_{belt}$ identifies the slot position in the phase A belt within one pole. With reference to Fig. 75, the parameters of the slot model with $k = 2$ correspond to the slot 3 and 15. Each of the n_c conductors is modeled as a series of

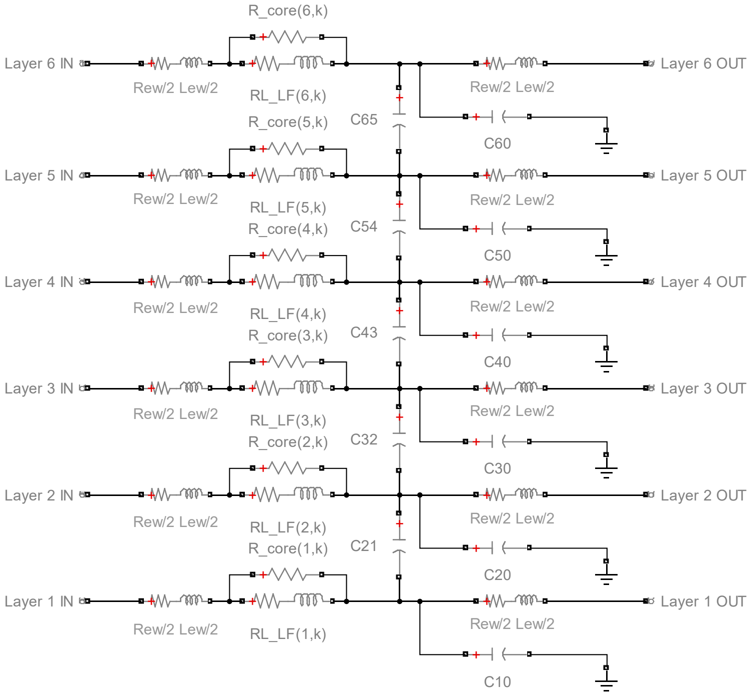

Figure 76: Slot Model

a front and a rear end winding resistance and high frequency inductance ($R_{ew}/2$ and $L_{ew}/2$), and low frequency (LF) equivalent inductance and resistance calculated through FEA (R_{LF} and L_{LF}). For each conductor, FEA electrostatic simulations with JMAG 2D are performed to determine the ground capacitances (C_{i0}, with $i = n_c, .., 1$), as well as mutual capacitances ($C_{i(i-1)}$, with $i = n_c, .., 2$) between adjacent conductors. Finally, a resistance (R_{core}) is placed in parallel with the low frequency parameters (R_{LF}, L_{LF}) to model the AC losses high frequency damping behavior, with the core losses having the main role.

Each stator slot is modeled as in Fig. 76, including its corresponding parameters, which are determined in the following subsection. A sub-circuit is created from each slot model, and then connected to the others, basing on the elementary paths illustrated in the winding diagram of Fig. 73.

Figure 77 shows the interconnection method for the conductors in slot 15, chosen as a representative example. Specifically, Figure 77 a) illustrates the connection logic through a circuit diagram, where each conductor is represented by an impedance that includes both the active and the end-winding parts. Figure 77 b) represents how the same connection strategy has been implemented in the Matlab Simulink environment. The left side of each slot represents the input for each slot conductor, while the right side is the output.

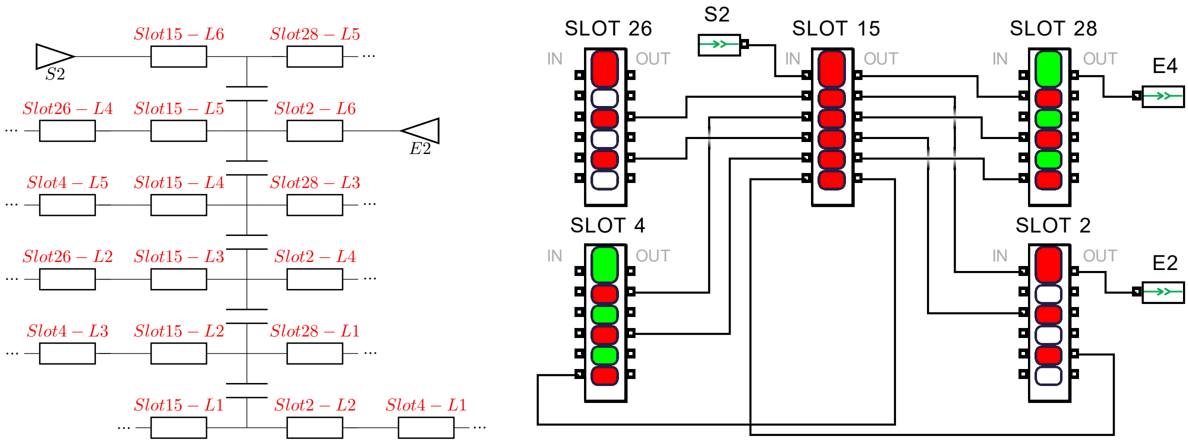

(a) (b)

Figure 77: Slots Connection Example: Slot 15

By connecting all the slots according to the elementary paths connections, a reconfigurable stator base model is obtained. Through reconfiguration of the elementary paths terminal connections, basing on the specific combination chosen from Table 34, it is possible to explore all the possible different paths connections and identify the most suitable for the voltage stress mitigation. As an example, Figure 78 shows the terminal connections for configuration 4312.

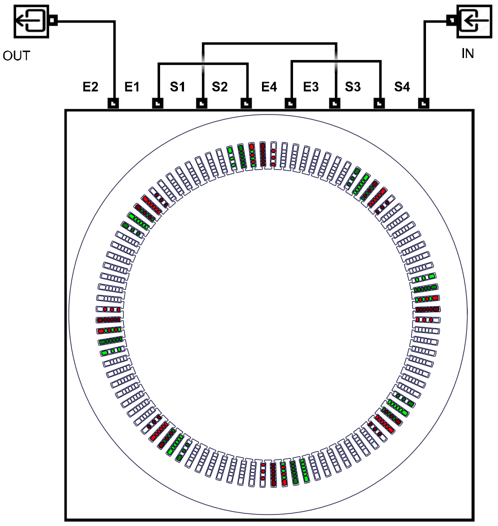

Figure 78: Stator Model: Configuration 4312

Slot Parameters Calculation

Here, the methodology used for the calculation of the slot parameters $(R_{LF}, L_{LF}, R_{core}, L_{ew}, C_{i0}, C_{ij})$ is illustrated.

- Capacitance Calculation

The capacitance values are calculated through FEA electrostatic simulations of one slot, as the dielectric properties are not frequency dependent. No capacitance is considered for the end winding regions, due to the absence of ferromagnetic material and the greater distance between the layers. Figure 79 shows the slot model, including the relevant materials, i.e. NO20 for the stator core, copper for the conductors, enamel and slot liner for the insulation system. The values of relative electric permittivity ϵ_r for the enamel and the liner are 3.9 and 2.4, respectively.

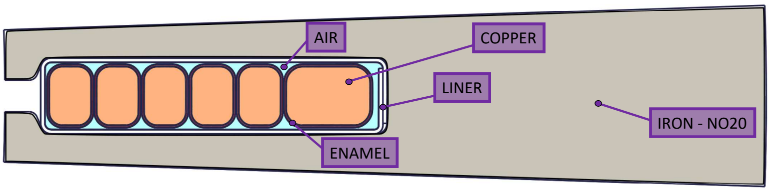

Figure 79: Slot Model for Capacitance Computation

The capacitance between two electrically insulated components can be determined as the ratio of the change in electric charge on their surfaces to their electric potential difference (5.1). Therefore, an electrostatic simulation is independently performed for each i^{th} conductor, ($i = n_c, .., 1$), on which an electric potential boundary of $V_i = 1\ V$ is applied, while $V_0 = 0\ V$ elsewhere. The ground capacitance C_{i0} is then computed by measuring the resulting amount of electric charge Q_0 at the stator tooth walls, while the mutual capacitance Cij is calculated from the amount of the electric charge Q_j on the j^{th} conductor facing the i^{th} conductor (j=5,..,1, $j \neq i$), as highlighted in eq. (5.1). Mutual capacitance between non-adjacent conductors are neglected due to their much inferior order of magnitude.

$$\begin{cases} C_{i0} = Q_0/(V_i - V_0) \\ C_{ij} = Q_j/(V_i - V_0) \end{cases} \tag{5.1}$$

All of the computed capacitances are reported in Table 35.

Ground Capacitances [pF]						**Mutual Capacitances [pF]**				
C60	C50	C40	C30	C20	C10	C65	C54	C43	C32	C21
49.8	21.6	21.4	21.4	21.4	28.3	28.3	24.4	25.9	25.9	25.9

Table 35: Capacitance Values

- Low Frequency Parameters Calculation

The LF resistance for each of the n_c conductor is analytically calculated through (5.2), where $\rho = 1.72 \times 10^{-8}\ \Omega m$ is the copper resistivity, $l = l_a$ is conductor length and S_i is the conductor cross section, which is bigger for the sixth conductor layer (S_6).

$$R_{LF}(i) = \rho l / S_i, \qquad \forall i,\ \ i = 1, .., n_c \tag{5.2}$$

The end winding resistance R_{ew} is calculated in the same way, supposing the total end winding length equal to the active length.

The LF equivalent inductance is calculated through a transient FEA electromagnetic simulation. The conductors of phase A are excited in series with a sinusoidal current having a root mean square (RMS) value of $I_{rms} = 1A$ and $f_{LF} = 100Hz$, while phases B and C are floating and not excited. The model includes one stator pole, i.e., half of the geometry shown in Fig. 75, where each highlighted conductor of phase A is independently modeled as a solid conductor. The flux linkage is then calculated independently for each single conductor, thus catching all inductance differences, which depend on the different layer or slot position. For each conductor, the value of equivalent inductance is computed through (5.3), where $\lambda_{rms}(i,k)$ is the RMS flux linkage of the i^{th} conductor layer located in the k^{th} slot position in the phase belt.

$$L_{LF}(i,k) = \frac{\lambda_{rms}(i,k)}{I_{rms}}, \quad \forall\, i,k \begin{cases} i = 1, \ldots, n_c \\ k = 1, \ldots, Z_{belt} \end{cases} \tag{5.3}$$

These values of equivalent inductances do not distinguish between mutual and self inductances [91], as all the conductors are simultaneously supplied, but allows a correct link between the actual feeding current and the flux linkages. The computed values which are adopted in the slot models of Figure 76 are shown in Table 36.

- High Frequency Parameters Calculation

The high frequency AC losses of the winding and the iron core, with the latter playing the main role, are modeled through the parallel resistance R_{core}, placed across the active part

Table 36: Low Frequency L_{LF} and End Winding L_{ew} Inductance $[\mu H]$

		Phase Belt Slot					**End Winding**
	k i	1	2	3	4	5	ALL
Conductor Layer	6	-	6.36	6.52	6.42	4.06	1.95e-2
	5	3.71	6.22	6.38	6.27	-	2.97e-2
	4	-	6.00	6.16	6.06	3.81	3.26e-2
	3	3.49	5.67	5.83	5.73	-	3.34e-2
	2	-	5.23	5.39	5.29	3.37	3.24e-2
	1	3.05	4.67	4.84	4.73	-	2.86e-2

of the winding, as proposed for the first time in [85]. Specifically, at high frequency, the reaction field of the eddy currents acts as a shield against the magnetizing flux generated by the current flowing in the winding's active portions, thus resulting in a reduction of the conductor inductance. Connecting R_{core} in parallel models this effect, as at higher frequency, the reactive component of the active part impedance becomes larger than the impedance of the R_{core} parallel branch. Consequently, more current flows through R_{core} rather than through the active part impedance, leading to a reduction in overall inductive behavior. From a physical perspective, such reaction field leads to additional power losses and, at high frequency, can also be interpreted as a significant reduction in the equivalent relative permeability of the iron core [92], which cannot be neglected. The main challenge about R_{core} estimation is that laminated cores, normally adopted for industrial or transport applications, lack material data above a few kHz. Hence, their high frequency behaviour can only be estimated through measurements or analytical formulation, causing some uncertainties. One of the simplest ways to determine R_{core} is through direct stator impedance measurement [93]. Figure 80 highlights the measured differential mode impedance frequency response. In particular, the equivalent R_{core} of the entire machine can be estimated at the first impedance resonance point f_{res}, where the inductive and capacitive contributions compensate each other. In this way, the impedance measured at this frequency is only resistive, accounting for both AC winding and iron core losses. Therefore, the value of R_{core} calculated from this measurement includes both contributions. For a single phase impedance measurement, $R_{core} \approx Z_p$ can be written, where Z_p is the resonance point impedance value ($f_{res} \approx 150\,kHz$, as can be seen in Fig. 80).

The actual value of each iron loss parallel resistance $R_{core}(i,k)$ can be approximated by dividing R_{core} by the total number of conductors N, as in (5.4).

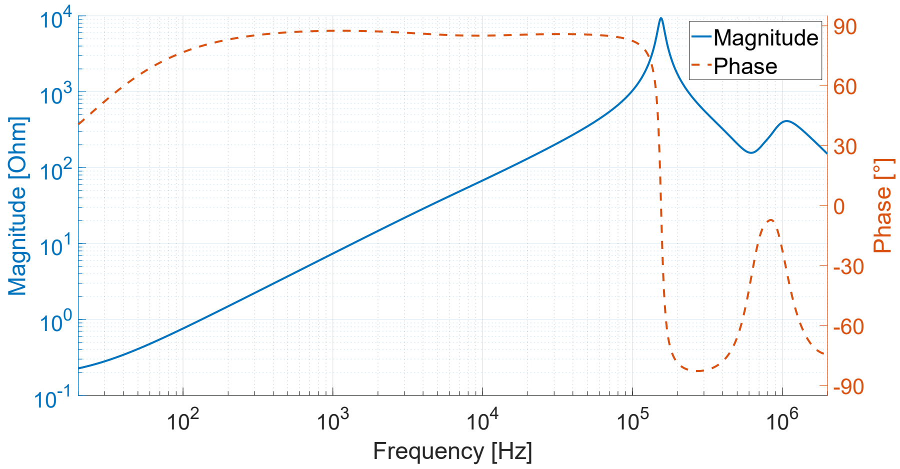

Figure 80: Measured Impedance Frequency Response - Differential Mode

$$R_{core}(i,k) \approx \frac{R_{core}}{N} \tag{5.4}$$

Finally, L_{ew} are calculated using a high frequency current supply at f_{res} with 1 A amplitude. The simulation is performed on a single slot model (similar to Fig. 76), where the conductors are surrounded by air rather than iron. Also in this case, the values of L_{ew} (in Table 36) are calculated from the flux linkage values, following a similar approach to (5.3).

5.1.4 Experimental Setup

The experimental setup is shown in Fig. 81, where one motor phase is fed by a SiC inverter through a 1.5 m long unipolar cable with a 4 mm^2 cross section. The increase in resistance caused by the cable, and thus its effect on the steady state voltage, is negligible because of its much shorter length with respect to the entire motor winding coil.

The inverter operates at low voltage values, in order to limit the maximum current since no rotor back electromotive force is present, i.e. only the stator is tested with no rotor. The DC bus has been set at 40 V and a few unipolar voltage pulses with a fixed duty cycle D of 0.5 excite one phase of the stator windings for each measurement cycle.

Four differential probes are connected to the oscilloscope and properly arranged to measure the voltage in three different stator locations ($1F$, $2F$, and MAX, as marked in Fig. 81) and at the inverter busbars, for sensing the input voltage. Thanks to the accessible welded side of

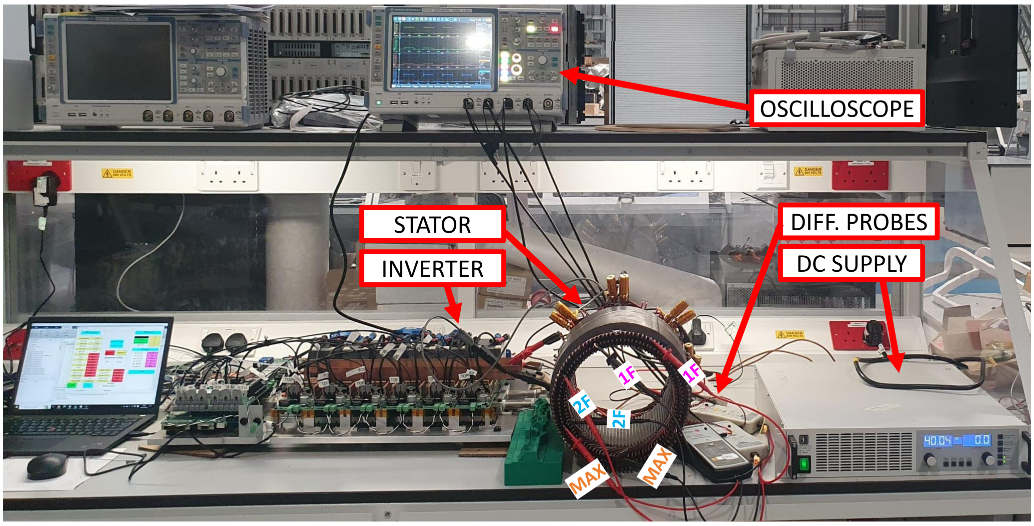

Figure 81: Experimental Setup

the stator, every inter-turn voltage can be measured using the winding diagram as a reference. Specifically, the differential probe leads are placed at the two welded spots that terminate the end winding portion of the analyzed conductors. As the end windings of two facing conductors branch out in different directions, the welded spots where contacting the differential probes leads are at different points. Appendix C provides a detailed explanation on how the voltage probes have been installed. The terminals of the four winding elementary paths are instead

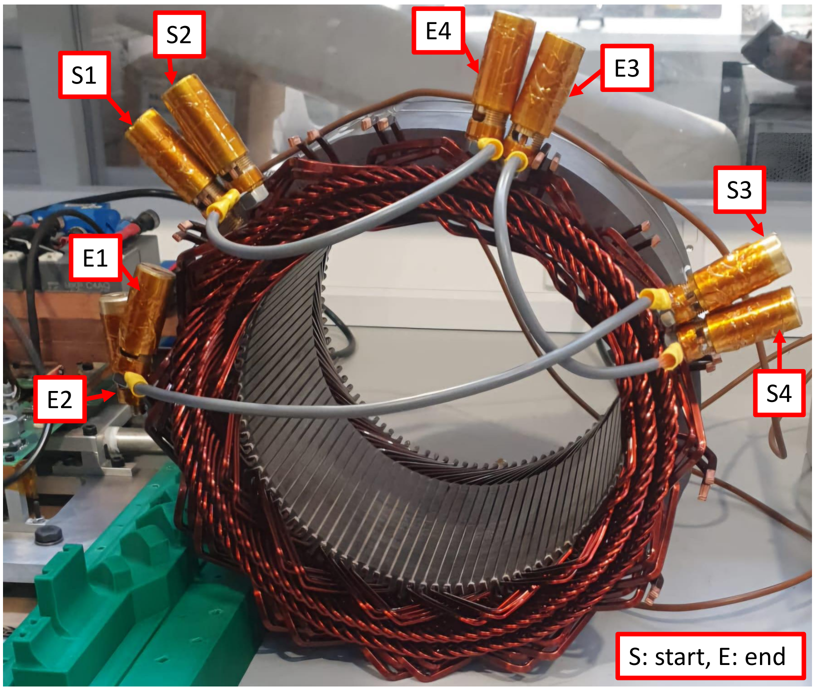

Figure 82: Terminals Connections

located on the bending side of the stator. The terminals connections are guaranteed through bronze connectors as shown in Fig. 82.

5.1.5 Model Validation and Results

This section presents the experimental results and compares them with the simulated ones to validate the model. Based on the results, key insights will be drawn, offering general guidelines for minimizing voltage stress on the insulation for hairpin windings. To validate the simulation model, a comparison between the experimental and simulated results is performed for each of the combinations reported in Table 34. Specifically, the measured voltage at the inverter terminals is provided as input of the voltage distribution model through a controlled voltage source. Consequently, the simulated inter-turn voltage at $1F$, $2F$ and MAX is compared to the experimental one. Figure 83 presents a comparison between the experimental and simulated voltage waveforms for all configurations. The top configurations correspond to the ones labeled as best in Table 34, while the bottom ones represent the worst cases. The voltage waveforms are shown in normalized values relative to the DC link steady-state voltage.

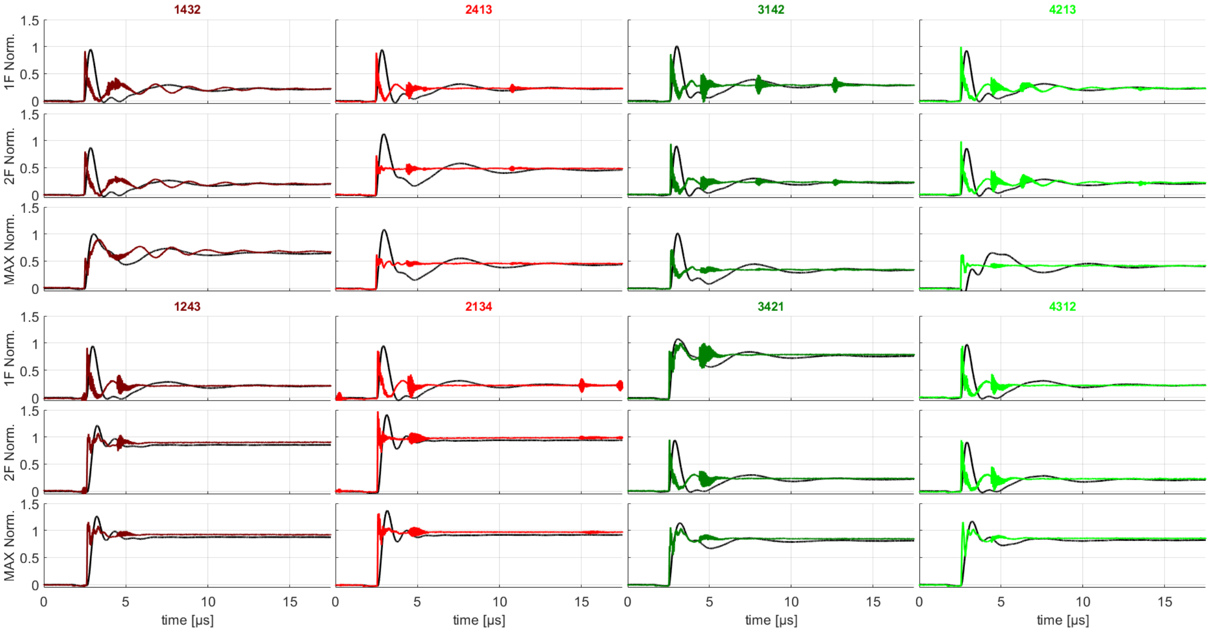

Figure 83: Voltage Waveforms: simulated in black, measured in colors.

Model Validation

The model reliability is evaluated by comparing, for each configuration, the peak value of the voltage waveforms in $1F$, $2F$, and MAX, as well as the steady state values. With regard to insulation stress and the risk of PD inception, the actual voltage waveform plays only a marginal role compared to the peak voltage value, which is the primary outcome considered in this model. On this basis, a good consistency between the measurements and the simulations is achieved, with an average accuracy of approximately 10% on the peak values, and most configurations remaining below this threshold. It should be also noted that the model is conservative, since the errors consist usually in an overestimation of the voltage stress, which is clearly preferable to an underestimation for a matter of reliability. Finally, the model also features an optimal match for the steady state values.

Results Discussion

The results confirm that the right choice of the series combination can reduce the voltage stress on the insulation. Specifically, the connections should be arranged in a way that the number of conductors in series between two adjacent conductors is reduced as much as possible [83], [84]. This condition is satisfied when paths sharing the same slots are not the first and last in the combination, but rather are consecutive in the series. For the winding diagram adopted in this study, the paths sharing the same slots are 1 with 3, and 2 with 4, thus justifying the classification shown in Table 34. When a short-pitch winding configuration is adopted, the initial path of the series combination should not be one of the most external in the phase belt, namely 1 and 4, since these share slots with paths belonging to other phases, thus resulting in a considerably high voltage stress. In fact, the number of series conductors between different phases is always greater than the distance between any conductor of a specific phase, leading to the exclusion of these configurations as optimal choices for reducing voltage stress. This also explains why the probing points 1F, 2F, and MAX were not selected in slots containing conductors from two different phases, half of which are floating since only one phase is fed. Based on these observations, the preferred series combinations that satisfy the design guidelines should start with elementary path 3 followed by 1 as well as 2 followed by 4. The experimental results confirm then that the best configuration is 3142.

Current Approach Limitations

The proposed modeling approach provides a reliable estimation of the maximum inter-turn voltage stress through fast time domain simulations in Matlab Simulink, with the aim of identifying possible mitigation strategies. Meanwhile, the adopted simplifications and possible sources of discrepancy between experimental and simulation results are discussed in this section:

- *Parameters are not frequency dependent.* Due to the impossibility of catching the parameters frequency dependency through time domain simulations, the R_{core} definition process is made to better address the frequency range relative to the voltage overshoot, which corresponds to the resonances in the differential mode impedance measurement in Fig. 80. Although this ensures a good correspondence for the peak voltage value, it results in a less precise estimation of the voltage waveform, as the higher frequency components are caught with less accuracy.

- *Capacitance estimation.* Local variation of capacitance due to geometric tolerances and effective dielectric permittivity are complex to be identified and quantified.
- *Materials data reliability.* The limited availability of high-frequency data, particularly for laminated iron cores, poses significant challenges in accurately modeling the machine's behavior in this operating range. As anticipated, the eddy current-induced variation in iron core impedance at high frequency affects the machine inductances, becoming the main source of uncertainty. While in this study this aspect is addressed through R_{core}, its estimation relies on direct measurements, thereby necessitating the availability of a physical prototype.

While addressing these issues would improve the correspondence of the simulated and experimental measurements in terms of voltage waveform, the proposed approach already provides reliable peak voltage estimation with significantly reduced computational effort. From a reliability perspective, the voltage waveform is of secondary importance, as when it comes to PD inception, it is the peak voltage value the main parameter to be monitored for the inter-turn voltage stress evaluation. On this basis, this study demonstrates good agreement between experimental and simulation results in terms of peak voltage estimation. Additionally, a more accurate voltage waveform estimation would require catching the whole frequency spectrum. Nonetheless, including frequencies beyond a few MHz would result in higher circuit complexity, because, as highlighted in [86], at such operating frequencies the voltage wavelength becomes comparable to the winding subsection, necessitating a finer circuit subdivision into more lumped parameters.

5.1.6 Rise Time Sensitivity Analysis

As mentioned above, the severity of voltage-induced stress on the insulation of two facing conductors largely depends on their relative positions in the series connection, and changing the series configuration allows to arrange adjacent conductors as closely as possible, thus reducing the overall insulation stress. Another critical aspect arises for conductors close to the motor terminals (the front conductors), where the high frequency voltage harmonic content is maximum and has not yet been partially filtered by the inductance and parasitic capacitance of the winding turns. The high frequency content strongly depends on the rise time. Hence, shorter rise times correspond to a greater stress, especially on the front conductors in the series. In contrast, as the rise time increases, the highest voltage difference tends to occur between facing conductors that are farther apart in the series, where the steady state voltage difference is the maximum. Consequently, it is not straightforward to predict whether the location of the most critical high-voltage stress is in MAX, 1F or 2F without considering the rise time.

This section presents a sensitivity analysis on the rise time and its impact for the different configurations. Specifically, a set of simulations is conducted for each configuration, each using a step waveform with a custom rise time. For each simulation, the peak voltage was recorded at locations 1F, 2F, and MAX. These results are shown in Figure 84, which highlights the normalized peak voltage at the three locations (1F, 2F, and MAX) at different rise times, for the configurations 4213 and 4312. A peak voltage of 1 p.u. corresponds to the inverter DC voltage.

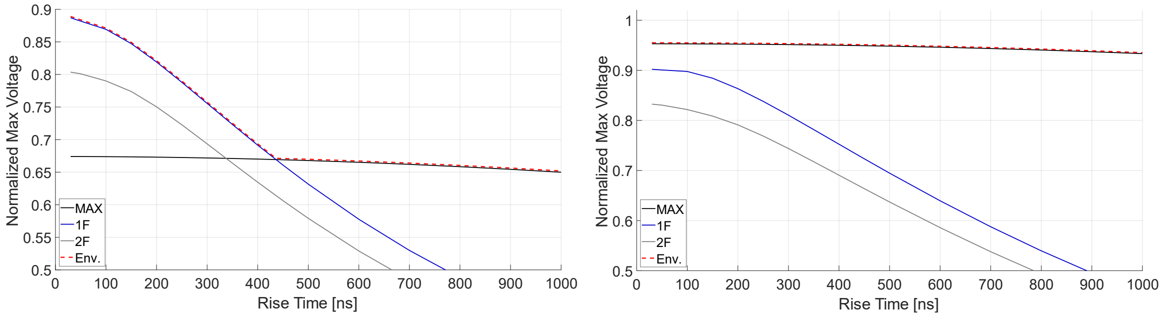

(a) **(b)**

Figure 84: Risetime Sensitivity Analysis - Configuration (a) 4213 and (b) 4312

An envelope curve can be extracted for each configuration, (hyphen red line) in Fig. 84 (a) and (b), indicating the highest voltage value in the series, at each rise time, independently on the winding location. The envelope curves for every configuration are compared in Fig. 85.

As anticipated in the previous sections, the series configurations which arrange adjacent conductors far apart from each other should be discarded. For these configurations, the most critical high voltage stress is at MAX location, independently on the rise time value. Such configurations are those represented by hyphen lines in Fig. 85, namely 1243, 2134, 3421, and 4312. This is clearly seen in Fig. 84 (b), showing that the peak value in 1F and 2F is always

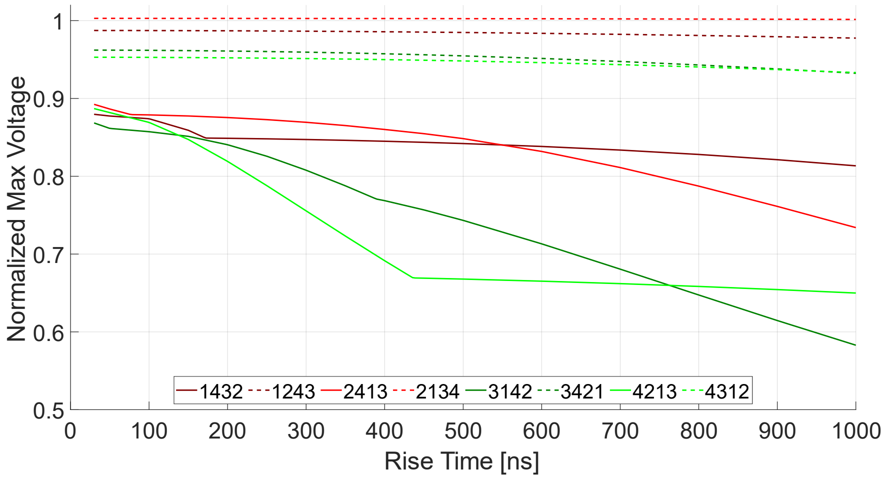

Figure 85: Highest voltage within phase A conductors at different risetime values for each configuration

below the peak value in MAX, which is nearly constant and has a lower dependency on the input rise time. For such configurations, it can be stated that the location and value of the maximum voltage stress is quite independent on the voltage rise time. Instead, arranging adjacent conductors as closely as possible generally reduces the maximum voltage stress, as seen from the configurations represented by solid lines in Fig. 85, such as 1432, 2413, 3142, and 4132. However, the most critical high-voltage stress location is at 1F for shorter rise times, while it shifts to MAX for longer ones. This occurs because the peak voltage value at the front conductors decreases as the rise time increases, as clearly observed in Fig. 84 (a), where the cross-over point rise time is about 440 ns. This decreasing trend can also be observed at MAX, provided that it is located at one of the first slots in the series, as observed for configurations 3142 and 2413, in Fig. 85. For these configurations, it is clear that the conductor location influences also the peak voltage dependence on the input rise time, which can be explained by the filtering action that the voltage wave has to face while traveling through the different turns. Such filtering action is limited for conductors close to the motor terminals, resulting in a high rise time dependency, while it can be more prevalent in farther ones.

5.2 Conclusions

This chapter proposed a reliability-oriented design approach as a key enabler for sustainability. In fact, it showed how a reliability-oriented design approach enables the safe integration of efficiency-enhancing technologies in electric drives, thereby contributing to the reduction of operational emissions.

In particular, the chapter addresses the implementation of WBG devices from the perspective of electric machine reliability. Although their high switching frequencies enable significant improvements in power density and efficiency, the associated fast voltage transients (high dV/dt) can promote early PD inception, posing challenges to the reliability of the stator winding insulation system.

To this purpose, the chapter examined how the reconnection of elementary paths in an improved reconfigurable hairpin windings diagram and the rise time affect voltage stress on winding insulation.

First, an accurate and simple high frequency lumped parameter network was used to calculate the voltage distribution within the conductors. Then, the model was validated using experimental results, showing a suitable level of consistency.

The voltage distribution of various elementary path series configurations are analyzed and compared. Based on the results, guidelines are proposed for series-connecting the modular, strongly symmetric elementary paths to reduce the maximum insulation inter-turn voltage stress. In the analyzed short-pitch winding, the maximum inter-turn voltage is expected to decrease by approximately 35% when the first and last elementary paths in the series do not share the same slot, and the initial series path avoids occupying the external slots of the phase belt.

Further analysis highlighted that meeting these criteria may not be sufficient if the rise times are very short. In such cases, stress reduction could be significantly lower than expected, leading to only 10-15% improvement compared to the initial worst-case scenario. This occurs because shorter rise times shift the location of the highest voltage stress toward the first turns, even though the number of series conductors between adjacent layers is lower than in other winding locations. In fact, first series conductors are highly affected by the voltage wave's high frequency content, which is gradually filtered as it propagates through the subsequent series turns. Hence, with short rise times on the order of tens of nanoseconds, it becomes essential to closely monitor the series conductors near the motor terminals. Additionally, when feasible, the use of active filters or multilevel inverters can help mitigate the effects of steep voltage transients and, consequently reduce their impact on the conductors in the first slots.

Although often overlooked in favor of electromagnetic performance optimization, a reliability-oriented approach is essential to the design of sustainable machines, as it allows a safe implementation of technologies enhancing the efficiency, ultimately reducing emissions in the operation stage of the life-cycle. To this end, the guidelines provided in this work offer a practical yet effective framework for implementing reliability-focused solutions, ensuring the integrity of the insulation system.

5.3 Contributions to research

This chapter provided guidelines and best practices for the reliability-oriented design of hairpin winding electric machines, thus addressing **OBJ5** of this thesis. The contributions to research brought by this chapter are the following:

- A simpler winding diagram reconfiguration method based on modularity is introduced, which is used to evaluate the maximum voltage stress within different winding diagram configurations. With this method, elementary winding paths are treated as modular units that can be reconnected, while their internal connection remains unchanged.
- The combined effect of the rise time variation and the winding configuration on the maximum voltage stress is investigated.

While the importance of minimizing the series connection distances between adjacent conductors underlined in previous research remains, this study brings attention to a critical yet previously overlooked factor in hairpin windings designs. Specifically, it demonstrates that for waveforms with rise times on the order of tens of nanoseconds, significant voltage stress can also occur between facing conductors near the motor terminals, even when they are separated by fewer series-connected conductors with respect to other points in the winding diagram.

Hence, the adoption of a hairpin windings scheme, which is merely focused on the minimization of the series connection distance, could result in a reduction of the maximum voltage stress which is lower than expected. Meanwhile, the presented study shows also that in terms of peak insulation voltage stress, not all the winding configurations are equally sensitive to rise time variations. In order to unequivocally determine the entity and position of the critical winding insulation stress, it is therefore mandatory to consider the combined effect of the adopted winding diagram configuration and rise time at the same time.

These findings are presented in this journal paper:

- G. Cutuli, M. Pastura, S. Nuzzo, D. Barater, T. Zou, D. Chen, C. Gerada and G. Franceschini, "On the Voltage Stress Reduction in Hairpin Windings: Guidelines and Critical Aspects," in IEEE Transactions on Transportation Electrification,

  doi: 10.1109/TTE.2025.3624866.

6. Conclusions

This chapter summarizes the general conclusions of the work and highlights the main objectives addressed during the Ph.D. together with its main contributions to research. It then presents the publications and activities carried out during the Ph.D., and concludes with considerations on potential directions for future work.

6.1 General Conclusions

This Ph.D. project focused on the design of sustainable electric machines for utility vehicle traction applications, with the objective of reducing the environmental impact at all stages of its life-cycle, including raw material extraction, production, operation, and end-of-life, where recyclability and reuse play a fundamental role.

To this end, this thesis investigated the implementation of two key sustainability-oriented technologies:

- the replacement of copper windings with aluminum, aimed at reducing environmental impact during material extraction, production, and end-of-life, due to its higher recyclability;
- the adoption of WBG devices, whose fast switching capability improves electric drive efficiency and consequently reduces emissions during operation.

These technologies are complementary, as together they tackle emissions in all stages of the electric machine life-cycle.

Meanwhile, their implementation introduces several constraints in the design of an electric machine, possibly affecting its power density and efficiency, thermal performance, reliability, and manufacturability.

In this framework, this Ph.D. project identified, analyzed, and mitigated the inherent challenges associated with the adoption of these sustainability-oriented technologies, demonstrating that environmentally conscious design choices can be successfully integrated into electric machines while preserving electromagnetic and thermal performance, efficiency, reliability and manufacturing feasibility.

6.1.1 Replacing Copper Hairpin Windings with Aluminum

The primary challenge identified is the higher electrical resistivity of aluminum compared to copper, which can lead to increased winding losses, potentially impacting machine efficiency and thermal performance during operation.

Different replacement scenarios were evaluated through electromagnetic and thermal analyses under peak, nominal, and driving cycle conditions. Based on this, copper and aluminum solutions were compared in terms of efficiency, cost, weight, and environmental impact.

The selected approach for converting copper to aluminum in utility traction applications is the **"windings drop-in replacement"**, where the stator geometry and drive characteristics remain unchanged, and only the conductor material is substituted.

In fact, by accepting higher thermal loads under peak operating conditions (which are rarely encountered in utility vehicles) using aluminum hairpin windings via a drop-in replacement enables reductions in weight, cost, and environmental impact, while maintaining acceptable thermal performance (with same cooling system) and comparable efficiency during operating conditions which are more representative of real user needs, such as a WLTP driving cycle.

This finding highlights that achieving sustainability often involves a shift in the design priorities: from a purely performance-driven to an application-driven approach, where the focus is on meeting real user needs rather than solely optimizing the product.

In addition, the winding drop-in replacement method effectively addresses the manufacturing challenges associated with adopting a different, more sustainable solution, as it requires no retooling of existing equipment and only minor adjustments to process parameters. This is demonstrated by the successful production of two aluminum hairpin stators on a line originally designed for copper.

In conclusion, replacing copper hairpin windings with aluminum through a drop-in approach is well suited for the utility vehicle in the automotive sector, which typically relies on pre-existing copper solutions. In fact, it does not require any modifications to existing designs or manufacturing lines, offering a cost-effective, lightweight, and sustainable alternative.

6.1.2 Adopting WBG devices

The main challenge is to prevent PDs that may arise from voltage stresses caused by the fast switching of WBG devices.

A high-frequency lumped-parameter model of stator hairpin windings was developed and validated against experimental results to assess how the reconnection of elementary paths in an improved reconfigurable hairpin winding layout and the rise time influence voltage stress on the winding insulation.

The results indicate that considering the combined effect of winding diagram configuration and rise time is essential for accurately predicting and mitigating voltage stress on the inter-turn insulation of hairpin windings.

This finding highlights the importance of a reliability-oriented design approach in the early stages of electromagnetic design as a pathway to sustainability. It enables the safe implementation of efficiency-enhancing strategies, such as WBG devices, which in turn contribute to reducing emissions during the operation of the electric machine.

6.1.3 Outcome

The outcome is that a direct drop-in replacement of copper with aluminum does not compromise efficiency and thermal performance in driving cycle conditions, which are most representative of real user needs, while the implementation of WBG devices is safe provided that reliability aspects on the winding diagram are taken into account from the early stages of the electromagnetic design.

Overall, this Ph.D. project concludes that a reliable design which is tailored to the actual user needs is a fundamental enabler for the development of a sustainable electric machine. This requires a redefinition of the design priorities, shifting from a performance-driven perspective to an application-driven methodology, in which the focus is no longer on the product itself but on the user needs.

6.2 Thesis Achievements and Contributions to Research

The achieved objectives of the thesis are reported in the following, as introduced in the introductive chapter.

OBJ1 *Motivate the potential of aluminum as a sustainable alternative.*

OBJ2 *Identify suitable design approaches for the development of aluminum hairpin winding machines and establish general comparison strategies with copper.*

OBJ3 *Provide guidelines for the electromagnetic and thermal design of aluminum hairpin machines for traction of utility vehicle.*

OBJ4 *Validate the manufacturing feasibility of implementing the aluminum hairpin winding solution.*

OBJ5 *Define guidelines and best practices for the reliability-oriented design of hairpin winding electric machines.*

The main contributions to research achieved throughout this Ph.D. work, along with the fulfillment of the related objectives, can be summarized as follows:

- The suitability of aluminum hairpin windings for electric traction machines in utility vehicles is systematically demonstrated through a per-unit-volume comparison with copper, showing that aluminum can potentially offer a more sustainable, cost-efficient, and lightweight alternative without compromising driving-cycle efficiency. This addresses **OBJ1**.
- Three general strategies are established for the development of the aluminum machine starting from a copper reference design, providing a structured framework for the winding material substitution in traction applications and addressing **OBJ2**.
- Guidelines for the electromagnetic design of copper-to-aluminum machine conversions are proposed, based on analyses under typical driving-cycle conditions. The approach emphasizes a drop-in winding replacement that preserves the existing design and manufacturing process, addressing part of the third objective of the Ph.D. project **OBJ3**.
- A thermal design feasibility assessment was conducted for drop-in replacements under peak, continuous, and driving-cycle conditions, demonstrating that a copper-to-aluminum hairpin drop-in conversion, preserving the same geometry and cooling system, can achieve

satisfactory thermal performance. This allows to fully address **OBJ3**.

- The impact of aluminum's different workability on the hairpin manufacturing process and its implications for electromagnetic design choices are investigated.
- The feasibility of a "drop-in" replacement is validated through the development of two aluminum hairpin stators on a production line originally designed for copper hairpin windings, thus addressing **OBJ4**.
- The process parameters of a hairpin manufacturing line initially designed for copper are adapted to account for the different workability of copper and aluminum, thus providing practical guidelines and best practices.
- Guidelines for reducing inter-turn voltage stress in hairpin windings caused by WBG devices are proposed through a simplified winding diagram reconfiguration method, thus addressing **OBJ5**. This modular approach treats elementary winding paths as independent units that can be reconnected without altering their internal connections.
- The combined effect of the rise time variation and the winding configuration on the maximum voltage stress is investigated, thus addressing **OBJ5**.

6.3 Publications and Activities Completed during the Ph.D.

The following conference papers have been published during the Ph.D. research:

- G. Cutuli, S. Nuzzo, T. Zou, G. Franceschini, C. Gerada and D. Barater, "Multi-objective Optimizations of Copper and Aluminum Hairpin Windings: a Comparison," 2023 IEEE Energy Conversion Congress and Exposition (ECCE), Nashville, TN, USA, 2023, pp. 3796-3801, doi: 10.1109/ECCE53617.2023.10362293.
- G. Petrelli, G. Cutuli, D. Barater S. Nuzzo, T. Zou, and C. Gerada, "On Comparing Aluminum and Copper in Wound Field Synchronous Motors for Traction Applications," 2024 International Conference on Electrical Machines (ICEM), Torino, Italy, 2024, pp. 1-7, doi: 10.1109/ICEM60801.2024.10700570.
- M. Raimondo, G. Cutuli, S. Nuzzo and D. Barater, "Assessing Thermal and Efficiency Aspects of Aluminum Hairpin Motors in Passenger Cars," 2024 International Conference on Electrical Machines (ICEM), Torino, Italy, 2024, pp. 1-7,

  doi: 10.1109/ICEM60801.2024.10700377.
- P. Falletta, G. Cutuli, S. G. Barbieri, V. Mangeruga, T. Zou and S. Nuzzo, "Comparison between Aluminum and Copper Hairpins on the Torsional-Flexural Instability Phenomenon in the Bending Process," 2025 IEEE Workshop on Electrical Machines Design, Control and Diagnosis (WEMDCD), Valletta, Malta, 2025,

  pp. 1-6, doi: 10.1109/WEMDCD61816.2025.11014164.
- F. Savi, G. Cutuli, S. Nuzzo and D. Barater, "System Level, Comparative Loss Evaluation of Interior Permanent Magnet Drive with Traditional and Predictive Control Strategies," 2025 IEEE Workshop on Electrical Machines Design, Control and Diagnosis (WEMDCD), Valletta, Malta, 2025, pp. 1-6, doi: 10.1109/WEMDCD61816.2025.11014128.
- A. Tinti, G. Cutuli, S. Nuzzo, G. Sala, D. Barater and G. Franceschini, "Slot Opening Influence on Short Circuit Current: A Sensitivity Analysis," 2025 IEEE Workshop on Electrical Machines Design, Control and Diagnosis (WEMDCD), Valletta, Malta, 2025, pp. 1-6, doi: 10.1109/WEMDCD61816.2025.11014169.

The following journals have been published in high-impact, peer-reviewed transactions:

- G. Cutuli, S. Nuzzo, D. Barater, T. Zou, S. Nategh and T. Bertoncello, "Replacing Copper With Aluminum in Hairpin Windings Motors Intended for Utility Cars," in IEEE Journal of Emerging and Selected Topics in Industrial Electronics, vol. 6, no. 3, pp. 864-876, July 2025, doi: 10.1109/JESTIE.2025.3546030.
- G. Cutuli, M. Pastura, S. Nuzzo, D. Barater, T. Zou, D. Chen, C. Gerada and G. Franceschini, "On the Voltage Stress Reduction in Hairpin Windings: Guidelines and Critical Aspects," in IEEE Transactions on Transportation Electrification,

  doi: 10.1109/TTE.2025.3624866.

The following Journal Magazine has been submitted to the IEEE Industrial Electronics Magazine (IEM) Transaction.

- G. Cutuli, S. Nuzzo, D. Barater, T. Zou, and C. Gerada, "Rethinking Hairpin Winding Design and Manufacturing: Aluminum as a Drop-In Replacement for Copper".

Finally, during the Ph.D., two industrial-scale aluminum hairpin winding stators for heavy-duty truck applications were successfully manufactured. They feature a dual three-phase configuration with disconnected neutrals, 96 slots, and six in-slot conductor layers, with the outermost layer adjacent to the stator yoke having a larger cross section. These stators are currently housed in the PEMC laboratory at the University of Nottingham.

6.4 Future Work

Future research directions include:

- Testing the two manufactured aluminum hairpin stators to assess their peak and continuous thermal performance, as well as temperature behavior under reproduced driving-cycle conditions, in comparison with an identical copper prototype.
- Investigating the PD phenomenon in aluminum hairpin windings, with a focus on evaluating the implications of the different insulation on the material, compared to copper.
- Expanding the research on reliability-oriented design by analyzing inter-turn short circuits, including the development of suitable models and their experimental validation under representative fault conditions.

Appendix

A. Preliminary Electromagnetic Design for an Aluminum Hairpin Winding Machine from Scratch: Slot Pole Combination Selection.

In this section, several electromagnetic considerations and case studies for the preliminary electromagnetic design of aluminum hairpin winding machines designed from scratch are presented.

The study is carried out for a given target power density. Specifically, the DC bus voltage and the maximum phase current are fixed, together with the stator outer diameter and the active length.

When designing a new machine from scratch, the first step is to analyze the slot–pole combination. In particular, the maximum allowed series turns per phase (N_s) is determined based on the selected DC link constraints, which limit the maximum line peak voltage at the desired base speed (eq. 2.15).

This is done using assumptions on the average flux density, i.e., the magnetic loading of the machine, which in a permanent magnet synchronous machine is primarily determined by the magnets' amount, placement, and remanence flux density. Based on the calculated N_s, different slot–pole combinations can be evaluated by varying the number of slots per pole per phase (q), the number of pole pairs (pp), the number of parallel paths per phase (N_{pp}), and the number of conductor layers per slot (n_L) (eq. 2.16). The objective of this study is to determine whether, for a given power density, machine topologies, defined by the slot–pole combination, n_L, and N_{pp}, can be identified that are more favorable when aluminum is adopted as winding material.

In a first case study, the machine topology is chosen to operate at an optimal electrical frequency, specifically, a high frequency at which the reduction in AC losses offered by aluminum compensates for the increase in DC losses compared to copper for the same conductor cross section. To achieve this, the slot–pole combination is selected to enable operation at a higher electrical frequency.

In a second case study, the focus is on reducing the DC Joule losses of aluminum while maintaining the same output power density. This is achieved by lowering the machine's electric loading (which directly affects Joule losses) and proportionally increasing the magnetic loading to preserve the same product of the two, ensuring the same output power. This redistribution of magnetic and electric loading results in different machine topologies optimized for aluminum, for which the associated advantages and criticalities will be discussed.

A.1 Operation at higher electrical frequency. Same electric loading and magnetic loading.

The first study assumes identical electric and magnetic loading for both copper and aluminum windings.

The selected slot–pole combination results in a higher operating frequency due to the increased number of *pp*. Under these conditions, the use of aluminum could be advantageous, as the AC effects, more pronounced at higher frequencies, can be mitigated by its higher resistivity.

Furthermore, although a higher number of *pp* increases the electrical operating frequency for a given mechanical speed of the machine, it also allows the yoke thickness (h_{yoke}) to be reduced, since the pole surface over which the flux of each pole is distributed becomes smaller. This reduction can lead either to a smaller stator outer radius (resulting in a lighter design) for a given slot height, or to a larger slot height for a given outer radius, which helps reduce the DC resistance for a specified electric loading. It should be noted that a higher number *pp* also leads to a higher slot number (Zs) for a given q. As a result, the slots become narrower since they must be distributed around the stator with a fixed outer radius. Consequently, the conductor cross section tends toward b/h (width over height) ratios below 1, which is more critical in terms of AC losses and could further justify the adoption of aluminum conductors.

One case study for a preliminary electromagnetic design is reported in the following:

Outer Stator Diameter, mm	210
Active Length, mm	100
DC bus Voltage, V	800
Max Phase Current, Arms	200
Base Speed, rpm	5000
Number of phases	3

The adopted assumptions are listed below:

- *Magnetic loading*: average airgap flux density (no load) B_{avg}=0.6 T (amplitude of first harmonic B_{pk}=0.94 T)
- *Tooth thickness (at mid-slot radius) equal to slot width (w_{slot})*, which is a good compromise between excessive tooth saturation and too narrow slots and thus too low b/h ratios of the conductor cross section
- h_{yoke} *is accordingly reduced with higher pp*, while the stator outer radius is kept constant, resulting in increased slot height (h_{slot}).

From eq. 2.15, the calculated N_s is 72. Some of the feasible slot pole combinations are:

1. pp=4, Z_s=72, n_L=8, N_{pp}=1
2. pp=6, Z_s=108, n_L=8, N_{pp}=2

The resulting motor geometry for the two cases is reported below, together with the geometric specifications:

STATOR	Zs=72, pp=4	Zs=108, pp=6	**ROTOR**	Zs=72, pp=4	Zs=108, pp=6
Stator inner diameter	136 mm	136 mm	Rotor outer diameter	134 mm	134 mm
Airgap thickness	1 mm	1 mm	Magnet pocket–airgap min distance	1 mm	1 mm
h_{yoke}	20 mm	17.6 mm	Magnet volume	116 cm3	116 cm3
h_{slot}	16 mm	18.4 mm	Magnet thickness	5 mm	5 mm
w_{slot}	3.36 mm	2.54 mm	Magnet width	29 mm	19.33 mm

The two machines exhibit the same magnetic loading, as they use the same amount and arrangement of permanent magnets, and the same current loading, since both the maximum phase current and N_s are identical for the two designs.

The configuration with a higher number of *pp* features a smaller h_{hoke}.

Consequently, the winding DC resistance is slightly lower. This can be inferred from N_{pp} and the conductor cross-sections values (S_{cond}), which are calculated in the following, based on the conductor's width (w_{cond}) and height (h_{cond}).

The conductor width and height are determined starting from the values of h_{slot}, w_{slot} and n_L. In particular, the thickness of the slot liner (t_l) and the one of the enamel (t_e) are 0.2 mm and 0.1 mm respectively. A spacing (s) of 0.05 mm is also considered between adjacent conductors and between the conductors and the slot walls. At the slot opening, an overlap of the liner is taken into account, as shown in the figure below.

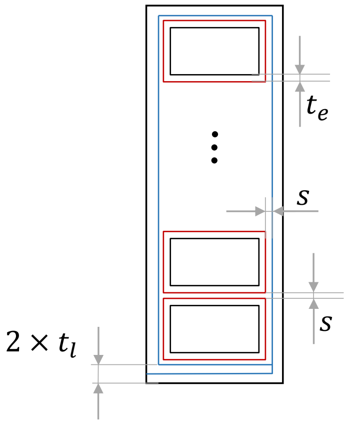

The calculated cross sections are:

Zs=72, pp=4	Zs=108, pp=6
w_{cond} x h_{cond} = 2.66 x 2.3 mm2 = **6.12 mm2**	w_{cond} x h_{cond} = 1.84 x 1.97 mm2 = **3.63 mm2**
Equivalent cross section: S_{cond} x N_{pp} = 6.12 mm2	Equivalent cross section: S_{cond} x N_{pp} = 7.26 mm2

The slot-pole combination featuring a higher number of poles has a higher equivalent cross section, which results in a lower DC resistance. Nonetheless, the conductor geometry tends to be narrower and taller, which is more critical for AC losses, especially as the fundamental frequency increases with higher *pp*.

For this purpose, a transient electromagnetic simulation is carried out for the machine with **108 slots and 6 pole pairs** operating at 10,000 rpm and 25 Nm, which represents a typical highway driving condition. Copper and aluminum windings are compared in terms of total

Joule losses and iron losses. The supplied phase current has a peak amplitude of 20 A, a frequency of 1 kHz, and a phase shift of 15° from the q-axis toward the negative d-axis.

The results are reported in the following table.

Zs = 108, pp = 6	Aluminum	Copper
Total Joule Losses [W]	301	371
Iron Losses [W]	855	854

Although aluminum produces lower Joule losses than copper due to the mitigation of AC effects, the dominant contribution still comes from iron losses, mainly because of the high electrical operating frequency. To reduce the iron losses and improve the machine efficiency under this driving condition, the operating frequency should be decreased. For this reason, the same comparison is performed for the machine with **72 slots and 4 pole pairs**, which operates at a lower electrical frequency due to the reduced number of pole pairs. The supply current amplitude and phase remain unchanged, while the electrical frequency decreases to 666.6 Hz.

The resulting losses for this slot pole combination are reported below.

Zs = 72, pp = 4	Aluminum	Copper
Total Joule Losses [W]	144	137
Iron Losses [W]	490	490

Although the iron loss is still the highest contribution, the total losses are lower for this slot pole, because of the lower operational frequency.

Consequently, it is not advantageous to design an aluminum hairpin machine from scratch with a design objective of converging toward a higher number of slots and pole pairs, which would result in operation at a higher electrical frequency. In fact, although aluminum can produce lower Joule losses than copper due to its reduced AC resistance, operating at such high frequencies significantly increases the iron losses, which remain the dominant contribution to the total losses. This is due to the fact that AC losses represent a relatively smaller portion of the overall losses.

In addition, higher operating electrical frequency are more demanding for the power electronics, which should work with higher switching frequencies for the same current waveform quality.

In contrast, a slot–pole combination with a lower number of poles is generally preferable for traction machines of utility cars, as it reduces the operating electrical frequency under the same driving conditions and therefore improves the machine efficiency.

A.2 Design with reduced electric loading. Product between electric and magnetic loading is constant.

To compensate for the increased resistivity of aluminum, one strategy could be to reduce the electric loading, which is directly proportional to the Joule losses. As the same power output is kept, the magnetic loading is proportionally increased.

For the same DC voltage limitation at a given base speed, increasing the magnetic loading of the aluminum machine design results in a lower N_s (eq. 2.15), and thus in a lower electric loading. Furthermore, based on eq. 2.16, for a given slot pole combination, and thus for a given q and pp, a lower number of N_s results in a lower n_L/N_{pp} ratio. This ratio is directly proportional to the phase DC resistance R_{ph}, as highlighted in the following equation, where the slot area S_{slot} is constant (uniquely defined by pp and q), and k_{fill} identifies the slot fill factor.

$$R_{ph} = \frac{\rho\, l_{active}}{N_{pp} S_{cond}} \propto \frac{1}{N_{pp} k_{fill} S_{slot}/n_L} \propto \frac{n_L}{N_{pp} k_{fill}} \tag{A.1}$$

This trend can be observed on the following case study, which has the same specification of the machine analyzed in the previous section, but a higher magnetic loading. Specifically, the magnetic loading B_{avg} is increased from 0.6 T to 0.72 T, and the resulting maximum allowed Ns is decreased from 72 to 60, resulting in a proportionally lower electric loading. Focusing on the slot pole combination with Z_s=72 and pp=4 (q=3), the effect of reducing N_s is seen in the following table, which compares the machine topology with N_s=72 and N_s=60.

Zs=72, pp=4 and **Ns=72 (B_{avg}=0.6 T)**	Zs=72, pp=4 and **Ns=60 (B_{avg}=0.72 T)**
n_L=6, N_{pp}=1	n_L=10, N_{pp}=2
n_L/N_{pp}=6	n_L/N_{pp}=5

As can be observed, having less series turns in a given slot pole combination leads to more conductors per slot and to more parallel paths per series, ultimately reducing the DC resistance. This reduces the equivalent conductor cross section, as can be seen in the following table:

Zs=72, pp=4 and Ns=72	Zs=72, pp=4 and Ns=60
w_{cond} x h_{cond} = 2.66 x 2.3 mm2 = **6.12 mm2**	w_{cond} x h_{cond} = 2.66 x 1.285 mm2 = **3.42 mm2**
Equivalent cross section: S_{cond} x N_{pp} = 6.12 mm2	Equivalent cross section: S_{cond} x N_{pp} = 6.84 mm2

A case study from the literature following the approach of increasing the magnetic loading for reducing the electric loading is found in [26], Design 2, where the phase current is reduced accordingly to the increase of magnetic loading, thus obtaining the same torque.

While this strategy allows to reduce the DC joule losses and mitigate the increased aluminum resistivity, it implies a higher magnetic loading, which, for a permanent magnet machine it is obtained by increasing the amount of magnets or its remanence flux density (which implies more rare-earth elements), whose environmental impact is critically high.

This vanishes the effort of adopting aluminum for sustainability purposes. In addition, a higher magnetic loading leads to higher values of flux density within the machine cores, thus increasing the iron losses, with negative implications on the machine driving cycle efficiency, as they represent the highest contribution.

For this reason, designing an aluminum machine from scratch adopting the same magnetic and electric loading is the most convenient strategy in terms of efficiency and sustainability. Furthermore, given that the highest losses contribution over typical driving cycle conditions of utility cars are given by the iron losses, which are highly sensitive to the operating frequency, it is convenient to design an aluminum machine which operates under the same operating frequency than copper, and thus, converging towards the same slot pole combinations (and thus pole pair number) as the copper solution.

Designing an aluminum machine with the same electric and magnetic loading of the copper benchmark which are currently used in automotive and operating under the same frequency range corresponds to the second scenario presented in this thesis, which deals with modifying an existing copper reference design. This explains why adopting the second scenario allows to provide valuable guidelines which are even valid for the first scenario. Specifically, when the second scenario is adopted, Strategy B is to be preferred, which consists in a drop-in replacement of the conductor material.

In fact, it allows to get weight, cost and sustainability advantages with respect to the copper machine, while having a slightly lower yet comparable efficiency over the WLTP driving cycle.

From a thermal perspective, it has been demonstrated that the increase of DC losses brought by the aluminum resistivity increase can be well managed using the same cooling system as the copper counterpart, as the resulting thermal performance under the driving cycle and at peak and continuous operations satisfies the operational requirements of traction applications.

Finally, the manufacturing feasibility is demonstrated and guidelines are provided by showcasing the complete manufacturing of two aluminum hairpin stator on a hairpin assembly line initially designed for copper.

B. Thermal Modelling

This section presents the modelling assumptions and conditions adopted for the thermal analysis described in Chapter 3, including convective heat transfer modelling, material properties, and thermal resistances. Finally, a comparison between the adopted FE model and the Ansys Motor-CAD thermal tool, based on a different modelling approach, is presented to support model validation and provide further insights.

B.1 Convective Heat Transfer

The convective heat transfer in the thermal model is applied through time-dependent profiles, mapped on the components surfaces interested by the convective heat transfer. These profiles are either HTC values or equivalent conductivity values and are calculated through semi-empirical analytical formulae, which are different depending on the modeled phenomenon:

B.1.1 Airgap heat transfer

The airgap heat transfer is modeled through an equivalent thermal conductivity, calculated as a function of the rotor surface peripheral velocity based on Taylor correlation.

This correlation determines the increase in heat transfer coefficient over that for pure conduction due to convection induced between two concentric cylinders rotating relative to each other. Specifically, the heat transfer is by pure conduction when the flow is laminar but there is an increase in heat transfer when the airgap Taylor number (Ta) increases above a critical value (i.e. $Ta = 41$) as the flow takes on a regular vortex pattern. Above a higher Ta the airgap flow becomes more turbulent and the heat transfer increases further. The Taylor number represents the ratio of centrifugal forces due to rotation to viscous forces.

Below, the Taylor number is reported, as a function of the Reynolds Number (Re) (representing the ratio between inertial and viscous forces), the airgap length (l_g), the rotor surface radius (R_rot). The Reynolds number $Re = \frac{\rho l_g v}{\mu}$ is calculated through the rotor peripheral velocity (v) (calculated from the driving cycle velocity profile), the air density (ρ) and dynamic viscosity

(μ).

$$Ta = Re\sqrt{\frac{l_g}{R_{\text{rot}}}} \tag{B.1}$$

The Taylor number is then used for calculating the Nusselt number (Nu), ultimately modeling the equivalent air thermal conductivity (k_eq), as a function of the air thermal conductivity k_air.

$$k_{eq} = \frac{Nuk_{air}}{2} \tag{B.2}$$

If Ta<41, then Nu=2 and the airgap heat transfer is purely conductive.

If 41<Ta<100, the flow takes on a vortex form and Nu is calculated as Nu=0.212 $Ta^{0.63}$ $Pr^{0.27}$.

If Ta<100, the flow becomes fully turbulent and Nu is calculated as Nu=0.386 $Ta^{0.5}$ $Pr^{0.27}$.

Pr is the Prandtl number $Pr = (\mu c_p)/k_{air}$, where c_p is the air specific heat. The Prandtl number represents the ratio between the momentum diffusivity and the thermal diffusivity. The air properties refer to a temperature of 60 °C. Finally, the heat transfer coefficient applied on the cylindrical outer surface of the rotor and on the cylindrical inner surface of the teeth is calculated as $h = k_{eq}/l_g$, where l_g is the airgap length.

B.1.2 Water Jacket Coolant Heat Transfer

The presence of the coolant flow in the water jacket is accounted in the thermal model through a heat transfer coefficient profile mapped on the water jacket walls.

As the coolant (EWG50/50) flow rate is steady (equal to 10 l/min), the heat transfer coefficient is constant for the whole driving cycle duration. However, the heat transfer coefficient is not homogeneous in space. The value of the heat transfer coefficient in correspondence of each point of the walls of the water jacket is calculated as a function of the coolant velocity in that point through correlations including the Nusselt number and Prandtl number of the coolant.

The coolant velocity field is calculated in a separated CFD simulation carried out on Particleworks simulation tool, which is based on a lagrangian approach as it discretize the fluid with small particles, each of which has its own velocity. Specifically, the heat transfer coefficient in each wall point is calculated from the velocity of the particle close to the point.

Below, the correlations used for calculating the Nusselt number are reported. The used correlations refer to flows in rectangular ducts and depend on the flow regime, which is indicated by the particle Reynolds number ($Re = (\rho D_h v)/\mu$ where D_h=4A/P is the hydraulic diameter of the water jacket channel, calculated through its cross-sectional area and perimeter, while ρ, μ, v are the fluid density, dynamic viscosity and particle velocity, respectively).

If the flow is laminar (Re<2300), then

$$\begin{aligned} Nu = 7.49 - 17.02\frac{H}{W} + 22.43\left(\frac{H}{W}\right)^2 - 9.94\left(\frac{H}{W}\right)^3 \\ + \frac{0.065\frac{D_h}{L}Re\,Pr}{1 + 0.04\left(\frac{D_h}{L}Re\,Pr\right)^{2/3}} \end{aligned} \tag{B.3}$$

where H and W are the channel height and width. If the flow is turbulent (Re>3000), then (Gnielinski's formula)

$$Nu = (f/8)(Re - 1000)Pr/[1 + 12.7(f/8)^{0.5}(Pr^{2/3} - 1)] \tag{B.4}$$

where $f = [0.790Ln(Re) - 1.64]^{-2}$ is the friction factor.

If the flow is transitional (2300<Re<3000), then the Nu is calculated from a linear interpolation between the maximum Nu calculated in laminar flow and the minimum calculated in turbulent flow conditions. Pr is the Prandtl number referring to the coolant properties, referring to 65 °C, which is the average temperature over the driving cycle of the coolant, as preliminary calculated through Motor-CAD.

B.1.3 Heat Transfer Coefficient on End Windings

The heat transfer between the end windings and the surrounding air in the machine end space is modeled through heat transfer coefficient. As the heat transfer depends on the velocity of the air, which depends upon the rotation of the rotor, the heat transfer coefficients are time-dependent, and are calculated based on the driving cycle velocity profile. For modeling the local air velocity differences in different regions of the end space, the local velocity value [vel] is calculated by multiplying the reference rotor peripheral velocity by a multiplying factor (from 0 to 1). The local velocity value (vel) is then used for calculating the heat transfer coefficient (h) as follows (Scubert correlation):

$$h = 15(1 + 0.4vel^{0.9}). \tag{B.5}$$

If the vel is zero, then the heat transfer coefficient is that of still air. In the FEM model, a multiplier factor of 1 is used for the internal faces of the first end winding (facing the airgap). For the frontal surfaces of the end winding, facing the end plates of the housing, a 0.7 multiplier is used. Finally, for the outermost surfaces of the last end winding, a 0.2 multiplier is adopted.

B.2 Material Properties, Slot Thermal Conductivity and Contact Resistances

The thermal properties of the materials used in the thermal model are specified in the following table:

Material	**Thermal Conductivity [W/m K]**	**Specific Thermal Capacity [J/kg K]**	**Density [kg/m3]**
Steel	16.27	502.48	8030
Magnets	7.6	460	7500
Iron	30	460	7650
Impregnation	0.9	300	1050
Copper	387.6	381	8978
Aluminum (winding)	236.5	895	2699
Aluminum (case)	180	963	2950

The slot liner and conductors' enamel are modeled through contact resistances applied on the slot walls and conductor active part walls. This approach allows to accurately model the in-slot heat transfer while avoiding to create their geometric entity, which would require a very fine mesh due to their small thickness (0.2 mm for the slot liner and 0.1 mm for the enamel), and thus, higher computational cost. The specific thermal resistance applied on the above-mentioned surfaces is calculated as: $R = t/k$ [(m^2 K)/W], where t is the material thickness

Interface	**Gap [mm]**
Stator Lamination – Housing	0.003
Magnet – Rotor Lamination	0.005
Rotor Lamination - Shaft	0.005
Bearing – Shaft	0.0112
Bearing – End Cap	0.0073

and k is the thermal conductivity (0.2 [W/m K] for the slot liner and 0.22 [W/m K] for the conductor enamel). Finally, the table below summarizes the gap used in the contact thermal resistances calculation, which are calculated with the same formulation used above, considering t=effective gap and k=air thermal conductivity.

B.3 Comparison between FE and Lumped Parameter Thermal Network Modelling

In the following, the comparison between the FE model adopted in this thesis and the Ansys Motor-CAD thermal tool is reported, for the thermal driving cycle analysis.

The main difference between the two tools is the modeling approach. In Ansys Fluent, a thermal finite-element analysis is performed, which solves the thermal conduction equations for each mesh element, while the conductive heat transfer is modeled on the relevant surfaces by applying on them heat transfer coefficients. The heat transfer coefficients are calculated from the convective fluid velocity field, which is either imposed or calculated through a CFD software, such as Particle-works used in the for modeling the water jacket flow.

In Motor-CAD, a thermal network model is used, where the different motor components are modeled through a lumped parameter thermal network (LPTN). The main advantage of a FEM model is its ability to accurately capture the formation of local hotspots and accurate gradients inside the machine components, while accounting for the actual machine geometry. In contrast, lumped parameter models are often preferred because they provide sufficiently accurate results while requiring significantly lower computational effort and enabling faster simulations.

The motor is divided into thermal nodes representing the main motor components and each node is connected by thermal resistances modeling the heat transfer (conductive, convective and radiative). The losses are the heat generation inputs connected to the thermal nodes generating those losses.

The machine model (radial and axial geometry) and the corresponding thermal network are shown below. For each component, the same color code is used for both the thermal network and the model geometry. The thermal capacitance is included in the nodes (circles), calculated based on the material specific heat capacity and the component volume. The resistance is included in the rectangular elements of the circuit, while the white squared elements represent the contact resistances between two motor components which are in contact, modeled through the gap at the interface. The thermal source for each component generating losses are the elements represented by two partially superimposed circles.

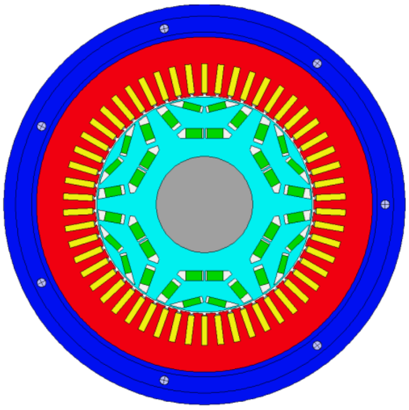

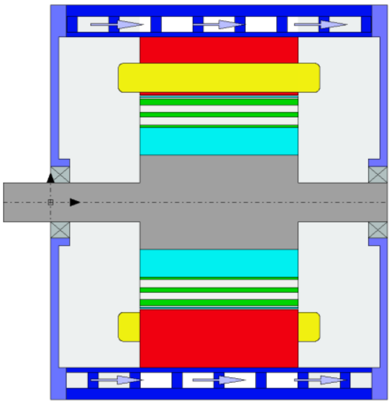

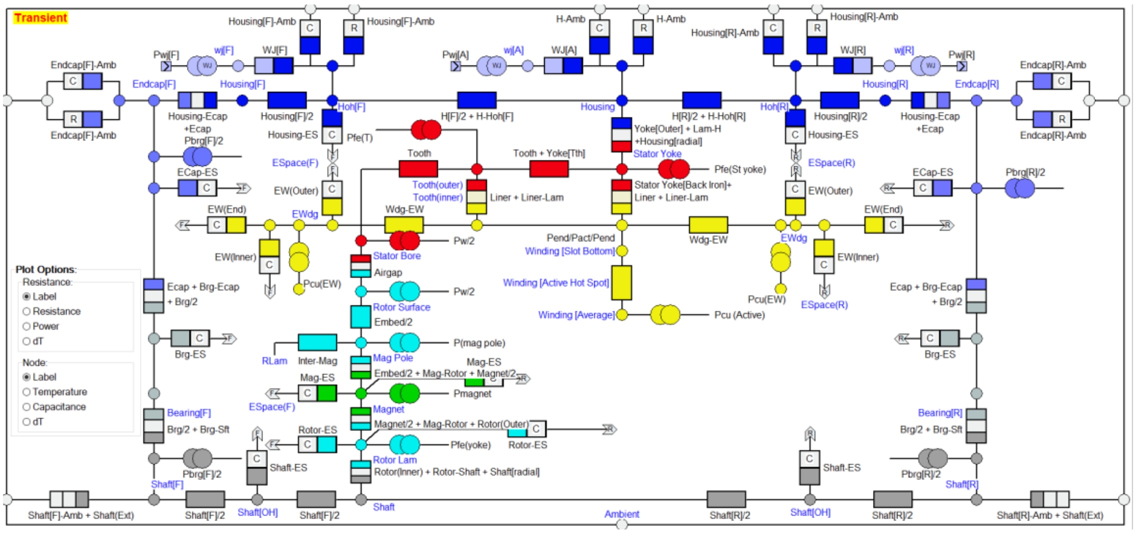

Plot Options:
Resistance:
● Label
○ Resistance
○ Power
○ dT
Node:
● Label
○ Temperature
○ Capacitance
○ dT

The same machine model (same geometry) and same operating conditions (of both the machine and the cooling circuit) are used in the two compared tools. The results of the comparison are shown in the following figures.

The LPTN provides a conservative estimation of temperature compared to FEM, primarily due to simplified thermal resistances and lumped parameter assumptions on the temperature

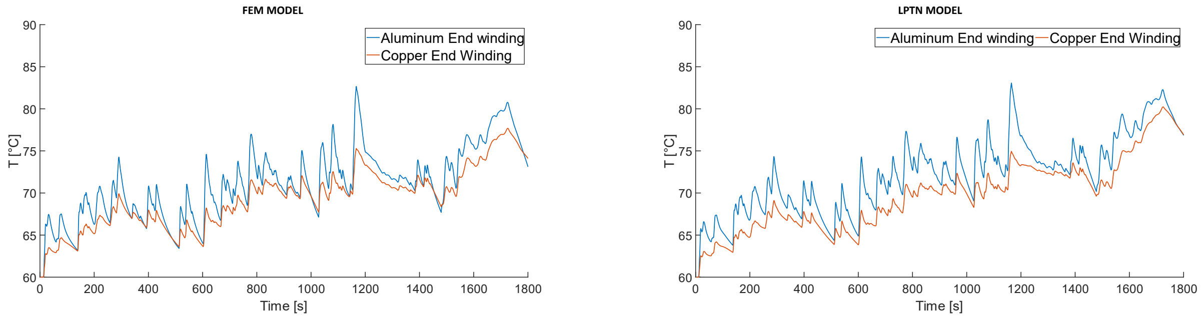

(a)

(b)

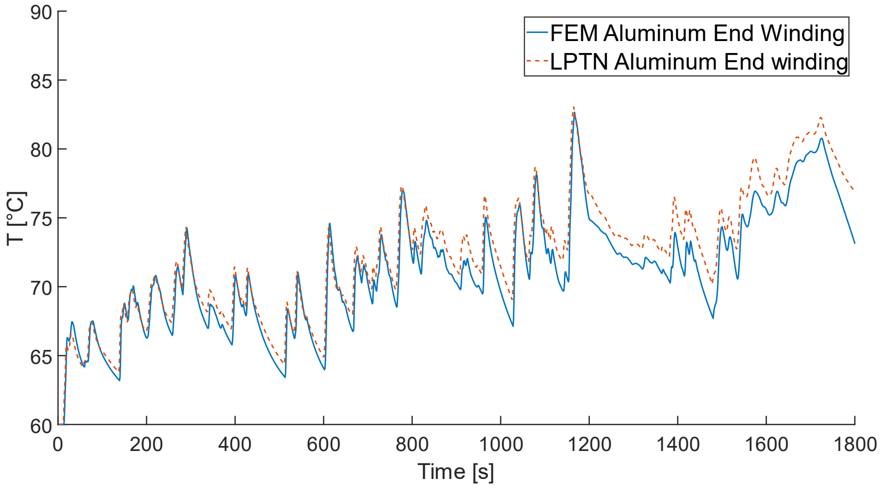

and capacitance in each component, while FEM captures spatial heat transfer more accurately. Meanwhile, as the trend and the temperature values show a good match (maximum temperature difference is below 3°C), the models validate each other.

The low computational burden of the LPTN could be exploited to extend the simulation time window up to reaching a relative steady-state in the driving cycle, thus performing a check on the maximum temperature values when the average temperature of each component remains constant over the driving cycle.

This can be done by periodically repeating the driving cycles, although this scenario would rarely happen in reality.

For the sake of completeness and for comparing copper and aluminum, a simulation performed on Motor-CAD over 4 driving cycles which repeat periodically is performed. The overall time window is sufficient for reaching the relative steady-state

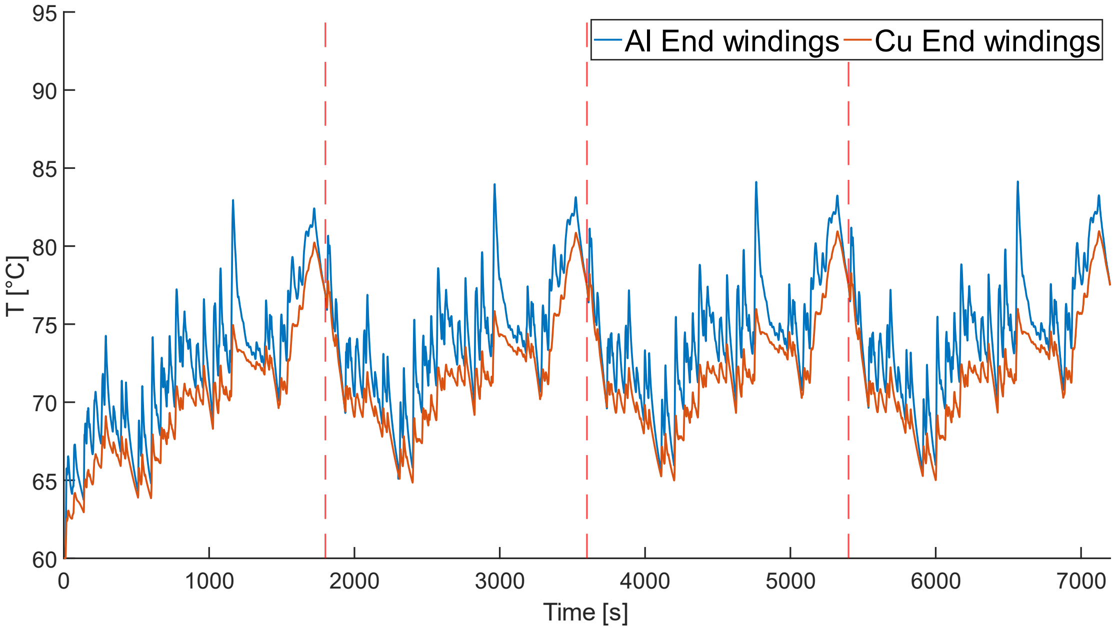

As it can be seen, the maximum temperature which is reached in the relative steady state condition is practically the same as that reached when simulating one driving cycle. The maximum temperature limit is well below the insulation thermal limit.

C. Clarification on how the voltage probe terminals have been placed on the welding spots of the prototype.

This section explains through an example how the voltage probe terminals have been placed on the welding spots of the prototype. The example refers to the experimental setup while configuration 1432 is tested.

As seen in the winding diagram below, in this configuration, 1F, 2F and MAX locations are as follows:

- 1F : It is in slot 27, between the 5th and the 4th conductor layer.
- 2F : It is in slot 51, between the 3rd and the 2nd conductor layer.
- MAX : It is in slot 64, between the 3rd and the 2nd conductor layer.

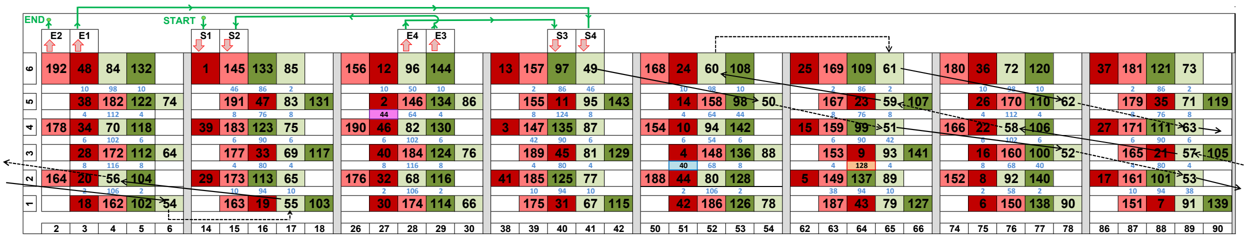

For understanding how to place the voltage probe terminals on the welding spot terminations, a magnification of the stator is reported in the figure below.

Specifically, we can distinguish three crowns of welding spots. The first crown (R1) is at the outermost radius and is made up by the welding spots joining the sixth conductor layers of the slot with the fifth ones. The second crown (R2) is at the middle radius, made up by the welding spots between the fourth and third conductor layers. The third crown (R3) is the innermost radius, whose welding spots join the second and the first layers.

As the first crown is the outermost, it is easy to understand in which slot number its conductors are, because the sixth conductor layer in the slot (i.e., the one with the biggest section) is the

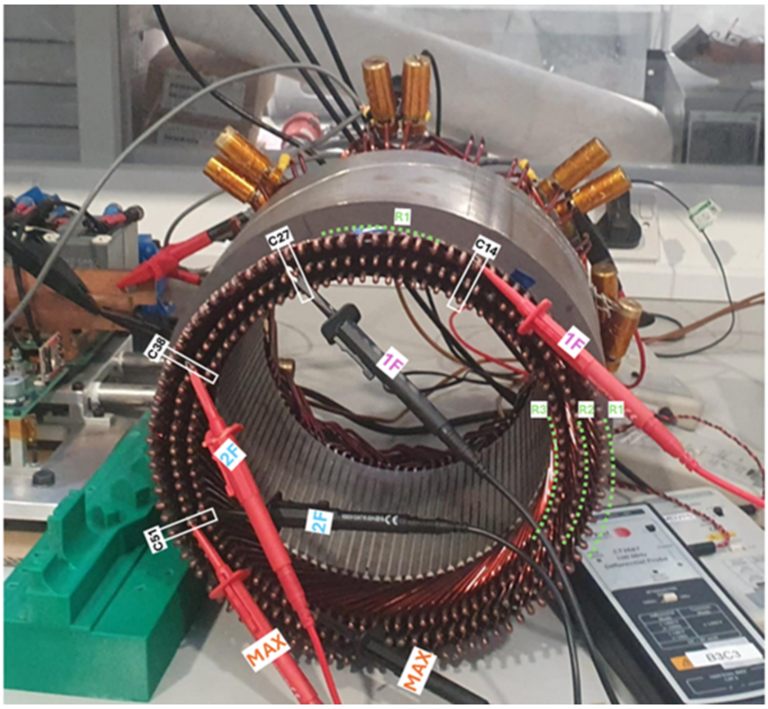

outermost, and easily detectable.

Based on this, the circumferential location of welding spot of R1 can be numbered according to the specific slot number. For instance, the welding spot on the first crown (R1), which has the sixth conductor layer of slot 14 is called "location C14 on the first crown (R1)". In general, Cx on R1 has the sixth conductor layer of slot x.

C14 on R1 joins the sixth conductor layer of slot 14 with its subsequent conductor in the series, which according to the winding diagram is the fifth conductor layer of slot 27.

This nomenclature is also extended to the welding spots of the second and third crown, as the circumferential location of each welding spot on these crowns can be referred to the circumferential location of the welding spot on the first crown, because they lie on the same radius.

This means that the circumferential location C14 makes us identify the even conductor layers of slot 14. Specifically, the 6th conductor layer of slot 14 is on C14 R1, the 4th conductor layer of slot 14 is on C14 R2, and the 2nd conductor layer of 14 is on C14 R3.

For identifying the odd conductor layers of each slot, it is sufficient to trace back their precedent conductors in the series, which, because of the transposition method adopted in the winding diagram, belong to an even conductor layer of another slot. For example, the 5th conductor layer of slot 27 is identified by tracing back on its precedent conductor in the series, which according to the winding diagram is the 6th conductor of slot 14, which we know is on C14 R1.

According to this explanation, the location 1F, 2F and MAX in the winding diagram can be identified on the welding spots as follows:

Table 37: Measurement points on winding diagram and welding spots

	On the winding diagram	**On the welding spots**
1F	between 5th and 4th of slot 27	High on R1 C14 – Low on R2 C27
2F	between 3rd and 2nd of slot 51	High on R2 C38 – Low on R3 C51
MAX	between 3rd and 2nd of slot 64	High on R2 C51 – Low on R3 C64

Bibliography

[1] M. Ge, J. Friedrich, and L. Vigna, *Where do emissions come from? 4 charts explain greenhouse gas emissions by sector*, `https://www.wri.org/insights/4-charts-explain-greenhouse-gas-emissions-countries-and-sectors`, Accessed: 2025-11-13, 2024.

[2] D. Barater, M. D. Nardo, T. Zou, and S. Nategh, «Guest editorial: High sustainable electric drives for transportation electrification», *IEEE Journal of Emerging and Selected Topics in Industrial Electronics*, vol. 6, no. 3, pp. 861–863, 2025. DOI: `10.1109/JESTIE.2025.3573052`.

[3] I. Petrov, M. Niemelä, P. Ponomarev, and J. Pyrhönen, «Rotor surface ferrite permanent magnets in electrical machines: Advantages and limitations», *IEEE Transactions on Industrial Electronics*, vol. 64, no. 7, pp. 5314–5322, 2017. DOI: `10.1109/TIE.2017.2677320`.

[4] R. Wilson, P. Kumar, and A. El-Refaie, «Analysis of reduced rare earth pm-assisted synchronous reluctance motor enabled with iron nitride for high-speed traction application», in *2025 IEEE International Electric Machines Drives Conference (IEMDC)*, 2025, pp. 1105–1110. DOI: `10.1109/IEMDC60492.2025.11061171`.

[5] M. Murataliyev, M. Degano, M. Di Nardo, N. Bianchi, and C. Gerada, «Synchronous reluctance machines: A comprehensive review and technology comparison», *Proceedings of the IEEE*, vol. 110, no. 3, pp. 382–399, 2022. DOI: `10.1109/JPROC.2022.3145662`.

[6] S. Mafrici, V. Madonna, C. Maria Meano, K. Friis Hansen, and A. Tenconi, «Switched reluctance machine for transportation and eco-design: A life cycle assessment», *IEEE Access*, vol. 12, pp. 68 334–68 344, 2024. DOI: `10.1109/ACCESS.2024.3400324`.

[7] G. Petrelli, S. Nuzzo, T. Zou, D. Barater, G. Franceschini, and C. Gerada, «Review and future developments of wound field synchronous motors in automotive», in *2023 IEEE International Conference on Electrical Systems for Aircraft, Railway, Ship Propulsion and Road Vehicles International Transportation Electrification Conference (ESARS-ITEC)*, 2023, pp. 1–6. DOI: `10.1109/ESARS-ITEC57127.2023.10114826`.

[8] A. Bindra, «Wide-bandgap-based power devices: Reshaping the power electronics landscape», *IEEE Power Electronics Magazine*, vol. 2, no. 1, pp. 42–47, 2015. DOI: `10.1109/MPEL.2014.2382195`.

[9] M. Alatalo, S. T. Lundmark, and E. A. Grunditz, «Electric machine design for traction applications considering recycling aspects-review and new solution», in *IECON 2011 - 37th Annual Conference of the IEEE Industrial Electronics Society*, 2011, pp. 1836–1841. DOI: `10.1109/IECON.2011.6119585`.

[10] E. Kasagga and A. EL-Refaie, «Recyclable electrical machine designs: Current approaches and perspectives», in *2024 International Conference on Electrical Machines (ICEM)*, 2024, pp. 1–7. DOI: `10.1109/ICEM60801.2024.10700498`.

[11] J. D. Widmer, R. Martin, and B. C. Mecrow, «Precompressed and stranded aluminum motor windings for traction motors», *IEEE Transactions on Industry Applications*, vol. 52, no. 3, pp. 2215–2223, 2016. DOI: `10.1109/TIA.2016.2528226`.

[12] *London metal exchange*, `https://www.lme.com/`, [Online; accessed 1-Dec-2025].

[13] *Idemat – calculation rules*, `https://www.ecocostsvalue.com/data-tools-books/idemat-calculation-rules/`, [Online; accessed 1-Dec-2025].

[14] A. Rassõlkin, A. Kallaste, S. Orlova, L. Gevorkov, T. Vaimann, and A. Belahcen, «Re-use and recycling of different electrical machines», *Latvian Journal of Physics and Technical Sciences*, vol. 55, Sep. 2018. DOI: `10.2478/lpts-2018-0025`.

[15] M. Pastura, D. Barater, S. Nuzzo, and G. Franceschini, «Investigation of resistivity impact on ac losses in hairpin conductors», in *IECON 2021 – 47th Annual Conference of the IEEE Industrial Electronics Society*, 2021, pp. 1–6.

[16] J. Pyrhönen, T. Jokinen, and V. Hrabovcová, *Design of Rotating Electrical Machines*, 2nd. John Wiley Sons, 2014, pp. 256–267.

[17] G. Cutuli, S. Nuzzo, T. Zou, G. Franceschini, C. Gerada, and D. Barater, «Multi-objective optimizations of copper and aluminum hairpin windings: A comparison», in *2023 IEEE Energy Conversion Congress and Exposition (ECCE)*, 2023, pp. 3796–3801.

[18] J. Pyrhönen, T. Jokinen, and V. Hrabovcová, *Design of Rotating Electrical Machines*, 2nd. John Wiley Sons, 2014, pp. 281–288.

[19] T. Zou et al., «A comprehensive design guideline of hairpin windings for high power density electric vehicle traction motors», *IEEE Transactions on Transportation Electrification*, vol. 8, no. 3, pp. 3578–3593, 2022.

[20] G. Pellegrino, T. M. Jahns, N. Bianchi, W. L. Soong, and F. Cupertino, *The Rediscovery of Synchronous Reluctance and Ferrite Permanent Magnet Motors: Tutorial Course Notes*. Cham: Springer, 2016, p. 126, ISBN: 978-3-319-32202-5. DOI: `10.1007/978-3-319-32202-5`.

[21] M. Pastura, R. Notari, S. Nuzzo, D. Barater, and G. Franceschini, «On the ac losses in the end conductors of hairpin windings», in *2022 International Conference on Electrical Machines (ICEM)*, 2022, pp. 1150–1155.

[22] United Nations Economic Commission for Europe, «Global technical regulation no. 15: Worldwide harmonized light-duty vehicles test procedure (wltp)», UNECE, Tech. Rep., 2014.

[23] Z. Shi et al., «Design optimization of a spoke-type axial-flux pm machine for in-wheel drive operation», *IEEE Transactions on Transportation Electrification*, vol. 10, no. 2, pp. 3770–3781, 2024. DOI: `10.1109/TTE.2023.3310738`.

[24] G. Petrelli, S. Nuzzo, D. Barater, T. Zou, G. Franceschini, and C. Gerada, «Preliminary sensitivity analysis and optimisation of a wound field synchronous motor for traction applications», in *2023 AEIT International Conference on Electrical and Electronic Technologies for Automotive (AEIT AUTOMOTIVE)*, 2023, pp. 1–6. DOI: `10.23919/AEITAUTOMOTIVE58986.2023.10217237`.

[25] APC UK, *Roadmaps*, APC UK Knowledge Base, Online, [Accessed: Dec. 12, 2025]. [Online]. Available: `https://www.apcuk.co.uk/knowledge-base/roadmaps/`.

[26] A. Acquaviva, M. Diana, B. Raghuraman, L. Petersson, and S. Nategh, «Sustainability aspects of electrical machines for e-mobility applications part ii: Aluminium hairpin vs. copper hairpin», in *IECON 2021 – 47th Annual Conference of the IEEE Industrial Electronics Society*, 2021, pp. 1–6. DOI: `10.1109/IECON48115.2021.9589649`.

[27] M. Raimondo, G. Cutuli, S. Nuzzo, and D. Barater, «Assessing thermal and efficiency aspects of aluminum hairpin motors in passenger cars», in *2024 International Conference on Electrical Machines (ICEM)*, 2024, pp. 1–7. DOI: `10.1109/ICEM60801.2024.10700377`.

[28] B. De Silva Guruwatta Vidanalage, Z. Li, A. Lombardi, and N. C. Kar, «A novel winding design for ev traction motors: Hybrid hairpin winding layout containing both copper and aluminum windings», in *2024 IEEE International Magnetic Conference (INTERMAG)*, 2024, pp. 1–6. DOI: `10.1109/INTERMAG56625.2024.10830469`.

[29] G. Petrelli, S. Nuzzo, T. Zou, G. Cutuli, D. Barater, and C. Gerada, «On comparing aluminum and copper in wound field synchronous motors for traction applications», in *2024 International Conference on Electrical Machines (ICEM)*, 2024, pp. 1–7. DOI: `10.1109/ICEM60801.2024.10700570`.

[30] A. Gneiting, F. Burkard, and N. Parspour, «Performance evaluation of aluminum and copper windings in electrically excited synchronous machines considering drive cycle efficiency and maximum continuous power», in *2025 IEEE International Electric*

Machines Drives Conference (IEMDC), 2025, pp. 1117–1122. DOI: `10.1109/IEMDC60492.2025.11060993`.

[31] G. Petrelli et al., «Comparison of aluminium and copper conductors in hairpin winding design for high power density traction motors», in *2022 International Conference on Electrical Machines (ICEM)*, 2022, pp. 1635–1641. DOI: `10.1109/ICEM51905.2022.9910796`.

[32] G. Cutuli, S. Nuzzo, D. Barater, T. Zou, S. Nategh, and T. Bertoncello, «Replacing copper with aluminum in hairpin windings motors intended for utility cars», *IEEE Journal of Emerging and Selected Topics in Industrial Electronics*, vol. 6, no. 3, pp. 864–876, 2025. DOI: `10.1109/JESTIE.2025.3546030`.

[33] J. Pyrhönen, T. Jokinen, and V. Hrabovcová, *Design of Rotating Electrical Machines*, 2nd. John Wiley Sons, 2014, pp. 63–71.

[34] G. Venturini, M. Carbonieri, L. Di Leonardo, and M. Popescu, «Hairpin windings for traction machines: Analysis and comparison», in *International Conference on Electrical Machines (ICEM)*, 2022, pp. 1655–1661. DOI: `10.1109/ICEM51905.2022.9910905`.

[35] R.-J. Wang and M. Kamper, «Evaluation of drive cycle-based traction motor design strategies using gradient optimisation», *Energies*, vol. 15, no. 3, p. 1095, 2022. DOI: `10.3390/en15031095`.

[36] G. Pellegrino, T. G. Jokinen, N. Bianchi, V.-M. Rissanen, and F. Cupertino, *The Rediscovery of Synchronous Reluctance and Ferrite Permanent Magnet Motors: Tutorial Course Notes* (Springer Briefs in Electrical and Computer Engineering). Springer, 2016.

[37] M. Di Nardo, M. Galea, C. Gerada, M. Palmieri, and F. Cupertino, «Multi-physics optimization strategies for high speed synchronous reluctance machines», in *2015 IEEE Energy Conversion Congress and Exposition (ECCE)*, 2015, pp. 2813–2820. DOI: `10.1109/ECCE.2015.7310054`.

[38] X. Sun, Z. Shi, G. Lei, Y. Guo, and J. Zhu, «Multi-objective design optimization of an ipmsm based on multilevel strategy», *IEEE Transactions on Industrial Electronics*, vol. 68, no. 1, pp. 139–148, 2021. DOI: `10.1109/TIE.2020.2965463`.

[39] N. Sarma, M. C. Kulan, and N. J. Baker, «A comprehensive review of thermal conductivity of stator windings in electric machines», *IEEE Access*, vol. 13, pp. 152 493–152 518, 2025. DOI: `10.1109/ACCESS.2025.3604580`.

[40] S. La Rocca et al., «Numerical study of the impact of different cooling arrangements on a high length/diameter ratio motor for electric commercial vehicle», in *2019 International Conference on Electrotechnical Complexes and Systems (ICOECS)*, 2019, pp. 1–5. DOI: `10.1109/ICOECS46375.2019.8949929`.

[41] G. Cutuli, D. Barater, S. Nategh, D. Ericsson, and M. Törmänen, «Aluminum hairpin solution for electrical machines in e-mobility applications : Part ii:thermal and cooling aspects», in *2022 International Conference on Electrical Machines (ICEM)*, 2022, pp. 511–517. DOI: `10.1109/ICEM51905.2022.9910683`.

[42] D. P. Kulkarni, G. Rupertus, and E. Chen, «Experimental investigation of contact resistance for water cooled jacket for electric motors and generators», *IEEE Transactions on Energy Conversion*, vol. 27, no. 1, pp. 204–210, 2012. DOI: `10.1109/TEC.2011.2177465`.

[43] S. Koshizuka and Y. Oka, «Moving-particle semi-implicit method for fragmentation of incompressible fluid», *Nuclear science and engineering*, vol. 123, no. 3, pp. 421–434, 1996.

[44] M. A. Sohail, Y. Chao, M. Husain, and R. ullah, «Detached eddy simulations an economical tool for cfd», in *Proceedings of 2012 9th International Bhurban Conference on Applied Sciences Technology (IBCAST)*, 2012, pp. 300–307. DOI: `10.1109/IBCAST.2012.6177569`.

[45] S. Nategh, «Thermal analysis and management of high-performance electrical machines», Ph.D. dissertation, KTH Royal Institute of Technology, 2013.

[46] V. Gnielinski, «New equations for heat and mass transfer in turbulent pipe and channel flow», *Int. Chem. Eng*, vol. 16, no. 2, pp. 359–368, 1976.

[47] D. Staton, A. Boglietti, and A. Cavagnino, «Solving the more difficult aspects of electric motor thermal analysis in small and medium size industrial induction motors», *IEEE Transactions on Energy Conversion*, vol. 20, no. 3, pp. 620–628, 2005. DOI: `10.1109/TEC.2005.847979`.

[48] S. Nategh, O. Wallmark, M. Leksell, and S. Zhao, «Thermal analysis of a pmasrm using partial fea and lumped parameter modeling», *IEEE Transactions on Energy Conversion*, vol. 27, no. 2, pp. 477–488, 2012. DOI: `10.1109/TEC.2012.2188295`.

[49] F. Hoffmann, B. Jux, and M. Doppelbauer, «Thermal modeling of the stator slot in electrical machines using an extended layer approach», in *IECON 2019 - 45th Annual Conference of the IEEE Industrial Electronics Society*, vol. 1, 2019, pp. 1405–1410. DOI: `10.1109/IECON.2019.8927002`.

[50] C. Zhao, H. Zhao, J. Li, X. Zhang, Y. Ruan, and H. Wang, «Aluminum windings and their manufacturing technologies in electrical machines: A review», in *2024 27th International Conference on Electrical Machines and Systems (ICEMS)*, 2024, pp. 1523–1530. DOI: `10.23919/ICEMS60997.2024.10921067`.

[51] A. Marfoli, M. D. Nardo, M. Degano, C. Gerada, and W. Jara, «Squirrel cage induction motor: A design-based comparison between aluminium and copper cages», *IEEE Open Journal of Industry Applications*, vol. 2, pp. 110–120, 2021. DOI: `10.1109/OJIA.2021.3073820`.

[52] M. Gröninger, F. Horch, A. Kock, M. Jakob, and B. Ponick, «Cast coils for electrical machines and their application in automotive and industrial drive systems», in *2014 4th International Electric Drives Production Conference (EDPC)*, 2014, pp. 1–7. DOI: `10.1109/EDPC.2014.6984384`.

[53] Y. Yamada, H. Sugimoto, and K. Imae, «Design of high slot fill aluminum winding in a permanent magnet synchronous machine with reduced winding loss», *IEEE Transactions on Industry Applications*, vol. 59, no. 2, pp. 1437–1445, 2023. DOI: `10.1109/TIA.2023.3240991`.

[54] R. Notari, S. Nuzzo, F. Savi, S. Defanti, and D. Barater, «An asymmetrical additively manufactured hairpin winding for increased efficiency and sustainability», *IEEE Transactions on Transportation Electrification*, vol. 10, no. 4, pp. 9529–9538, 2024. DOI: `10.1109/TTE.2024.3374515`.

[55] A. Selema, M. N. Ibrahim, and P. Sergeant, «Additively manufactured ultralight shaped-profile windings for hf electrical machines and weight-sensitive applications», *IEEE Transactions on Transportation Electrification*, vol. 8, no. 4, pp. 4313–4324, 2022. DOI: `10.1109/TTE.2022.3173126`.

[56] F. Wu, A. M. EL-Refaie, and A. Al-Qarni, «Additively manufactured hollow conductors integrated with heat pipes: Design tradeoffs and hardware demonstration», *IEEE Transactions on Industry Applications*, vol. 57, no. 4, pp. 3632–3642, 2021. DOI: `10.1109/TIA.2021.3076423`.

[57] J. Van Damme, H. Vansompel, and G. Crevecoeur, «Anodized aluminum foil winding axial flux machine for direct-drive robotic applications», *IEEE Transactions on Industrial Electronics*, vol. 70, no. 10, pp. 10 409–10 419, 2023. DOI: `10.1109/TIE.2022.3220894`.

[58] J. D. Widmer, C. M. Spargo, G. J. Atkinson, and B. C. Mecrow, «Solar plane propulsion motors with precompressed aluminum stator windings», *IEEE Transactions on Energy Conversion*, vol. 29, no. 3, pp. 681–688, 2014. DOI: `10.1109/TEC.2014.2313642`.

[59] J. D. Widmer, R. Martin, and B. C. Mecrow, «Precompressed and stranded aluminum motor windings for traction motors», *IEEE Transactions on Industry Applications*, vol. 52, no. 3, pp. 2215–2223, 2016. DOI: `10.1109/TIA.2016.2528226`.

[60] R. Wrobel, N. Simpson, P. H. Mellor, J. Goss, and D. A. Staton, «Design of a brushless pm starter-generator for low-cost manufacture and a high-aspect-ratio mechanical space envelope», in *2015 IEEE Energy Conversion Congress and Exposition (ECCE)*, 2015, pp. 813–820. DOI: `10.1109/ECCE.2015.7309773`.

[61] S. G. Barbieri, V. Mangeruga, M. Giacopini, and S. Mantovani, «Structural analysis of the forming process for hairpin windings for electric motor applications: Torsional-flexural instability issues», in *2022 International Conference on Electrical Machines (ICEM)*, pp. 1137–1143. DOI: `10.1109/ICEM51905.2022.9910827`.

[62] V. Mangeruga, S. G. Barbieri, M. Giacopini, F. Giuradei, P. Vai, and C. Gerada, «Investigation on the torsional–flexural instability phenomena during the bending process of hairpin windings: Experimental tests and fe model validation», 6, vol. 12, 2024. DOI: `10.3390/machines12060396`. [Online]. Available: `https://www.mdpi.com/2075-1702/12/6/396`.

[63] P. S. e. a. Ghahfarokhi, «Hairpin windings manufacturing, design, and ac losses analysis approaches for electric vehicle motors», in *2021 11th International Electric Drives Production Conference (EDPC)*, pp. 1–7. DOI: `10.1109/EDPC53547.2021.9684208`.

[64] M. Weigelt, A. Riedel, M. Masuch, A. Mahr, T. Gläßel, and J. Franke, «Potentials of an explicit finite element analysis of the bending processes for coated copper wires», in *2017 7th International Electric Drives Production Conference (EDPC)*, 2017, pp. 1–5. DOI: `10.1109/EDPC.2017.8328151`.

[65] T. Glaessel, D. B. Pinhal, M. Masuch, D. Gerling, and J. Franke, «Manufacturing influences on the motor performance of traction drives with hairpin winding», in *2019 9th International Electric Drives Production Conference (EDPC)*, 2019, pp. 1–8. DOI: `10.1109/EDPC48408.2019.9011872`.

[66] A. Riedel et al., «Challenges of the hairpin technology for production techniques», in *2018 21st International Conference on Electrical Machines and Systems (ICEMS)*, 2018, pp. 2471–2476. DOI: `10.23919/ICEMS.2018.8549105`.

[67] BMW Group Corporate Communications, *BMW Group Prototype Production E-Drivetrains: Scene 1 of 6: E-Drive Component*, `https://www.press.bmwgroup.com/global/tv-footage/detail/PF0005720/bmw-group-prototype-production-e-drivetrains/5`, Accessed: 2025-20-12.

[68] N. Trahair, *Flexural-Torsional Buckling of Structures (1st ed.)* CRC Press, 1993. [Online]. Available: `https://doi.org/10.1201/9780203755938`.

[69] O. Belluzzi, *Scienza delle costruzioni* (Scienza delle costruzioni v. 3). N. Zanichelli, 1961. [Online]. Available: `https://books.google.it/books?id=YG6bfQSncSMC`.

[70] A. Udabe, I. Baraia-Etxaburu, and D. G. Diez, «Gallium nitride power devices: A state of the art review», *IEEE Access*, vol. 11, pp. 48 628–48 650, 2023. DOI: `10.1109/ACCESS.2023.3277200`.

[71] B. Shi et al., «A review of silicon carbide mosfets in electrified vehicles: Application, challenges, and future development», *IET Power Electronics*, vol. 16, no. 12, pp. 2103–2120, 2023. DOI: `https://doi.org/10.1049/pel2.12524`. eprint: `https://ietresearch.onlinelibrary.wiley.com/doi/pdf/10.1049/pel2.12524`. [Online]. Available: `https://ietresearch.onlinelibrary.wiley.com/doi/abs/10.1049/pel2.12524`.

[72] S. S. Vala, A. B. Mirza, A. I. Emon, and F. Luo, «A review of partial discharge in stator winding of rotating machines fed by voltage source pwm motor drives», *IEEE Transactions on Industry Applications*, vol. 60, no. 3, pp. 3790–3807, 2024. DOI: `10.1109/TIA.2024.3356488`.

[73] M. Diab, W. Zhou, C. Emersic, X. Yuan, and I. Cotton, «Impact of pwm voltage waveforms on magnet wire insulation partial discharge in sic-based motor drives», *IEEE Access*, vol. 9, pp. 156 599–156 612, 2021. DOI: `10.1109/ACCESS.2021.3129266`.

[74] H. Kim, A. Anurag, S. Acharya, and S. Bhattacharya, «Analytical study of sic mosfet based inverter output dv/dt mitigation and loss comparison with a passive dv/dt filter for high frequency motor drive applications», *IEEE Access*, vol. 9, pp. 15 228–15 238, 2021. DOI: `10.1109/ACCESS.2021.3053198`.

[75] S. Zhao, X. Zhao, Y. Wei, Y. Zhao, and H. A. Mantooth, «A review of switching slew rate control for silicon carbide devices using active gate drivers», *IEEE Journal of Emerging and Selected Topics in Power Electronics*, vol. 9, no. 4, pp. 4096–4114, 2021. DOI: `10.1109/JESTPE.2020.3008344`.

[76] W. Zhou, X. Yuan, and Z. Zhang, «An active dv/dt filter to combat motor terminal overvoltage in sic-based adjustable speed drives», *IEEE Transactions on Industrial Electronics*, vol. 72, no. 1, pp. 1076–1081, 2025. DOI: `10.1109/TIE.2024.3406874`.

[77] T. Lackie, Y. Jiang, L. Shillaber, and T. Long, «Motor overvoltage mitigation by active cancellation of reflections using parallel sic devices with a coupled inductor», *IEEE Transactions on Power Electronics*, vol. 38, no. 9, pp. 11 368–11 384, 2023. DOI: `10.1109/TPEL.2023.3288458`.

[78] G. Suresh, H. Toliyat, D. Rendusara, and P. Enjeti, *IEEE Transactions on Power Electronics*, vol. 14, no. 1, pp. 23–30, 1999. DOI: `10.1109/63.737589`.

[79] Y. Xie, J. Zhang, F. Leonardi, A. R. Munoz, M. W. Degner, and F. Liang, «Voltage stress modeling and measurement for random-wound machine windings driven by inverters», *IEEE Transactions on Industry Applications*, vol. 56, no. 4, pp. 3536–3548, 2020. DOI: `10.1109/TIA.2020.2986184`.

[80] M. Pastura et al., «Partial discharges in electrical machines for the more electric aircraft—part i: A comprehensive modeling tool for the characterization of electric drives based on fast switching semiconductors», *IEEE Access*, vol. 9, pp. 27 109–27 121, 2021. DOI: `10.1109/ACCESS.2021.3058083`.

[81] Y. Xie, J. Zhang, F. Leonardi, A. R. Munoz, M. W. Degner, and F. Liang, «Modeling and verification of electrical stress in inverter-driven electric machine windings», *IEEE Transactions on Industry Applications*, vol. 55, no. 6, pp. 5818–5829, 2019. DOI: `10.1109/TIA.2019.2937068`.

[82] A. Hoffmann and B. Ponick, «Method for the prediction of the potential distribution in electrical machine windings under pulse voltage stress», *IEEE Transactions on Energy Conversion*, vol. 36, no. 2, pp. 1180–1187, 2021. DOI: `10.1109/TEC.2020.3026531`.

[83] X. Ju, Y. Zhang, G. Liu, Y. Cheng, and S. Cui, «Interturn voltage stress comparison and analysis of different typology of hairpin windings for ev traction machines», *IEEE Transactions on Transportation Electrification*, vol. 11, no. 1, pp. 1257–1267, 2025. DOI: `10.1109/TTE.2024.3403148`.

[84] X. Ju et al., «Voltage stress calculation and measurement for hairpin winding of ev traction machines driven by sic mosfet», *IEEE Transactions on Industrial Electronics*, vol. 69, no. 9, pp. 8803–8814, 2022. DOI: `10.1109/TIE.2021.3116577`.

[85] S. Scheuermann, M. Doppelbauer, B. Hagemann, A. Jarosz, and B. Schmitz-Rode, «Validation of a slot-based high-frequency model of a hairpin winding stator in time-domain», in *2022 International Conference on Electrical Machines (ICEM)*, 2022, pp. 1648–1654. DOI: `10.1109/ICEM51905.2022.9910882`.

[86] M. Keller, T. Petri, M. Waldhof, F. Schuller, M. Maier, and N. Parspour, «Modeling the dynamic voltage distribution in electric traction motor windings and its application on hv optimal winding design», *IEEE Transactions on Industry Applications*, vol. 60, no. 3, pp. 3820–3829, 2024. DOI: `10.1109/TIA.2024.3357053`.

[87] J. Dittmann and B. Ponick, «Comparison of the measured and simulated potential distributions in an inverter-fed hairpin stator winding», in *IECON 2023- 49th Annual Conference of the IEEE Industrial Electronics Society*, 2023, pp. 1–5. DOI: `10.1109/IECON51785.2023.10312452`.

[88] H. Peng et al., «Voltage distribution modeling along stator windings in permanent magnet synchronous machines using coil-based grey box models», *IEEE Transactions on Energy Conversion*, vol. 39, no. 3, pp. 1994–2007, 2024. DOI: `10.1109/TEC.2024.3370800`.

[89] J. Jiang et al., «Comparative study of stranded and hairpin windings for 250kw continuous operation of high-speed heavy-duty ev traction motor», *IEEE Transactions on Industry Applications*, pp. 1–15, 2025. DOI: `10.1109/TIA.2025.3583649`.

[90] T. Zou et al., «A comprehensive design guideline of hairpin windings for high power density electric vehicle traction motors», *IEEE Transactions on Transportation Electrification*, vol. 8, no. 3, pp. 3578–3593, 2022. DOI: `10.1109/TTE.2022.3149786`.

[91] G. Berardi, S. Nategh, and N. Bianchi, «Inter-turn voltage in hairpin winding of traction motors fed by high-switching frequency inverters», in *2020 International Conference on Electrical Machines (ICEM)*, vol. 1, 2020, pp. 909–915. DOI: `10.1109/ICEM49940.2020.9270727`.

[92] K. G. N. B. Abeywickrama, T. Daszczynski, Y. V. Serdyuk, and S. M. Gubanski, «Determination of complex permeability of silicon steel for use in high-frequency modeling of power transformers», *IEEE Transactions on Magnetics*, vol. 44, no. 4, pp. 438–444, 2008. DOI: `10.1109/TMAG.2007.914857`.

[93] A. Moreira, T. Lipo, G. Venkataramanan, and S. Bernet, «High frequency modeling for cable and induction motor overvoltage studies in long cable drives», in *Conference Record of the 2001 IEEE Industry Applications Conference. 36th IAS Annual Meeting (Cat. No.01CH37248)*, vol. 3, 2001, 1787–1794 vol.3. DOI: `10.1109/IAS.2001.955774`.